THERMAL STRATIFICATION WITHIN URBAN STREET CANYONS: SARA3DCLIMAT FLOW SIMULATIONS

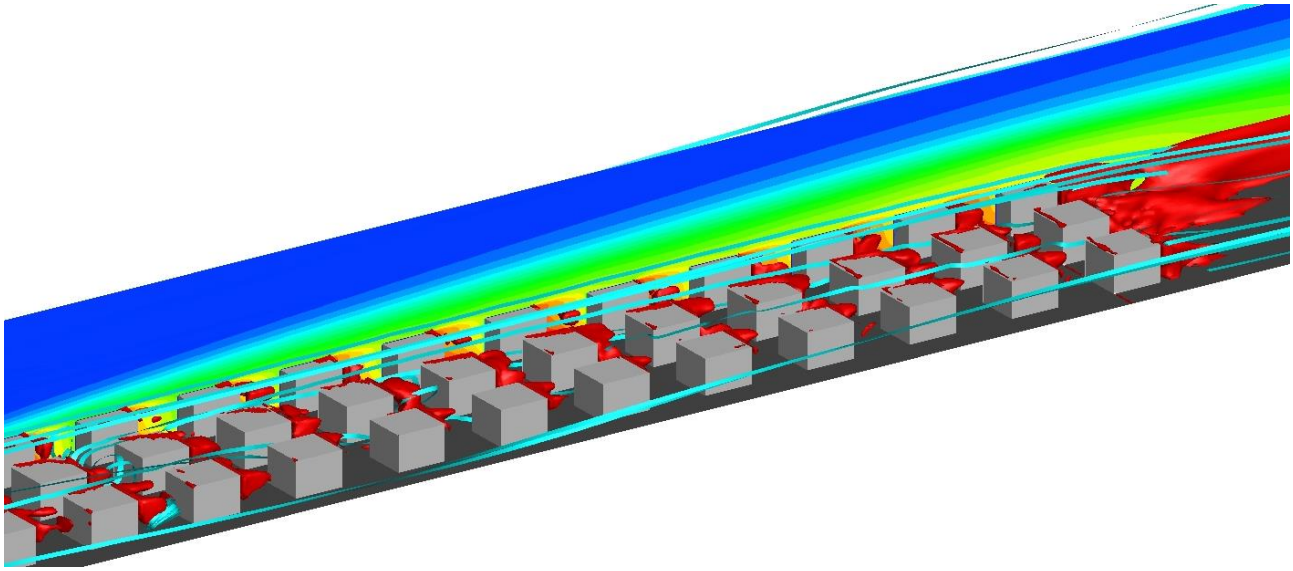

Prepared by:

M.P. Meyer

(4236440)

Supervisor:

Dr. *S. Kenjereš*

Reviewers:

Prof. Dr. C.R. Kleijn

Dr. S.R. de Roode

P.J.C Schrijvers

Prepared for:

DELFT UNIVERSITY OF TECHNOLOGY

FACULTY OF APPLIED SCIENCES

DEPARTMENT OF CHEMICAL ENGINEERING

TRANSPORT PHENOMENA SECTION

8 April 2014

Key words: Thermal stratification; Urban atmospheric flow; Turbulent Prandtl number; T-RANS; Hybrid LES/T-RANS

Cover page image: Illustration of part of the urban domain investigated, with a homogeneous city block array (grey block elements), for the weak unstable stratification case, with hybrid model. Cyan ribbons represent velocity stream trances. Red iso-surfaces bound locally stable stratified regions in the domain, as calculated by Eq. 2.4, depicting the presence of locally stable stratification under bulk unstable conditions. In the background, a temperature contour is plotted on the central y-plane; showing profiles within the urban street canyon, in addition to the urban atmospheric plume.

ACKNOWLEDGEMENTS

Firstly, I would like to thank my supervisor, Dr. Saša KENJEREŠ, of Delft University of Technology (TU Delft), for allowing me the privilege of conducting my master's thesis project with him. His continual motivation, enlightenment and support, coupled with his 'open-doors' policy and freedom of work style, made my project enjoyable and greatly aided in its successful completion. Special mention must be made of Dr. Kenjereš's enthusiasm for the field of advanced transport phenomena and development of his code (SARA3DCLIMAT), which was truly an inspiration. I wish him all the success with research and development of SARA3DCLIMAT and future projects.

Thanks must also go to everyone involved behind the scene. With continual encouragement, motivation and support from Thea and Marijke; as well as technical support from various PhD students at the Transport Phenomena group and ICT support staff during the project.

TERMS OF REFERENCE

This thesis report is submitted to the Transport Phenomena section, Department of Chemical Engineering, in partial fulfilment of the requirements for a degree of Master of Science (MSc) in Chemical Engineering (Process Engineering track), at the Delft University of Technology (TU Delft), for the academic year 2013/2014.

The thesis project, with 40 ECTS, had a period commencing at the start of the academic year (2nd of September 2013) and concluded with a final presentation and submission of this report on the 8th of April 2014.

The MSc project specific learning objectives are as follows, as adapted from [1, 2]:

1. Understanding, integration and application of fundamental scientific knowledge, to solving practical research problems at an MSc level.
2. Ensure a clear understanding of the problem and key questions to be addressed.
3. Active and responsible role in problem formulation, hypothesis proposition, research planning as well as project execution and hypothesis testing.
4. Utilise knowledge and technical expertise available within the field of research.
5. Follow safe practices, good conduct, competence and accuracy, while conducting research project.
6. Critically appraise hypothesis predicted results and actual achieved results.
7. Clearly, concisely and accurately convey research a finding in a final report, presentation, being capable of scientifically defending the research and findings, enticing scientific discussion and debate.

SYNOPSIS

For this study, Urban Heat Island (UHI) consequential urban atmospheric thermally stratified buoyancy influences were investigated, utilising an in-house Computational Fluid Dynamic (CFD) modelling code, SARA3DCLIMAT. The code is based on transient-Reynolds Averaged Navier-Stokes (T-RANS) and hybrid Large Eddy Simulation (LES)/T-RANS methods, with modification to dissipation coefficient to the turbulent kinetic energy dissipation conservation equation. For the study, it was hypothesised that SARA3DCLIMAT would be capable of accurately predicting thermally stable and unstable stratified turbulent urban atmospheric buoyancy flows.

In general, SARA3DCLIMAT simulated flow profiles showed strong temporal and spatial dependence, typical of turbulent flows; with SARA3DCLIMAT being found to accurately predict isothermal flow profiles. Varied degrees of accuracy in flow profiles were observed for the various investigated stratification cases, when compared to wind tunnel experimental data from Uehara *et al*. [3].

SARA3DCLIMAT found was capable of predicting expected temperature profiles, with steep temperature gradients towards street level and in the mixing layer between bulk and street canyon flows. From simulations, it was shown that the presence of the urban array and thermally stratified buoyancy flows could alter the average street canyon temperature by up to ±20%. However, in comparison to wind tunnel data from Uehara *et al*. [3], it was seen that in all cases, especially stable stratification, temperature profiles were grossly incorrectly over predicted for stable stratification and *vice versa* for unstable stratification. Generally, it was found that SARA3DCLIMAT was unable to capture turbulence dampening as observed in Uehara *et al*. [3].

Overall, the hybrid method was found to be more suited at predicting thermally stratified buoyancy flow profiles, than the T-RANS method. The hybrid method displayed better flow profile capturing with prediction of peak and bulge profiles, which were often not predicted by the T-RANS method. This can be attributed to the hybrid methods decrease in turbulent timescale and thus increased frequency

capturing, thereby allowing it to better model resolved turbulent profiles. However, the hybrid method was still found to be insufficient at predicting global stratification effects, particularly for turbulent supressing stable stratification; partly due to its foundations on high Reynolds flow models.

Various investigations into the effects of time step independence, effects of varied inlet velocity and turbulent kinetic energy dissipation profiles and altered turbulent Prandtl number constants were also conducted as further investigations for the improvement of SARA3DCLIMAT. Time step was shown to have negligible influence on statistical flow profiles, for the investigated systems; while due to turbulent spatial and temporal tendencies, sampling canyon and statistical period were shown to be important factors influencing statistical turbulence data. Isothermal inlet velocity profile was shown to have an influence downstream flow profiles, affecting re-circulation profiles and thus potential heat conduction rates; while changes to inlet turbulent kinetic energy dissipation profiles were found only to alter velocity deviation rates, due to changes to turbulent kinetic energy.

Investigations into influences of turbulent Prandtl number and local thermal stabilities revealed that both had significant influence on temperature and temperature deviation profiles, altering turbulent heat conduction rates and thus thermally stratified flow profiles. Local thermal stability was found to vary, even with constant bulk stability, in some cases even displaying local regions of reversed stability. Utilising calculations for local Richardson number and the Ellison model for calculation of turbulent Prandtl numbers, it was shown that the latter could have values ranging from 0.4 to infinity; although taken as constant in many CFD models, including those used in this study.

As preliminary investigations for future studies, an expanded and anisotropic turbulent heat flux model (Generalised Gradient Diffusion Hypothesis (GGDH)) was simulated; along with LES simulations, using Smagorinsky closure. Use of the anisotropic heat flux model was only found to significantly improve hybrid simulation accuracy, particularly with regard to advection and temperature profiles. This was due to more realistic heat

flux capturing and inclusion of shear stress flux contributions in GGDH and higher frequency capturing in the hybrid method. LES simulations were also found to result in improved simulation performance, due to the methods increased frequency capturing and general higher accuracy compared to T-RANS methods.

As a consequence of this study, the following potential areas of future investigation/improvement were recommended:

1. Conduct simulations with the hybrid model, utilising the GGDH model, modified inlet velocity profile and turbulent Prandtl number value of 0.4
2. Investigate a higher order, AFM turbulent heat flux model
3. Investigate a higher order ASM turbulent stress models
4. Addition of turbulent viscosity adaptation to the hybrid model
5. Adaption of SARA3DCLIMAT for local stability conditions, in particular stable stratification
6. Simplification of thermal stratification investigation geometry

CONTENTS

LIST OF ACRONYMS

AFM	Algebraic Flux Model
BSA	Burst Spectrum Analysers
CFD	Computational Fluid Dynamics
DNS	Direct Numerical Solutions
EDM	Eddy (turbulent) Diffusivity Models
EVM	Eddy (turbulent) Viscosity Model
GGDH	Generalised Gradient Diffusion Hypothesis
LDA	Laser Dopper Anemometer
LES	Large Eddy Simulation
MSc	Master of Science
PBL	Planetary Boundary Layer
RANS	Reynolds Averaged Navier-Stokes
SARA3DCLIMAT	Delft University of Technology in-house CFD simulation code
SGDH	Simple Gradient Diffusion Hypothesis
SMC	Second-Moment Closures
TP	Transport Phenomena
T-RANS	Transient Reynolds Averaged Navier-Stokes
TU Delft	Delft University of Technology
UBL	Urban Boundary Layer
UCL	Urban Canopy Layer
UHI	Urban Heat Island

LIST OF SYMBOLS

C_{μ}	k-ε model empirical coefficient
C_k	Convective transport of turbulent kinetic energy
C_p	Specific heat capacity [$J.kg^{-1}.K^{-1}$]
$C_{\varepsilon 1}$	k-ε model empirical coefficient
$C_{\varepsilon 2}$	k-ε model empirical coefficient
$C_{\varepsilon 3}$	k-ε model empirical coefficient
d	Space between buildings [m]
D_k	Turbulent kinetic energy diffusive rate
e	Energy [J]
F	Body force term [$Pa.m^{-1}$]
g	Gravitational force [$m^2.s^{-1}$]
G_k	Rate of turbulent kinetic energy production due to buoyancy
Gr	Grashof number
H	Building height [m]
h	Height [m]
H^s	Energy source term [$kg.J.m^{-3}.s^{-1}$]
J	Temperature wall function expression
k	Turbulence kinetic energy [m^2s^{-2}]
k_R	Residual turbulent energy
L	Length scale
L_k	Local rate of change of turbulent kinetic energy
n	Moles [mol]
N_x	Number of control volumes in the x-direction
N_y	Number of control volumes in the y-direction
N_z	Number of control volumes in the z-direction
p	Pressure [Pa]
$\wp$	Deviatory pressure
P_k	Rate of production of turbulent kinetic energy due to mean flow deformation
Pr	Prandtl number
q	Energy flux [$W.m^{-2}$]
q^s	Specific internal energy generation [$J.kg^{-1}.s^{-1}$)
R	Ideal gas constant [$J.K^{-1}.mol^{-1}$]
Re	Reynolds number
Ri	Richardson number
r^s	Mass source term [$kg.m^{-3}.s^{-1}$]
S_{ij}	Turbulent strain tensor
T	Temperature [K]

T^*	Dimensionless wall function temperature
T_a	Free stream atmospheric temperature
T_f	Street temperature
$\mathcal{T}$	Durbin time limiter
U	Streamwise velocity component [m.s^{-1}]
U^*	Dimensionless wall function streamwise velocity
U_{700}	Streamwise velocity component at height 700 mm [m.s^{-1}]
U_∞	Free-stream streamwise velocity component [m.s^{-1}]
V	Lateral velocity component [m.s^{-1}]
Vol	Volume [m^{-3}]
W	Vertical velocity component [m.s^{-1}]
x	x-coordinate
y	y-coordinate
y^*	Dimensionless wall function y-coordinate
z	z-coordinate
z_0	Roughness parameter [mm]
α	Thermal diffusivity [m^{2}s-1]
α^{hybrid}	LES/T-RANS hybrid parameter
β	Expansion coefficient [K^{-1}]
δ_{ij}	Kronecker delta function
∂_t	First order partial temporal derivative
∂_{x_i}	First order partial derivative with respect to variable x_i
$\partial_{x_i x_j}$	Second order partial derivative with respect to variable x_i and x_j
Δt	Time step
ε	Rate of turbulent energy dissipation
η_k	Kolmogorov length scale
λ	Thermal conductivity [W.m^{-1}.K^{-1}]
μ	Dynamic viscosity [Pa.s]
ν	Kinematic viscosity [m^2.s^{-1}]
ζ	AFM heat flux coefficient
ρ	Density [kg.m^{-3}]
σ_Φ	Standard deviation of variable ϕ
τ	Turbulent time scale
τ_{ij}	Viscous stress tensor
Φ	Variable ϕ
χ	Viscosity ratio

1. INTRODUCTION

1.1. Subject and Research goals

Air flow profiles within urban areas are of particular and increasing interest (for example refer to [4, 5, 6, 7, 8]), especially when considering current trends in population and urbanisation growth rates [9, 10, 11]. These factors not only result in higher population and building densities, but also increased pollutant emission, as well as increased hazard and risk potentials to harmful airborne substances [12, 13, 14, 15]; especially when compared to counterpart rural areas [16]. Therefore, the understanding and capability of predicting air flow profiles within urban areas are of great importance for urban area design; and in the formulation of emergency evacuation plans and procedures for airborne disasters.

Due to temporal and spatial dependences of air flow profiles, as well as their unpredictability, especially in highly turbulent urban areas [4, 6, 7, 17], field monitoring of urban atmospheric profiles is particularly challenging [18]. Thus scaling and/or simulation (the latter using computational fluid dynamics (CFD)) are useful tools in studying and therefore predicting urban air flow profiles.

An important factor affecting atmospheric flow is thermal stratification and its resultant buoyancy effects. Atmospheric thermal stratification in urban areas differs to in rural areas ("natural" conditions), due to a phenomenon known as the Urban Heat Island (UHI); whereby urban temperatures are different compared to natural conditions as a consequence of the urban area [17].

This report investigates thermal stratification influences on urban air flow profiles, as predicted by a Delft University of Technology (TU Delft) in-house code (SARA3DCLIMAT); along with simulated air flow profile accuracy validation with data available in literature.

1.2. Background to this study

Urban airflow patterns have been investigated at the Transport Phenomena (TP) group, since the conception of SARA3DCLIMAT by Saša Kenjereš, in 1999 [19]. The

code has been developed to simulate and predict climatic air flows and its properties, based on understandings of fluid flow mechanics.

This report builds on previous work with SARA3DCLIMAT; with the goal of expanding the knowledge of urban climatic flows within the TP group; in addition to investigating the simulation accuracy and applicability of SARA3DCLIMAT to atmospheric thermal buoyancy effects.

1.3. Research objectives

The objectives of this report are to:

- Outline the UHI effect and thermally stratified buoyancy influences on the urban atmospheric climate; with an overview of the current state of research and state of SARA3DCLIMAT.
- Investigate and discuss the effects of thermal stratification in urban areas, as predicted by SARA3DCLIMAT; along with comparisons to expectations.
- Compare and validate SARA3DCLIMAT with experimental findings of thermal stratification effects in urban areas, available in literature.
- Draw conclusions from the effects of thermal stratification in urban atmospheres; along with the applicability of SARA3DCLIMAT.
- Recommend potential areas of modification to SARA3DCLIMAT, with regard to urban atmospheric thermally stratified buoyancy flows; with possible areas of future investigation of- and expansion to SARA3DCLIMAT.

1.4. Limitations and Scope of Investigation

Investigations for this project were limited to a theoretical and numerical evaluation of thermally stratified influences in an idealised urban street canyon array. No practical experimentation was conducted as part of this study; instead suitable scientific data was used for simulation accuracy validation. Limitations were due to the inherent complexity of fluid flow, particularly in urban areas, time restrictions (project period: 02/09/2013 – 28/03/2014) and computational resource limitations.

The scope of the project is in the investigation of thermally stratified buoyancy influences on urban atmospheric air profiles, using SARA3DCLIMAT. Thus, the investigations of reactive components, solar radiation, geographical, geometric and other atmospheric influences were not conducted in this study. Additionally, the

modification and evaluation of previous SARA3DCLIMAT adaptations were also not investigated as part of this thesis; with only various in-build modules being utilised for investigation of applicability and usefulness.

1.5. Plan of Development

The report begins with an overview of urban climate classification, the UHI phenomenon and a literature review of thermally stratified buoyancy influences on the urban atmosphere (Chapter 2). This includes a discussion of the current state and techniques of research in the field, development of SARA3DCLIMAT with previous theses, as well as current challenges faced and gaps in the field.

In Chapter 3, challenges and gaps in the study of urban atmospheric thermally stratified effects are summarised and this project's hypothesis explicitly stated; along with an overview of the investigation and potential implications of the study.

Turbulent, non-isothermal atmospheric air flow theory is then highlighted in Chapter 4, with important factors and considerations for urban atmospheric thermally stratified flow simulation being discussed. Focus is given to the various modules available and already implemented in SARA3DCLIMAT, which will be used.

Research methodology is detailed in Chapter 1; beginning with an overview of the research case used for SARA3DCLIMAT verification, forming the basis of investigation. Experimental setup is then outlined, describing the various simulation domains, properties and boundary conditions used in the investigation; as well as the various SARA3DCLIMAT modules used and investigated in this study.

Investigation results are presented and discussed in Chapter 6; with simulated effects of thermal stratification being detailed discussed and compared to literature, expectations, as well as validated with scientific findings. Conclusions of the investigation of SARA3DCLIMAT and urban atmospheric thermally stratified buoyancy effects are then drawn in Chapter 7; with recommendations for potential areas of modification in SARA3DCLIMAT and future studies being stated and discussed in Chapter 8.

2. THERMALLY STRATIFIED BUOYANCY FLOWS

This chapter highlights the basic theory required to describe, understand and predict urban atmospheric thermally stratified buoyancy flow profiles, along with a scientific review of the effects of thermal stratification on urban climates. The chapter includes a summary of the development of SARA3DCLIMAT for its use in urban atmospheric simulation. To conclude the chapter, an overview of current and foreseen challenges is provided. Theoretical modelling and simulation tools are described in Chapter 4.

2.1. Urban atmospheric layer classification

Settlements by their very nature modify their environments; urban areas are no exception to this, with urban areas having noticeable and unique effects on their local (immediate) and global environment, such as on wind flow patterns, atmospheric humidity and energy balances [20], as outlined in section 2.2. Urban area structure and typical atmospheric profile patterns has led to the classification of several urban atmospheric layers [17, 21], as illustrated in Figure 2.1.

As shown in Figure 2.1, urban atmospheres consist of a Urban Canopy Layer (UCL), extending from ground level to approximately building roof height; typically on a micro-scale (10^{-2} – 10^{3} m) [17]. Above the UCL, the Urban Boundary Layer (UBL) extends up to the prevailing Planetary Boundary Layer (PBL). The UBL varies in thickness, depending on several factors, such as regional wind strength and intensity as well as UCL influences, but is typically on a local- to meso-scale (10^{2} – 10^{4} m and 10^{4} – 10^{5} m respectively) [17]. Focus of this study is the UCL, where the micro-scale profiles are typically more challenging to predict (as described in section 2.3.1) and influence on human activity is greatest [21].

2.2. Influences of urban areas on their climates

Urban areas have a noticeable and complex influence their local and global environments, affecting wind flow patterns, atmospheric energy balances and the consequential effects on flow profiles, described as follows.

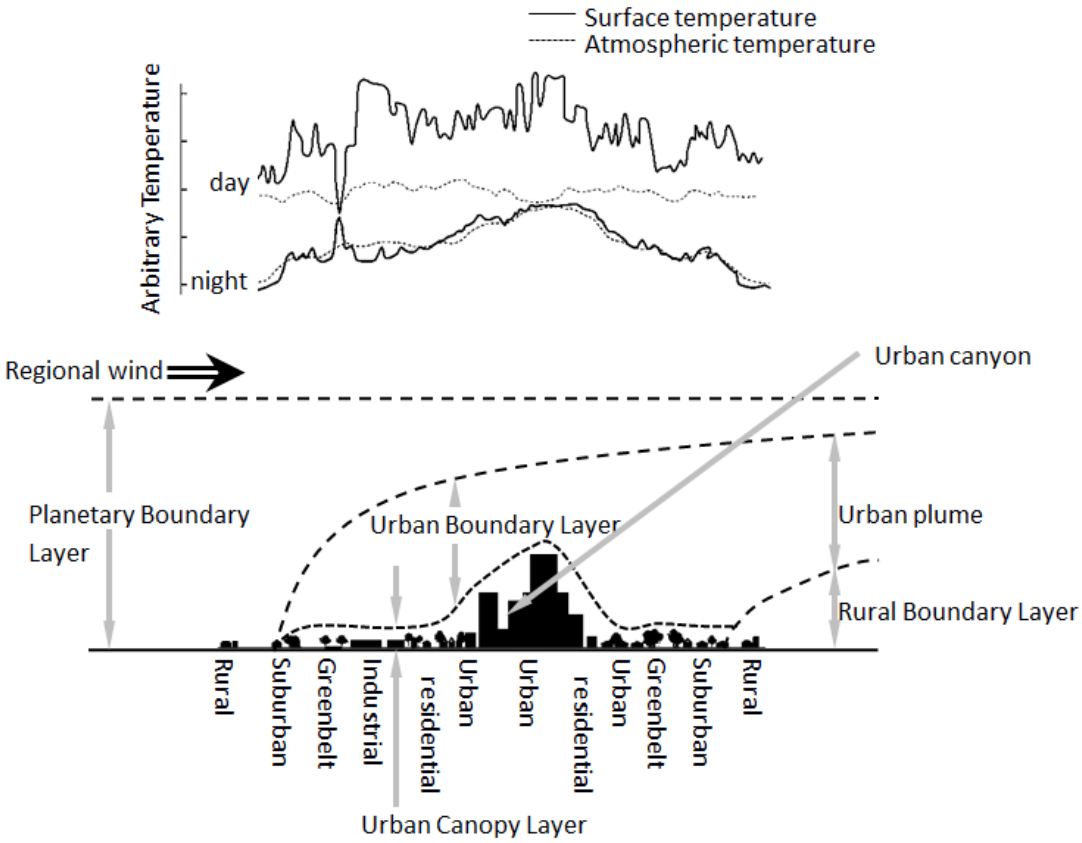

Figure 2.1: Illustration of urban temperature and atmospheric layer profiles

(modified from [22])

2.2.1. Urban area effects on wind flow patterns

Urban areas can have wind speeds reduced by up to 39% compared to rural areas [20], while the converse is also possible [23]. Urban structures, in addition to being obstructions, are typically more impermeable, taller, structurally denser and rougher than rural and natural structures (typical urban area roughness length: 1.5 – 10 m; compared to grassland roughness length: 0.0003 – 0.1 m [17]). Urban structures therefore result in the creation of more turbulent and smaller scale motions, often having unique micro climates [17]. Additionally, urban structures also result in the creation of the UBL, an intermediate transition layer between the turbulent UCL and prevailing PBL. Effects of urban structures on wind flow patterns are conveyed and often observed downstream, within the urban plume.

2.2.2. Urban area effects on atmospheric energy balances

There are several different and complex factors, which in combination can affect urban energy balances. Such factors include:

- Diurnal temperature cycle
- Geographical features
- Local meteorological conditions
- Latent heat effect (Evapotranspiration)
- Regional wind flow profiles
- Anthropogenic heat sources
- Urban geometric properties
- Urban structure radiative properties
- Urban structural thermal properties

Differences between these factors in urban and rural (natural) areas results in differing energy balances due to varied absorption and/or emission rates, thus energy accumulation (or dissipation). This translates into offsets between observed urban and rural climatic temperatures, as illustrated in Figure 2.1. The latter temperature offset phenomenon is known as the Urban Heat Island (UHI) effect and is discussed in further detail in section 2.2.3.

2.2.3. The Urban Heat Island (UHI) effect

Urban areas typically have differing simultaneous temperatures compared to their surrounding rural area (refer section 2.2.2), as illustrated in Figure 2.2; with definition of the UHI intensity:

$$UHI\ intensity \equiv \Delta T_u = T_u - T_r \qquad \text{Eq. 2.1}$$

UHI effects can occur in the urban sub-surface, surface and atmosphere [17], all being related and influencing each other; with UHI intensities being highly dependent on specific urban area and location properties [21, 17]. Settlement UHI atmosphereic effects have been shown to occur in locations with as low 1000 inhabitants [17].

Atmospheric and surface UHI effects, both located in the UCL, are of particular interest as both directly affect human wellbeing and activities [21]. Surface UHI

effects occur primarily during the day, with solar heating of urban structures. As illustrated in Figure 2.2, atmospheric UHI effects are mainly experienced during the night, mainly due to slow release of heat by urban structures; with nocturnal UHI intensities of up to 10°C [21]. Solar heating of urban structures, coupled with atmospheric properties and atmospheric UHI effects also results in the creation of steep daytime temperature gradients near urban surfaces (within 0.5 m), with more gradual gradients in the bulk UCL and atmosphere [7]. Atmospheric UHI effects are the focus of this study.

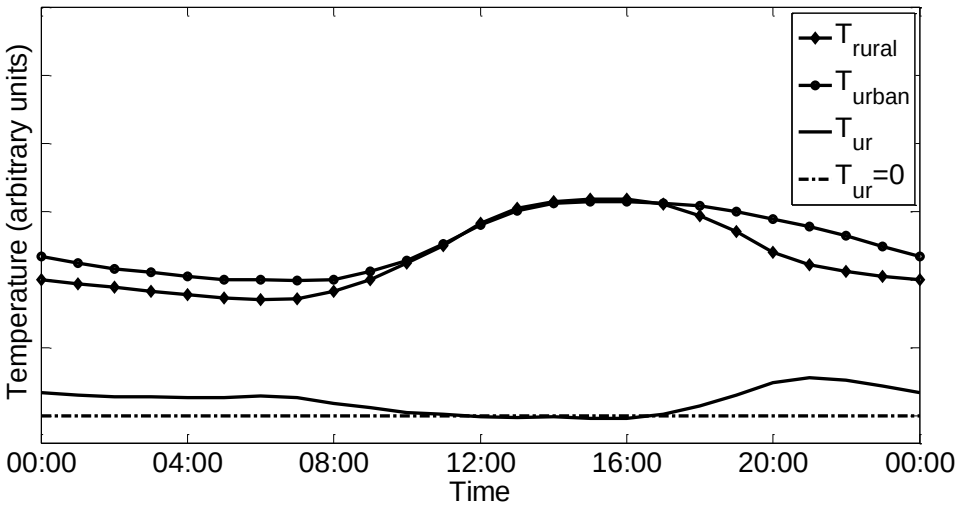

Figure 2.2: Illustration of typical atmospheric UHI intensities as a function of time

2.3. Thermal stratified buoyancy effects on urban atmospheres

The UHI influences urban temperature profiles (specifically atmospheric), thereby altering urban stratification and resulting in changes to air density profiles (illustrated by Figure 2.3 – refer to Appendix A.1), thus buoyancy and consequential convective flows. These stratification buoyancy effects are the focus of this investigation, with three classes of stratification being distinguishable, namely neutral, stable and unstable.

The remainder of this chapter discusses current research techniques used to study thermal stratified buoyancy effects (section 2.3.1), prediction using dimensionless numbers (section 4.2), types of stratification and their expected effects on the urban atmosphere (sections 2.3.3, 2.3.4 & 2.3.5), development of SARA3DCLIMAT (section 2.4) and current challenges faced in the field (section 2.5).

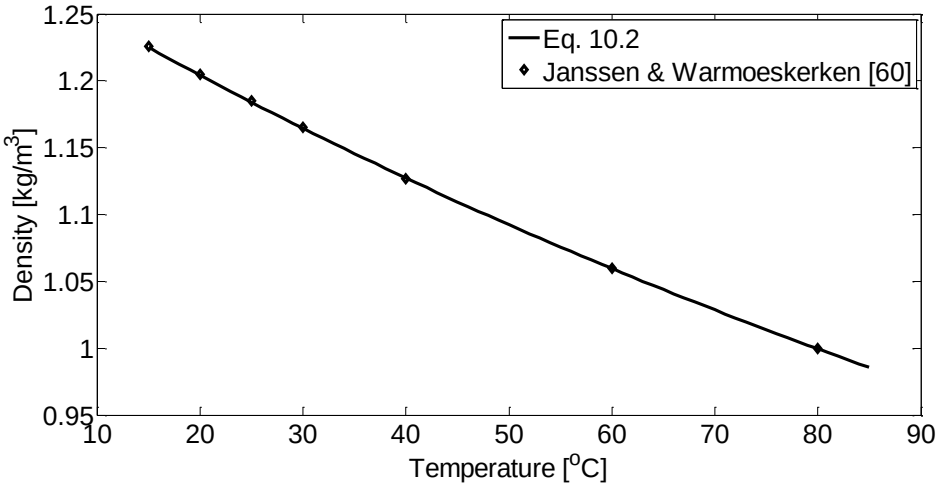

Figure 2.3: Relationship between atmospheric density and temperature

2.3.1. Research techniques

There are three main research methods for investigating urban thermally stratified buoyancy effects, namely field investigation, laboratory scale experimentation and computational simulation, as described below.

Field investigation of urban atmospheric stratification effects are typically conducted by measuring parameters in existing urban areas, utilising fixed point stations, mobile traverses, satellite imagery or combinations of the methods (for example: [7, 20, 18, 24, 25]). Field investigations allow for real time and space monitoring of atmospheric conditions in existing urban areas and have been conducted in a variety of locations and differing atmospheric conditions, such as Łódź, Poland [20]; Gaborone, Botswana [25] and Hannover, Germany [18]. Major challenges faced with field research investigations include the susceptibility to uncontrollable climate conditions and the scale of measurements required for accurate and useful investigation, especially when considering sizes of urban areas and their climatic micro-scales.

Laboratory experimentation for the study of urban stratification effects entails wind tunnel and/or water tank measurement studies of modelled and scaled urban area (for example: [3, 26, 27, 28]). Laboratory experiments have the advantage over field studies in that desired investigations conditions can be accurately controlled and manipulated (provided required systems are in place) and the domain size is often significantly reduced through scaling, thereby

decreasing spatial measurement requirements. Laboratory investigations still however pose many limitations to the study of urban thermal stratification, for example with limitations of spatial measurements (even though significantly reduced compared to field investigations) and an increase in the influence of scaling disturbances, such as flow pattern influences from instrumentation.

Computation simulation of urban stratification effects involve the mathematical resolving and/or modelling of the fluid flow governing relations, using Computational Fluid Dynamics (CFD). CFD simulations allow for temporal and spatial simulation of the domain of interest, thereby allowing for complete overview of the system under investigation, unlike field and laboratory investigations which only allow for measurements at certain locations. CFD also allows for the control and investigation of individual parameters, often not possible in field investigations and potentially complicated in laboratory studies. Major disadvantages of CFD is the questionable accuracy and validity of the resolved and/or modelled parameters, due to the use of various simplifications and modelling relations used to save on computational time and power requirements. Hence CFD simulations are often validated with field and/or laboratory studies for applicability validation.

2.3.2. Prediction techniques: Dimensionless numbers

Due to the complexity of atmospheric flow profiles and the effects of thermally stratified buoyancy, various dimensionless number ratios can be used for describing and predicting urban atmospheric flows. Dimensionless numbers, along with their importance in estimating and predicting urban thermally stratified buoyant flow profiles are highlighted as follows:

2.3.2.1. Reynolds number

Reynolds number (Re) is a measure of the importance of (forced) convective momentum transport (inertial effects) relative to diffusive momentum transport (viscous effects). Building and roughness Reynolds numbers ($\mathrm{Re_H}$ and $\mathrm{Re_{z_0}}$ respectively) are defined as follows:

$$Re_H \equiv Re = \frac{\rho U_\infty H}{\mu} = \frac{U_\infty H}{\nu} \qquad \text{Eq. 2.2}$$

$$Re_{z_0} = \frac{\rho U_{z_0} z_0}{\mu} = \frac{U_{z_0} z_0}{\nu}$$ Eq. 2.3

At (building) Reynolds numbers less than 2500, flow is typically governed by viscous forces and will tend to be smooth and constant, that is laminar; while at higher Reynolds numbers, flow will be governed by inertial forces and tend to be chaotic and turbulent. Thus the Reynolds number is an indication of the degree of convective turbulence, with higher Reynolds numbers ($\mathrm{Re} > 2500$) typically being turbulent. Urban atmospheric flows have Reynolds numbers typically greater than a critical value (Re_{cr}) of 4000 [29]; urban flows can therefore be considered turbulent.

2.3.2.2. Richardson number

The Richardson number is a general measure of the potential gravitational buoyant energy and the kinetic energy; with two types being defined, namely: local (or flux) and bulk Richardson numbers.

The Richardson flux number is defined as the ratio between local buoyant turbulent kinetic energy (thermal) production (G_k) to the local shear turbulent kinetic energy (mechanical) production (P_k) (Eq. 2.4); with the turbulent flow terms being discussed further in section 4.3.

$$Ri_f = -\frac{G_k}{P_k} = -\frac{g_i \beta \left(\overline{T' U_i'}\right)}{\left(\overline{U_i' U_j'}\right) \partial_{x_j} \left(\overline{U_i}\right)}$$ Eq. 2.4

The bulk Richardson number is defined as the bulk fluid buoyant turbulent kinetic energy relative to the bulk shear turbulent kinetic energy. Therefore, the bulk Richardson number can be calculated from the ratio between the Grashof number and the square of the Reynolds number (Eq. 2.5). Where the Grashof number is a measure of the buoyant momentum transport (natural convective buoyant effects), relative to the diffusive momentum transport (viscous effects). Thus, Grashof number is the Reynolds number equivalent for natural convective (buoyancy) flows.

$$Ri_b \equiv Ri = \frac{Gr}{Re^2} = -\frac{gH\beta\Delta T}{U_\infty{}^2} \qquad \text{Eq. 2.5}$$

When a system is isothermal, that is there are no temperature gradients, Richardson numbers will be zero and the system is said to be neutrally thermal stratified. With this case, temperature will have no influence on the buoyancy and hence turbulent energy ratios and resultant flow profiles.

Due to the dependence of Richardson numbers on temperature gradients, Richardson numbers can have varied magnitudes, depending on local and bulk degrees of heating; but are typically of magnitude less than unity [7]. Additionally, as temperature gradients can be in any direction, Richardson numbers can also be positive or negative. That is, a positive temperature gradient (increasing temperature with increasing height, for example with the ground temperature warmer than ambient air), Richardson numbers will be positive. In this case, systems are said to be stably stratified, as warmer, less dense air will naturally tend to remain above denser cooler air. The converse is also possible, that is with a negative temperature gradient systems will be unstably stratified. Unstable as warmer, less dense air will tend to naturally move upwards, displacing cooler denser air and *vice versa*. Hence the Richardson number can be used to determine local and bulk stratification conditions, as well as the stratification extent.

Local Richardson numbers can be used as indications if thermal stratification is turbulent kinetic energy enhancing, or destructing; with the boundary between the two conditions being defined by the critical Richardson number (Ri_{cr}). Typically, positive Richardson flux numbers (indicating stable stratified conditions), result in decreased thermal turbulent kinetic energy, up to the critical Richardson flux number, at which turbulent flow breaks down, re-laminating; with the converse case also being true. Under local equilibrium flow conditions, the critical Richardson number for inviscid fluids is 0.25 [30]; while for atmospheric flow conditions it has shown to range from 0.08 to 0.4 [31], with typically 0.1 being used [32]. Urban climates can have varying Richardson numbers (of magnitude orders typically less than unity [7]), depending on their local and bulk degrees of heating and Reynolds numbers.

2.3.2.3. Prandtl number

The Prandtl number (Pr) is a measure of the importance of momentum diffusivity relative to the thermal diffusivity. There are two types of Prandtl number important for urban atmospheric flows, namely molecular and turbulent Prandtl numbers which can be respectively defined as follows:

$$Pr = \frac{\nu}{\alpha} = \frac{\mu C_p}{\lambda} \qquad \text{Eq. 2.6}$$

$$Pr_t = \frac{\nu_t}{\alpha_t} = \frac{\mu_t C_p}{\lambda_t} \qquad \text{Eq. 2.7}$$

Typically, at low Prandtl numbers ($Pr \ll 1$), thermal diffusivity typically dominates, thus heat conduction is the main method of heat transfer; whereas at high Prandtl numbers ($Pr \gg 1$), momentum diffusivity dominates, thus heat is mainly transferred by convection, rather than by heat conduction.

Urban areas typically have an atmospheric molecular Prandtl number between 0.70 and 0.72, being dependent on the atmospheric temperature, as illustrated in Appendix A.5. Thus momentum and thermal diffusivities will be equally important in urban atmospheric flows.

The turbulent Prandtl number for atmospheric conditions shows a strong dependence on thermal stratification conditions, particularly with stable stratified conditions. The turbulent Prandtl number for unstably stratified conditions can vary between 0.3 and 1.4; while for stable stratified conditions it can vary between 1 and 100 [32]. The latter is illustrated by relation between Richardson flux number (Ri_f) and turbulent Prandtl number (Pr_t) in Figure 2.4. Many CFD models, including SARA3DCLIMAT, make use of a constant turbulent Prandtl number, with value depending on the domain and model, refer to section 4.3.

2.3.2.4. Viscosity ratio

The viscosity ratio (χ) is the ratio of the turbulent (eddy) viscosity to the molecular viscosity, as shown in Eq. 2.8. This ratio is used to determine the

presence and measure the influence of turbulence, by comparing turbulent and molecular stress strengths. Typically, viscosity ratios of greater than 100 indicate the presence of turbulent flows.

$$\chi = \frac{\mu_t}{\mu} \qquad \text{Eq. 2.8}$$

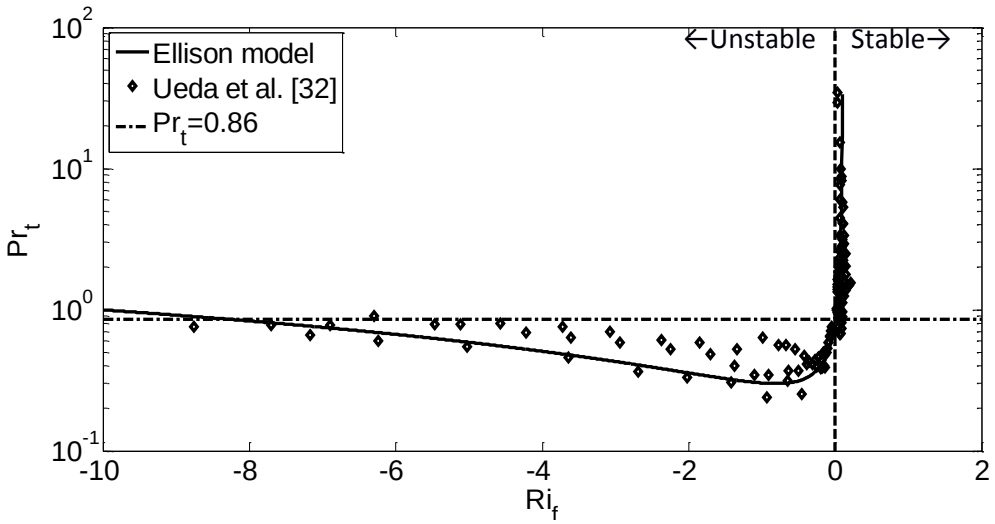

Figure 2.4: Relationship between turbulent Prandtl and Richardson number

(Modified from Ueda et al. [32], refer to section 4.3.2.5)

2.3.3. Effects of neutral stratified buoyancy

Neutral stratification occurs with isothermal conditions, when there are no temperature gradients. Thus with neutral stratification, temperature will have no influence on urban atmospheric profiles, behaving as a passive scalar.

Neutral stratification conditions can be expected to be a median between stable and unstable stratification conditions, with the former tending to be governed by damped-Reynolds type flow, decreasing turbulence, while the latter tends to be governed by buoyancy and be turbulence enhancing. The expected median characteristics can be observed from Uehara *et al*. wind tunnel experimental research [3], where neutral stratification can be seen to be the median between stable and unstable parameters, such as stress and flow variance profiles.

The neutral stratification condition is therefore the investigation control, for comparison of thermal stratified buoyancy effects on urban atmospheric profiles.

2.3.4. Effects of stable stratified buoyancy

Stable thermal stratification occurs in urban atmospheres when the air temperature gradient is positive, for example when air temperature is greater than ground temperature; hence with positive Richardson numbers.

With stable thermal stratified flow, denser fluid tends to flow beneath less dense fluid, with reduced interaction drive and turbulence between the stratification layers, compared to neutral stratified flows. Thus, there can be expected to be reduced turbulence, shear and dampening of parameters due to stable stratification, potentially resulting in flow re-laminating within street canyons.

The dampening of parameters can be seen with the decrease in stream-wise velocity compared to isothermal conditions in smoke rake experiments by Ogawa *et al*. [33] and Ohya *et al*. [34], from decreases in magnitude of street canyon velocity and shear from experiments by Uehara *et al*. [3], and from observed negative second order correlations from Ueda *et al*. [32].

Re-laminating of street canyon atmospherics, was observed in the work by de Haan [35], whereby it resulted in divergent SARA3DCLIMAT simulations, due to decreased Reynolds flows and the inability of the code to simulate low Reynolds flows at that stage. Flow lamination was also apparent in the work by Uehara *et al*. [3] for the strongly stable stratification case, were the stream-wise velocity within the street canyon approaches zero.

Stable thermal stratification has also been show to increase the turbulent Prandtl number (see [36, 32]), thereby illustrating a decrease in the influence of thermal stratification and buoyant flows to turbulent flows and an overall suppression of turbulence with stable stratification.

2.3.5. Effects of unstable stratified buoyancy

Unstable thermal stratification occurs in urban atmospheres when the air temperature gradient is negative, for example when air temperature is cooler than ground temperature; hence with negative Richardson numbers.

With unstable thermal stratified flow, denser fluid tends to flow above less dense fluid, with increased natural tendency to interact and the less dense fluid to displace the denser fluid (and *vice versa*) between the stratification layers compared to isothermal conditions. Thus unstable stratification can be expected to enhance turbulence, increasing shear and amplification of flow parameters, as a result of the induced buoyant convective flow, typically within the forced air flow. The enhancing fact can also be observed from the work of Ogawa *et al*. [33] and Uehara *et al*. [3], where increased unstable stratification resulted in increased turbulence due to buoyant flows.

2.4. Previous theses with SARA3DCLIMAT

The Development of SARA3DCLIMAT by the TP group, led by Saša Kenjereš, over the years by the work of various theses is summarised in Table 2.1 . Note that the summary discusses fluid flow phenomena theory which is expanded in Chapter 4.

2.5. Current challenges in thermal stratification research

The main challenge experienced with field and laboratory thermal stratification studies is the spatial and temporal resolution of parameter determination to a finite number of points and time intervals, in the domains of interest. The latter thereby limits the extent of investigation, especially of concern for highly variable urban micro-climates. Instrumentation also potentially interferes with measurements, thereby affecting flow profiles within the urban atmosphere. Additionally, field and laboratory studies are also typically intensive and time consuming processes, with the almost inability for condition manipulation with field studies.

CFD simulation offers an alternative to field and laboratory experiments, with an ability to determine parameters at every temporal and spatial point in the domain, allowing for a complete domain overview. Current computational power results in use of simplifications, approximations and modelling with CFD simulations to reduce simulation complexity, therefore decrease computational periods and increasing stability. This therefore results in the need for validation of CFD simulations with field and/or laboratory experimentation, or at least complete resolution of the domain of interest to obtain non approximated solutions.

CFD simulation of thermally stratified buoyant flows is particularly challenging due to the variable nature of urban atmospheres, the nature of stratification effects (namely turbulence enhancing or inhibiting), and the current nature and design of CDF techniques. Current CFD techniques are based on high Reynolds flows, making them numerically unstable for the low Reynolds (laminar type) flows which are commonly experienced with stable stratified turbulent supressing flows, as has been experienced with SARA3DCLIMAT [35].

Table 2.1: Development of SARA3DCLIMAT

Year	Description	Ref
1999	Foundation, numerical modelling of buoyancy-driven flows as well as the accuracy and usefulness of T-RANS and a T-RANS/LES hybrid.	[19]
2006	Study of turbulent and dispersion flows over hills and in urban landscapes, investigating the effects of time scale limiters and a hybrid T-RANS/LES model. Validated turbulent kinetic energy and dispersion with field and experimental results.	[37]
2008	Case study of SARA3DCLIAMT with the TU Delft campus, highlighting the limitations of simulations with fixed point boundary conditions and choice of domain compared to actual system.	[23]
2009	SARA3DCLIMAT modifications, including improved mesh refinement procedures wall functions and roughness. Inclusion of vegetative models into the code.	[38]
	Additional vegetative models to SARA3DCLIMAT and validation with wind tunnel experiments.	[39]
2010	Modification of the standard k-ε turbulence model, investigating the effects of Durbin time scale limiter and the Renormalisation Group (RNG) model.	[40]
	Modification of the standard k-ε turbulence model, investigating the effects of Durbin time scale limiter RNG model and a hybrid T-RANS/LES model.	[41]
2012	Expansions of the hybrid model, inclusion of a turbulent viscosity closure modification, as well as investigations on LES filter length.	[42]
	Expansion of hybrid modelling [41] and addition of reactive modelling to SARA3DCLIMAT, with a proof of concept study.	[43]
	Comparison of turbulent model modification effects on accuracy and inclusion of thermally buoyancy effects into SARA3DCLIMAT.	[44]
2013	Continuation of work by Verdult [44] into thermally stratified buoyancy effects (one unstable and one stable case), with validation with wind tunnel experimentation.	[35]

3. HYPOTHESIS

This chapter summarises current gaps in CFD simulation of urban atmospheric thermally stratified buoyancy flows, specifically highlighting gaps within SARA3DCLIMAT. Additionally, the study's hypothesis is explicitly stated, followed by an overview of required investigations; with the chapter concluding with a discussion of potential implications of the study.

3.1. Gaps in the field of urban thermally stratified buoyancy flow simulation

The UHI and resultant thermally stratified buoyancy effects are of great influence on urban flow profiles and micro-climates; resultant from enhanced or supressed thermal buoyant turbulence. Investigations into urban thermally stratified buoyancy flow effects can be conducted by field studies, laboratory experiments and/or CFD simulation. The use of CFD is a viable alternative, offering significant advantages over other techniques (refer to section 2.5); allowing for profile determination in the entire spatial and temporal domain of interest. However, due to the complexity in fluid flow phenomena, current computational capabilities as well as various simplifications and modifications, the use of CFD for practical engineering applications is restricted and requires validation.

From a literature review of thermally stratified buoyancy effects, it can be seen that little work has been conducted on stably stratified conditions; due to its turbulent supressing nature, historical development of CFD models for high Reynolds flows and because of the complexity of urban atmospheric flows. Thus, there is a need for a generic CFD model that is capable of accurately predicting atmospheric profiles for a variety of atmospheric stratified buoyancy conditions, while maintaining simplicity and reduced computational requirements: the goal of SARA3DCLIMAT.

3.1.1. Gaps in SARA3DCLIMAT for use in urban atmospheric simulation

Since its conception, SARA3DCLIMAT has been expanded, modified and validated for a number of urban atmospheric applications, including the addition of a successful porous vegetative model [38]. It was not until recently that urban

atmospheric thermal buoyancy effects were investigated [44, 35], with limited success due to divergent and inconclusive solutions, especially with stably stratified conditions. As a result of the work by de Haan [35], the code has been modified and updated; however, these updates, along with a more extensive study of SARA3DCLIMAT, are yet to be investigated and validated.

3.2. Hypothesis

SARA3DCLIMAT, along with various investigated modules and options, will be capable of simulating thermally stable and unstable stratified buoyant turbulence and flow profiles; being comparable to and validated with laboratory experimental findings from Uehara *et al*. [3] (refer to section 5.1).

3.3. Overview and extent of investigation

The proposed study will involve the validation of the hypothesis by investigating the effect of thermally stratified buoyancy (stable and unstable) on wind speed profiles (velocity, shear stress and velocity variances) and temperature profiles (including temperature variances), utilising various CFD techniques integrated into SARA3DCLIMAT (refer Chapters 4 & 1). Findings will be compared to non-buoyant (isothermal) simulation results, investigating stratification effects on flow profiles.

Additionally, hypothesis justification and confirmation of SARA3DCLIMAT applicability to urban thermal stratification cases will involve validation of simulation findings with experimental findings from Uehara *et al*. [3]. Hence, the study will mimic Uehara *et al*. [3] experimental conditions as closely as possible for fair and comparable validation. Due to project limitations, further field and/or laboratory experimentation will not be conducted as part of the study.

3.4. Implications of research

Studies of thermal buoyancy effects, particularly in urban climates and investigations on the hypothesis will have substantial benefits to the field of CFD, the development of SARA3CLIMAT as well as for use in urban development and planning research, discussed as follows:

3.4.1. Implications for CFD and SARA3DCLIMAT

This study expands the understandings of atmospheric flows within the TP group, adding knowledge on thermal buoyancy effects within urban atmospheres; as well as building to the validation and improvement of SARA3DCLIMAT, in its ability to predict urban atmospheric flow profiles.

Validation of the proposed hypothesis will confirm the capability and accuracy of SARA3DCLIMAT in predicting atmospheric thermal buoyancy effects, an important atmospheric influence. This will allow for the further development of SARA3DCLIMAT into a more robust, capable and universal atmospheric simulation tool, potentially with the future inclusion of solar radiation effects, reactive atmospheric components, particulate density buoyancy effects, as well as humidity-cloud coverage and precipitation effects, within realistic urban areas. Validation of the hypothesis opens the additional possibility for use of SARA3DCLIMAT for a variety of engineering applications involving buoyant heat transfer, such as in furnaces, nano-reactors and electronics.

Disproval of the proposed hypothesis, although not desired, will also aid in the development of SARA3DCLIMAT, by identification of potentially problematic areas and issues of concern; with possible solutions and recommendations being provided as a result of this study.

3.4.2. Implications for urban planning and development

UHIs and consequential thermal stratification and buoyancy influences have great impact on urban atmospheres. Thus, the ability to understand and predict their effects has several implications and advantages for urban planning and development. For example in the corrective re-design of current and better design of future urban areas, or in assistance with formulation of emergency evacuation plans; all without the need for field and/or scaled experimentation.

4. FLUID FLOW PHENOMENA THEORY

In this chapter, the various theoretical tools are discussed; which form the foundation of SARA3DCLIMAT and are utilised and investigated as part of this study into the effects of thermally stratified buoyancy effects in urban atmospheres and validity.

The chapter begins by outlining the governing fundamental fluid flow conservation equations, along with various assumptions and simplifications applicable for this study (section 4.1). Various methodologies used to solve the conservation equations are then outlined (section 4.2), with further detail being given, in subsequent sections, on the closure problem techniques used in SARA3DCLIMAT for this study.

4.1. Conservation laws

Although urban atmospheric flow profiles can be complex, often displaying regions of both laminar and turbulent flow [45, 46], it is believed that the flow profiles can be exactly described by a set of governing fluid flow phenomena conservation equations; in the case of this study: for mass, momentum and energy. These conservation laws can be written in terms of generic instantaneous differential equations, respectively [47, 48]:

$$\partial_t(\hat{\rho}) + \partial_{x_i}(\hat{\rho}\,\hat{U}_i) = \hat{r}_i^s \qquad \text{Eq. 4.1}$$

$$\partial_t\left(\hat{\rho}\,\hat{U}_i\right) + \partial_{x_j}\left(\hat{\rho}\,\hat{U}_j\,\hat{U}_i\right) = -\partial_{x_i}\left(\hat{p}\right) - \partial_{x_j}\left(\hat{\tau}_{ij}\right) + \hat{F}_i \qquad \text{Eq. 4.2}$$

$$\partial_t\left(\hat{\rho}\,\hat{e}\right) + \partial_{x_j}\left(\hat{\rho}\,\hat{U}_j\,\hat{e}\right) = -\partial_{x_j}\left(\hat{q}_i^s\right) + \hat{H}_i^s \qquad \text{Eq. 4.3}$$

4.1.1. Air property assumptions

The three governing conservation equations (Eq. 2.1, Eq. 2.2 and Eq. 2.3) are generic and describe fluid properties for any fluid in continuum. However, for the case of urban atmospheric flows, several assumptions for fluid properties can be made for simplification of the conservation equations, namely:

1. Air is an ideal gas, being incompressible and affected only by gravity (no other forces).
2. Air has constant physical properties with the exception of density (refer to points 3 and 4).
3. Air density variations (ρ') are negligible, except when multiplied by the effects of gravity (the Boussinesq approximation).
4. Density variations, when applicable, are given by the thermal expansion expression: $\rho = \rho_{ref}\left(1 - \beta\left(T - T_{ref}\right)\right)$.
5. Air is a Newtonian fluid, with linear viscous stresses as defined by Newton's law.
6. Air is a Fourierian fluid, with heat transfer defined by Fourier's law.
7. Air is assumed to be dry and contain only unreactive species of uniform concentration, thus there are no mass and/or energy sources/sinks.

4.1.2. Simplifications to the conservation equations

Making use of the above assumptions for the urban atmospheric system to be investigated (section 4.1.1), the conservation equations (Eq. 4.1, Eq. 4.2 & Eq. 4.3) can be simplified and re-written in the following instantaneous forms (as shown in Appendix B):

$$\partial_{x_i}(\hat{U}_i) = 0 \qquad \text{Eq. 4.4}$$

$$\bar{\rho}\partial_t\left(\hat{U}_i\right) + \bar{\rho}\hat{U}_j\partial_{x_j}\left(\hat{U}_i\right) = -\partial_{x_i}\left(\hat{\wp}\right) + \mu\partial_{x_j x_j}\left(\hat{U}_i\right) - g_i\bar{\rho}\beta\left(\hat{T} - \bar{T}\right) \qquad \text{Eq. 4.5}$$

$$\bar{\rho}\partial_t\left(\hat{T}\right) + \bar{\rho}\hat{U}_j\partial_{x_j}\left(\hat{T}\right) = \frac{\mu}{Pr}\partial_{x_j x_j}\left(\hat{T}\right) \qquad \text{Eq. 4.6}$$

4.2. Conservation law solution techniques

The conservation equations, even when simplified for the urban atmospheric system under investigation (Eq. 4.4, Eq. 4.5 & Eq. 4.6), are non-linear partial differential equations of higher order, which together with urban geometric, turbulent and micro-climatic features, make them complex and challenging to solve directly. Thus, numerical techniques are often used to determine resolved and/or modelled solutions to the conservations equations; with discretisation of the

domain into a number of control volumes confined within the spatial and/or temporal boundary of the system [49]; the basis of CFD simulation methods.

4.2.1. Complete resolution techniques

Complete resolution techniques entail the full numerical discretisation of the conservation equations for the period and domain of interest; in order to numerically solve fluid flow profiles at every spatial and temporal instant; as is done with Direct Numerical Simulation (DNS) methods. These methods result in highly irregular and oscillatory flow profiles, being dependent on the spatial location and temporal instant; as illustrated with the instantaneous velocity (Û) profile in Figure 4.1.

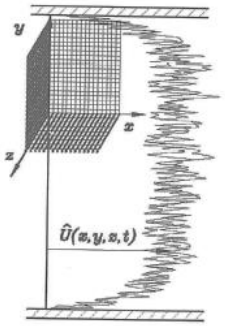

Figure 4.1: Illustration of instantaneous profiles obtained from DNS [49]

Figure 4.1 also depicts the relative control volume size; as compared to other CFD simulation techniques (refer to Figure 4.2 & Figure 4.3). Reasons for the comparatively finer control volume resolution is due to DNS methods having to resolve the conservation equations for a range of flow profiles and eddy scales, namely from large energetic eddies to small dissipative eddies at the Kolmogorov scale. Hence, DNS methods require resolutions of at least local Kolmogorov scales in order to fully resolve turbulent flow profiles [46, 49] (refer Appendix C). These required spatial and temporal resolutions make DNS methods extremely computationally expensive, thereby limiting their usage to systems with low Reynolds flows (laminar like flow) and simplistic geometries [49, 50]. For the urban atmospheric system to be investigated, it can be shown that the required spatial and temporal resolutions would be of the order 10^{-4} m ($\approx 10^{12}$ domain control volumes) and 10^{-3} s respectively (calculations in Appendix C).

Thus, for practical engineering application, the only viable approach for fluid profile simulation with current computational capabilities is to pre-process and model the conservations equations (in partial of fully), prior to their discretisation and simulation [49]; thereby decreasing the computational requirements and strain. Pre-processing and modelling techniques are discussed in the following sub-section.

4.2.2. Modelling techniques

In order to decrease the computational complexity required to numerically resolve the conservation equations, they are often simplified by pre-processing and modelling techniques, using various possible methods. The principle behind modelling techniques is that instantaneous variables can be decomposed into average ensemble values and fluctuations from these average terms (known as Reynolds decomposition); being subsequently filtered (if required by the modelling technique) and the conservations equations simplified using averaging methods. There are two main groups of averaging techniques, namely Reynolds Averaged Navier-Stokes (RANS) and Large Eddy Simulation (LES).

4.2.2.1. Reynolds Averaged Navier-Stokes

RANS methods entail statistically ensemble averaging the conservation equations; typically in time, for stationary systems in which time scales do not vary significantly compared to turbulence scales [49]. Thus, with RANS methods, the conservation equations are effectively modelled with their mean flow properties, rather than instantaneous properties, as illustrated in Figure 4.2; with the time averaged velocity ($\overline{U}$) profile of the instantaneous profile that is shown in Figure 4.1.

Due to the modelling of fluid phenomena with their statistically averaged values, RANS methods are less influenced by profile fluctuations, thereby substantially reducing the computational complexity as well as spatial and temporal resolutions (as illustrated with grid resolutions compared to DNS methods (Figure 4.1)). Thus, RANS methods can be utilised for systems with high Reynolds flows and complex geometries, where ensemble variations are not of great influence or accurate and exact solutions necessary.

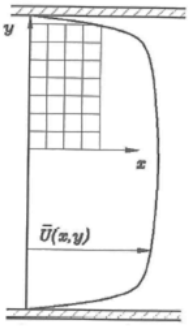

Figure 4.2: Illustration of time averaged profiles obtained from RANS [49]

RANS simplification and ensemble averaging techniques result in conservation laws being dependent on statistically averaged profiles and turbulence correlations; as illustrated from time averaged RANS conservation equations (Eq. 4.7, Eq. 4.8 and Eq. 4.9) derived from the simplified conservation equations (section 4.1.2) (steps provided in Appendix C).

$$\partial_{x_i}\left(\bar{U}_i\right)=0 \qquad \text{Eq. 4.7}$$

$$\bar{\rho}\partial_t\left(\bar{U}_i\right)+\bar{\rho}\bar{U}_j\partial_{x_j}\left(\bar{U}_i\right)=-\partial_{x_i}\left(\bar{\wp}\right)+\partial_{x_j}\left\{\mu\partial_{x_j}\left(\bar{U}_i\right)-\bar{\rho}\left[\left(\overline{U_i^{'}U_j^{'}}\right)\right]\right\} \qquad \text{Eq. 4.8}$$

$$\bar{\rho}\partial_t\left(\bar{T}\right)+\bar{\rho}\bar{U}_j\partial_{x_j}\left(\bar{T}\right)=\partial_{x_j}\left\{\frac{\mu}{Pr}\partial_{x_j}\left(\bar{T}\right)-\bar{\rho}\left[\left(\overline{T^{'}U_j^{'}}\right)\right]\right\} \qquad \text{Eq. 4.9}$$

From the above RANS conservation equations it can be seen that the second order turbulence correlations are enclosed in parentheses (round brackets) and are the only additional terms, compared to instantaneous conservation equations. Solution methods for the above RANS conservation equations and their turbulence correlations are highlighted in sections 4.2.2.3 (along with those for LES) and 4.3. The above RANS correlations contain turbulence information which is lost due to Reynolds averaging and have the following physical interpretations:

$-\bar{\rho}\left(\overline{U_i^{'}U_j^{'}}\right)\equiv\tau^t{}_{ij}$ — **turbulent stress tensor**: turbulent transport of momentum per unit volume ($\bar{\rho}U_i'$) by velocity fluctuation (U_j').

$C_p\bar{\rho}\left(\overline{T^{'}U_j^{'}}\right)\equiv q^t{}_j$ — **turbulent heat flux vector**: turbulent transport of enthalpy per unit volume ($C_p\bar{\rho}T'$) by velocity fluctuation (U_j').

4.2.2.2. Large Eddy Simulation

With LES methods, small spatial and/or temporal sub-grid scale motions, which are smaller than a predefined filter scale, are statistically modelled, similar to RANS ensemble averaging techniques; while larger scale motion is directly resolved in time and space, as done with DNS methods. The partial filtering typically results in decreased small instantaneous variation capturing (compared to DNS); with higher capturing compared to complete ensemble averaging (such as from RANS). The latter is illustrated in the filtered velocity profile ($\tilde{U}$) of Figure 4.3, which is less 'jaggered' compared to the instantaneous profile (Figure 4.1), while showing more detail than the time averaged profile (Figure 4.2).

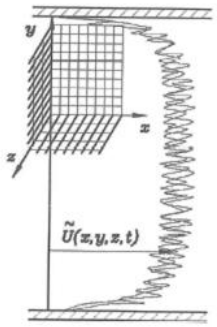

Figure 4.3: Illustration of LES-filtered profiles obtained from LES [49]

LES methods are often considered a median between DNS and RANS methods; with LES methods simplifying the conservation equations, thereby reducing computational complexity, while maintaining part of the accuracy of DNS methods. Thus, LES methods are often used for flow simulations of higher Reynolds flows and increased geometric complexity compared to DNS, with the choice of filtering scales playing an important role. However, due to scale filtering LES methods typically experience resolution difficulties in highly turbulent sub-scale regimes, such as in near-wall regions, where large eddy motion is absent and accurate modelling requires increased resolutions.

LES simplification and filtering techniques can be used to reduce the conservation equations, similarly as done with RANS (refer to Appendix B), resulting in the equations being dependent on filtered profiles and filtered products [46], as illustrated in the following equations:

$$\partial_{x_i}\left(\tilde{U}_i\right)=0 \qquad \text{Eq. 4.10}$$

$$\tilde{\rho}\partial_t\left(\tilde{U}_i\right)+\tilde{\rho}\partial_{x_j}\left(\widetilde{U_iU_j}\right)=-\partial_{x_i}\left(\tilde{p}\right)+\partial_{x_j}\left[\mu\partial_{x_j}\left(\tilde{U}_i\right)\right] \qquad \text{Eq. 4.11}$$

$$\tilde{\rho}\partial_t\left(\tilde{T}\right)+\tilde{\rho}\partial_{x_j}\left(\widetilde{TU_j}\right)=\partial_{x_j}\left[\frac{\mu}{Pr}\partial_{x_j}\left(\tilde{T}\right)\right] \qquad \text{Eq. 4.12}$$

From the above LES conservation equations, the filtered product terms are different from the product of the separate filtered profiles; making solution of the LES conservation equations challenging [46]. The difference between the filtered product terms and product of the filtered terms is defined as the residual stress tensor, analogous to the Reynolds stress tensor of RANS methods [46]. The residual stress tensors have the following physical interpretations:

$-\tilde{\rho}\left(\widetilde{U_iU_j}-\tilde{U}_i\tilde{U}_j\right)\equiv\tilde{\rho}\tau^R{}_{ij}$ — **residual stress tensor**: residual turbulent momentum energy per unit volume due to filtering.

$C_p\tilde{\rho}\left(\widetilde{TU_j}-\tilde{T}\tilde{U}_j\right)\equiv C_p\tilde{\rho}q^R{}_j$ — **residual heat flux vector**: residual turbulent enthalpy per unit volume due to filtering.

4.2.2.3. Solution of modelled simplified conservation equations.

With RANS and LES techniques, modelling results in the formulation of higher order moment correlation and residual terms [49]; thus for both techniques there is a closure problem, whereby the conservations laws and statistically modelled turbulence terms have to be closed with a set of approximate moment definitions.

Solution of the turbulence correlation terms can be obtained by manipulation of the correlation equations for fluctuating/sub-scale variables, resulting in moments of higher order, thereby further complicating solution [49]. There are a variety of closure methods, as discussed by Hanjalić *et al*. [49] and Pope [46], with degree depending on the desired complexity.

Several modelling techniques have been implemented into SARA3DCLIMAT and studied over the years. The following sections discuss such RANS and LES

closure techniques (sections 4.3 and 4.4) which will be utilised as part of this study, as investigated by previous theses (refer to section 2.4); as well as techniques that will be adapted as part of SARA3DCLIMAT validation. Additionally, a hybrid LES/RANS method is also highlighted for use in this study (section 4.5), previously investigated with SARA3DCLIMAT [37, 41, 42].

4.3. Closure of the RANS conservation equations

The RANS averaged conservation equations can be closed using the various Eddy Viscosity/Diffusivity Models (EVM/EDM) or Second-Moment Closures (SMC) [49]. Only a modified two-equation k-ε linear EVM model will be used in this study for RANS closure, as the model has proven robustness, known short-comings [49], it is the most widely used turbulence closure model and has been well tested and expended within SARA3DCLIMAT.

4.3.1. The standard two-equation k-ε linear EVM

The standard two-equation k-ε linear EVM is based on the Boussinesq assumption, in which the turbulent stress and flux tensors ($\tau^t{}_{ij}$ and $q^t{}_j$) are estimated as being proportional to the mean rate of strain, with the inclusion of an isotropic term (Eq. 4.13) and isotropic temperature gradient (Eq. 4.14) respectively; analogous to Newtonian viscous stresses and Fourier heat flux.

In the standard two-equation k-ε linear EVM expressions, the turbulent viscosity (μ_t) is determined from the characteristic length and time scales [49], as shown in Eq. 4.15. C_μ is an empirical coefficient (value provided in section 5.2.5).

$$\overline{U_i^{'}U_j^{'}} = -\frac{\tau^t{}_{ij}}{\bar{\rho}} = \frac{\mu_t}{\bar{\rho}}\left(\left(\frac{2}{3}\frac{\bar{\rho}}{\mu_t}k\delta_{ij}\right) - \left(\partial_{x_j}\left(\bar{U}_i\right) + \partial_{x_i}\left(\bar{U}_j\right)\right)\right) \qquad \text{Eq. 4.13}$$

$$\overline{T^{'}U_j^{'}} = \frac{q^t{}_j}{C_p\bar{\rho}} = -\frac{\mu_t}{\bar{\rho}}\frac{1}{Pr_t}\frac{\partial T}{\partial x_j} \qquad \text{Eq. 4.14}$$

$$\mu_t = C_\mu\bar{\rho}\frac{k^2}{\varepsilon} \qquad \text{Eq. 4.15}$$

The turbulent Prandtl number (Pr_t) is the relation between eddy momentum and eddy thermal diffusivities, as described in section 2.3.2.3. SARA3DCLIMAT utilises a constant emperical coefficient Prandtl number (refer to section 5.2.5).

The Kronecker delta function (δ_{ij}) is used to determine the isotropic nature of the turbuelnt stress tensor, that is:

$$\begin{aligned} &if \quad i = j \quad \delta_{ij} = 1 \\ &\quad i \neq j \quad \delta_{ij} = 0 \end{aligned} \qquad \text{Eq. 4.16}$$

The turbulent strain tensor is defined as:

$$\left(\partial_{x_j}\left(\bar{U}_i\right) + \partial_{x_i}\left(\bar{U}_j\right)\right) = 2S_{ij} \qquad \text{Eq. 4.17}$$

The turbulent kinetic energy (k) is as defined in Eq. 4.21. The conservation equation, as shown in Eq. 4.19, can be found from Reynolds decompostion of the Navier-Stoke equation, multiplication by velocity fluctuation and averaging of the resultant expression [49].

$$k = \frac{1}{2}\left(\overline{U_i' U_i'}\right) \qquad \text{Eq. 4.18}$$

$$\underbrace{\partial_t(k)}_{L_k} + \underbrace{\bar{U}_j \partial_{x_j}(k)}_{C_k} = \underbrace{\partial_{x_j}\left(\left(\nu + \frac{\nu_t}{Pr_k}\right)\partial_{x_j}(k)\right)}_{D_k} - \varepsilon - \underbrace{g_i \beta\left(\overline{T' U_i'}\right)}_{G_k} - \underbrace{\left(\overline{U_i' U_j'}\right)\partial_{x_j}\left(\bar{U}_i\right)}_{P_k} \qquad \text{Eq. 4.19}$$

Terms in the kinetic turbulent kinetic energy conservation (Eq. 4.19) have the following physical interpretations [49]:

- L_k – local rate of change of k
- C_k – convective transport of k
- $\mathrm{D_k}$ – turbulent kinetic energy diffusive rate, made up of the viscous diffusion ($\mathrm{D_k}^{\nu}$), turbulent diffusion due to velocity fluctuations ($\mathrm{D_k}^{t}$) and the diffusion due to pressure fluctuations ($\mathrm{D_k}^{p}$). Where: ν_t is the turbulent kinematic viscosity; σ_k is the turbulent kinetic energy Prandtl number
- ε – rate of dissipation of k into heat, as defined in Eq. 4.20

- G_k – rate of production (generation) of k due to buoyancy effects, that is the conversion of potential energy into turbulent kinetic energy
- P_k – rate of production of k due to mean-flow deformation

Turbulent kinetic energy dissipation (ε) is as defined in Eq. 4.20. To solve the dissipation term, and thus close the set of conservation equations, a turbulent kinetic energy dissipation energy conservation equation is required. This is found similarly to the turbulent kinetic energy equation, that is: Navier-Stokes equation decomposition, velocity fluctuation multiplication, followed by partial differentiation with respect to x_j, multiplication by $2\nu\partial_{x_j}(U_i')$ and finally averaged and modelled [49]; to obtain Eq. 4.21.

$$\varepsilon = \frac{1}{2}\nu\overline{\left(\frac{\partial U_i'}{\partial x_j} + \frac{\partial U_i'}{\partial x_j}\right)} \qquad \text{Eq. 4.20}$$

$$\underbrace{\partial_t(\varepsilon)}_{L_\varepsilon} + \underbrace{\bar{U}_j\partial_{x_j}(\varepsilon)}_{C_\varepsilon} = \underbrace{\partial_{x_j}\left(\left(\nu + \frac{\nu_t}{Pr_\varepsilon}\right)\partial_{x_j}(\varepsilon)\right)}_{D_\varepsilon} + \frac{\varepsilon}{k}\left(\underbrace{C_{\varepsilon 1}P_k}_{P_\varepsilon} + \underbrace{C_{\varepsilon 3}G_k}_{G_\varepsilon} - C_{\varepsilon 2}\varepsilon\right) \qquad \text{Eq. 4.21}$$

The turbulent time scale (τ) is defined as the ratio between turbulent kinetic energy (k) and turbulent kinetic energy dissipation (ε) [49]. The remaining terms in the turbulent kinetic energy and dissipation conservation equations are empirical coefficients (refer to section 5.2.5); which are determined experimentally and/or from DNS simulations [49].

The Boussinesq assumption and resulting closed set of two-equation k-ε linear EVM expressions, as defined above, makes it possible to combine fluid and turbulence properties as illustrated in Eq. 4.22. The latter allows for simplification of the resultant conservation equations to forms similar as the RANS simplified equations (Eq. 4.7, Eq. 4.8 and Eq. 4.9), with the only differences being fluid properties being replaced by their combined effective properties.

$$\mu_{eff} = \mu + \mu_t \qquad \text{Eq. 4.22}$$

The closure problem is therefore reduced to finding an expression for the turbulent viscosity (μ_t), assuming turbulent Prandtl number ($\mathrm{Pr_t}$) remains

constant. Using this, expressions for both the turbulent stress and heat flux tensors can be determined.

It is important to note that the isotropic nature of the Boussinesq assumptions is in fact inaccurate, as experimental research [51] has shown the tensors to be anisotropic, with directional dependent non-uniformness. However, the assumption greatly simplifies modelling and closure of the conservation equations; it is therefore used, with several modifications, as described in the following sub-section (4.3.2).

4.3.2. Improvements to the standard two-equation k-ε linear EVM

Due to the isotropic nature of the Boussinesq assumptions and the anisotropic nature of real systems, the standard two-equation k-ε linear EVM, as well as SARA3DCLIMAT has been tested and modified over the past few decades. Theory related to several modifications with proven improvements, in addition to modifications investigated in this study is discussed as follows.

4.3.2.1. The Durbin time-scale limiter

The standard two-equation k-ε linear EVM turbulence model is known to over predict the turbulent time scale (τ), thus turbulent kinetic energy (k), especially near stagnation points. This is due to underestimations of turbulent kinetic energy dissipation and overestimates in turbulent viscosity [52].

Therefore, the Durbin time-scale limiter ($\mathcal{T}$), along with changes in the expressions of turbulent viscosity (μ_t) (Eq. 4.15) and the turbulent energy dissipation conservation equation (Eq. 4.21), are used in SARA3DCLIMAT. The Durbin time-scale limiter introduces bounds to the turbulent time scale and thus the turbulent viscosity; thereby reducing the rate of production of turbulent kinetic energy due to mean flow deformation (P_k). Additionally the introduction of the Durbin time-scale limiter also places a bound on the production term in the turbulent energy dissipation conservation equation, thereby increasing dissipation of turbulent kinetic energy.

Use of the Durbin time-scale limiter with the dissipation conservation equation has been show to result in divergent solutions [6, 40]; therefore use

of the limiter in this investigation with SARA3DCLIMAT is restricted to the calculation of the turbulent viscosity only.

$$\mathcal{T} = min\left[\tau, \frac{0.6}{\sqrt{6}C_{\mu}\left|0.5\left(\partial_{x_j}\left(\bar{U}_i\right)+\partial_{x_i}\left(\bar{U}_j\right)\right)\right|}\right] \equiv \left[\tau, \frac{0.6}{\sqrt{6}C_{\mu}\left|S_{ij}\right|}\right] \qquad \text{Eq. 4.23}$$

$$\mu_t = C_{\mu}\bar{\rho}\,k\mathcal{T} \qquad \text{Eq. 4.24}$$

$$\partial_t(\varepsilon)+\bar{U}_j\partial_{x_j}(\varepsilon) = \partial_{x_j}\left(\left(\nu+\frac{\nu_t}{Pr_{\varepsilon}}\right)\partial_{x_j}(\varepsilon)\right)+\frac{1}{\mathcal{T}}\left(C_{\varepsilon 1}P_k + C_{\varepsilon 3}G_k - C_{\varepsilon 2}\varepsilon\right) \qquad \text{Eq. 4.25}$$

4.3.2.2. Wall functions

The standard two-equation k-ε linear EVM is only valid for high Reynolds flows [49], often not present in viscous near wall region flows where flow becomes more laminar. To overcome these applicability restrictions, wall functions that model flows in this viscous buffer layer are often used, bridging fluid properties between the turbulent standard two-equation k-ε linear EVM applicable area and wall region. These functions, based on similarity and empirical relations [49], have been fully integrated into SARA3CLIMAT [35, 38, 49] and are as follows:

Velocity:

$$U^* = \rho\left(C_{\mu}\right)^{0.25}\frac{\left(k_P\right)^{0.5}}{\tau_w}U_P = \begin{cases} \dfrac{1}{\kappa}ln(Ey^*) & if\ y^* \geq 11.63 \\ y^* & if\ y^* < 11.63 \end{cases} \qquad \text{Eq. 4.26}$$

$$y^* = \left(C_{\mu}\right)^{0.25}\frac{\rho\left(k_P\right)^{0.5}y_P}{\mu} \qquad \text{Eq. 4.26.1}$$

Where: κ is the von Kárman constant, $\kappa = 0.41$; E is the constant in the law-of-the-wall, $E = 9.5$; C_{μ} is a constant, 0.09; k_P is the turbulent kinetic energy (k) at the centre point of the wall-nearest control cell; y_P is the distance of the cell centre point to the wall; U_P is the velocity at the centre point of the cell; τ_w is the wall shear stress.

Temperature:

$$T^* = \left(C_\mu\right)^{0.25}\left(k_P\right)^{0.5}\left(\frac{\rho C_p\left(T_P - T_w\right)}{q_w}\right) = \begin{cases} \sigma_T\left(\frac{1}{\kappa}\ln\left(Ey^*\right) + J\right) & if\ y^* \geq 11.63 \\ Pr(y^*) & if\ y^* < 11.63 \end{cases} \quad \text{Eq. 4.27}$$

$$J = 9.24\left(\left(\frac{Pr}{Pr_t}\right)^{0.75} - 1\right)\left(1 + 0.28exp\left(-0.007\frac{Pr}{Pr_t}\right)\right) \quad \text{Eq. 4.27.1}$$

Where: T_P is the temperature at the centre point of the cell; T_w is the wall surface temperature; q_w is the wall heat flux; $Pr_t$is the turbulent Prandtl number for the mean temperature.

Turbulent kinetic energy (k):

There is no wall function for the k equation; instead the Neumann zero-gradient wall condition is used, in the direction normal to the wall.

$$\frac{\partial k}{\partial x_n} = 0 \quad \text{Eq. 4.28}$$

In addition to the above k equation Neumann boundary condition, the rate of dissipation and production of turbulent kinetic energy at the first wall grid cell is calculated as follows:

$$\varepsilon_P = \left(C_\mu\right)^{0.75}\frac{{k_P}^{1.5}}{\kappa y_P} \quad \text{Eq. 4.29}$$

$$\left(\rho P_k\right)_P \approx \tau_w \frac{\partial \bar{U}}{\partial y}|_P = \tau_w \frac{\tau_w}{{C_\mu}^{0.25}\kappa\rho{k_P}^{0.5} y_P} \quad \text{Eq. 4.30}$$

4.3.2.3. Transient-RANS

RANS models are based in steady-state flow properties, where fluctuations are ensemble averaged and thus information lost; while turbulence, by its very nature, is spatially and temporally dynamic. Therefore, in modelling of turbulent flows, it is necessary to take into consideration spatial and temporal

dependence; as well as where possible, maintaining the simplicity of RANS models for reduced computational requirements compared to other simulation and modelling techniques.

The latter spatial and temporal dependence can be obtained utilising Transient-RANS (T-RANS) models, whereby local ensemble (specifically time) derivatives of local variable are solved for small ensemble (time) intervals in the RANS conservation equations [49].

Averaged profiles (such as velocity) and resolved turbulence tensors (stress and heat flux) are calculated with T-RANS models as illustrated in Eq. 4.31 and Eq. 4.32. T-RANS models combine averaged (RANS) modelled variables with resolved spatial and temporal contributions, to obtain spatial and temporal total turbulent profiles. Resolved contributions of turbulent kinetic energy represent large scale turbulent kinetic energy variations (refer Eq. 4.33).

$$\overline{\phi_i} = \frac{1}{N}\sum_{n=1}^{N}\hat{\phi}_i^{\,n} \qquad \text{Eq. 4.31}$$

$$\overline{\phi_i'\phi_j'} = \frac{1}{N}\sum_{n=1}^{N}\left[\left(\hat{\phi}_i^{\,n} - \overline{\phi}_i\right)\left(\hat{\phi}_j^{\,n} - \overline{\phi}_j\right)\right] \qquad \text{Eq. 4.32}$$

$$k_{res} = \sum_i \frac{1}{2}\overline{U_i'U_i'} = \sum_i \frac{1}{N}\sum_{n=1}^{N}\frac{1}{2}\left[\left(\hat{U}_i^{\,n} - \overline{U_i}\right)^2\right] \qquad \text{Eq. 4.33}$$

4.3.2.4. Turbulent heat flux models

In the standard two-equation k-ε linear EVM, turbulent heat flux ($q^t{}_j$) is modelled based on the Boussinesq assumption, being proportional to the isotropic temperature gradient (refer to section 4.3.1, Eq. 4.14), commonly referred to as the Simple Gradient Diffusion Hypothesis (SGDH). As discussed in section 4.3.1, the assumptions isotropicity has been shown to be inaccurate for real systems [19, 51]. Kenjereš [19] showed that isotropic modelling of turbulent viscosity is not appropriate for buoyancy driven flows due to the relation between the one-directional gravitational force and local temperature gradients in the presence of shear. However, the SGDH is still utilised, with known inaccuracies, due to its resultant model simplifications.

In order take into account the dependence of turbulent heat flux in the presence of shear, while maintaining the simplicity of the SGDH, the Generalised Gradient Diffusion Hypothesis (GGDH) was proposed by Ince *et al.* [53]. With the latter, turbulent heat flux is dependent on anisotropic temperature gradients, as well as shear tensors, as illustrated by Eq. 4.34.

$$\overline{T'U_j'} = -C_\theta \tau \left(\overline{U_i'U_j'} \right) \frac{\partial T}{\partial x_j} \qquad \text{Eq. 4.34}$$

Where, the coefficient (C_θ) is a constant in SARA3DCLIMAT (0.15); although it is often derived such that in horizontal shear flow it reduces to the expression for SGDH, with no additional terms [53], as shown in Eq. 4.35.

$$C_\theta = \frac{3}{2}\left(\frac{C_\mu}{\sigma_t} \right) \qquad \text{Eq. 4.35}$$

Hanjalić [54] showed that SGDH and GGDH type heat flux models are inaccurate in Rayleigh- Bénard convective flows, where temperature gradients can be zero and/or in the direction on the heat flux vector. Thus, several extended Algebraic Flux Models (AFM) have been proposed to take into account effects of shear stress on heat flux (as with GGDH), in addition to temperature fluctuations. SARA3DCLIMAT currently utilises a model proposed and investigated by Kenjereš *et al*. [55] (Eq. 4.36). Where constant terms (C_θ, ξ and η) are as defined by Kenjereš *et al*. [55] and $\tau_{\theta i}$ is the subscale turbulent heat flux.

$$\overline{T'U_j'} = -C_\theta \tau \left(\left(\overline{U_i'U_j'} \right) \frac{\partial T}{\partial x_j} + \xi \tau_{\theta i} \frac{\partial \overline{U_i}}{\partial x_j} + \eta \beta g_i \left(\overline{T'T'} \right) \right) \qquad \text{Eq. 4.36}$$

As can be seen from the SGDH, GGDH and AFM turbulent heat flux expressions (Eq. 4.14, Eq. 4.34 and Eq. 4.36), the models are built-up from each other, with increasing complexity and studies increased accuracy. All three models have been integrated into SARA3DCLIMAT; however are yet to be investigated for urban atmospheric thermal stratified buoyancy effects. Thus, the SGDH will be used with initial investigations, with further studies into the accuracy compared to GGDH and the Kenjereš-AFM.

4.3.2.5. Turbulent Prandtl number

As discussed in section 2.3.2.3, local stratification conditions have shown to have an influence on local momentum and thermal diffusivities, hence local turbulent Prandtl numbers. Ueda *et al*. [32] showed that this influence is particularly pronounced with stably stratified conditions.

Currently, many CFD turbulence models, including SARA3DCLIMAT make use of a constant turbulent Prandtl number for model simplicity. However due to the strong dependence on local stratification conditions, various models have been postulated [36], relating the turbulence Prandtl number to local stratification conditions, through Richardson numbers. One such model was proposed by Ellison [56, 31], is shown in Eq. 4.37, as discussed by Ueda *et al*. [32] and Mossel [36] (refer to Figure 2.4).

$$Pr_t = \frac{\left(1 - Ri_f\right)^2}{\nu_0 \left(1 - \frac{Ri_f}{Ri_{f,cr}}\right)} \qquad \text{Eq. 4.37}$$

The critical Richardson number ($Ri_{f,cr}$) is the local Richardson number at which thermal stratification will have no enhancing influences on fluid flow. The value is less than unity and typically of the order 0.08 – 0.4 [31], with a value of 0.1 providing best empirical relation [32]. ν_0 is the inverse of the turbulent Prandtl number at neutral stratification conditions, with an empirical best fit value of $5/6$ [32].

SARA3DCLIMAT currently makes use of a constant turbulent Prandtl number ($\mathrm{Pr}_t = 0.84$), which will be used for the basis of this study. Sensitivity analyses will be conducted as part of the study (refer to Chapter 1), to investigate the effects of varied turbulent Prandtl number on SARA3DCLIMAT accuracy.

4.4. Closure of the LES conservation equations

As with RANS methods, LES methods result in simplification of the conservations equations, along with the formulation of filtered product terms: residual stress and heat flux tensors. Likewise, LES methods have to be closed to obtain a full set of conservation expressions, the simplest of which is the Smagorinsky closure model.

With the Smagorinsky model, the residual stresses are modelled utilising the EVM, relating residual terms to rates of strain or temperature gradient [46], as illustrated by Eq. 4.38 and Eq. 4.39. Residual turbulent energy (k_R) is defined in Eq. 4.40.

$$\tau^R{}_{ij} = \frac{\mu_t^{LES}}{\tilde{\rho}}\left(\left(\frac{2}{3}\frac{\tilde{\rho}}{\mu_t^{LES}}k_R\delta_{ij}\right)-\left(\partial_{x_j}\left(\bar{U}_i\right)+\partial_{x_i}\left(\bar{U}_j\right)\right)\right) \quad \text{Eq. 4.38}$$

$$q^R{}_j = -\frac{\mu_t^{LES}}{\tilde{\rho}}\frac{1}{Pr_t}\frac{\partial T}{\partial x_j} \quad \text{Eq. 4.39}$$

$$k_R = \frac{1}{2}\tau^R{}_{ii} \quad \text{Eq. 4.40}$$

The Smagorinsky model expresses the turbulent viscosity as in Eq. 4.41, where C_s is the Smagorinsky coefficient (0.1 [46]), Δ^{LES} is the filter length and $\left(2S_{ij}S_{ij}\right)^{1/2}$ the characteristic filtered strain rate; turbulent Prandtl number is again constant ($\mathrm{Pr}_t = 0.4$).

$$\mu_t^{LES} = \rho\left(C_s\Delta^{LES}\right)^2\left(2S_{ij}S_{ij}\right)^{1/2} \quad \text{Eq. 4.41}$$

This study will not specifically investigate LES-exclusive techniques and their applicability; but rather use results from Smagorinsky-closure LES simulations performed by Saša Kenjereš during the project, as described in section 5.3.8.2, for comparison of RANS methods with typical LES methods and potentials.

4.5. Hybrid LES/RANS model

LES methods are typically more accurate than RANS methods, at cost of computational requirements, especially in regions where flow scales are larger than filtered scales, such as non-wall regions [49]. Conversely, RANS methods typically have substantially reduced computational requirements and increased accuracy in near-wall regions due to the use of several modifications. Therefore, to combine the advantages of both methods, there have been attempts in CFD modelling to combine LES and T-RANS methods into a hybrid method; with the aim of increasing simulation accuracy, while maintaining minimal computational complexity. For example refer to [37, 41, 42, 55, 57]. Due to varied types of data obtained from the

two methods: filtering by LES and averaging by RANS, current challenges include integration and compatibility of the methods, especially at method boundaries [49]; however, the similar conservation equation forms allows for their combination.

A hybrid LES/T-RANS method has been successfully integrated into SARA3DCLIMAT and studied [37, 41, 42], which will be utilised in this study. The SARA3DCLIMAT hybrid method uses the T-RANS method as a basis, with LES methods being used to modify the dissipation coefficient $C_{\varepsilon 2}$, as well as the turbulent viscosity [42], as discussed below. Only the former hybrid modification will be utilised in this study.

4.5.1. Hybrid modification to the dissipation coefficient: $C_{\varepsilon 2}$

Modification to the dissipation coefficient ($C_{\varepsilon 2}$) in the turbulent kinetic energy dissipation conservation equation (Eq. 4.21) will result in a change to the dissipation term. Thus, a decrease in the coefficient will translate into decreased turbulent kinetic energy dissipation (ε) rate of dissipation, hence an increased rate of turbulent dissipation and a reduction of turbulent kinetic energy (k). Increased turbulent dissipation and coupled decreased turbulent kinetic energy will also translate into decreased turbulent viscosity and thus the capturing of higher frequencies with T-RANS models. Changes to the dissipation coefficient ($C_{\varepsilon 2}$) by SARA3DCLIMAT hybrid LES/T-RANS can be summarised as follows [42]:

$$C_{\varepsilon 2}^{\ hybrid} = C_{\varepsilon 1} + \frac{C_{\varepsilon 2} - C_{\varepsilon 1}}{\alpha^{hybrid}} \qquad \text{Eq. 4.42}$$

$$\alpha^{hybrid} = \max\left(1, \frac{L_{RANS}}{L_{LES}}\right) = \max\left(1, \frac{\frac{k^{3/2}}{\varepsilon}}{\left(\Delta_x \Delta_y \Delta_z\right)^{1/3}}\right) \qquad \text{Eq. 4.42.1}$$

At near-wall boundaries, RANS turbulent length scales are typically smaller than for LES, thus the α-factor will tend to unity and hybrid coefficient towards $C_{\varepsilon 2}$; hence the hybrid model towards a RANS model. Conversely, typically in free-stream regions, the hybrid model tends to a higher frequency RANS model and thus a LES model. The use of this modification and the α-factor allows for a seamless transition in $C_{\varepsilon 2}$ coefficient modification.

5. METHODOLOGY

This chapter discusses the methodology used to investigate the proposed hypothesis (refer to section 3.2); where SARA3DCLIMAT is postulated to accurately simulate thermally stratified buoyant flows as outlined in this chapter, with experimental wind tunnel validations with findings by Uehara *et al*. [3].

The chapter begins be discussing the wind tunnel experiment and findings by Uehara *et al*. [3] (abbreviated as "Uehara"), setting the basis for hypothesis investigation and SARA3DCLIMAT validation. Following the latter, the experimental methodology is outlined, with descriptions of simulation domains and properties, as well as conducted experimental investigations.

5.1. Description of the Uehara wind tunnel experiment

For purposes of hypothesis investigation and SARA3DCLIMAT validation, wind tunnel findings from Uehara were used; with expansion to the work by de Haan [35]. The following section describes the Uehara experimental domain setup and investigation conditions.

5.1.1. Wind tunnel experimental setup

The Uehara study made use of an atmospheric diffusion wind tunnel located at the Japanese National Institute of Environmental Studies. The test section, of volume 2 m high, 3 m wide and 24 m long, consisted of a turbulent flow generation zone followed by the investigation zone (refer to Figure 5.1).

The flow generation zone was made up of an inlet tripping fence followed by an undisclosed number of Styrofoam roughness elements (100mm X 100mm X 50mm (length, width, height) in a regular spaced array, with spacing 100mm. The investigation zone consisted of a regular array of Styrofoam city block elements (total number unspecified, dimensions: 100mm X 100mm X 1000mm (length, width, height)) with a streamwise spacing of 100mm and perpendicular spacing

of 50mm. Seeding particles were emitted from the leading city element row, with flow measurements being taken in the central vertical section of the fifth street canyon (between the fifth and sixth city block rows), from ground level (2 mm or 0.2 mm for velocity and temperature profiles respectively) up to 700 mm. Magnesium carbonate powder (Ø5 µm) and a three-colour argon Laser Dopper Anemometer (LDA) were used to measure point velocities; while temperature profiles were measured using a cold wire installed leeward of the LDA.

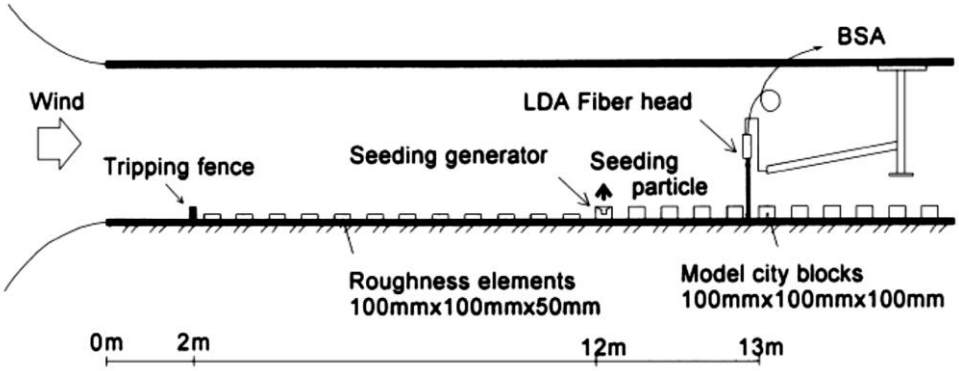

Figure 5.1: Uehara wind tunnel setup [3]

5.1.2. Experimental inlet flow conditions

The Uehara wind tunnel experiment was seemingly not made in mind for use in CFD simulation validation, due to the apparent lack of inlet flow conditions. Uehara only provides approach streamwise flow velocity profiles (illustrated in Figure 5.2); along with stating that the free-stream velocity was at least 1.5 m/s, in order to achieve above critical Reynolds flow at isothermal conditions (refer to Table 5.1 for Uehara Reynolds number). Additionally, it is assumed that the inlet temperature profile is uniform.

A literature review by de Haan [35] reviled that there are no concessive and unanimous inlet conditions that have been used in CFD validation cases with Uehara. In the work by de Haan, possible various inlet flow conditions were investigated in order to mimic the Uehara approach flow conditions; however with limited success. The inlet flow profiles used in this study are a result of investigations and findings by de Haan [35].

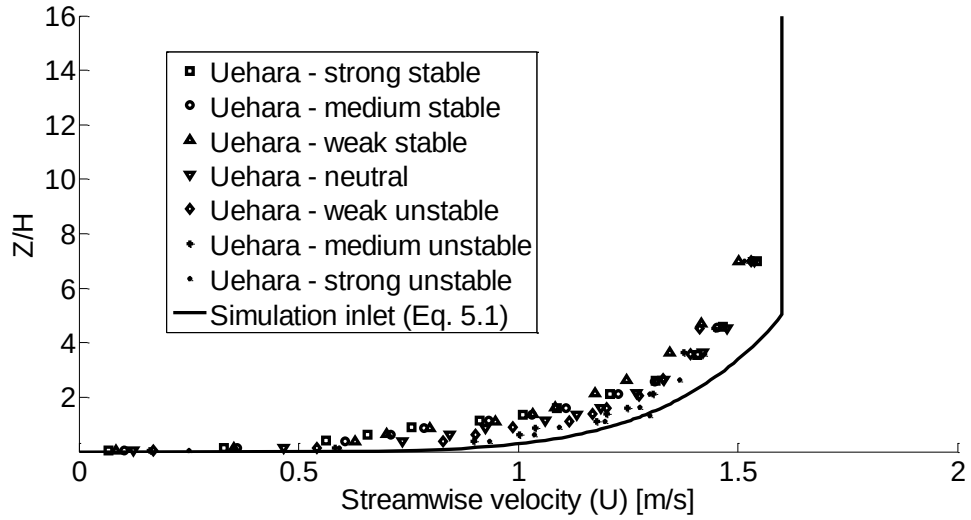

Figure 5.2: Uehara approach- and simulated inlet streamwise velocity profiles

5.1.3. Stratification conditions investigated

The Uehara investigated thermally stratified conditions are listed in Table 5.1:

Table 5.1: Uehara thermal stratification conditions

Stratification Condition	Air temperature (T_a) [^{o}C]	Floor temperature (T_f) [^{o}C]	Ri_b [-]	Re_H [-]
Strong stable	78	21	0.071	7407
Medium stable	58	21	0.049	8160
Weak stable	38	21	0.024	8917
Neutral	20	20	0	10160
Weak unstable	19	40	-0.031	10170
Medium unstable	19	59	-0.060	10160
Strong unstable	20	79	-0.088	10010

5.2. Simulation setup

This section describes the simulation setup used to investigate the proposed hypothesis for the general case. Descriptions include an outline of the simulation domain (5.2.1), inlet conditions (5.2.2) and boundary conditions (5.2.3); in addition to simulation and SARA3DCLIMAT numerical solver properties (5.2.5).

5.2.1. Definition of simulation domains

The investigation domain was chosen to as closely and practically possible mimic the Uehara wind tunnel experiment, with the inclusion of estimations, assumptions and symmetry conditions, as well as simulation adaptions. These can be expected to reduce computational complexity, while having negligible/minimal influences on simulation results.

Uehara does not specify the exact number of city block elements and rows used in wind tunnel experimentation, but does specify array and city block element dimensions (refer to section 5.1.1). Based on these Uehara specifications the urban array was exactly mimicked, with identically sized buildings (100mm X 100mm X 100mm) and street canyons (streamwise spacing of 100mm, perpendicular spacing of 50mm). To limit computational complexity, while taking into consideration findings and recommendations from de Haan [35], it was chosen to simulate only a restricted number of street canyons compared to the presumed Uehara case; while increasing the number compared to simulations by de Haan [35]. The simulated grid consisted of sixteen building element rows in five columns in an Uehara array, as illustrated in Figure 5.3 (where the building height (*H*) is 0.1 m). This is compared to Uehara maximum possible buildings, of 15 rows by 20 columns.

The simulation domain consisted of an entrance (stabilisation) zone, of length 6*H* (600mm), followed by the 31*H* -length (3100mm) building canyon array and a 30*H* (3000mm) exit (wake) zone. The total height of the domain was 16h (1600mm); while the length was 9*H* (900mm), with *H* (100mm) spacing between the side boundaries and the nearest building. Within the domain, there were several monitoring points, two of which were used for this study. The latter two monitoring points were located in the central y-plane of the 15th street canyon, at heights of 1.85×10^{-2} m ($1.85 \times 10^{-1}H$) ("point 1") and 2.29×10^{-1} m ($2.29H$) ("point 2"); as illustrated in Figure 5.3.

The generated mesh consisted of heterogeneously sized cuboids, refined towards surface boundaries (building elements and floor), as illustrated in Figure 5.4; with grid sizes ranging from 1.5×10^{-3} to 1×10^{-1} m. The latter heterogeneity allowed for increased simulation accuracy in those regions, while

reducing computational complexity for remaining volumes. The grid resolution was refined compared to de Haan [35], in order to increase simulation accuracy. The Investigation domain consisted of 20 streamwise and 10 perpendicular grid cells between buildings; with the entire domain made up of approximately 12.5 million control volumes (906 X 151 X 92 (N_x X N_y X N_z)).

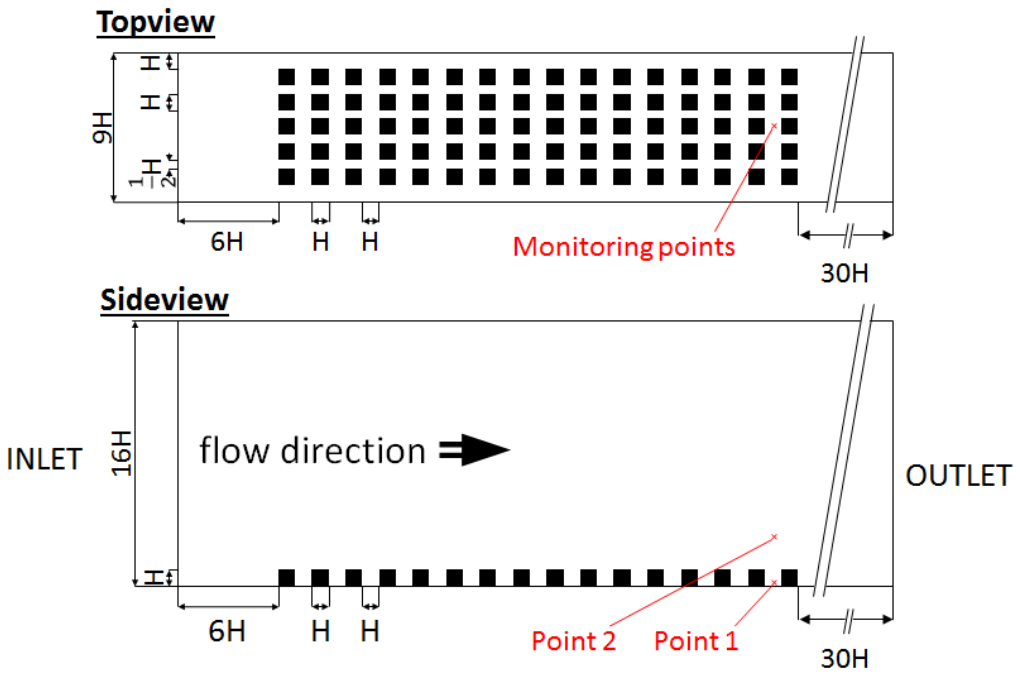

Figure 5.3: Simulation domain schematic. top: x-y plane; bottom: x-z –plane

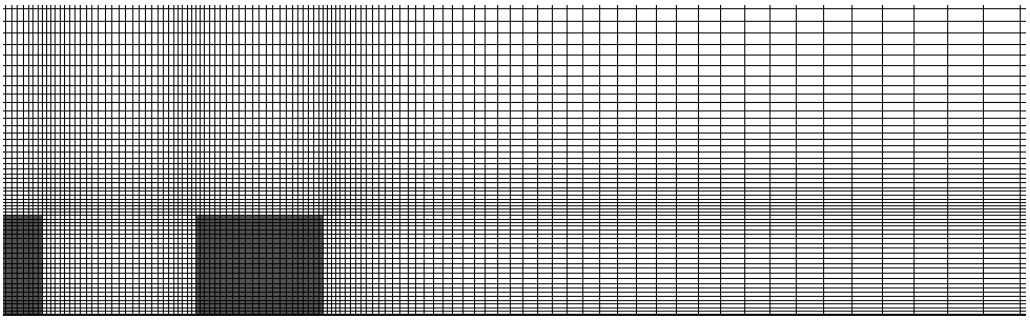

Figure 5.4: Illustration of simulaiton mesh resolution in a section on the x-z plane

5.2.2. Overview of investigation inlet conditions

As discussed in section 5.1.2, determination of the exact Uehara inlet conditions is challenging, with the inlet conditions as a result of the work by de Haan [35] being utilised in this study. The inlet conditions are as summarised as follows:

5.2.2.1. Inlet velocity profiles

The inlet streamwise velocity (U_{in}), taken as fully developed, is as given by Eq. 5.1 with a free streamwise velocity (U_∞) of 1.6m/s, occurring above a height ($z(U_\infty)$) of 500 mm. It is to be noted that the simulated inlet velocity profile is identical for all cases and is larger than all Uehara approach profiles (refer Figure 5.2). The latter similarity in inlet velocity profile was chosen as it would allow for better understanding and comparisons of thermal stratification effects and because it had proven convergence [35].

$$U_{in} = \min\left(U_\infty\left(\frac{z}{z(U_\infty)}\right)^{1/6}, U_\infty\right) = \min\left(1.6\left(\frac{z}{0.5}\right)^{1/6}, 1.6\right) \qquad \text{Eq. 5.1}$$

The perpendicular and vertical inlet velocity components are assumed to be negligible, thus equal to zero.

5.2.2.2. Inlet pressure profile

For this investigation, pressure differences are assumed not to be the driving force for fluid flow. Hence the inlet and outlet pressures are taken as ambient atmospheric pressure, thus 1 atm.

5.2.2.3. Inlet temperature profile

The inlet temperature profiles are taken as constant, equal to the Uehara atmospheric temperatures for cases to be investigated, refer section 5.2.4.

5.2.2.4. Inlet turbulent kinetic energy (k) profile

The inlet turbulent kinetic energy profile is assumed to be constant and dependent on the free stream velocity, as shown by Eq. 5.2. I is defined as the turbulence intensity, with an assumed value 5% being used for this investigation [44, 35]. Thus the constant turbulent kinetic energy value for simulations was 9.6×10^{-3} J/kg.

$$k_{in} = \frac{3}{2}(IU_\infty)^2 \qquad \text{Eq. 5.2}$$

5.2.2.5. Inlet turbulent kinetic energy dissipation (ε) profile

The inlet turbulent kinetic energy dissipation profile is assumed to be dependent on the turbulent kinetic energy (Eq. 5.3). The inlet viscosity ratio (χ_{in}), defined in section 2.3.2.4, is empirically determined and for this study had a value of 500 (refer to section 5.2.5). Thus, the constant turbulent kinetic energy dissipation value can be shown to be 9.2×10^{-4} m^2/s^3.

$$\varepsilon_{in} = \frac{C_\mu k_{in}^{\ 2}}{\chi_{in} \nu} \qquad \text{Eq. 5.3}$$

5.2.3. Domain boundary conditions

Simulation domain inlet boundary conditions are as specified in section 5.2.2; while for outlet boundary conditions are given by the von Neumann condition, in which the normal-directional derivative is set as zero.

The symmetry boundary condition is used for the domain side walls and upper surface, in which all fluxes across the boundary are set as zero. This allows for simplification of the domain of interest, by allowing reduction of the domain size, with negligible influence to investigations in the domain central plain.

The domain floor and building obstacles are treated as adiabatic physical boundaries. They are treated as obeying the non-slip condition as well as having a viscous sub-layer, where wall functions (see section 4.3.2.2) are used to describe the viscous low Reynolds near-wall flow. Additionally, the urban array floor section is assumed to have constant temperature, with value being determined by the investigated case.

5.2.4. Investigation stratification conditions and properties

Table 5.2 lists the Uehara thermal stratification cases used in this study, along with corresponding reference atmospheric properties. Thermally stratified buoyancy effects are the foundation for this study, thus comparisons of the various cases and their influences on atmospheric flow profiles are presented throughout Chapter 6 (specifically highlighted in section 6.3), with various supplementary investigations being conducted, as described in section 5.3.

Table 5.2: Domain properties for investigated thermal stratification cases

	Strong stable	Weak stable	Neutral	Weak unstable	Strong unstable
Air temperature (T_a)[°C]	78	58	38	20	19
Floor temperature (T_f)[°C]	21	21	21	20	40
Density (ρ)[kg/m^3]	1.005	1.066	1.134	1.204	1.208
Dynamic viscosity (μ)[10^{-5} Pa.s]	2.096	2.004	1.910	1.824	1.819
Kinematic viscosity (ν)[10^{-5} m^2/s]	2.085	1.880	1.684	1.514	1.505
Thermal conductivity (λ) [10^{-2} W/(m/K]	2.993	2.851	2.706	2.572	2.565
Specific heat capacity (Cp) [J/(kg.K]	1.011	1.008	1.005	1.002	1.002
Prandtl number (Pr)[-]	0.7081	0.7087	0.7096	0.7105	0.7106
Thermal expansion coefficient (β) [10^{-3}/K]	2.848	3.020	3.214	3.411	3.423

5.2.5. Simulation and solver properties

Table 5.3 lists the standard coefficient, constant and parameter values used in the various modelling equations; while Table 5.4 summarises the standard simulation and SARA3DCLIMAT solver properties used in this study. Deviations from these standard values for the basis of experimental investigations and sensitivity analyses conducted as SARA3DCLIMAT improvement studies, as described in section 5.3.

Table 5.3: Summary of coefficient, constant and parameter values

Parameter	Value
C_μ	0.09
$C_{\varepsilon 1}$	1.44
$C_{\varepsilon 2}$	1.92
$C_{\varepsilon 3}$	1.44

Parameter	Value
Pr_t	0.86
σ_k	1
σ_ε	1.3
χ	2×10^{-3}

The simulation procedure consisted of the following steps:

1. Domain discretisation, mesh generation and simulation definition.

2. Start-up: RANS simulation, with a single large time step (10^9 s) and 500 iterations; to obtain steady-state averaged profiles. Alternatively, data of previously statistically collected data of similar stratification cases was used.
3. Intermediate transient: T-RANS simulation with 600 time steps of Δt seconds; to obtain steady-oscillatory transient profiles.
4. Transient data collection: T-RANS simulation with time steps of Δt seconds for a specified period to collect statistical transient profiles.

Table 5.4: Summary of standard simulation and solver properties

Property description	Specification
Model type	T-RANS & Hybrid LES/T-TRANS
Closure model	k-ε linear EVM
Modifications	Durbin limiter
Turbulent flux model	SGDH
Numerical method	Semi Implicit Method For Pressure Linked Equations (SIMPLE) algorithm
Differencing scheme	Linear Unwinding Differencing Scheme (L-UDS)
Time integration method	2nd order fully implicit, three-time step scheme
Standard time step	1 second (refer section 6.5)
Standard statistical period	500 seconds (refer section 6.1)
Standard max. iterations	20
Average street canyon	Average of canyons 10, 11, 12, 13, 14 (refer section 6.2)
Relaxation factors	(Percentage carry-over from pervious)
Stress	100%
Flux	100%
Velocity	40%
Pressure	10%
k	40%
ε	40%
ν_t	40%
Temperature	40%
Temperature variance	40%

5.3. Simulation investigations

This section describes various SARA3DCLIMAT simulation investigations conducted as part of this study to investigate the proposed hypothesis and the improvement of SARA3DCLIMAT validity. Descriptions include various investigations conducted to determine standard procedures, such statistical period span and sampling canyon location. The effect of thermal stratification is then compared to isothermal conditions (the control case) as well as Uehara. Following these comparisons, supplementary investigations are conducted on the effects of time step on simulated flow profiles, inlet velocity and turbulent kinetic energy variation sensitivity analyses, effects of turbulent Prandtl number changes as well as preliminary further investigations conducted. Summary of all investigated cases can be found in Appendix Q.

5.3.1. Statistical data sensitivity analysis

Generally, increased statistical sampling numbers would increase accuracy and reliability of statistical data, with values being closer to averages with no changes in standard deviation. However, for practical purposes, it is often not feasible, as well as resource and time consuming for vast sample collection. Therefore, to determine the effects of statistical data collection period on results, various statistical collation periods were compared; thereby optimising turbulent statistical data collection periods, while allowing for fair comparison and validation of simulations with wind tunnel experiments. Statistical periods ranged from 50 to 2000 simulation seconds in some cases. Results for statistical independence investigations can be found in section 6.1.

5.3.2. Temporal effects and influences on sampling canyon

Investigations by de Haan [35] revealed strong dependence of flow profiles on relative street canyon location. This influence of sampling canyon location and effects on flow profiles is of particular importance for comparisons of global urban atmospheric thermal stratification effects, while disregarding influences of urban array geometric features; as well as for in comparisons with Uehara, where measurements are made in the fifth canyon. Therefore, to ensure canyon independence, various flow profiles were compared, in addition to with Uehara

data; thereby allowing for determination of an average urban street canyon in the investigation domain. Results are presented and discussed in section 6.2.

5.3.3. T-RANS and Hybrid LES/T-RANS simulations

To investigate effectiveness and accuracy of the Hybrid LES/T-RANS, with dissipation coefficient $C_{\varepsilon 2}$ modification, compared to T-RANS, simulations were conducted in duplicate, for both techniques. Results are presented throughout Chapter 6, with stratification comparisons provided in section 6.3, while general T-RANS and hybrid LES/T-RANS comparisons are provided in section 6.4.

5.3.4. Confirmation of time step (Δt) independence

For the domains investigated, Kolmogorov time scale can be shown to have a minimum value of approximately 1.5×10^{-3} seconds (refer Appendix C). Thus for DNS simulations, the timescale would have to be at least this value. Typically for LES, values of 100 times the Kolmogorov time scale are used; while much larger values are can be used for T-RANS, due to its simplifications. Therefore a standard value of one second was used (refer section 5.2.5).

To determine dependence of the standard time step (Δt) on simulations and thus independence of results on the chosen time step, simulations were repeated with two alternative time steps; for comparison with standard time step. The latter was done with half (0.5 seconds) and twice (2 seconds) the standard time step. Findings can be found in section 6.5.

5.3.5. Inlet velocity sensitivity analysis

Preliminary investigations of inlet velocity profile conditions revealed SARA3DCLIMAT inlet profiles differed from Uehara approach profiles (refer Figure 5.2). However, it was expected that these simulation differences would have negligible measureable effects on well-developed downstream canyon profiles. To investigate and confirm this, the inlet velocity power-law expression for the isothermal case was re-calibrated with Uehara data and re-simulated. This was compared with standard simulation and Uehara data; results are presented in section 6.6.

5.3.6. Inlet turbulent kinetic energy dissipation sensitivity analysis

Due to the lack of- and uncertainty in Uehara inlet profile conditions, specifically inlet turbulent kinetic energy dissipation (ε_{in}) (refer section 5.2.2.5), large variances in Uehara measured velocities and differences with initial investigation profiles, effects of decreased inlet turbulent kinetic energy dissipation were investigated. Inlet turbulent kinetic energy was decreased by decreasing the inlet viscosity fraction (χ_{in}), from 500 to 2000 for strong stable and unstable cases.

It was expected that changes to the inlet viscosity fraction and thus inlet turbulent kinetic energy dissipation, would alter the free-stream flow and profile; while having negligible and filtered effects on the downstream turbulent street canyon turbulent flow profiles. This would be due to altered boundary conditions for the dissipation term, thereby affecting solution of its conservation equation. Findings are presented and discussed in section 6.7.

5.3.7. Turbulent Prandtl number sensitivity analysis

Turbulent Prandtl number (Pr_t) has been found to be strongly related to stratification conditions, particularly stable stratification (refer section 2.3.2.3). To investigate this influence, a preliminary investigation of effects of altered turbulent Prandtl number on flow profiles was conducted for each weak stratification hybrid LES/T-RANS case; namely with turbulent Prandtl numbers of 0.4 and 0.1, compared to the standard value of 0.86. These decreases in turbulent Prandtl number are expected to enhance turbulent thermal diffusivity, thereby increasing turbulent mixing due to thermal stratification effects. This is expected to better heat transfer and mixing within the street canyon, possibly allowing for simulation of relatively constant Uehara temperature profiles. Results of this preliminary investigation are presented in section 6.8.

To further investigate the effect of thermal stratification influences on turbulent Prandtl number, local Richardson flux numbers and Ellison modelled turbulent Prandtl numbers (refer section 4.3.2.5) were determined for standard cases. Results are presented in sections 6.3.2.4 and 6.3.3.4.

5.3.8. Further development to standard simulations

Further development to the standard T-RANS and hybrid LES/T-RANS GGDH SARA3DCLIMAT model were investigated by way of initial studies into turbulent heat flux model expansion into non-isotropic modes, as well as LES simulations, as described below.

5.3.8.1. Turbulent heat flux model simulations

Studies into the influence of turbulent heat flux isotropicity and the choice of model were investigated by conducting simulations with the GGDH turbulent heat flux model (as described in section 4.3.2.4); for comparison with the standard SGDH model used (refer to section 5.2). Variations between the standard SGDH and GGDH simulation definitions are summarised in Table 5.5. Results from GGDH simulations, along with comparison with standard simulations, are presented in section 6.9.1.

Table 5.5: GGDH simulation setting variations from standard simulations

Altered property/parameter	Specification/Value
Turbulent flux model	GGDH
Parameter relaxation factor	
Flux	10%
U	20%
V	20%
W	20%
ν_t	20%
Temperature	20%
Temperature variance	20%

5.3.8.2. Comparison with LES

To compare the overall accuracy of the conducted SARA3DCLIMAT simulations (T-RANS and hybrid LES/T-RANS) with proven higher accuracy and reduced computational complexity from LES closure techniques, Saša Kenjereš performed LES simulations, utilising Smagorinsky closure towards the completion of this study. An identical domain and mesh size was used for the LES simulations, with settings used summarised in Table 5.6. Results and

comparisons to simulations conducted as part of this study, as well as to Uehara findings found in section 6.9.2.

Table 5.6: Summary of LES simulation settings used by Saša Kenjereš

Altered property/parameter	Specification/Value
Closure model	Smagorinsky closure
Filter length	$(\Delta x \Delta y \Delta z)^{1/3}$
Time step	0.1 second
Pr_t	0.4
Parameter relaxation factor	
U	60%
V	60%
W	60%
ν_t	90%
Temperature	60%

6. RESULTS AND DISCUSSION

In this chapter, results from the various investigations (refer section 5.3) are presented and discussed; with the purpose of discussing simulation sensitivity with various parameters; as well as thermal stratified buoyancy effects in the urban atmosphere and validity of SARA3DCLIMAT.

6.1. Representative statistical independence

Figure 6.1 illustrates typical turbulent flow profiles for cases investigated in this study; showing simulated vertical velocity time series at isothermal conditions, at the location of monitoring point 1 (refer section 5.2.1, Figure 5.3), for the T-RANS and hybrid methods. Additional profile time series are provided in Appendix F.

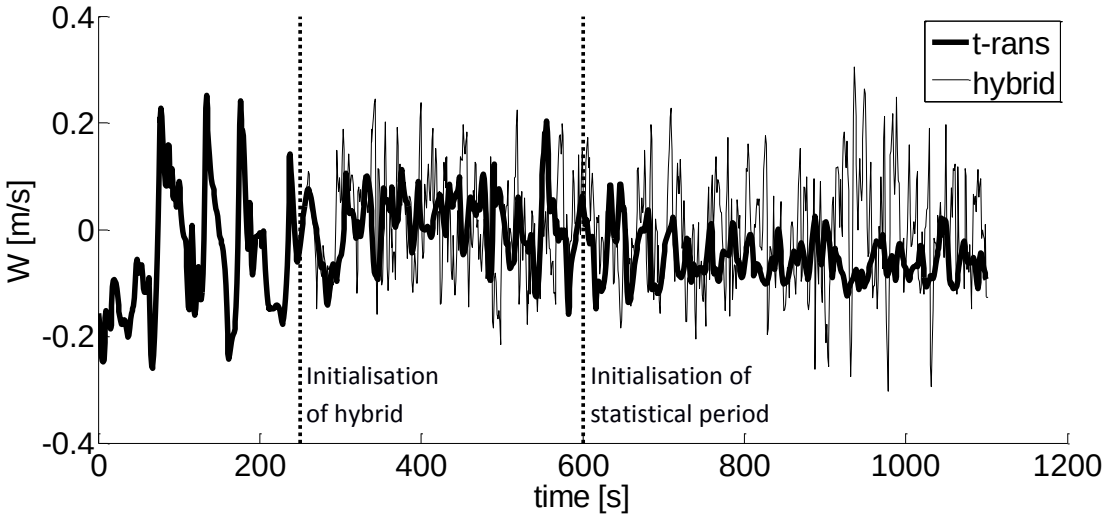

Figure 6.1: Vertical velocity timeseries for isothermal cases with standard settings at monitoring point 1

Note: Hybrid simulations initialised after 250 seconds; while statistics were collected after a transitional stabilisation period of 600 simulation seconds.

Considering domain free-stream residence times (≈ 4 seconds), typical observed turbulent time scales ($\sim 10^{-2}$ seconds), as well as investigations of profile time series (refer Appendix F), it was confirmed that the initial point for statistics

collection and statistical period are important factors in determining average turbulence data for a typical street canyon. This is due to temporal dependences of turbulence and its effects on turbulent stabilisation (transitional initial period).

Taking transitional periods and observed profiles into consideration, it was decided that the standard statistical collection initialisation point will be started after 600 transient simulation seconds. This would allow for sufficient stabilisation periods prior to collection of statistical turbulent data.

The importance of statistical period span was determined by comparing averaged data after various statistical periods, as illustrated in Table 6.1 and Appendix G. The table lists average temperatures (Ave. T) and standard deviations (St. d.) at various statistical periods, for various stratification conditions at monitoring point 1.

Table 6.1: Effect of statistical period on average temperature profile

	Statistical period [s]	**Strong stable**		**Weak stable**		**Weak unstable**		**Strong unstable**	
		Ave. T [^{o}C]	St. d. [^{o}C]	Ave. T [^{o}C]	St. d. [^{o}C]	Ave. T [^{o}C]	St. d. [^{o}C]	Ave. T [^{o}C]	St. d. [^{o}C]
T-RANS	50	72.14	1.71	35.73	0.78	22.78	1.09	29.47	1.97
	250	70.94	2.10	35.95	0.49	22.49	1.08	29.41	2.14
	500	71.11	1.88	35.96	0.51	22.39	1.13	29.44	2.28
	1000	71.38	1.87	35.99	0.47	22.29	1.16	29.35	2.33
	2000	-	-	36.04	0.45	22.37	1.21	29.30	2.32
Hybrid	50	73.09	1.89	36.25	0.82	21.18	0.81	28.43	2.56
	250	73.15	2.17	36.39	0.82	21.11	0.95	26.56	2.38
	500	73.40	2.14	36.31	0.86	21.17	1.04	26.40	2.56
	1000	73.26	2.18	36.31	0.84	21.20	1.06	26.44	2.83
	2000	-	-	36.32	0.82	21.24	1.05	26.44	2.80

Where: Ave. T is the average temperature; St. d is the standard deviation, both calculated from the set of instantaneous values. Values given are for at monitoring point 1.

As can be seen in Table 6.1, there are differences in point temperatures and deviations, with changing statistical period, as expected. Largest differences can be seen between statistical periods of 50 and 250 simulated seconds; which was also observed in averaged canyon flow profiles (refer Appendix G). Acceptable

agreement was observed after statistical periods of greater than 250 statistical seconds for most cases, with little differences being observed in flow profiles. Thus, for the investigated domain and system, statistical periods of 50 seconds were found to be able to predict general turbulent flow profiles; but statistical independence was only typically observed after periods longer than 250 simulation seconds. Taking the latter into account and increased reliability with increased statistical period, a standard statistical period of 500 simulation seconds was used.

6.2. Temporal effects and influences on sampling canyon location

Spatial and sampling canyon location were shown to have great influence on flow profiles, as expected; displaying typical turbulent flow zones, such as regions of acceleration, deceleration, impingement, separation, reattachment, recirculation and shear. Additionally, the influence of the urban array was seen with the creation of the UBL, UCL and urban plume, on flow profiles. The influence of spatial and sampling location and the urban array can be illustrated with the highly varied temperature profile for the strong stable stratification case, using standard simulation settings (refer section 5.2) and the T-RANS model.

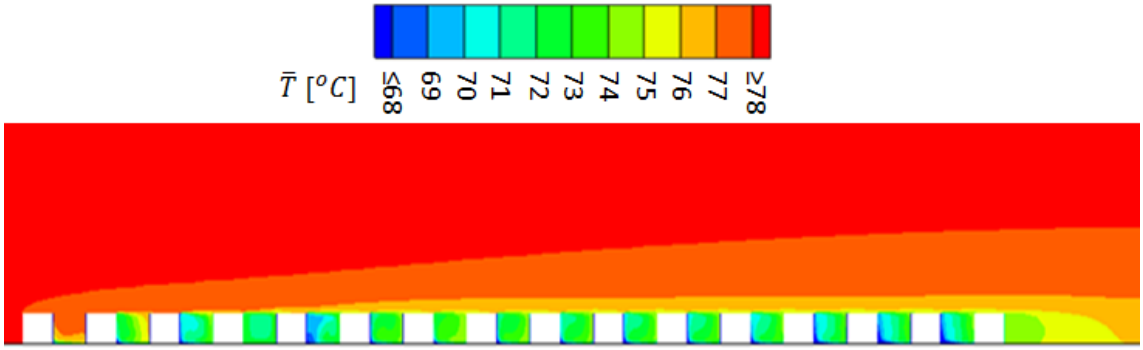

Figure 6.2: Temperature profile for strongly stably stratified condtion, in the central x-z plane using standard simulation settings (T-RANS)

Selected flow profiles for the various canyons are provided in Appendix H. As illustrated in Appendix H, sampling canyon location also has significant influence on flow profiles, especially within the first seven canyons and particularly the first canyon. This can be explained as flow stabilisation to the urban array, to achieve consistent flow profiles within the downstream canyons. The latter is especially noticeable with temperature profiles for the unstable stratification case, which are

only consistent after the ninth canyon. It is also interesting to note that within the last street, profiles also varied from that in upstream canyons; this is particularly noticeable with the streamwise velocity profile of the stably stratified case. This is a consequence of recirculation zones in the urban plume entering the street canyon.

Taking influences of street canyon sampling location into consideration as well as aims for this investigation, it was decided not to use flow profiles for the first nine canyons, to allow for urban array flow stabilisation; as well as not for the last canyon, thereby disregarding influences of recirculation from the urban wake. Additionally, to obtain better statistical results and allow for better evaluation of typical stratification effects, average flow profiles of canyons 10 to 14 were used.

6.3. Thermally stratified buoyancy effects

This section discusses the simulated stratification effects on various flow profiles, with use of the T-RANS and hybrid LES/T-RANS models with standard simulation settings (refer Chapter 1). Comparisons with the isothermal condition are made for investigation of stratification effects on flow profiles; along with simulation validation with Uehara wind tunnel experimental findings.

6.3.1. Neutral stratification

Neutral stratification can be considered the control case in this study, for comparison of temperature stratification influences on flow profiles.

Typical turbulent kinetic energy contours for the neutral stratification case are illustrated in Figure 6.3, along with imposed velocity vectors, for the second and third last street canyons (refer Appendix P for all stratification turbulent kinetic energy contour plots). From the plots it can be seen that there is typically higher turbulent kinetic energy on the windward side of a building compared to the leeward side, as expected due to wind separation, shear stress and re-circulation factors. It is also interesting to note that the hybrid method typically had higher corresponding turbulent kinetic energy values compared to the T-RANS method, as explained in section 4.5.

6.3.1.1. Isothermal flow velocity profiles

Simulation velocity profiles for the neutral stratification case are illustrated in Figure 6.4; along with Uehara values.

From the plots it can be seen that the T-RANS and hybrid methods similarly predict the streamwise velocity profile; with close agreement with Uehara data, only slightly over predicting in the UBL and under predicting in the UCL. The hybrid method was found to significantly better predict streamwise velocity variance and overall shape, with close agreement with Uehara. Conversely, the T-RANS method was found to be incapable of predicting and matching Uehara data, with almost complete lack of the UCL/UBL boundary at the building height.

Evaluations of other velocity components revealed significant differences between the T-RANS and hybrid methods, with the latter predicting significantly higher lateral velocities and standard deviations. Lateral velocity profiles were found to be of order significantly lower (approximately 50 times lower) than vertical velocity profiles. With the latter, both methods predicted not only different magnitudes, but also directions; with a general upward flow predicted by the hybrid method and re-circulatory type motions predicted by the T-RANS method. As with streamwise velocity deviations, the hybrid had better agreement with Uehara data, due to increased resolved contributions with the method resultant from the methods increased frequency capturing.

6.3.1.2. Isothermal flow stress profiles

From the plots (Figure 6.4), it can be seen that the streamwise-vertical shear stress contribution is of order 10 to 100 times greater than other shear stress components. Additionally, hybrid method profiles were more varied than T-RANS profiles, mainly due to increased varied resolved contributions and the increased frequency capturing by the hybrid method. This generally results in better agreement with Uehara data, as shown with the plot of streamwise-vertical shear stress.

In all cases, it was observed that the UCL/UBL boundary resulted in peak contributions, followed by interlayer stabilisation boundaries. This can be

attributed to flow obstructions resulting in flow re-circulation, thus an increased flow gradient between layers and increased shear stress; which is propagated and decays due to drag and pull effects.

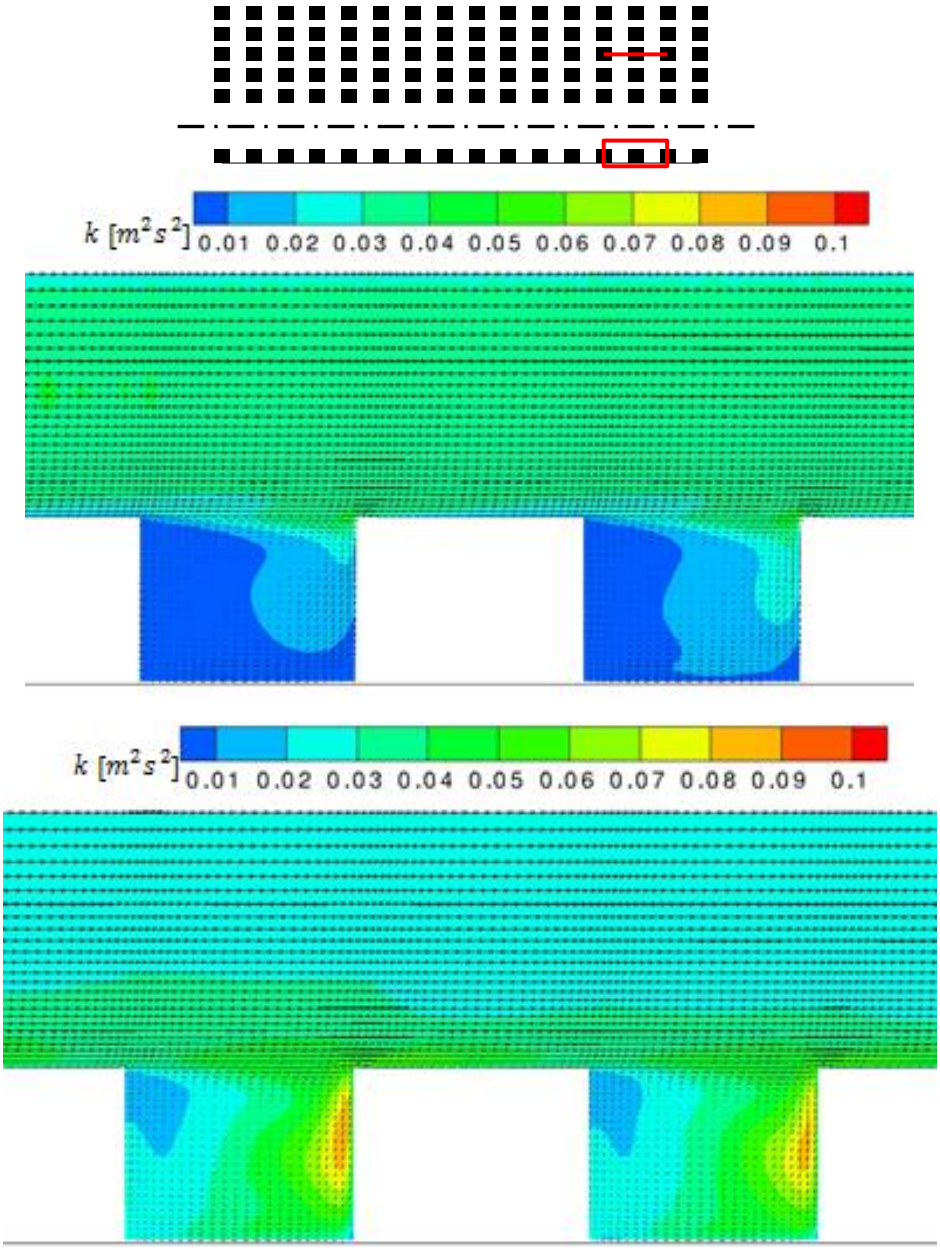

Figure 6.3: Neutral stratification standard k-profiles and velocity vectors (top: T-RANS; bottom: hybrid)

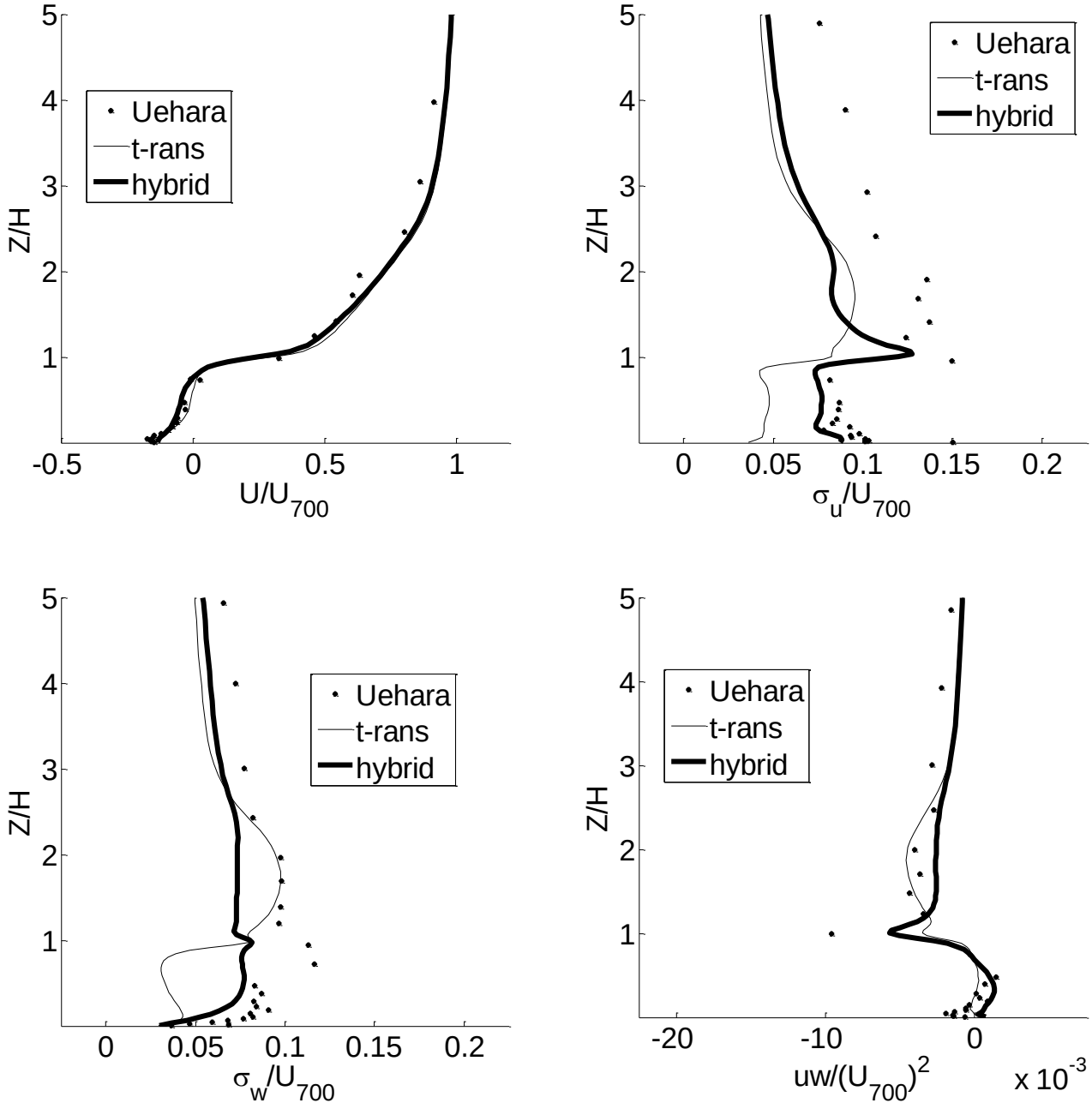

Figure 6.4: Neutral stratification standard velocity flow profiles

6.3.2. Stable stratification

Stable stratification was expected to damp turbulence and heat conduction (hence increase turbulent Prandtl number), thereby dampening flow profiles, compared to neutral stratification; with potential flow re-lamination. Figure 6.5 and Figure 6.6 illustrate stable stratification turbulent kinetic energy profiles, in comparison to isothermal conditions for T-RANS and hybrid models respectively. From the plots it can be seen that in general, increasing stable stratification decreased turbulent kinetic energy within the UBL, however the converse was observed in the UCL.

6.3.2.1. Stable stratification effects on flow velocities

Figure 6.7 and Figure 6.8 show the velocity profile results for strong and weak stable stratification cases respectively, with Uehara data being provided where available for validation purposes.

From the weak stable stratification case it can be seen that both the T-RANS and hybrid method are relatively able to simulate Uehara streamwise velocity profiles; with over estimation of values, especially towards street level. However, for the strong stratification case, SARA3DCLIMAT was unable to simulate the streamwise stagnation, with over predictions within the UCL. Comparing stable stratification plots with isothermal plots it can be seen that there is little difference between the streamwise velocity profiles, further illustrating SARA3DCLIMAT's inability to simulate the Uehara observed flow dampening and stagnation with increasing stable stratification. This inability can also be seen with the streamwise velocity deviation plots, with little variation from the neutral stratification case.

Evaluation of the lateral and vertical velocity and velocity deviation profiles, compared to neutral stratification profiles reveals a slight dampening of velocity profiles; with similar trends between T-RANS and hybrid methods, the latter resulting in reduced profile amplitudes. Little difference is observed between velocity deviation profiles with comparison of stable and neutral stratification conditions. The hybrid method, although inaccurate compared

to Uehara data, as able to obtain profile shapes. Thus stable stratification dampening effects seemingly had no influence.

6.3.2.2. Stable stratification effects on flow stresses

Comparison of stable stratification shear stress profiles with isothermal plots (Figure 6.4) reveals that in general increased stable stratification has a smoothening effect on stress profiles, with decreased variations and amplitudes. Additionally, a slight dampening of streamwise-vertical shear stresses is observed with stable stratification compared to the isothermal case. Hybrid methods resulted in best agreement with Uehara data, with over prediction with strong stable stratification in the UCL and UBL, compared to under prediction under isothermal conditions.

6.3.2.3. Stable stratification effects on temperature profiles

Stable stratification temperature and temperature deviation profiles are shown in Figure 6.9 (strong stable) and Figure 6.10 (weak stable).

From temperature profile plots, it can be seen that there is a steep temperature gradient within close proximity to street level ($^{z}/_{H} < 0.1$), as expected due to decreased turbulent mixing in near-wall laminar regions. This steep temperature gradient was also observed to have a large degree of deviation (up to 30%), due to modelled contributions. Large temperature gradients were also observed in the UCL/UBL transition layer; a result of mixing between the UCL climate and bulk fluid. Presence of the urban array and the resulting simulated effects on atmospheric flow was found to lead to a temperature decrease of up to 10%.

T-RANS and hybrid methods were seen to result in similar temperature profiles in the UBL and towards street level ($^{\mathrm{z}}/_{\mathrm{H}} < 0.1$); however, differences were observed within the upper UCL, with lower temperatures being predicted by the T-RANS method. The latter method also predicted temperature profiles that are indicative of strong re-circulatory vortices within street canyons, in agreement with velocity profiles (Figure 6.7 and Figure 6.8).

Comparison of temperature and deviation with Uehara revealed that SARA3DCLIMAT significantly over predicted temperature profiles, in excess of 20% within the UCL; thus insufficient cooling of UCL air, hence the reason for investigations into decreases in turbulent Prandtl number and therefore increased heat conduction capabilities (refer section 6.8 and further investigations in section 6.3.2.4). Comparisons with temperature deviation revealed that simulations were unable to match Uehara findings, particularly near street level and free stream regions. The hybrid method can be seen to better predict the UCL/UBL transition boundary, with capture of Uehara profile peaks and initial values.

It should be noted that there is not agreement with Uehara data, as significantly large temperature deviation values are obtained well above the UCL, which is practically not likely in the free stream region. Additionally, Uehara findings show low deviation values in the near street level region, also not in agreement with literature, with temperature gradients typically being experienced and therefore large deviations.

6.3.2.4. Stable stratification effects on stratification stability

Making use of expressions for local Richardson flux number (Eq. 2.4) and modelled simplifications for the advection terms (Eq. 4.13 and Eq. 4.14), local Richardson flux numbers were calculated from statistical simulation results for stable stratification results. Profiles of the local Richardson flux number for the two stable stratification cases are presented in Figure 6.11, along with illustration of critical Richardson number. Utilising the Ellison model (as described in section 4.3.2.5, Eq. 4.37), turbulent Prandtl profiles for corresponding local Richardson numbers were plotted, as in Figure 6.12.

As can be seen in Figure 6.11, stable stratification Richardson flux numbers are mainly positive, as expected due to positive temperature gradients within the street canyon; with varied degrees of stability mainly due to changing temperature gradient. Negative Richardson numbers, indicative of unstable stratification, can also be seen (especially with the T-RANS method) to occur towards the UCL/UBL boundary. The latter is due to reversed temperature gradients (refer section 6.3.2.3) and varied magnitude of the advection terms.

Therefore with the presence of bulk stable stratification, varied local stratification conditions (both stable and unstable) were observed. Local stratifications above the street canyon are also seen to be neutral, due to the negligible temperature gradients predicted in the upper regions of the UBL.

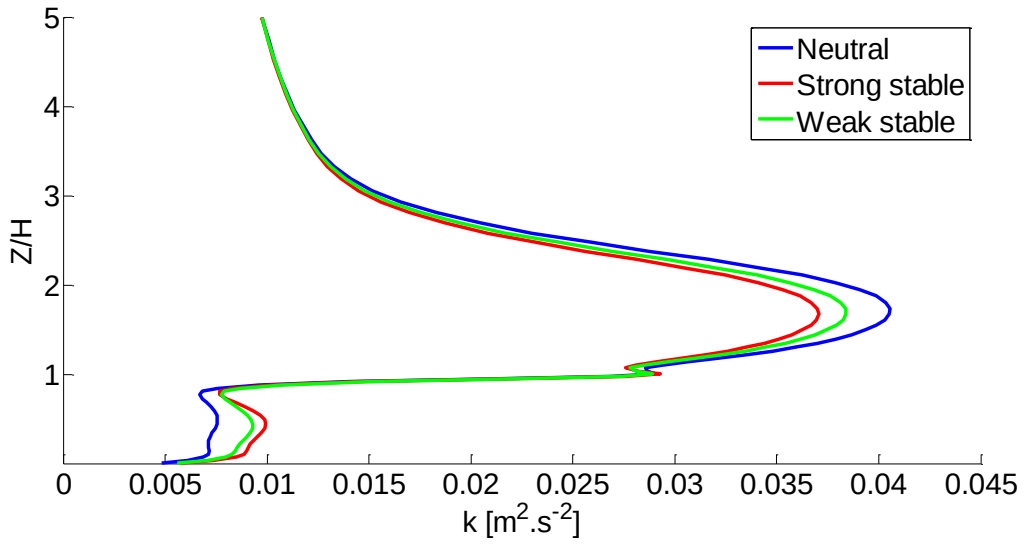

Figure 6.5: Comparison of neutral and stable stratification T-RANS model standard turbulent kinetic energy profiles

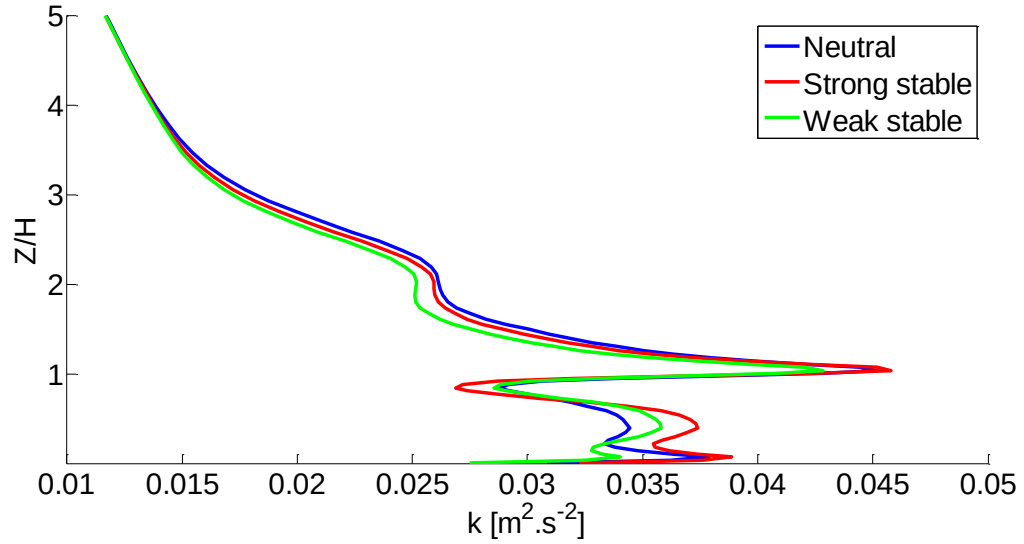

Figure 6.6: Comparison of neutral and stable stratification hybrid model standard turbulent kinetic energy profiles

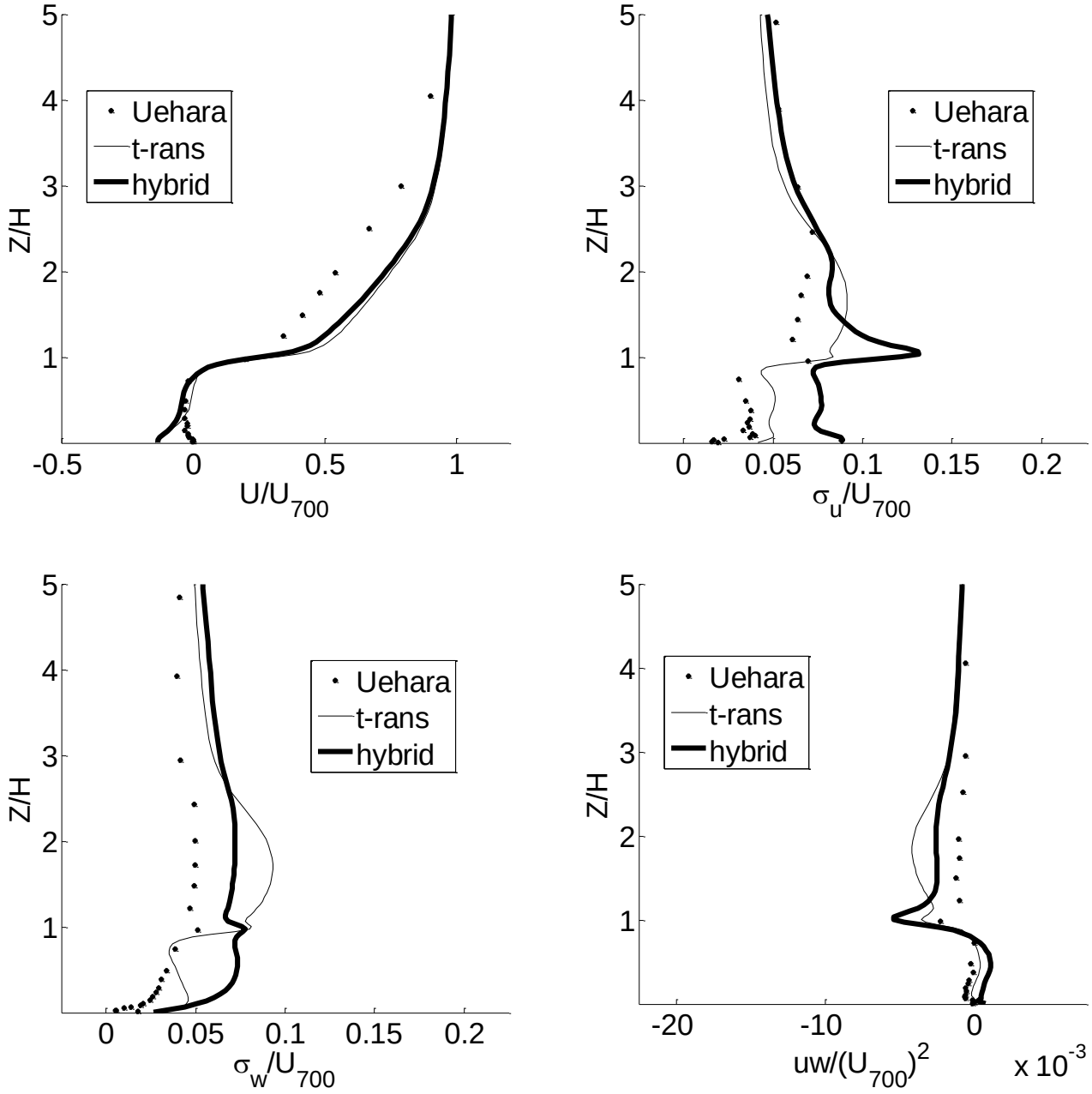

Figure 6.7: Stong stable stratification standard velocity flow profiles

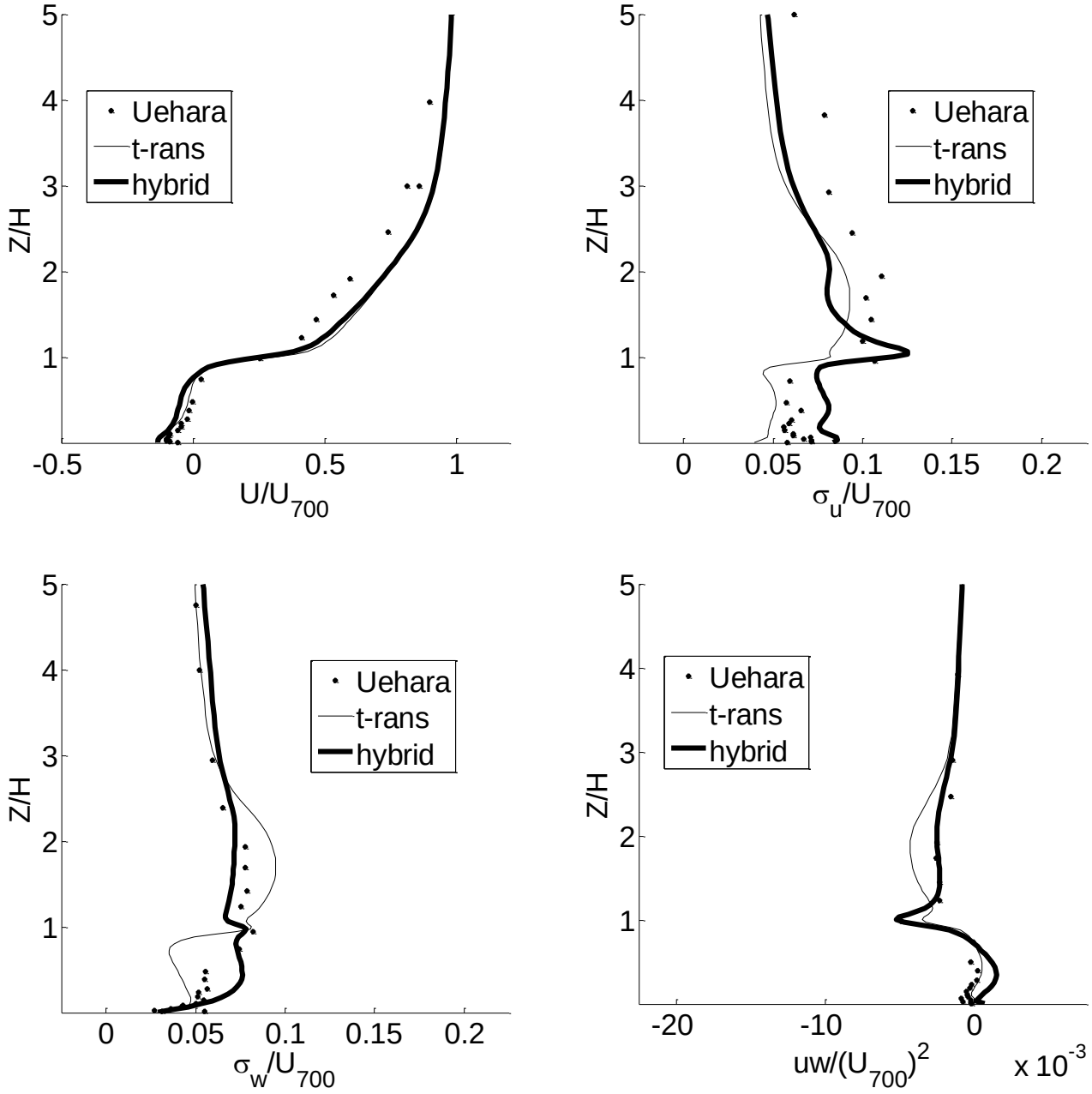

Figure 6.8: Weak stable stratification standard velocity flow profiles

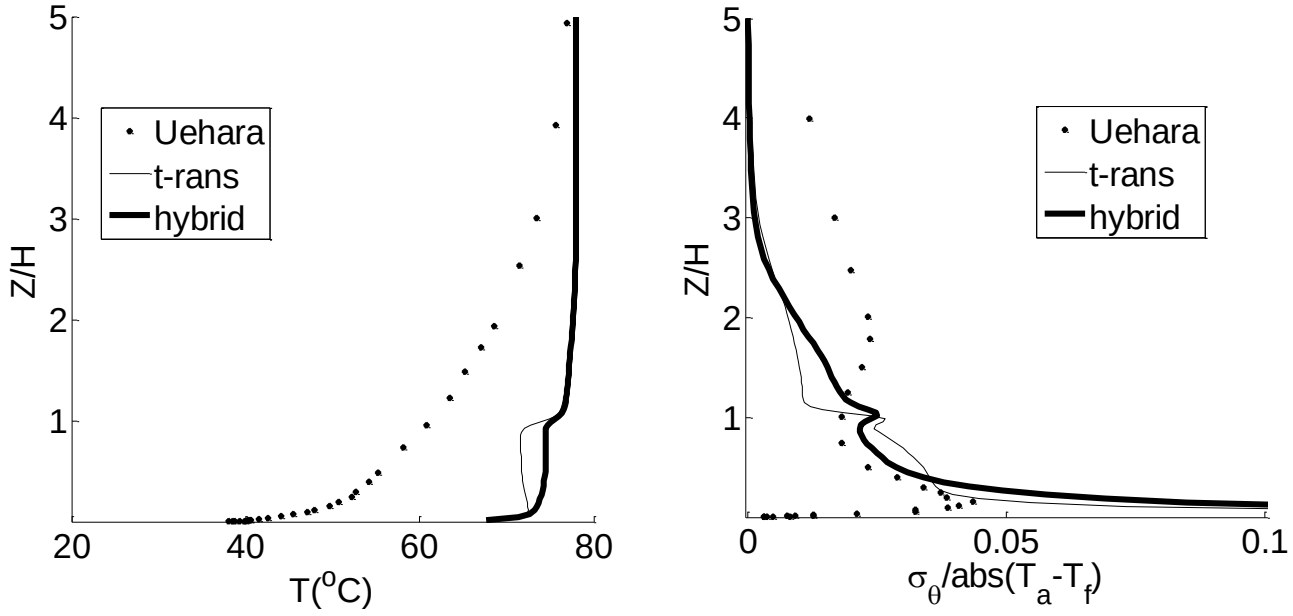

Figure 6.9: Stong stable stratification standard temperature profiles

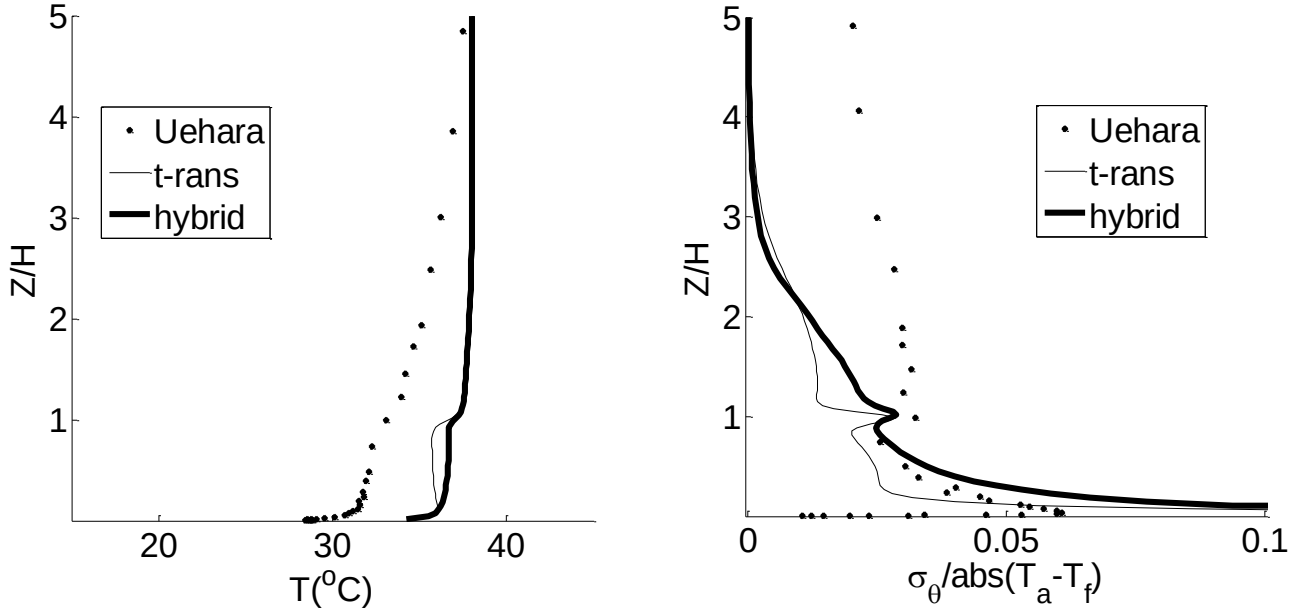

Figure 6.10: Weak stable stratification standard temperature profiles

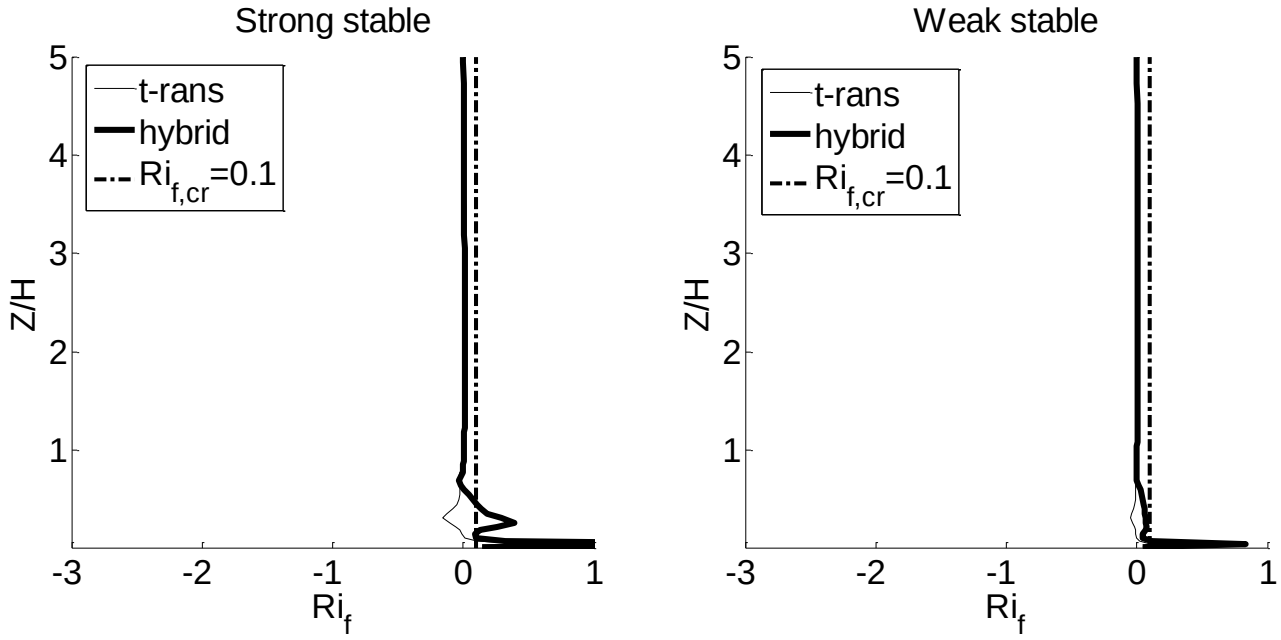

Figure 6.11: Stable stratification local Richardson flux profiles

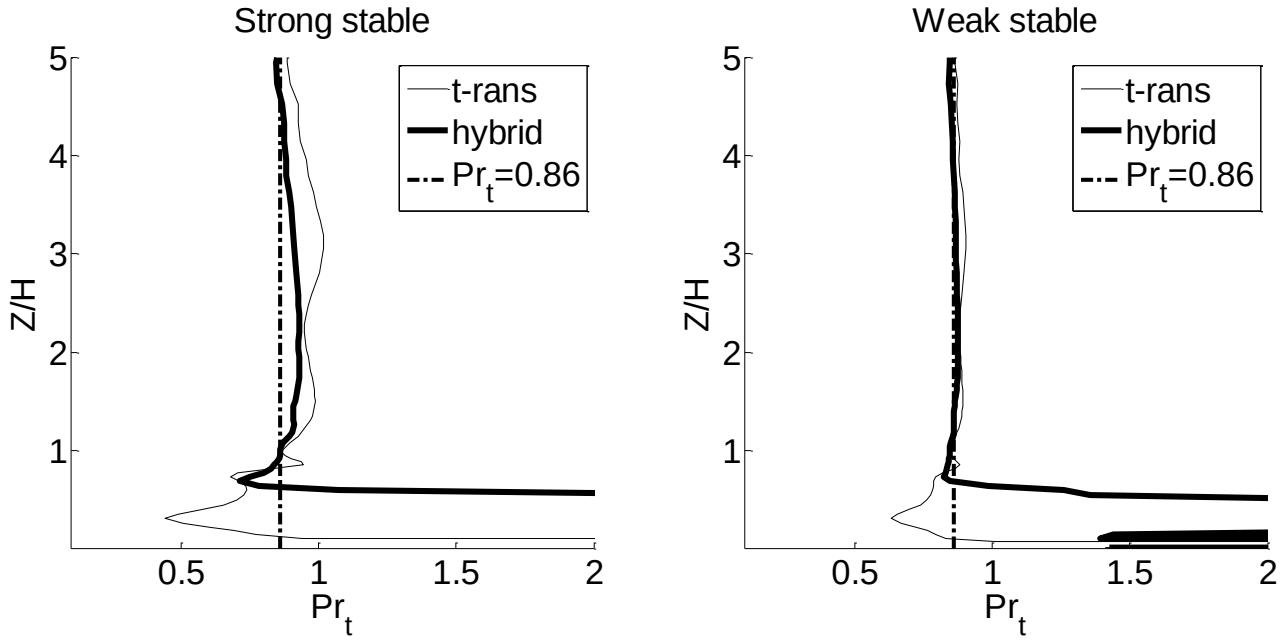

Figure 6.12: Stable stratification (Ellison) modelled turbulence Prandtl number

6.3.3. Unstable stratification

Unstable stratification was expected in enhance turbulence and heat conduction, thereby amplifying flow profiles compared to neutral stratification; thereby improving the high Reynolds flow models used in SARA3DCLIMAT and therefore better agreement in validations. Figure 6.13 and Figure 6.14 illustrate unstable stratification turbulent kinetic energy profiles, in comparison to isothermal conditions for T-RANS and hybrid models respectively. From the plots it can be seen that in general, increasing unstable stratification resulted in the expected increase in turbulent kinetic energy within the UCL and UBL.

6.3.3.1. Unstable stratification effects on flow velocities

Figure 6.15 and Figure 6.16 show velocity profiles for the strong and weak unstable stratification investigations respectively. Uehara profiles are provided where available for validation.

From the velocity plots, it can be seen that SARA3DCLIMAT is able to predict streamwise velocity profiles, compared to Uehara profiles; with better prediction with weak unstable compared to strong unstable. However SARA3DCLIMAT under predicts the streamwise UCL velocity, while slightly over predicting it in the free stream region; better Uehara agreement is observed with the hybrid method, than with the T-RANS method; due to improved frequency capturing. Compared to isothermal conditions, unstable stratification was found to decrease streamwise velocity in the UCL, with increasing bulk unstable stratification; while slightly increasing the velocity in the lower UBL. This decrease in UCL streamwise velocity with increasing instability can be explained by an increased upward velocity and thus, decreased re-circulation within the canyon. This increased upward velocity can be seen to be larger than with isothermal conditions, thereby illustrating the influence of thermal buoyancy on air flow.

Evaluation of velocity deviations revealed that unstable stratification slightly increases deviations and deviation amplifications, compared to isothermal conditions. This is expected as unstable stratification will increase turbulence and thus the variability of flow. It is interesting to note that the hybrid method is able to capture larger increases in deviation, due to increased frequency

capturing. However, compared to Uehara profiles, simulated velocity deviations were significantly lower, especially compared to with the neutral stratification case, with only the hybrid method being able to capture overall profiles and better Uehara agreement.

6.3.3.2. Unstable stratification effects on flow stresses

Comparison of the stress plots with neutral stratification plots (Figure 6.4) reveals that in general unstable stratification decreased the streamwise-vertical shear stress, while increasing lateral-vertical and streamwise-lateral stresses. This can be expected due to changes in velocity profiles compared to isothermal conditions and therefore shear rates between velocity components. It is interesting to note that in all cases peak shear rates were observed in the UCL/UBL boundary, as expected due to maximum mixing rates between micro flow profiles at obstacle boundaries. Comparison of streamwise-vertical shear stress profiles showed that SARA3DCLIMAT under predicted Uehara profiles, especially the UCL/UBL peak at $^{z}/_{H} = 1$.

6.3.3.3. Unstable stratification effects on temperature profiles

Unstable stratification temperature profiles are shown in Figure 6.17 (strong unstable) and Figure 6.18 (weak unstable).From temperature profile plots it can be seen that, as with stable stratification, steep temperature gradients occur in close proximity to the street level, as expected due to decreased turbulent mixing in this near wall laminar region. Likewise a steep temperature gradient was observed in the UCL/UBL boundary, resulting from the mixing of the cooler UBL with the warmed canyon flow. Thus simulation of the urban array resulted in expected temperature profiles, with a 30% increase in temperature compared to natural conditions and approximately a 10% increase from atmospheric ground temperature to temperature at the UCL/UBL transition.

Due to sharp temperature gradients and temperature ranges within the canyon, large temperature deviations were observed from simulations, as expected; along with peaked deviations in the UCL/UBL transition and negligible values in free-stream bulk flow regions.

T-RANS methods were observed to predict larger temperature gradients in the UCL/UBL boundary, propagating into larger temperatures within the canyon. The latter is indicative of better cooling of the canyon and therefore enhanced mixing, especially within the lower UBL. As with stable stratification, reversed temperature gradients were observed in the upper layer of the UCL, illustrating the presence of strong re-circulatory flows within the canyon. This is in agreement with velocity profile plots.

Comparison of temperature profiles with Uehara values showed that SARA3DCLIMAT generally under predicted temperature, with better agreement from T-RANS simulations and hybrid methods better predicting profile shapes. The former is due to the steeper T-RANS temperature gradients in the lower UBL; while the latter due to better prediction of velocity profiles by the hybrid method in combination with increased frequency capturing leading to better profile prediction. However, validation with unstable temperature stratification revealed similar results to as with stable stratification, that is significant over prediction towards street level; along with under prediction in the free stream region. However with the expected large temperature gradients towards street level along with temperature ranges larger deviations were expected than in Uehara, while in the near-isothermal free stream region no temperature deviations can be expected, as predicted by Uehara.

6.3.3.4. Unstable stratification effects on stratification stability

As with stable stratification, local Richardson flux number and Ellison modelled turbulent Prandtl number profiles were determined for both unstable stratification cases; refer Figure 6.19 and Figure 6.20 respectively.

As can be seen in Figure 6.19, under bulk unstable stratification conditions, local Richardson flux numbers are mainly negative, as expected, with a peak instability towards street level, due to the occurrence of strongest temperature gradients in that location. As with stable stratification, local stratification conditions also tend towards neutral conditions in free stream flow regions, due to negligible temperature gradients in the region. It is interesting to note however that under strong unstable stratification

conditions, locally stable conditions were experienced, more so with the T-RANS method, in the upper region of the UCL. This is due to increased flow re-circulation, especially with strong unstable stratification, resulting in street canyons having central vortices with decreased temperature. Therefore, as seen with stable stratification, unstable stratification also resulted in varied degrees of local stratification, potentially with occurrence of local stabilities.

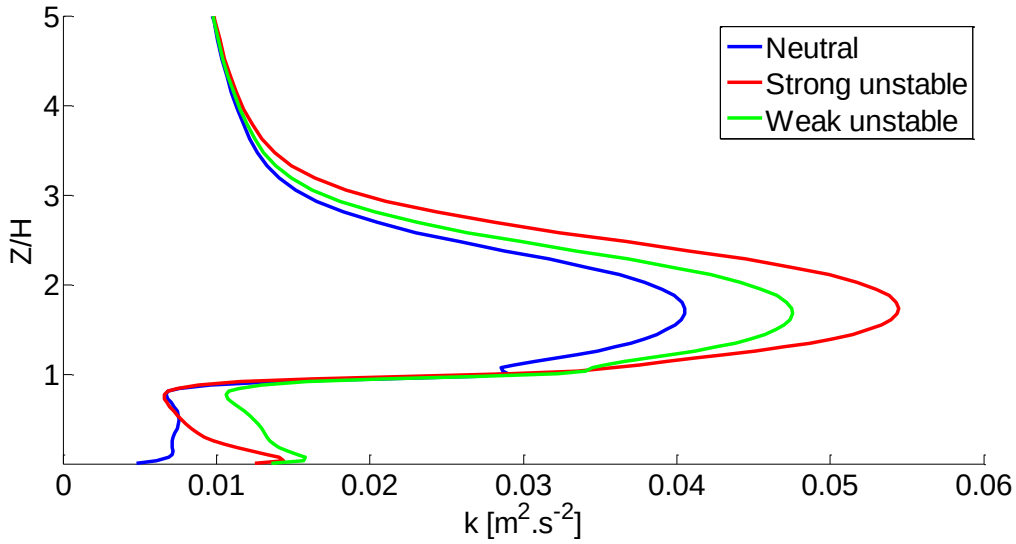

Figure 6.13: Comparison of neutral and unstable stratification T-RANS model standard turbulent kinetic energy profiles

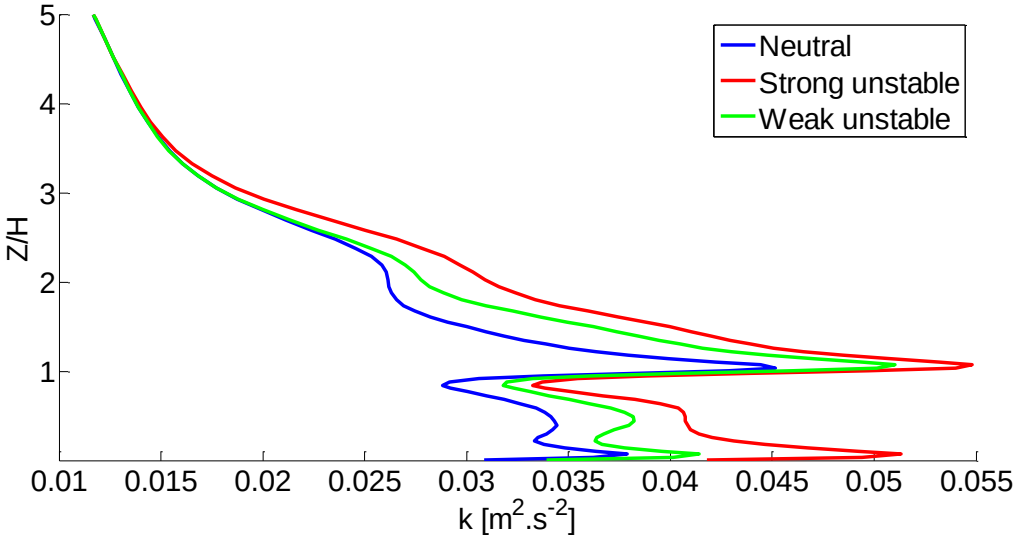

Figure 6.14: Comparison of neutral and unstable stratification hybrid model standard turbulent kinetic energy profiles

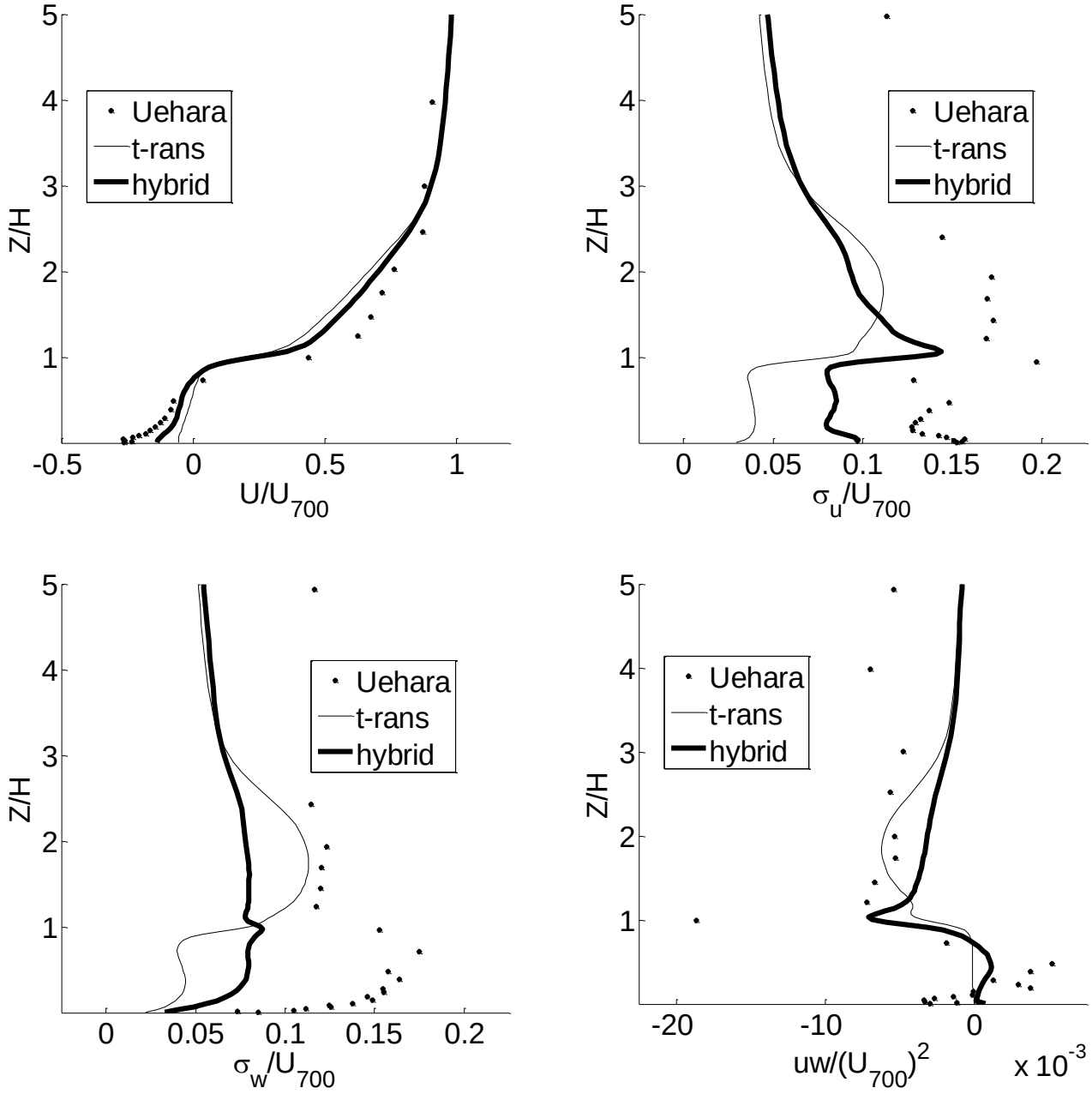

Figure 6.15: Stong unstable stratification standard velocity flow profiles

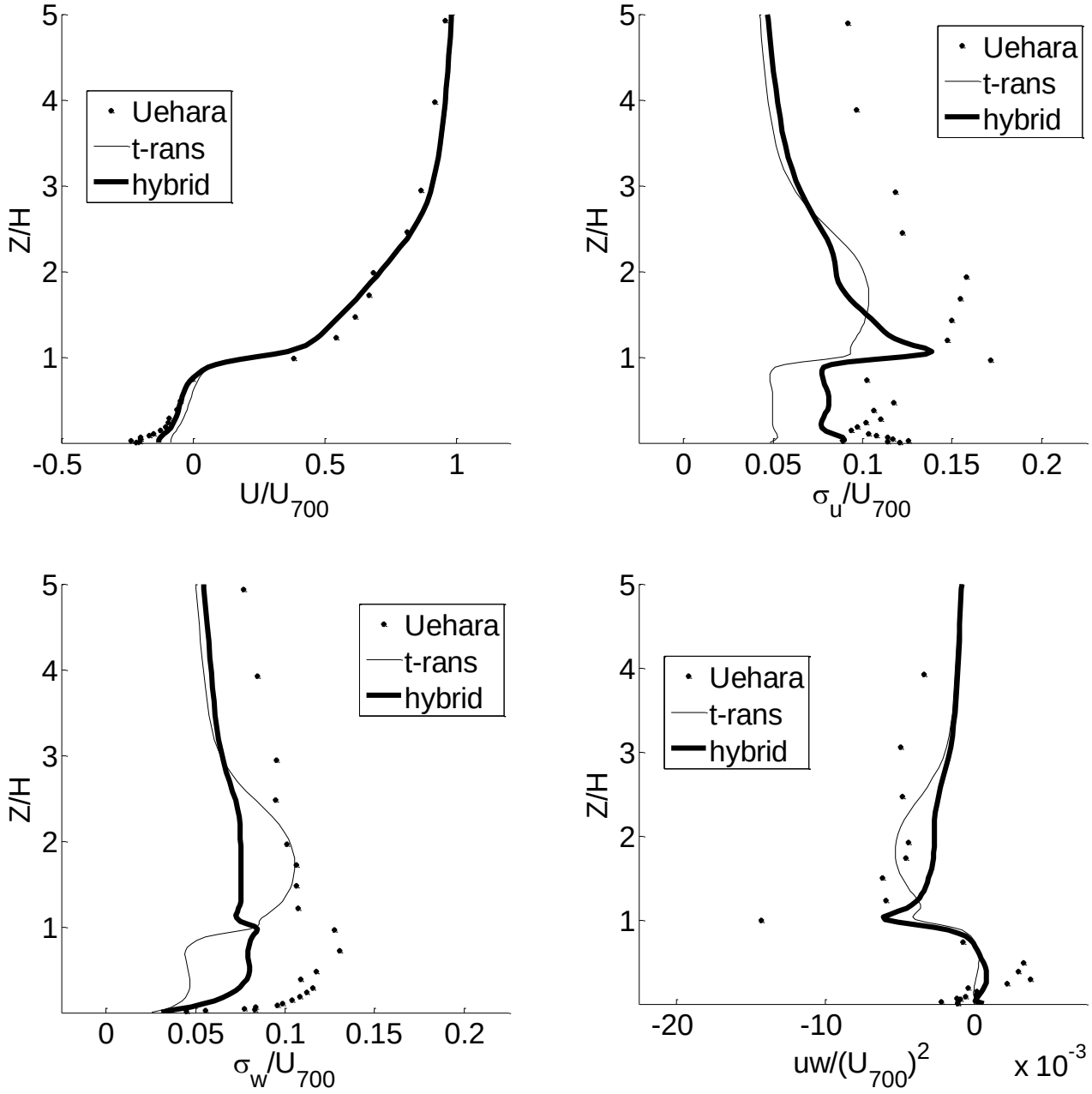

Figure 6.16: Weak unstable stratification standard velocity flow profiles

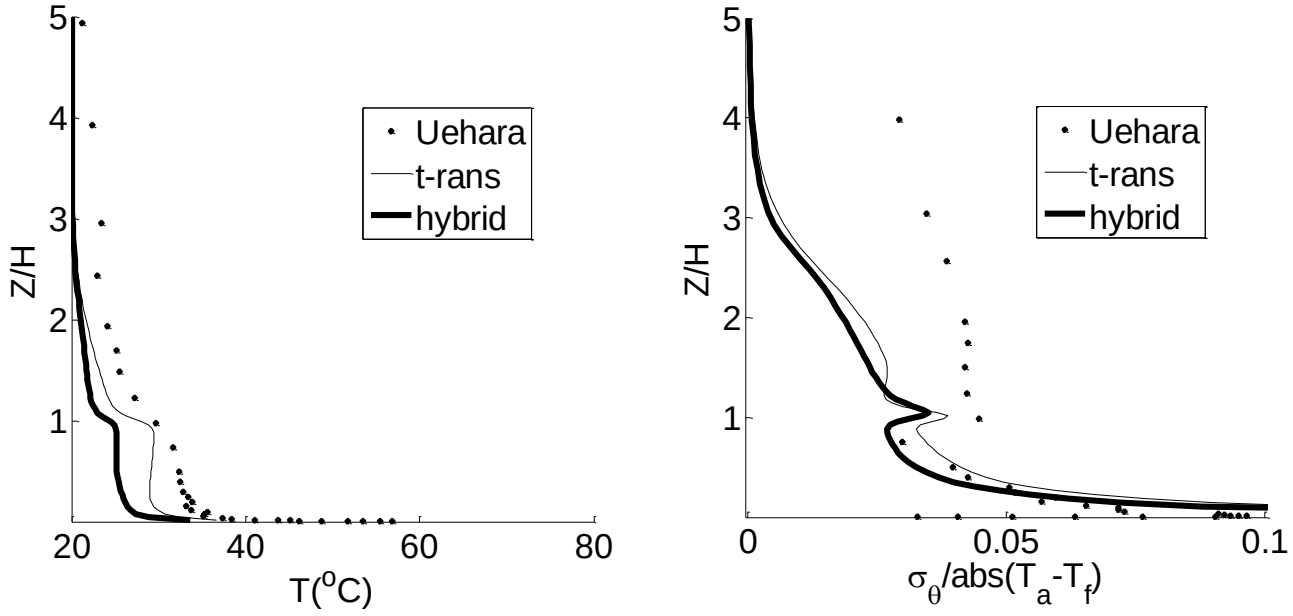

Figure 6.17: Stong unstable stratification standard temperature profiles

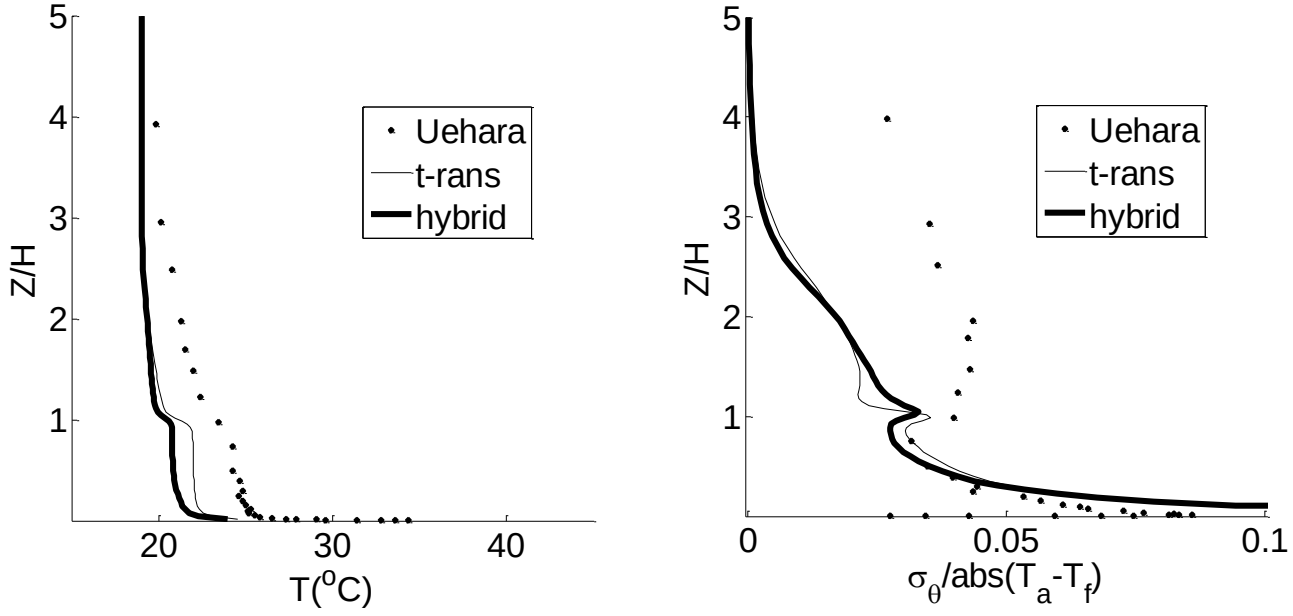

Figure 6.18: Weak unstable stratification standard temperature profiles

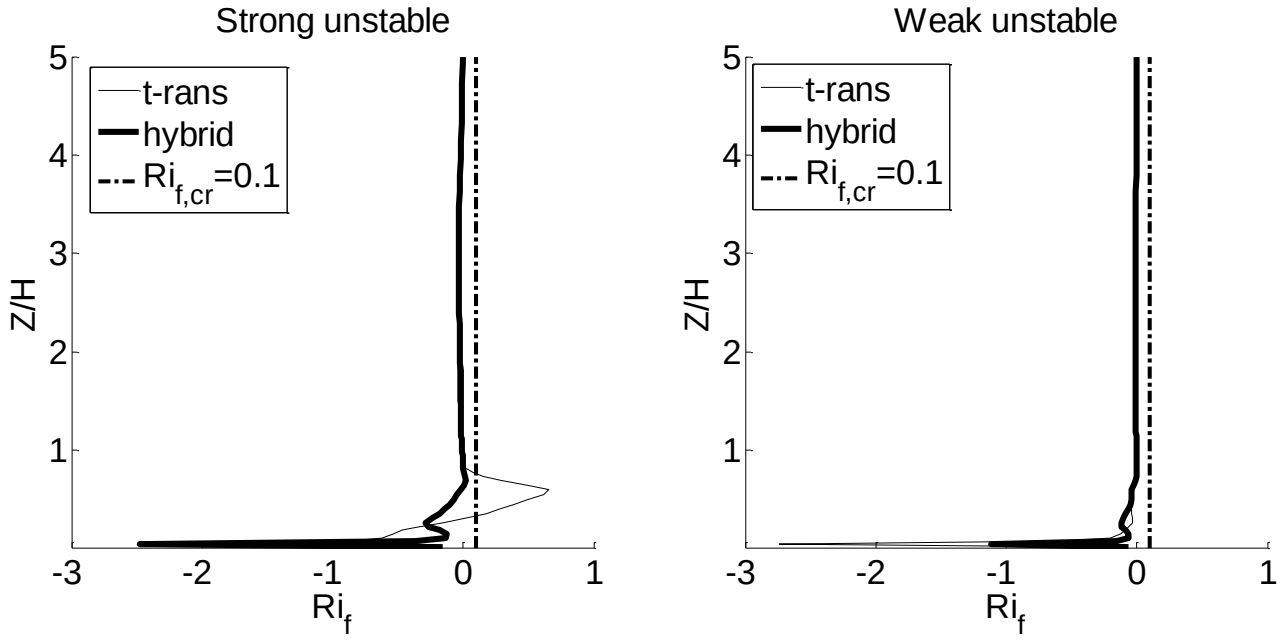

Figure 6.19: Unstable stratification local Richardson flux profiles

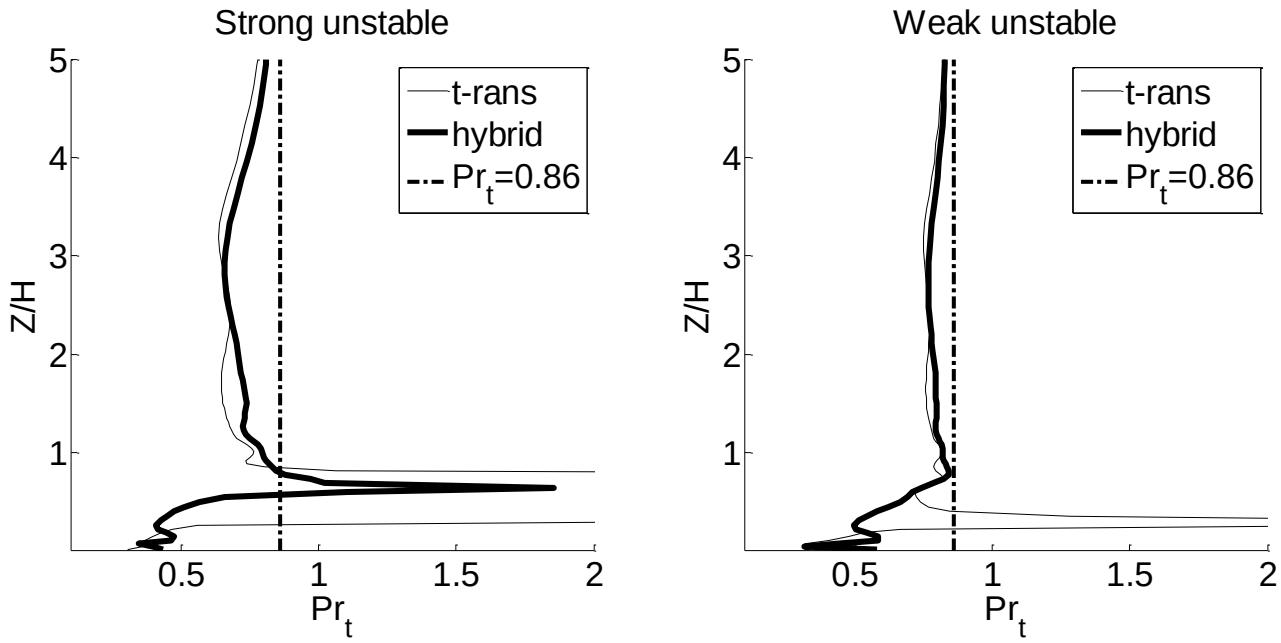

Figure 6.20: Unstable stratification (Ellison) modelled turbulence Prandtl number

6.4. General comparisons of T-RANS and hybrid LES/T-RANS

Comparisons of profile time-series reviled that in general the hybrid method resulted in an increased profile frequency, with increased fluctuations compared to the T-RANS method, as illustrated in Figure 6.21. The figure shows a time series plot of the isothermal vertical velocity (W) at monitoring point 1 (refer Figure 5.3). Refer to Appendix F, for additional time series plots. This expected increase in profile frequency capturing is a consequence of the hybrid method lowering turbulent timescale (τ). This is resultant from the methods changes to rate of dissipation in the turbulent kinetic energy dissipation conservation equation (refer section 4.5.1, Figure 6.5, Figure 6.6, Figure 6.13 and Figure 6.14).

Additionally, the hybrid method was found to alter turbulent flow profiles, varying profile ranges and averaged profiles, as illustrated by the increased vertical velocity amplitudes in Figure 6.21; being attributed to lowering of turbulent timescale.

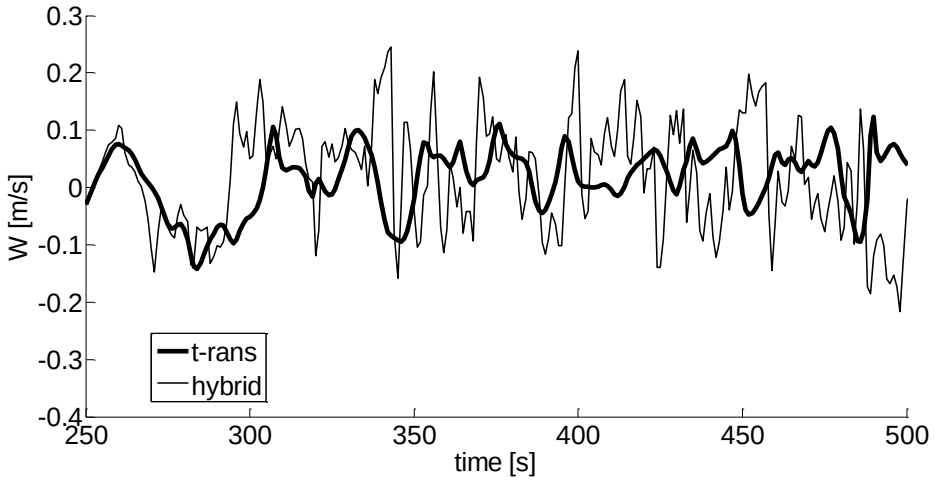

Figure 6.21: W-time series for the standard isothermal T-RANS and Hybrid test case

Variation by the hybrid method compared to the T-RANS method, due to increased frequency capturing, in addition to natural spatial and temporal dependence of turbulence, requires comparisons of statistical averaged profiles for fair comparison. Section 6.3 provides detail on such data along with comparisons, for standard simulation and statistical settings used in this study (refer section 5.2.5).

Analyses of these statistically processed profile plots revealed that in general, the hybrid method was better able to predict streamwise velocity profiles with closer

agreement with Uehara, compared to the T-RANS method. Both methods were seen to fairly accurately predict neutral stratification velocities, with slight over predictions in the near wall boundary (street).

With regard to velocity variances and stresses, it was observed that the hybrid method was better able to predict profiles within the UCL, compared to the T-RANS method and Uehara profiles; with the presence of peak values at the UCL/UBL boundary, which was often completely lacking with T-RANS profiles. The latter observations were due to increased resolved contributions with the hybrid method, allowing for better capturing of turbulent variations, compared to modelled contributions. However, the T-RANS method was found to be more suited in the UBL, with better capturing of profile bulges above the buildings. This was due to increased modelled contributions from the T-RANS method in this region (reduced in hybrid method), a consequence of more time consistent flow profiles.

The hybrid method was found to be incapable of accurately mimicking Uehara temperature profiles, especially within the UCL and compared to the T-RANS method; the latter also with limited capability. T-RANS was found to be more accurate for unstable stratification conditions. However, the hybrid method, although being more inaccurate, was able to predict profile shapes better than the T-RANS method. The latter, giving temperature profiles typical of re-circulation vortices; which is in agreement with velocity profiles.

The T-RANS method was found to be more capable at predicting temperature variance profiles, compared to the hybrid method; with more accurate prediction of the building level peak and above canyon level bulge. However, both methods were found to significantly over predict temperature variances towards street level, while under predicting them towards the free-stream zone. Over predictions were results of overestimates in temperature variances due to large scale turbulent variations, from higher resolved contributions; while under estimates are due to insufficient modelled and resolved contributions.

It should be noted however, that while there was no agreement with Uehara temperature variance profiles, Uehara show relatively large free stream (≈30% street canyon peak or ≈75% building height value) and negligible street level temperature variances, which is not in agreement with literature expectations with

flow and temperature profiles, as temperature is expected to vary negligible in the free stream region, while having large variable gradients at street level.

6.5. Time step independence

Figure 6.22 illustrates general observations from investigations into time step independence for T-RANS and hybrid methods, at monitoring point 1 for isothermal conditions. The plot includes data for the three investigated time steps, namely the standard one second, as well as half and twice the standard.

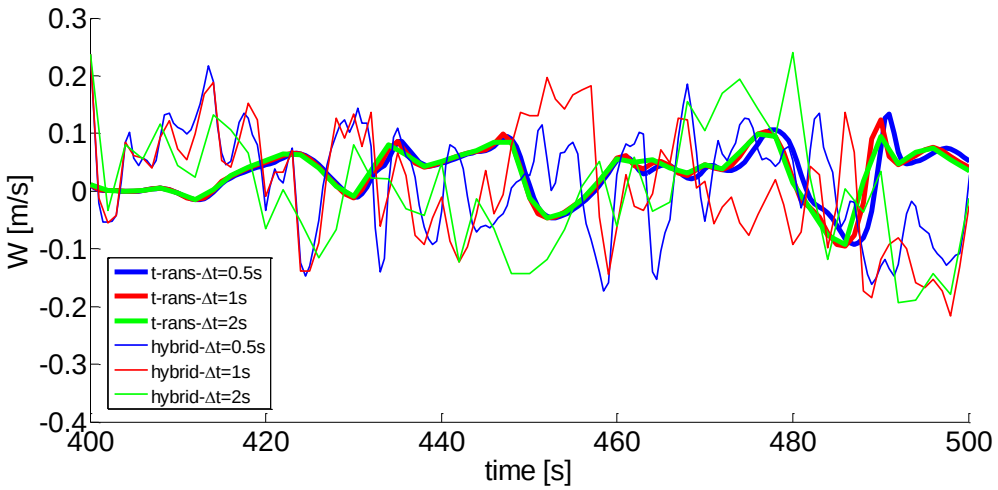

Figure 6.22: Vertical velocity time series for isothermal T-RANS test cases at monitoring point 1

As can be seen from the figure, profiles with smaller time steps resulted in smoother profiles, as well as increased deviation from each other with time period. The former is due to increased temporal resolution; which together with turbulence's dependence on local flow condition history results in the latter, with increased deviation amplification with time; hence increased frequency capturing with a decreased time steps, which was more observed with the hybrid method due to the methods already increase in frequency capturing. Therefore, as with T-RANS and hybrid method comparisons, long-time statistically averaged profiles are required for minimal time step influences and fair comparison (refer section 6.1).

Taking into account long-time statistically averaging of flow profiles, influences of time step were determined the ratio between perturbed time steps and the standard time step (as per Eq. 6.1); utilising a standard statistical period of 500

seconds and an average street canyon (refer section 5.2.5). Results of time step perturbation investigations are presented in Appendix J.

$$\text{normalisation} = \frac{value_{\Delta t}}{value_{\Delta t=1}} \qquad \text{Eq. 6.1}$$

Analyses revealed that for the T-RANS method, similar profiles are most obtained with the three different time steps; with closer agreement between the standard and half-standard time steps. Slight discrepancies were observed for velocity and shear profiles, particularly within the street canyon; however on further investigation and comparison of profiles it was revealed that these can be attributed differences between profiles and near zero values of the normalisation standard time step value. For the hybrid method, time step variations were found to have even less of an effect on the statistically averaged profiles, compared to with the T-RANS method; with better agreement between time step simulations.

Time step perturbations were therefore found to have no significant influence on simulated statistical results; thus for ease of processing and tracking, to obtain a relatively refine time resolution, while reducing the time required for statistical simulation, a standard time step of one second was chosen for this study.

6.6. Inlet velocity variation effects

A least-squares re-calibration of the standard inlet velocity power-law expression with Uehara approach flow profiles, using an updated free stream velocity (U_∞) (assumed to be equal to Uehara velocity values at a height of 700 mm (U_{700}))) and height (z(U_∞)), revealed that the power law is in fact better fitted with a power law of order one quarter (Eq. 6.2); as illustrated in Figure 6.23.

$$U_{in} = \min\left(U_\infty\left(\frac{z}{z(U_\infty)}\right)^{1/4}, U_\infty\right) = \min\left(1.5\left(\frac{z}{0.7}\right)^{1/4}, 1.5\right) \qquad \text{Eq. 6.2}$$

From the figure, it can be seen that the better-fit (least squares) power law expression generally under estimates approach flow profiles compared to Uehara data. This is due to the limitation of the free stream velocity of no more than 1.5 m/s, with corresponding height of $\frac{z}{H} = 7$. This better fit to Uehara data should allow

for closer correlation with flow profiles. However, it was expected that these decreases in approach flow profiles (up to 15%), would have negligible effect on statistically averaged profiles, in the fully developed down-stream section of the urban array. The influence of inlet flow profile and confirmation of negligible difference between the two power law approach profiles are discussed below, as investigated for the neutral stratified test case.

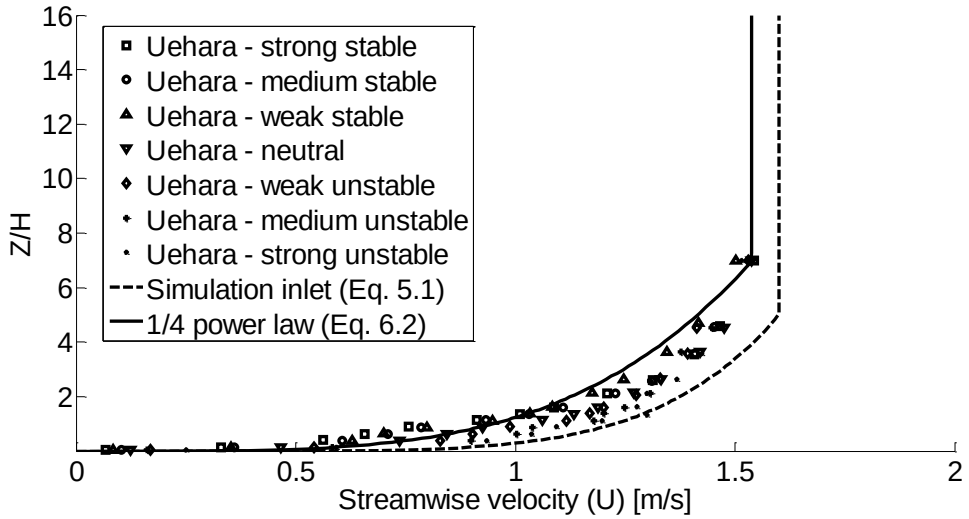

Figure 6.23: Uehara approach flow profiles, showing used and re-calibrated simulation power-law values

Profile results for the isothermal case with modified inlet velocity are provided in Appendix K. Analyses revealed that the modified and generally decreased inlet velocity profile did have an influence on downstream canyon profiles, as investigated for average street canyon profiles. The modification affected the streamwise velocity profile, with not under prediction in the free stream region, as opposed to the standards over estimation; along with significant increased under prediction with modified inlet conditions within the UCL, particularly towards street level. Only a significant deviation was observed with vertical velocity profiles from the T-RANS method, with the modification drastically decreasing values compared to the standard case. Decreased free stream velocity profile can be expected due to the modification and lowering of velocity from the inlet conditions; while decreased UCL and street level reverse flow can be explained from the decrease in velocity at that level compared to standard simulation velocities. However, it was expected

that this decrease in velocity would enhance re-circulation velocities, bettering agreement with Uehara profiles; but the converse was observed.

Flow deviation profiles were found to be in better agreement with Uehara profiles, with closer agreement with free stream values as well as better peak capturing and profile modelling, compared to the standard simulation and particularly for the T-RANS method. The can be explained from decreased average velocity profiles and thus the decreased potential and range for deviation due to decreased turbulent kinetic energy. Likewise, similar improvements were also observed for streamwise-vertical shear stress component.

Thus the choice of simulation inlet velocity was found to in fact affect downstream flow profiles; with better agreement to Uehara isothermal profiles, particularly in free stream regions and profile shape matching, with the modified profile.

6.7. Effect of inlet turbulent kinetic energy dissipation variation

Plots of the evaluation of changes to inlet viscosity fraction (χ_{in}), and accompanying changes to inlet turbulent kinetic energy dissipation, for the strong stable and unstable stratification conditions can be found in Appendix L. Analyses of the results revealed that changes to the inlet kinetic energy dissipation value has influences on velocity and velocity deviation profiles, with increased velocity profile variance (in particular vertical velocity); in addition to increased free stream velocity deviation values, compared to the standard test cases investigated. This expected increase in velocity deviation is a result of increased turbulent kinetic energy and thus turbulence, which was found to propagate into the street canyons. Investigations also revealed that there were no significant influences of the decrease in inlet turbulent kinetic energy to the energy equation (temperature profile) (less than 1% change); likewise to temperature deviation profiles.

6.8. Turbulent Prandtl number investigations

Effects of turbulent Prandtl number on flow profiles were found to have negligible influence on velocity profiles, except vertical velocity as expected due to increased heat conduction within the street canyon (refer Appendix M). There was however, noticeable effect with temperature profiles (refer Figure 6.24 and Appendix M), with a decrease in turbulent Prandtl number to 0.4 significantly improving

temperature profiles compared to Uehara. This can be explained by the increased turbulent heat conduction capability with the simulations.

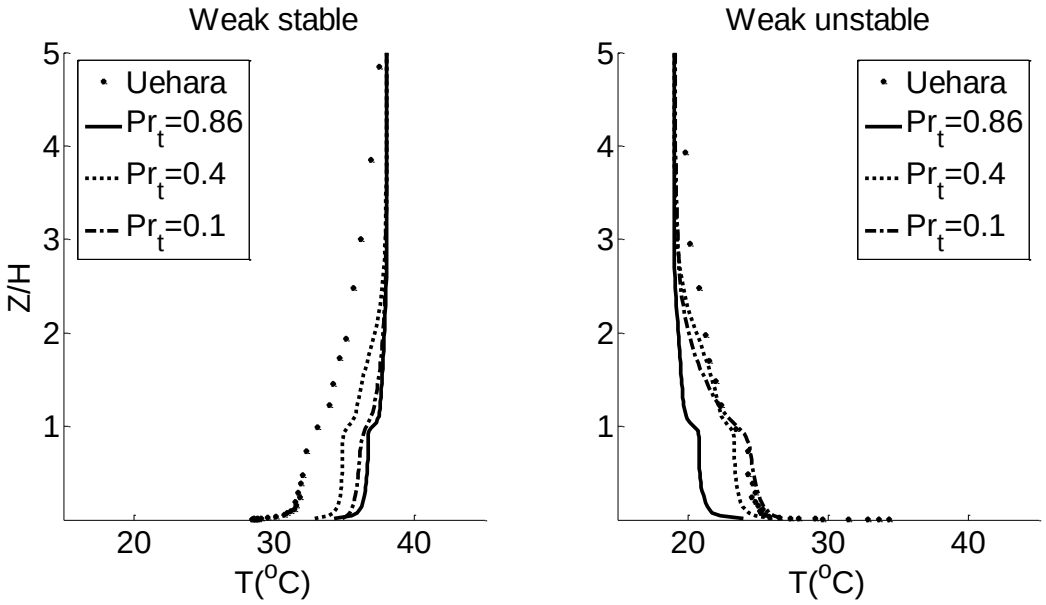

Figure 6.24: Effects of turbulent Prandtl number on hybrid model temperature profiles

Further decrease in the turbulent Prandtl number, to a value of 0.1, was found to further improve agreement with Uehara temperature profiles for the weak unstable stratification case in the UBL; however this was not the case for the weakly stable case, with only slight improvement to standard simulation profiles. This was expected for the unstable case, with possible saturation of mixing capability and turbulent Prandtl number (as illustrated in Figure 2.4). However the results for the stable case were not expected and could be explained by increased deviation from the true value and over estimation of heat conduction from true values.

Improvements in stable stratification temperature prediction, with varied turbulent Prandtl number, can be explained utilising corresponding Ellison modelled turbulent Prandtl number plots (Figure 6.12). In the UCL/UBL transition region, turbulent Prandtl numbers lower than the used constant value ($\mathrm{Pr_t} = 0.86$) are calculated; hence resulting in the observed better prediction, due to enhanced turbulent heat conduction. This effect is propagated into lower regions with no improvement, as

can be seen with the similar profiles and slight increased and improved gradient of the standard turbulent Prandtl number.

Observed improvements in unstable stratified temperature prediction with varied turbulent Prandtl number, can also be explained using the Ellison modelled turbulent Prandtl number plots for unstable stratification (Figure 6.20). From the latter plots, it can be seen for the weak unstable hybrid case, the turbulent Prandtl number is generally below the used constant value of 0.86 in the UBL, while dropping significantly below it within the UCL; even below $\mathrm{Pr_t} = 0.4$ in some instants. Therefore, use of the higher neutral stratification turbulent Prandtl number in this unstable region inhibits the heat conduction and mixing capabilities, hence improved Uehara correlation with increased capability (lower turbulent Prandtl numbers, as predicted by the Ellison model). The latter is particularly noticeable in the lower UBL and transition into UCL, with close agreement with Uehara data and better agreement with lower constant turbulent Prandtl numbers in the middle and lower sections of the street canyon; while increased deviation of the lower values towards street level where instability normalises.

6.9. Further development to standard simulations

Further developments to SARA3DCLIMAT, for use in simulating thermally stratified buoyancy effects were conducted as preliminary future investigations; utilising various findings from this study. Results and comparisons with standard and Uehara results are presented and discussed below.

6.9.1. Turbulent heat flux model simulations

Plots for comparison of the GGDH to standard simulation results and Uehara data for the various stratification cases are provided in Appendix N.

Comparing GGDH plots with SGDH and Uehara plots, it can be seen that the choice of turbulent heat flux model and introduction of anisotropicity has negligible effect on streamwise velocity. The latter was expected as main effects of the turbulent heat flux model are to the conservation of energy equation, with only consequential effects to the Navier-Stoke and continuity equations. There is therefore improvement to temperature profiles, especially for the hybrid model; although still insufficient compared to Uehara.

In general, increased complexity of the turbulent heat flux model had negligible influence on the T-RANS model, with only slight increases in comparability to Uehara and when compared to influences on the hybrid model. Reasons for this negligible influence to the T-RANS model are due to the methods longer modelling timescales that are negligibly affected by anisotropic effects as well as comparably lower shear stresses predicted by the T-RANS method. Conversely, more significant influences of GGDH were observed for the hybrid method, in particular in the UCL/UBL boundary and lower UBL, with increased peak and bulge capturing, which in most cases was in better agreement with Uehara. These effects in the hybrid method are attributed to the methods higher frequency capturing and thus more affected by anisotropic effects; thus the GGDH method was better able to take into consideration influences of temperature gradients and shear stresses, as described in section 4.3.2.4.

6.9.2. Comparison with LES

Plots of LES simulated profiles, with comparisons to standard T-RANS and hybrid models as well as Uehara data are provided in Appendix O. Comparisons of the LES profiles revealed that in general LES improved streamwise velocity profiles, with better agreement with Uehara compared to T-RANS and hybrid methods, for neutral and unstable stratification conditions. However the converse was true for stable stratification cases, with increased over prediction by the LES method. This can be explained by the increased frequency capturing by the LES method; as observed with the similarities in vertical velocity profiles for the LES and hybrid methods.

Coupled to increased frequency capturing by the LES method, prediction of the velocity deviations by the LES method were also improved and in closer agreement with Uehara data. As with velocity profiles this was particularly for unstable and neutral stratification conditions; with better capturing of peak values and the overall profiles by LES simulations. However LES methods were found to grossly underestimate velocity deviations profiles in the free stream region, especially compared to the T-RANS and hybrid methods. However this can be expected due to the use of an unchanged mesh, which is was too course in the free stream region for LES simulations. LES methods were found to overestimate Uehara velocity deviations, as with velocity profiles.

Similar findings were found for streamwise-vertical shear stress LES simulated profiles, with better prediction of unstable and neutral stratification and overestimation of stable profiles. Stable overestimates can also be attributed to used LES model being better suited for higher Reynolds flows and thus unable to simulate the low Reynolds flows experienced with stable stratification; hence over predicting due to turbulence feeding rather than required suppression.

Generally, the isotropic heat flux LES method used was found to better predict Uehara temperature profile shapes, compared to standard simulations; along with close agreement to Uehara data with strong stable stratification conditions and particularly at near wall regions of street level. As with velocity profiles, this can again be attributed in increased frequency capturing, as well as decreases in the used constant turbulent Prandtl number used (as seen for the weak stable stratification case (refer section 6.8)) and an altered turbulent viscosity.

Likewise LES simulations were found to drastically improve temperature variance profiles; especially in the UCL/UBL and surrounding regions, with better profile shape and peak capturing, along with drastically decreased near wall values. Although the latter were still found to be significantly larger than Uehara values, leading to similar conclusions as discussed in section 6.3.2.3, that is non-agreement with the Uehara profiles at the near-wall region.

7. CONCLUSIONS

In this report, urban atmospheric thermally stratified buoyancy flows were studied, as well as simulated by SARA3DCLIMAT; an in-house T-RANS and hybrid LES/T-RANS code.

Investigations conducted included effects of simulation time step and canyon sampling location on flow profiles. Although affecting temporal turbulence dependence, the former was shown to have no significant influence on typical turbulent flow profiles; while due to capturing of turbulent spatial dependence, the former was shown to be of importance, with averaged data from the 10^{th} to 14^{th} street canyons being used for analyses of typical turbulence data in the investigated domain.

Simulated stratified flow profiles were compared with simulated isothermal flow conditions and expectations from literature findings; as well as being validated with wind tunnel experiments by Uehara *et al*. [3]. Comparisons with isothermal conditions revealed SARA3DCLIMAT predicted unstable stratified buoyancy effect profiles relatively well. With simulations being able to capture enhancing of vertical velocity, due to heat convection; as well as prediction of expected canyon temperature profiles, with steep temperature gradients at surfaces and the UCL/UBL boundary, with more gradual gradients in the bulk fluid. Likewise, with stable stratification, SARA3DCLIMAT predicted a slight dampening of profiles, with smoothening of profile variations; as well as steep near surface temperature gradients. Simulations revealed that in general, the UCL had a differing average temperature differing from bulk UBL temperatures by up to approximately ±20%, as expected from literature findings.

Validation of SARA3DCLIMAT with Uehara *et al*. [3] revealed that for neutral stratification conditions, simulation were comparable to wind tunnel experimentation; although with potential for improvement, such as with effects of inlet velocity profile. Validation of unstable stratification cases showed reasonable comparability, with close agreement and at least correct profile shape prediction; however temperature profiles

were grossly under estimated in all simulations. The latter was potentially due to insufficient heat mixing capability, for example caused by too high values of turbulent Prandtl number used resulting in an under prediction of thermal buoyancy conduction. Stable stratification validations revealed that SARA3DCLIMAT over predicted profiles, being unable to sufficiently suppress flow profiles, as compared to wind tunnel experimental data. As with Unstable stratification conditions, SARA3DCLIMAT incorrectly predicted stable stratification temperature profiles, over estimating them compared to Uehara *et al*. [3]. It is to be noted that there is not full agreement with Uehara profiles, specifically advection and temperature profiles, due to non-agreement with practical expectations.

Generally, the hybrid method was found to improve simulation results, flow profile shape prediction and have better capturing of peak values, compared to the T-RANS method and Uehara *et al*. [3] validation. This can be attributed to the methods increased frequency capturing through reduction of turbulence timescales, allowing better modelling of the temporal and spatial varying turbulent flow.

Additionally, influence of inlet velocity and turbulent kinetic energy dissipation profiles were investigated. Inlet velocity was found to have noticeable influences on the investigated isothermal canyon profiles, affecting re-circulation profiles as well as velocity deviation values; thus potentially heat conduction rates. Change to inlet turbulent kinetic energy dissipation profile was found to have negligible influence on UCL flow profiles, only affecting free stream velocity deviation profiles due to a coupled increase in turbulent kinetic energy that is conveyed through the domain UBL.

Investigations into local stratification profiles and effects of varied turbulent Prandtl number, revealed that even under constant bulk stratification conditions, local stratification has spatial dependence, with the possibility of reverse stability. In general, a decreased turbulent Prandtl number (therefore increased head conduction capability) bettered agreement with Uehara, with seemingly a saturation point between values of 0.4 and 0.1. Utilising local stratification conditions and the Ellison

model, it was shown that the turbulent Prandtl number is anything but constant for stratified turbulent flows with values varying from 0.3 to infinity.

Preliminary future investigations, through GGDH, revealed that use of an anisotropic shear stress heat flux model, although altering flow profiles, particularly with in the UCL and UCL/UBL boundary and specifically for the hybrid method, did not globally improve validation with Uehara *et al*. [3].

LES simulations revealed close agreement and improvement to the hybrid method, illustrating the shift to LES of the hybrid method. The LES method was found to significantly improve neutral and unstable stratification simulations; which unfortunately was not the case with stable stratification. This was attributed to the increased frequency capturing and use of inappropriate modelling techniques based on high Reynolds flows; thus an inability to simulate laminating flow. Observed improvements with LES temperature profiles were also attributed to a change in the value of turbulent Prandtl number used, as observed with turbulent Prandtl number investigations with the hybrid model. However it is to be noted that LES methods generally under predicted three stream deviation profiles, potentially due to the use of an unmodified grid resolution, resulting in the observed decreases in accuracy.

8. RECOMMENDATIONS

As a consequence of this study, the following potential areas of modification and future areas of investigation with SARA3DCLIMAT are recommended:

1. **Conduct simulations with the hybrid model, utilising the GGDH model, modified inlet velocity profile and turbulent Prandtl number value of 0.4**

   As an immediate extension to this investigation, it is recommended that supplementary investigations be conducted with the used hybrid method, making use of the GGDH model, an adapted inlet velocity profile and a constant turbulent Prandtl number of 0.4. The GGDH model was shown to improve hybrid profile agreement with Uehara *et al*. [3], as was a decreased turbulent Prandtl number. However the combination of these two changes were not investigated and are expected to improve turbulent heat mixing as well as increased heat flux capturing. Additionally, changes to the inlet velocity profile were shown to influence downstream flow advection terms and are therefore expected to improve hybrid validation agreement with Uehara *et al*. [3].

2. **Investigate a higher order, AFM turbulent heat flux model**

   The anisotropic GGDH model was found to influence the hybrid method, favourably for unstable stratification. Therefore, to further study influences of turbulent heat flux model, it is suggested to additionally investigate the AFM turbulent heat flux model, already integrated into SARA3DCLIMAT. It is believed that AFM would allow for better capturing of turbulent heat flux in the hybrid method, by addition of contributions from temperature variance and convective transport. This can be expected to better the currently incorrectly simulated temperature values and deviation profiles and thus thermal convective buoyancy.

3. **Investigate a higher order ASM turbulent stress models**

   It is recommended to investigate the ASM model currently integrated into SARA3DCLIMAT, initially for the neutral stratification case and then all other cases.

The standard two-equation k-ε linear EVM was used in this study due to its proven numerical stability, however it models turbulent stress proportionally to its mean rate of strain. This is known to result in under estimation of stresses [46], therefore use of higher order turbulent stress models, as with higher order turbulent heat flux models, will result in increased capturing of stress contributions and thus accuracy.

4. Addition of turbulent viscosity adaptation to the hybrid model

An additional hybrid LES/T-RANS modification to turbulent viscosity has previously been integrated and successfully investigated with SARA3DCLIMAT [42]. Therefore, it is proposed that this model adaptation be investigated as an expansion to this investigation of thermally stratified buoyancy flows. This hybrid model will tend to decrease turbulent viscosity (up to a LES limit), thereby increasing turbulent kinetic energy value predictions and turbulence timescale. Thus, the modification will increase LES-type modelling in free-stream regions, increasing simulation accuracy, while maintaining part of the computational simplicities of the T-RANS method.

5. Adapt and investigate the code for local stability conditions

5.1. Variable turbulent Prandtl number

It is proposed that the Ellison model be integrated into SARA3DCLIMAT, to replace the current use of a constant turbulent Prandtl number. This would allow for modelling of the conservation equations on local stratification conditions, with varied turbulent Prandtl number. Hence, allowing for better prediction of turbulent heat flux spatial dependencies, with increased capturing of local stabilities/instabilities.

5.2. Altered turbulent kinetic energy dissipation equation

Freedman *et al*. [58] proposed modification of the ε-equation, specifically $C_{\varepsilon 1}$ and $C_{\varepsilon 2}$, under stable stratification conditions, as a function of local Richardson number. This adaption is believed to enhance turbulent kinetic energy dissipation, decreasing over-estimates in turbulent kinetic energy; thus suppressing turbulence in stable stratified flows, as insufficiently done in this study's investigations. Such modifications are recommended to be integrated into SARA3DCLIMAT and investigated.

6. Simplification of thermal stratification investigation geometry

It is proposed that future stratification effect studies initially use a simplified geometry, free of obstacles and flow obstructions, with potential further simplification into a 2-D system. Obstacles resulted in too varied turbulence scales, resulting in the use of varied grid resolutions and therefore comprisable accuracy between flow regions; which where potentially insufficient in this studies stable stratified simulations. This simplification can be done, for example, using experimental work by Ueda *et al*. [32] and/or Mossel [36] for validation. Geometric simplification would allow for validation of thermally stratification models under simplified free-flow conditions, from which increased complexity effects of urban turbulence can then be built on.

It is interesting to note that as a consequence of this study and LES investigations by Saša Kenjereš, various additional LES closure models and adaptions (such as laminar wall modifications) are currently being investigated with the LES method; expanding to this investigation and with the goal of validation of SARA3DCLIMAT with Uehara *et al*. [3] and thus accurate simulation of thermal stratification effects within the urban atmospheric climate. However these simulations are computationally intensive and time consuming; thus, ideally adaptations should be made to the hybrid method utilised in this study.

9. BIBLIOGRAPHY

[1] TUDelft, “Course browser searcher,” 2013. [Online]. Available: http://studiegids.tudelft.nl/a101_displayCourse.do?course_id=29012. [Accessed 13 September 2013].

[2] TUDelft, “Master Thesis (MEP) grading scheme,” Delft University of Technology, The Netherlands, 2013.

[3] K. Uehara, S. Murakam, S. Oikawa and S. Wakamatsu, “Wind tunnel experiments on how thermal stratification affects flow in and above urban street canyons,” *Atmospheric Environment,* vol. 34, no. 10, pp. 1553-1562, 2000.

[4] J.-F. Sini, S. Anquetin and P. G. Mestayer, “Pollutant dispersion and thermal effects in urban street canyons,” *Atmospheric Environment,* vol. 30, no. 15, pp. 2659-2677, August 1996.

[5] T. Ichinose, K. Shimodozono and K. Hanaki, “Impact of anthropogenic heat on urban climate in Tokyo,” *Atmospheric Environment,* vol. 33, no. 24-25, pp. 3897-3909, 1999.

[6] R. Berkowicz, R. Britter and S. D. Sabatino, “Optimisation of modelling methods for traffic pollution in streets,” European Commission, 2004.

[7] Y. Nakamura and T. Oke, “Wind, temperature and stability conditions in an east-west oriented urban canyon,” *Atmospheric Environment,* vol. 22, no. 12, pp. 2691-2700, 1988.

[8] I. Panagiotou, M. K. -A. Neophytou, D. Hamlyn and R. E. Britter, “City breathability as quantified by the exchange velocity and its spatial variation in real inhomogeneous urban geometries: An example from central London urban area,” *Science of The Total Environment,* vol. 442, no. 1, pp. 466-477, 2013.

[9] P. D. United Nations: Department Economic & Social Affairs, “World Urbanization Prospects: The 2011 Revision,” United Nations, New York, 2012.

[10] P. D. United Nations: Department Economic & Social Affairs, “World Population Prospects - The 2012 Revision,” United Nations, New York, 2013.

[11] World_Bank, “World Development Indicators | The World Bank,” The World Bank, 2013. [Online]. Available: http://wdi.worldbank.org/table/3.12. [Accessed 18 September 2013].

[12] D. E. Abbey, N. Nishino, W. F. McDonnell, R. J. Burchette, S. F. Knutsen, W. L. Beeson and J. X. Yang, “Long-term inhalable particles and other air pollutants related to mortality in nonsmokers,” *American Journal of Respiratory and Critical Care Medicine,* vol. 159, no. 2, pp. 373-382, 1999.

[13] J. Fenger, “Urban air quality,” *Atmospheric Environment,* vol. 33, no. 29, pp. 4877-4900, 1999.

[14] Y. Zhou and J. I. Levy, “The impact of urban street canyons on population exposure to traffic-related primary pollutants,” *Atmospheric Environment,* vol. 42, no. 13, pp. 3087-3098, 2008.

[15] A. J. Cohen, H. R. Anderson, B. Ostro, K. D. Pandey, M. Krzyzanowski, N. Künzli, K. Gutschmidt, C. A. P. III, I. Romieu, J. M. Samet and K. R. Smith, “Urban air pollution,” in *Comparative quantification of health risks*, Geneva, World Health Organisation, 2004, pp. 1353-1434.

[16] H. Hertel and M. E. Goodsite, “Urban air pollution climates throughout the world,” Royal Society of Chemistry, 2009.

[17] T. R. Oke, Boundary layer climates, London: Methuen & Co. Ltd, 1987.

[18] “TRAPOS,” National Environmental Research Institute Denmark, 20 July 2007. [Online]. Available: http://www2.dmu.dk/AtmosphericEnvironment/TRAPOS/. [Accessed 9 September 2013].

[19] S. Kenjereš, “Numerical medelling of complex buoyancy-driven flows,” Delft University of Technology, The Netherlands, 1999.

[20] K. Fortuniak, K. Kłysik and J. Wibig, “Urban–rural contrasts of meteorological parameters in Łódź,” *Theoretical and Applied Climatology,* vol. 84, no. 1-3, pp. 91-101, 2006.

[21] D. M. Yow, “Urban Heat Islands: Observations, Impacts, and Adaptation,” *Geography Compass,* vol. 1, no. 6, pp. 1227-1251, 2007.

[22] EPA, “Reducing Urban Heat Islands: Compendium of strategies - Urban Heat Island basics,” United States Environmental Protection Agency, 2013.

[23] S. Valk, “Numerical simulations of turbulent fl‡ows in complex urban areas: Case of the Delft University of Technology Campus,” Delft University of Technology, The Netherlands, 2008.

[24] Z. Bottyán, A. Kircsi, S. Szegedi and J. Unger, “The relationship between built-up areas and the spatial development of the mean maximum urban heat island in Debrecen, Hungary,” *International Journal of Climatology,* vol. 25, no. 3, pp. 405-418, 2005.

[25] P. Jonsson, “Vegetation as an urban climate control in the subtropical city of Gaborone, Botswana,” *International Journal of Climatology,* vol. 24, no. 10, pp. 1307-1322, 2004.

[26] R. Dimitrova, J.-F. Sini, K. Richards, M. Schatzmann, M. Weeks, E. P. García and C. Borrego, “Influence of thermal effects on the wind field within the urban environment,” *Boundary-Layer Meteorology,* vol. 131, no. 2, pp. 223-243, 2009.

[27] E. Yee, R. M. Gailis, A. Hill, T. Hilderman and D. Kiel, “Comparison of Wind-tunnel and Water-channel Simulations of Plume Dispersion through a Large Array of Obstacles with a Scaled Field Experiment,” *Boundary-Layer Meteorology,* vol. 121, no. 3, pp. 389-432, 2006.

[28] J. Allegrini, V. Dorer and J. Carmeliet, “Wind tunnel measurements of buoyant flows in street canyons,” *Building and Environment,* vol. 59, pp. 315-326, 2013.

[29] W. H. Snyder, “Similarity criteria for the application of fluid models to the study of air pollution meteorology,” *Boundary-Layer Meteorology,* vol. 3, no. 1, pp. 113-134, 1972.

[30] J. W. Miles, “On the stability of heterogeneous shear flows,” *Journal of Fluid Mechanics,* vol. 10, no. 4, pp. 496-508, 1961.

[31] T. H. Ellison and J. S. Turner, “Turbulent entrainment in stratified flows,” *Journal of Fluid Mechanics,* vol. 6, no. 3, pp. 423-448, 1959.

[32] H. Ueda, S. Mitsumoto and S. Komori, “Buoyancy effects on the turbulent transport processesin the lower atmopshere,” *Quarterly Journal of the Royal Meteorological Society,* vol. 107, no. 453, pp. 561-578, 1981.

[33] Y. Ogawa, P. G. Diosey, K. Uehara and H. Ueda, “A wind tunnel for studying the effects of thermal stratification in the atmosphere,” *Atmospheric Environment,* vol. 15, no. 5, pp. 807-821, 1981.

[34] Y. Ohya and T. Uchida, “Turbulence Structure of Stable Boundary Layers with a Near-Linear Temperature Profile,” *Boundary-Layer Meteorology,* vol. 108, no. 1, pp. 19-38, 2003.

[35] O. M. de Haan, “Validation of flows simulations in urban street canyons with thermal stratification using wind tunnel experiments,” Delft University of Technology, The Netherlands, 2013.

[36] M. Mossel, “Thermal stratification of turbulent air flows in a rectangular channel,” Delft University of Technology, The Netherlands, 1995.

[37] R. Hagenzieker, “Numerical simulations of turbulent fows over hills and complex urban area with dispersion of pollutants,” Delft University of Technology, The Netherlands, 2006.

[38] B. ter Kuile, “Numerical simulations of pollutants in urban areas with vegetation using a modified k-ε model,” Delft University of Technology, The Netherlands, 2009.

[39] L. Tan, “Numerical comparison of models for vegetation effects on airflows using the k-ε turbulence model,” Delft University of Technology, The Netherlands, 2009.

[40] C. L. Chao, “Numerical analysis of turbulent dispersion of pollutants in simplified urban areas at laboratory scale,” Delft University of Technology, The Netherlands, 2010.

[41] T. Busking, “Numerical studies of transient effects in turbulent dispersion of pollutants in simplified urban areas at laboratory scale,” Delft University of Technology, The Neatherlands, 2010.

[42] S. de Wildt, “Capturing transient effects in turbulent flows with passive scalars over urban areas with hybrid les/t-rans approaches,” Delft University of Technology, The Netherlands, 2012.

[43] M. van der Houwen, “Numerical analysis of turbulent dispersion of reactive pollutants in simplified urban areas,” Delft University of Technology, The Netherlands, 2012.

[44] M. Verdult, “Numerical simulations of turbulent flows in simplified 2-D street canyons,” Delft University of Technology, The Netherlands, 2012.

[45] P. Salizzoni, L. Soulhac and P. Mejean, “Street canyon ventilation and atmospheric turbulence,” *Atmospheric Environment,* vol. 43, no. 32, pp. 5056-5067, 2009.

[46] S. B. Pope, Turbulent Flows, Cambridge: University Press, 2000.

[47] K. Hanjalić and S. Kenjereš, “‘T-RANS’ simulation of deterministic eddy structure in flows driven by thermal buoyancy and Lorentz force,” *Flow, Turbulence and Combustion,* vol. 66, no. 4, pp. 427-451, 2001.

[48] W. M. Deen, Analysis of transport phenomena, New York: Oxford University Press, 2013.

[49] K. Hanjalić, S. Kenjereš, M. J. Tummers and H. J. J. Jonker, Analysis and modelling of physical transport phenomena, 1st ed., The Netherlands: VSSD, 2009.

[50] M. Hadžiabdić, “LES, RANS and combined simulation of impinging flows and heat transfer,” Delft University of Technology, The Netherlands, 2006.

[51] F. G. Schmitt, “About Boussinesq's turbulent viscosity hypothesis: historical remarks and a direct evaluation of its validity,” *Comptes Rendus Mécanique,* vol. 335, no. 9-10, pp. 617-627, 2007.

[52] P. Durbin, “On the k-3 stagnation point anomaly,” *International Journal of Heat and Fluid Flow,* vol. 17, no. 1, pp. 89-90, 1996.

[53] N. Ince and B. Launder, “On the computation of buoyancy-driven turbulent flows in rectangular enclosures,” *International Journal of Heat and Fluid Flow,* vol. 10, no. 2, pp. 110-117, 1989.

[54] K. Hanjalić, “One-point closure models for buoyancy-driven turbulent flows,” *Annual Review of Fluid Mechanics,* vol. 10, pp. 321-347, 2002.

[55] S. Kenjereš and K. Hanjalić, “LES, T-RANS and hybrid simulations of thermal convection at high Ra numbers,” *International Journal of Heat and Fluid Flow,* vol. 27, no. 5, pp. 800-810, 2006.

[56] T. Ellison, “Turbulent transport of heat and momentum from an infinite rough plane,” *Journal of Fluid Mechanics,* vol. 2, no. 5, pp. 456-466, 1957.

[57] S. Kenjereš and K. Hanjalić, “Tackling complex turbulent flows with transient RANS,” *Fluid Dynamics Research,* vol. 41, no. 1, pp. 012201 (1-32), 2009.

[58] F. R. Freedman and M. Z. Jacobson, “Modification of the standard ε-equation for the stable ABL through enforced consistency with Monin–Obukhov similarity theory,” *Boundary-layer Mereorology,* vol. 106, no. 3, pp. 383-410, 2003.

[59] K. Kadoya, N. Matsunaga and A. Nagashima, “Viscosity and thermal conductivity of dry air

in the gaseous phase," *Journal of Physical and Chemical Reference Data,* vol. 14, no. 4, pp. 947-970, 1985.

[60] L. P. B. M. Janssen and M. M. C. G. Warmoeskerken, Transport phenomena data companion, 3rd ed., The Netherlands: VSSD, 2006.

[61] S. I. Sandler, Chemical, Biochemical, and Engineering Thermodynamics, 4th ed., USA: John Wiley & Sons Inc, 2006.

[62] "Air Properties," The Engineering ToolBox, [Online]. Available: http://www.engineeringtoolbox.com/air-properties-d_156.html. [Accessed 05 09 2013].

[63] R. Perry and D. Green, "Physical and Chemical Data," in *Perry's Chemical Engineers'handbook*, 6th ed., USA, McGraw-Hill Book Company, 1997, pp. 3-104.

[64] S. Kenjereš and B. ter Kuile, "Modelling and simulations of turbulent flows in urban areas with vegetation," *Journal of Wind Engineering and Industrial Aerodynamics,* vol. 123, no. A, pp. 43-55, 2013.

[65] J.-J. Kim and J.-J. Baik, "Urban street-canyon flows with bottom heating," *Atmospheric Environment,* vol. 35, no. 20, pp. 3395-3404, 2001.

[66] W. C. Cheng, C.-H. Liu and D. Y. C. Leung, "On the correlation of air and pollutant exchange for street canyons in combined wind-buoyancy-driven flow," *Atmospheric Environment,* vol. 43, no. 24, pp. 3682-3690, 2009.

[67] R. A. Memon and D. Leung, "On the heating environment in street canyon," *Environmental Fluid Mechanics,* vol. 11, no. 5, pp. 465-480, 2011.

[68] X. Xie, C.-H. Liu, D. Y. C. Leung and M. K. H. Leung, "Characteristics of air exchange in a street canyon with ground heating," *Atmospheric Environment,* vol. 40, no. 33, pp. 6396-6409, 2006.

[69] T. R. Oke, "Street design and urban canopy later climate," *Energy and Buildings,* vol. 11, no. 1-3, pp. 130-113, 1988.

[70] EPA, "Heat Island Effect," United States Environmental Protection Agency, 2013. [Online]. Available: http://www.epa.gov/heatisland/index.htm. [Accessed 05 September 2013].

[71] G. Medic and P. A. Durbin, "Toward improved prediction of heat transfer on turbine blades," *Journal of Turbomachinery,* vol. 124, no. 2, pp. 187-192, 2002.

[72] S. Kenjereš, "Transient analysis of Rayleigh-Bénard convection with a RANS model," *International Journal of Heat and Fluid Flow,* vol. 20, no. 3, pp. 329-340, 1999.

[73] T. R. Karl, H. F. Diaz and G. Kukla, "Urbanization: Its Detection and Effect in the United States Climate Recor," *Journal of Climate,* vol. 1, no. 11, pp. 1099-1123, 1988.

[74] A. Kovar-Panskus, L. Moulinneuf, E. Savory, A. Abdelqari, J.-F. Sini, J.-M. Rosant, A. Robins and N. Toy, "A Wind Tunnel Investigation of the Influence of Solar-Induced Wall-Heating on the Flow Regime within a Simulated Urban Street Canyon," *Water, Air and Soil Pollution: Focus,* vol. 2, no. 5-6, pp. 555-571, 2002.

[75] Y. Ohya, M. Tarsuno, Y. Nakamura and H. Ueda, “A thermally stratified wind tunnel for environmental flow studies,” *Atmospheric environment,* vol. 30, no. 16, pp. 2881-2887, 1996.

[76] W. Cheng and C.-H. Liu, “Large-eddy simulation of turbulent transports in urban street canyons in different thermal stabilities,” *Journal of Wind Engineering and Industrial Aerodynamics,* vol. 99, no. 4, pp. 434-442, 2011.

[77] P. A. Mirzaei and F. Haghighat, “Approaches to study Urban Heat Island – Abilities and limitations,” *Building and Environment,* vol. 45, no. 10, pp. 2192-2201, 2010.

[78] H. Hattori, T. Houra and Y. Nagano, “Direct numerical simulation of stable and unstable turbulent thermal boundary layer,” *International Journal of Heat and Fluid Flow,* vol. 28, no. 6, pp. 1262-1271, 2007.

[79] Z.-t. Xie, “Large-eddy simulation of stratification effects on dispersion in urban environments,” *Journal of Hydrodynamics,* vol. 22, no. 5, pp. 1003-1008, 2010.

[80] X. Qiu, D.-x. Zhang, Z.-m. Lu and Y.-l. Liu, “Turbulent Mixing and Evolution in a Stably Stratified Flow with a Temperature Step,” *Journal of Hydrodynamics, Series B,* vol. 21, no. 1, pp. 84-92, 2009.

[81] X. Qiu, Y.-x. Huang, Z.-m. Lu and Y.-l. Liu, “Large eddy simulation of turbulent statistical and transport properties in stably stratified flows,” *Journal of Applied Mathematics and Mechanics,* vol. 30, no. 2, pp. 153-162, 2009.

[82] A. A. Townsend, “Turbulent flow in a stably stratified atmosphere,” *Journal of Fluid Mechanics,* vol. 3, no. 4, pp. 361-372, 1958.

10. APPENDICES

A. AIR PROPERTIES

The following appendix outlines the thermodynamic relations and derivations and calculation of air's properties for use in the SARA3DCLIMAT simulation code.

A.1. Density

Air is assumed to be an ideal gas, therefore obeys the idea gas equation:

$$pV = nRT \qquad \text{Eq. 10.1}$$

The above equation can be rewritten to express the density of an idea gas as follows (illustrated in Figure 10.1):

$$\rho = \frac{n}{V} \times \frac{Mr_{air}}{1000} = \frac{p}{RT} \times \frac{Mr_{air}}{1000} [\text{kg.m}^{-3}] \qquad \text{Eq. 10.2}$$

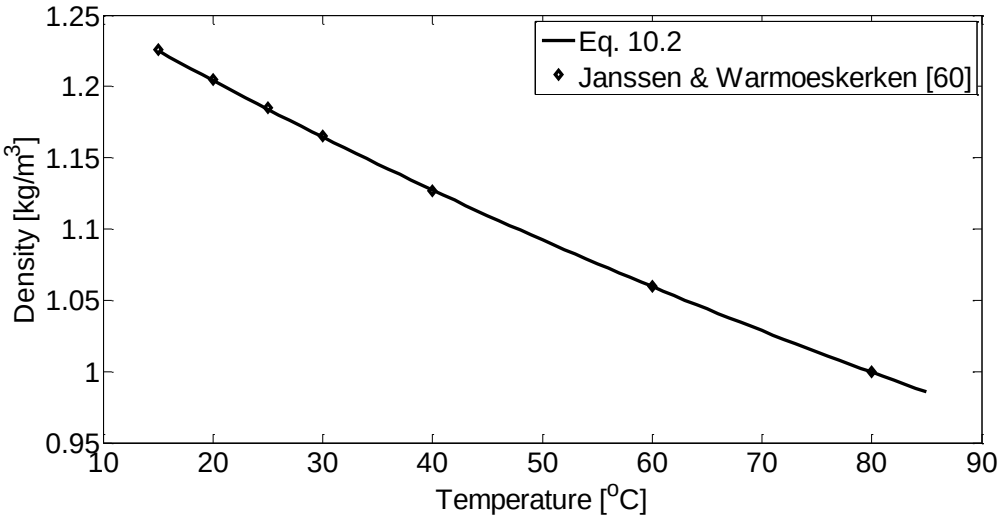

Figure 10.1: Air density-temperature relation, using Eq. 10.2

A.2. Viscosity

The dynamic viscosity (μ) of air was calculated as described by Kadoya *et al*. [59] using the following expressions (Eq. 10.3), with constants as per

$$\nu = \frac{\mu}{\rho} \qquad \text{Eq. 10.4}$$

Table 10.1. Kinematic viscosities (ν) were then calculated using dynamic viscosities and the corresponding densities. Calculated values were crossed-checked with data available in literature [60]. Viscosity values are illustrated in Figure 10.2.

$$\eta = \mathrm{H_c}\left(\eta_0 + \Delta\eta\right)[Pa.s] \qquad \text{Eq. 10.3}$$

$$\eta_0 = A_1 T_r + A_{0.5} T_r^{0.5} + \sum_{i=0}^{-4} A_i T_r^i \qquad \text{Eq. 10.3.1}$$

$$\Delta\eta = \sum_{i=1}^{4} B_i \rho_r^i \qquad \text{Eq. 10.3.2}$$

$$T_r = \frac{T}{T^*} \qquad \text{Eq. 10.3.3}$$

$$\rho_r = \frac{\rho}{\rho^*} \qquad \text{Eq. 10.3.4}$$

$$\nu = \frac{\mu}{\rho} \qquad \text{Eq. 10.4}$$

Table 10.1: Viscosity expression constants [59]

T^*	132,5 [K]
ρ^*	314,3 [kg.m^{-3}]
$\mathrm{H_c}$	6,1609E-06 [Pa.s]
A_1	0,128517 [-]
$A_{0.5}$	2,60661 [-]
A_0	-1.00000 [-]
A_{-1}	-0,709661 [-]
A_{-2}	0,662534 [-]

A_{-3}	-0,1978546 [-]
A_{-4}	0,00770147 [-]
B_1	0,465601 [-]
B_2	1,26469 [-]
B_3	-0,511425 [-]
B_4	0,274600 [-]

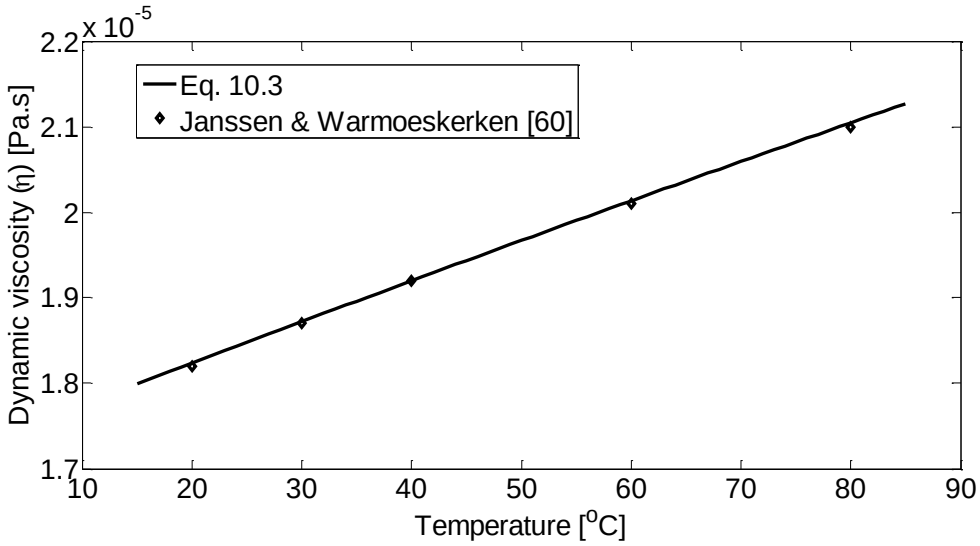

Figure 10.2: Air dynamic viscosity-temperature relation

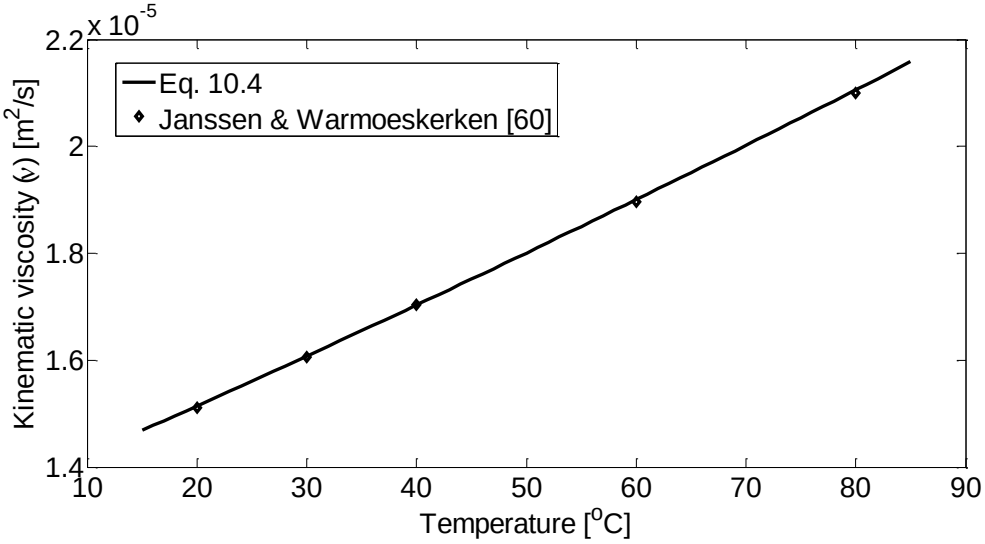

Figure 10.3: Air kinematic viscosity-temperature relation

A.3. Thermal Conductivity

The thermal conductivity (λ) of air was calculated as described by Kadoya et al. [59] using the following expressions (Eq. 10.5), with constants as per Table 10.2. The calculated values were also crossed-checked with data available in literature [60]. Viscosity values are illustrated in Figure 10.4.

$$\lambda = \Lambda\left(\lambda_0 + \Delta\lambda\right)[W.m^{-1}.K^{-1}] \qquad \text{Eq. 10.5}$$

$$\lambda_0 = C_1 T_r + C_{0.5} T_r^{0.5} + \sum_{\iota=0}^{-4} C_i T_r^i \qquad \text{Eq. 10.5.1}$$

$$\Delta\lambda = \sum_{i=1}^{5} D_i \rho_r^i \qquad \text{Eq. 10.5.2}$$

$$T_r = \frac{T}{T^*} \qquad \text{Eq. 10.5.3}$$

$$\rho_r = \frac{\rho}{\rho^*} \qquad \text{Eq. 10.5.4}$$

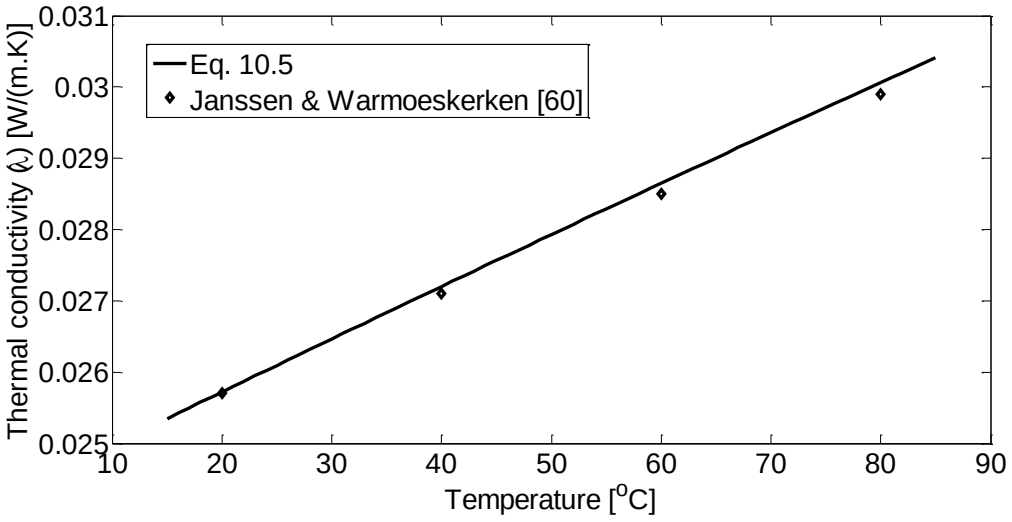

Figure 10.4: Air thermal conductivity-temperature relation

Table 10.2: Thermal conductivity expression constants [59]

T^*	132,5 [K]
ρ^*	314,3 [kg.m^{-3}]
Λ	25.9778^{E}-3 [W.m^{-1}.K^{-1}]
C_1	0.239503 [-]
$C_{0.5}$	0.00649768 [-]
C_0	1.00000 [-]
C_{-1}	-1.92615 [-]
C_{-2}	2.00383 [-]
C_{-3}	-1.07553 [-]
C_{-4}	0.229414 [-]
D_1	0.402287 [-]
D_2	0.356603 [-]
D_3	-0.163159 [-]
D_4	0.138059 [-]
D_5	-0.0201725 [-]

A.4. Specific Heat Capacity

Air's specific heat capacity (C_p) was calculated as described in Sandler [61], using the following expression, with constants shown in Table 10.3. Figure 10.5 illustrates the specific heat capacity-temperature relationship for air, in comparison to data available on The Engineering ToolBox [62].

$$C_p = \frac{\left(A + B.T + C.T^2 + D.T^3\right)}{Mr_{air}} [kJ.kg^{-1}.K^{-1}] \qquad \text{Eq. 10.6}$$

Table 10.3: Specific Heat Capacity of air expression constants [61]

A	28.088	[J.mol^{-1}.K^{-1}]
B	1,97E-03	[J.mol^{-1}.K^{-2}]
C	4,8E-06	[J.mol^{-1}.K^{-3}]
D	-1,965E-09	[J.mol^{-1}.K^{-4}]

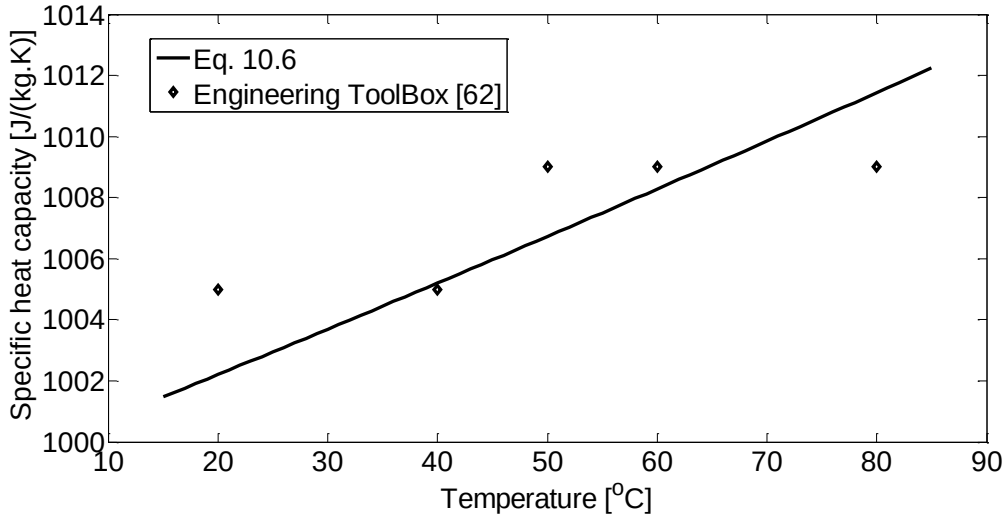

Figure 10.5: Air specific heat capacity-temperature relation

A.5. Prandtl number

The Prandtl number (Pr) – temperature relation for air was calculated using the following expression, with Figure 10.6 illustrating the relationship in comparison to values obtained from The Engineering ToolBox [62].

$$Pr = \frac{C_p \eta}{\lambda} \ [-] \qquad \text{Eq. 10.7}$$

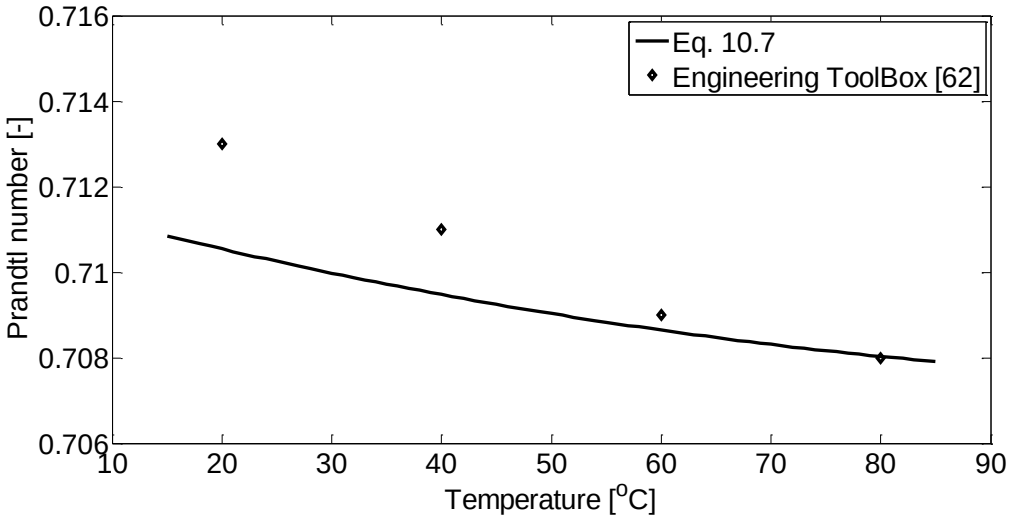

Figure 10.6: Prandtl number-temperature relation, using Eq. 10.7

A.6. Thermal Expansion Coefficient

The thermal expansion coefficient (β) of an ideal gas is simply the inverse of its absolute temperature [63], as illustrated in the expression below. Figure 10.7 illustrates the thermal expansion coefficient – temperature relation for air.

$$\beta = T^{-1}[K^{-1}] \qquad \text{Eq. 10.8}$$

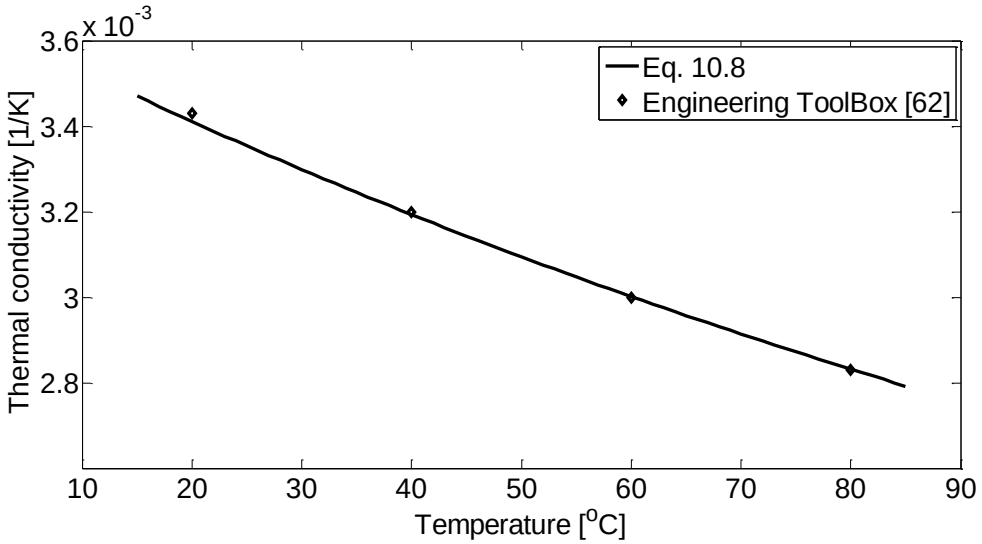

Figure 10.7: Thermal expansion coefficient-temperature relation, using Eq. 10.7

B. CONSERVATION EQUATIONS

This appendix details the steps in simplification of the conservation equations (continuity, Navier-Stokes and energy equations), as specified in section 4.1; in addition to further simplification by Reynolds averaging techniques as described in section 4.2.

Simplifications and assumptions used are outlined in section 4.1.1, along with the resultant simplified conservation. Final Reynolds averaged conservation equations are listed in section 4.2.2.1.

B.1. Continuity equation

The continuity equation written in one of its basic forms and in terms of instantaneous properties is as follows:

$$\partial_t(\hat{\rho}) + \partial_{x_i}(\hat{\rho}\hat{U}_i) = \hat{r}_i \qquad \text{Eq. 4.1}$$

Using the assumptions and simplifications, as specified in section 4.1.1, the above continuity equation can be simplified as follows:

$$\Rightarrow \underbrace{\partial_t(\hat{\rho})}_{\text{assump. 1\&3}} + \underbrace{\hat{\rho}\partial_{x_i}(\hat{U}_i)}_{\text{assump. 1\&3}} = \underbrace{\hat{r}_i}_{\text{assump. 7}}$$

$$\Rightarrow \hat{\rho}\,\partial_{x_i}(\hat{U}_i) = 0$$

$$\Rightarrow \partial_{x_i}(\hat{U}_i) = 0 \qquad \text{Eq. 4.4}$$

Applying Reynolds decomposition to the above simplified continuity equation results in the following:

$$\hat{U}_i \equiv \bar{U}_i + U_i'$$

Using Reynolds averaging techniques, the Reynolds decomposed continuity equation is simplified as follows:

$$\overline{\partial_{x_i}\left(\bar{U}_i\right)}+\overline{\partial_{x_i}\left(U_i'\right)}=0$$

$$\Rightarrow \partial_{x_i}\left(\bar{U}_i\right)+\partial_{x_i}\left(\overline{U_i'}\right)=0$$

$$\Rightarrow \partial_{x_i}\left(\bar{U}_i\right)+\cancel{\partial_{x_i}\left(\overline{U_i'}\right)}=0$$

$$\Rightarrow \partial_{x_i}\left(\bar{U}_i\right)=0 \qquad \text{Eq. 4.7}$$

B.2. Navier-Stokes equation

The Navier-Stokes equations written in one of their basic forms and in terms of instantaneous properties is as follows:

$$\partial_t\left(\hat{\rho}\,\hat{U}_i\right)+\partial_{x_j}\left(\hat{\rho}\,\hat{U}_j\,\hat{U}_i\right)=-\partial_{x_i}\left(\hat{p}\right)-\partial_{x_j}\left(\hat{\tau}_{ij}\right)+\hat{F}_i \qquad \text{Eq. 4.2}$$

Using the assumptions and simplifications, as specified in section 4.1.1, the Navier-Stokes equations can be simplified as follows:

$$\Rightarrow \partial_t\left(\hat{\rho}\hat{U}_i\right)+\partial_{x_j}\left(\hat{\rho}\hat{U}_j\hat{U}_i\right)=-\partial_{x_i}\left(\hat{p}\right)-\partial_{x_j}\left(\hat{\tau}_{ij}\right)+\hat{F}_i$$

$$\partial_{x_j}\left(\hat{\tau}_{ij}\right)=\partial_{x_j}\left(-\mu\partial_{x_j}\left(\hat{U}_i\right)\right) \text{ - assump. 5}$$

$$\Rightarrow \partial_{x_j}\left(\hat{\tau}_{ij}\right)=-\mu\partial_{x_j x_j}\left(\hat{U}_i\right) \text{ - assump. 2}$$

$$\hat{F}_i=\hat{\rho}g_i \text{ - assump. 1}$$

$$\Rightarrow \hat{F}_i=\left(\bar{\rho}+\rho'\right)g_i \text{ - assump. 3}$$

$$\Rightarrow \hat{F}_i=\left(\bar{\rho}-\bar{\rho}\beta\left(\hat{T}-\bar{T}\right)\right)g_i \text{ (gravitational and buoyant forces) - assump. 4}$$

Hydristatic solution ($U_i=0,$ incompressible, isothermal)

$$\Rightarrow \cancel{\partial_t\left(\hat{\rho}\,\hat{U}_i\right)}+\cancel{\partial_{x_j}\left(\hat{\rho}\,\hat{U}_j\,\hat{U}_i\right)}=-\partial_{x_i}\left(\hat{p}\right)+\cancel{\mu\partial_{x_j x_j}\left(\hat{U}_j\right)}+\left(\bar{\rho}-\bar{\rho}\beta\cancel{\left(\hat{T}-\bar{T}\right)}\right)g_i$$

$$\Rightarrow -\partial_{x_i}\left(\hat{p}\right)+\bar{\rho}g_i$$

$$\Rightarrow \hat{p} = \bar{\rho} g_i x_i$$

$$\therefore \ \hat{\wp} = \hat{p} + \bar{\rho} g_i x_i$$

Expanding the terms on the left-hand side of the Navier-Stokes Equation:

$$\partial_t\left(\hat{\rho}\hat{U}_i\right) + \partial_{x_j}\left(\hat{\rho}\ \hat{U}_j\hat{U}_i\right) \equiv \hat{\rho}\partial_t\left(\hat{U}_i\right) + \hat{U}_i \underbrace{\cancel{\partial_t\left(\hat{\rho}\right)}}_{\text{assump. 1\&3}} + \left(\hat{\rho}\hat{U}_i\right) \underbrace{\cancel{\partial_{x_j}\left(\hat{U}_j\right)}}_{\text{continuity eqn}} + \left(\hat{U}_j\right)\partial_{x_j}\left(\hat{\rho}\hat{U}_i\right)$$

$$\Rightarrow \hat{\rho}\partial_t\left(\hat{U}_i\right) + \underbrace{\hat{\rho}\left(\hat{U}_j\right)\partial_{x_j}\left(\hat{U}_i\right)}_{\text{assump. 1\&3}}$$

Combining everything gives:

$$\Rightarrow \bar{\rho}\partial_t\left(\hat{U}_i\right) + \bar{\rho}\hat{U}_j\partial_{x_j}\left(\hat{U}_i\right) = -\partial_{x_i}\left(\hat{\wp}\right) + \mu\partial_{x_j x_j}\left(\hat{U}_i\right) - g_i\bar{\rho}\beta\left(\hat{T} - \bar{T}\right) \qquad \text{Eq. 4.5}$$

Applying Reynolds decomposition to the above simplified Navier-Stokes equations results in the following:

$$\hat{U}_i \equiv \bar{U}_i + U_i'$$

$$\hat{U}_j \equiv \bar{U}_j + U_j'$$

$$\hat{\wp} \equiv \bar{\wp} + \wp'$$

$$\hat{T} \equiv \bar{T} + T'$$

Left-hand side

$$\Rightarrow \bar{\rho}\partial_t\left(\bar{U}_i + U_i'\right) + \bar{\rho}\left(\bar{U}_j + U_j'\right)\partial_{x_j}\left(\bar{U}_i + U_i'\right)$$

Right-hand side

$$\Rightarrow -\partial_{x_i}\left(\bar{\wp} + \wp'\right) + \mu\partial_{x_j x_j}\left(\bar{U}_i + U_i'\right) - g_i\bar{\rho}\beta\left(T'\right)$$

Using Reynolds averaging techniques, the Reynolds decomposed Navier-Stokes equations are simplified as follows:

Left-hand side

$$\overline{\bar{\rho}\partial_t\left(\bar{U}_i + U_i'\right)} + \overline{\bar{\rho}\left(\bar{U}_j + U_j'\right)\partial_{x_j}\left(\bar{U}_i + U_i'\right)}$$

$$\Rightarrow \bar{\rho}\partial_t\left(\bar{U}_i\right) + \bar{\rho}\left(\bar{U}_j\right)\partial_{x_j}\left(\bar{U}_i\right) + \bar{\rho}\cancel{\left(\overline{U_j'}\right)}\partial_{x_j}\left(\bar{U}_i\right) + \bar{\rho}\left(\bar{U}_j\right)\partial_{x_j}\cancel{\left(\overline{U_i'}\right)} + \bar{\rho}\left(\overline{U_j'}\right)\partial_{x_j}\left(\overline{U_i'}\right)$$

$$\Rightarrow \bar{\rho}\partial_t\left(\bar{U}_i\right) + \bar{\rho}\left(\bar{U}_j\right)\partial_{x_j}\left(\bar{U}_i\right) + \bar{\rho}\left(\overline{U_j'}\right)\partial_{x_j}\left(\overline{U_i'}\right)$$

$$\Rightarrow \bar{\rho}\partial_t\left(\bar{U}_i\right)+\bar{\rho}\left(\bar{U}_j\right)\partial_{x_j}\left(\bar{U}_i\right)+\underbrace{\bar{\rho}\partial_{x_j}\left(\overline{U_i'U_j'}\right)}_{\text{continuity eqn}}$$

Right-hand side

$$\overline{-\partial_{x_i}\left(\bar{\wp}+\wp'\right)}+\overline{\mu\partial_{x_jx_j}\left(\bar{U}_i+U_i'\right)}-\overline{g_i\bar{\rho}\beta\left(T'\right)}$$

$$\Rightarrow -\partial_{x_i}\left(\bar{\wp}\right)-\partial_{x_i}\left(\cancel{\overline{\wp'}}\right)+\mu\partial_{x_jx_j}\left(\bar{U}_i\right)+\mu\partial_{x_jx_j}\left(\cancel{\overline{U_i'}}\right)-g_i\bar{\rho}\beta\left(\cancel{\overline{T'}}\right)$$

$$\Rightarrow -\partial_{x_i}\left(\bar{\wp}\right)+\mu\partial_{x_jx_j}\left(\bar{U}_i\right)$$

Combining to give:

$$\Rightarrow \bar{\rho}\partial_t\left(\bar{U}_i\right)+\bar{\rho}\bar{U}_j\partial_{x_j}\left(\bar{U}_i\right)=-\partial_{x_i}\left(\bar{\wp}\right)+\partial_{x_j}\left(\mu\partial_{x_j}\left(\bar{U}_i\right)-\bar{\rho}\left\{\left(\overline{U_i'U_j'}\right)\right\}\right) \qquad \text{Eq. 4.8}$$

B.3. Energy equation

The energy equation written in one of its basic forms and in terms of instantaneous properties is as follows:

$$\partial_t\left(\hat{\rho}\,\hat{e}\right)+\partial_{x_j}\left(\hat{\rho}\,\hat{U}_j\,\hat{e}\right)=-\partial_{x_j}\left(\hat{q}_i^s\right)+\hat{H}_i^s \qquad \text{Eq. 4.3}$$

Using the assumptions and simplifications, as specified in section 4.1.1, the above energy equation can be simplified as follows:

$$\Rightarrow \partial_t\left(\hat{\rho}\,\hat{e}\right)+\partial_{x_j}\left(\hat{\rho}\,\hat{U}_j\,\hat{e}\right)=-\partial_{x_j}\left(\hat{q}_i^s\right)+\hat{H}_i^s$$

$$\hat{e}=C_p\left(\hat{T}-T_{ref}\right)\ \left(T_{ref}\ \text{taken as } 0\right)$$

$$\partial_{x_j}\left(\hat{q}_i\right)=\partial_{x_j}\left(-\lambda\partial_{x_j}\left(T\right)\right)\text{ - assump. 6}$$

$$\hat{H}_i=0\text{ - assump. 7}$$

Combining everything:

$$\Rightarrow \hat{\rho}\partial_t\left(C_p\hat{T}\right)+\hat{\rho}\partial_{x_j}\left(U_jC_p\hat{T}\right)=\lambda\partial_{x_jx_j}\left(T\right)$$

$$\Rightarrow \hat{\rho}\partial_t\left(\hat{T}\right)+\hat{\rho}\partial_{x_j}\left(U_j\hat{T}\right)=\frac{\lambda}{C_p}\partial_{x_jx_j}\left(T\right)$$

$$Pr=\frac{\nu}{\alpha}=\frac{\mu C_p}{\lambda} \qquad \text{Eq. 10.9}$$

Thus:

$$\Rightarrow \bar{\rho}\partial_t\left(\hat{T}\right)+\bar{\rho}\hat{U}_j\partial_{x_j}\left(\hat{T}\right)=\frac{\mu}{Pr}\partial_{x_jx_j}\left(\hat{T}\right) \qquad \text{Eq. 4.6}$$

Applying Reynolds decomposition to the above simplified energy equation results in the following:

$$\hat{U}_j \equiv \bar{U}_j + U_j'$$
$$\hat{T} \equiv \bar{T} + T'$$
$$\Rightarrow \bar{\rho}\partial_t\left(\bar{T}+T'\right)+\bar{\rho}\left(\bar{U}_j+U_j'\right)\partial_{x_j}\left(\bar{T}+T'\right)=\frac{\mu}{Pr}\partial_{x_jx_j}\left(\bar{T}+T'\right)$$

Using Reynolds averaging techniques, the Reynolds decomposed continuity equation is simplified as follows:

Left-hand side

$$\overline{\bar{\rho}\partial_t\left(\bar{T}+T'\right)}+\overline{\bar{\rho}\left(\bar{U}_j+U_j'\right)\partial_{x_j}\left(\bar{T}+T'\right)}$$
$$\Rightarrow \bar{\rho}\partial_t\left(\bar{T}\right)+\bar{\rho}\partial_t\left(\cancel{\overline{T'}}\right)+\bar{\rho}\left(\bar{U}_j\right)\partial_{x_j}\left(\bar{T}\right)+\bar{\rho}\left(\cancel{\overline{U_j'}}\right)\partial_{x_j}\left(\bar{T}\right)+\bar{\rho}\left(\bar{U}_j\right)\partial_{x_j}\left(\cancel{\overline{T'}}\right)+\bar{\rho}\left(\overline{U_j'}\right)\partial_{x_j}\left(\overline{T'}\right)$$
$$\Rightarrow \bar{\rho}\partial_t\left(\bar{T}\right)+\bar{\rho}\left(\bar{U}_j\right)\partial_{x_j}\left(\bar{T}\right)+\bar{\rho}\left(\overline{U_j'}\right)\partial_{x_j}\left(\overline{T'}\right)$$
$$\Rightarrow \bar{\rho}\partial_t\left(\bar{T}\right)+\bar{\rho}\left(\bar{U}_j\right)\partial_{x_j}\left(\bar{T}\right)+\underbrace{\bar{\rho}\partial_{x_j}\left(\overline{T'U_j'}\right)}_{\text{continuity eqn}}$$

Right-hand side

$$\overline{\frac{\mu}{Pr}\partial_{x_jx_j}\left(\bar{T}+T'\right)}$$
$$\Rightarrow \frac{\mu}{Pr}\partial_{x_jx_j}\left(\bar{T}\right)+\frac{\mu}{Pr}\partial_{x_jx_j}\left(\cancel{\overline{T'}}\right)$$
$$\Rightarrow \frac{\mu}{Pr}\partial_{x_jx_j}\left(\bar{T}\right)$$

Combining to give:

$$\Rightarrow \bar{\rho}\partial_t\left(\bar{T}\right)+\bar{\rho}\bar{U}_j\partial_{x_j}\left(\bar{T}\right)=\partial_{x_j}\left(\frac{\mu}{Pr}\partial_{x_j}\left(\bar{T}\right)-\bar{\rho}\left\{\left(\overline{T'U_j'}\right)\right\}\right) \qquad \text{Eq. 4.9}$$

C. TURBULENCE SCALES

The following appendix lists the various turbulence scales used in Computational Fluid Dynamics (CFD), as well as sample calculations that utilise the turbulent scales and are stated in the main report.

C.1. Turbulence time scales

Equations to calculate the various turbulence time scales are shown below (Hanjalić *et al*. [49]).

Large energetic eddies $$\tau_{tur} = \frac{k}{\varepsilon}$$

Small eddies $$\vartheta_{tur} = \left(\frac{\nu}{\varepsilon}\right)^{1/2}$$

Dissipative eddies $$\vartheta_{tur} = \left(\frac{\nu}{\varepsilon}\right)^{1/2}$$

C.2. Turbulence length scales

Equations to calculate the various turbulence length scales are shown below (Hanjalić *et al*. [49]).

Large energetic eddies $$l_{tur} = \frac{k^{3/2}}{\varepsilon}$$

Small eddies $$\lambda_{tur} = \left(10\nu\frac{k}{\varepsilon}\right)^{1/2}$$

Dissipative eddies $$\eta_{tur} = \left(\frac{\nu^3}{\varepsilon}\right)^{1/4}$$

C.3. Kolmogorov scales for the domain under investigation

Using the following approximations and values obtained from simulations, the Kolmogorov length and time scales can be calculated as follows:

Kolmogorov length scale $\equiv \eta_{tur} = \left(\frac{\nu^3}{\varepsilon} \right)^{1/4}$

$\nu_{air} \approx 1.5 \times 10^{-5} m^2.s^{-1}$

$\varepsilon_{\max} \approx 6.5 m^2.\mathrm{s}^{-3}$ (from simulations)

$$\eta_{tur} = \left(\frac{\left(1.5 \times 10^{-5}\right)^3}{6.5} \right)^{1/4} = 1.5 \times 10^{-4} m$$

Kolmogorov time scale $\equiv \vartheta_{tur} = \left(\frac{\nu}{\varepsilon} \right)^{1/2}$

$\nu_{air} \approx 1.5 \times 10^{-5} m^2.s^{-1}$

$\varepsilon_{\max} \approx 6.5 m^2.\mathrm{s}^{-3}$ (from simulations)

$$\vartheta_{tur} = \left(\frac{1.5 \times 10^{-5}}{6.5} \right)^{1/2} \approx 1.5 \times 10^{-3} s$$

C.4. Number of grid cells required with DNS of the Urban system

An order of magnitude of the number of grid cells for DNS simulation of the street canyon array used in this study can be approximated using the Kolmogorov length scale for dissipative eddies, as given in C.2. This is calculated as follows:

$L_x = 6.7m$

$L_y = 0.9m$

$L_z = 1.6m$

$$\#cells_i = \frac{L_i}{\eta_{tur}}$$

$\#cells_x \approx 45000$

$\#cells_y \approx 6000$

$\#cells_z \approx 11000$

$\therefore total\ number\ of\ cells \approx \mathbf{3 \times 10^{12}}$

D. DEVELOPMENT OF SARA3DCLIMAT

This appendix contains detail on SARA3DCLIMAT development (refer Table 2.1).

D.1. SARA3DCLIMAT foundation [19]

The SARA3DCLIMAT code was initially founded as part of the PhD thesis of Kenjereš [19], in which he investigated the numerical modelling of buoyancy driven flows, specifically the ground heating of flat and wavy plates. Additionally Kenjereš investigated the accuracy and practical usefulness of the Transient Reynolds Averaged Navier-Stoke (T-RANS) and a hybrid method (refer to section 4.3 and 4.5 respectively) compared to DNS and LES.

D.2. Application to urban environments and dispersion, as well as time limiter modifications [37]

The MSc thesis of Hagenzieker used the SARA3DCLIMAT code to study turbulent and dispersion flows over hills and urban landscapes, investigating factors such as time scale limiters, wall functions and turbulent kinetic energy production, as well as a hybrid T-RANS and LES model. For the 3D urban configuration, Hagenzieker showed that the Durbin time scale limiter increased the accuracy of the modelled turbulent kinetic energy, even though comparably different to wind tunnel experiments; with under prediction in the UCL and over prediction in the UBL. Even considering the latter, the code was able to accurately predict pollutant dispersions.

D.3. Practical application of SARA3DCLIMAT to the TU Delft campus [23]

In Valk's BSc thesis, the practical usefulness and application of CFD simulation to urban planning was highlighted with the use of isothermal turbulent flow modelling in the TU Delft campus. Valk also pointed out the limitations of CFD modelling, especially around use of fixed boundary conditions and choice of domain modelling.

D.4. Inclusion of vegetation models in SARA3DCLIMAT [38, 64]

As part of his MSc thesis, ter Kuile investigated the inclusion of vegetative models to the SARA3DCLIMAT code, in addition to the modification of the code with improved mesh refinement methods and the modification of wall functions and roughness.

ter Kuile showed that the modified model with mesh refinement under predicted turbulent kinetic energy, while over predicted dispersion and concentration levels. The study also highlighted the importance of surface roughness with the absence of obstacles and *vice versa*.

D.5. Expansion of vegetation models in SARA3DCLIMAT [39]

The BSc thesis of Tan investigated the effect of vegetation on turbulent wind flow, with the implementation and comparison of several vegetation models with wind tunnel experiments. Tan showed the importance of choice of vegetation model, not only on the computational accuracy, but also the CFD simulation convergence.

D.6. Modification of standard k-ε turbulence model [40]

Chao investigated the modification of the standard k-ε turbulence model on the turbulent dispersion of pollutants as part of this MSc thesis. Modifications included the addition of a complete and partial Durbin time scale limiter, as well as the Renormalisation Group (RNG) model. Additionally Chao investigated two concentration closure models, namely the Simple Gradient Diffusion Hypothesis (SGDH) and the Generalised Gradient Diffusion Hypothesis (GGDH). Chao found that the complete Durbin time scale limiter resulted in divergent solutions, while use of the partial Durbin time scale limiter and RNG resulted in more accurate turbulent kinetic energies compared to those from wind tunnel measurements and being able to better predict parameters at stagnation points; however still having under predictions in the UCL.

D.7. Modification of standard k-ε turbulence model [41]

In addition to the work by Chao [40], Busking also studied the effects of modifications to the standard k-ε turbulence model on pollutant dispersion. Modifications included the Durbin time scale limiter, RNG model as well as a hybrid T-RANS/LES. Busking showed that all modification improved simulation accuracy, better predicting turbulent kinetic energy profiles and other flow and dispersion parameters. The hybrid model gave the best improvements, partially resolving flow parameters; however the method increased simulation times compared to the standard k-ε turbulence model.

D.8. Monitoring of transient effects and hybrid simulation modification [42]

de Wildt studied the transient effects of turbulent flows as part of her MSc thesis investigating the influence of turbulent viscosity closure, the difference between T-RANS and a hybrid T-RANS/LES with Smagorinsky model, as well as the influence of filter length on LES. de Wildt showed that the hybrid was best able to and most accurately predict turbulent flows, being able to predict flow features such as flow back above high obstacles, which the T-RANS models was not able to predict. de Wildt also shows that filter length had little influence in the urban domain due to similar grid lengths within the urban canyon.

D.9. Expansion to Busking and addition of a reactive pollutant model [43]

As part of his MSC thesis, van den Houwen expanded to the hybrid modelling of Busking [41] by adding more statistics to the dataset. Additionally, van den Houwen modified SARA3DCLIMAT to include for the modelling of reactive pollutant dispersion. van den Houwen showed that the hybrid model improved simulation accuracy for a single obstacle case, better predicting turbulent kinetic energy; however the reverse was found for the homogenous obstacle array, where the hybrid model greatly under predicts turbulent kinetic energies and dispersion. van den Houwen's pollutant model was also found to calculate reasonable and expected profile; however the method remained a proof of concept, with no validations being conducted.

D.10. Comparison of turbulence model modification and addition of thermal buoyancy effects [44]

Verdult, in his BSc thesis, compared the Durbin time scale limiter and RNG modifications, on their effects on simulation accuracy. Verdult found the differences in effects not to be significantly comparable, with validations based on streamline analyses. Verdult also included thermally stratified buoyancy effects into SARA3DCLIMAT, on a 2D scale; but was however not able to find convergent solutions due to the choice of boundary conditions and the choice of domain.

D.11. Validation of SARA3DCLIMAT thermally stratified buoyancy turbulence flow simulations [35]

de Haan, as part of his MSc thesis, investigated the effects of thermally stratified buoyancy in urban climates, expanding on the work of Verdult [44]. de Haan found that the code was able to accurately predict flow parameters for the neutral and unstable stratification cases; not however for the stably stratified case, due to re-laminating of air flow in stably stratified flows. The latter resulted in over predictions of turbulent kinetic energy in the high Reynolds number flow models.

E. UEHARA CALCULATIONS

This section outlines the calculations used to calculate various parameters from the Uehara *et al.* [3] data.

E.1. Calculation of actual approach velocity profiles

Uehara *et al.* [3] provides the following data, from which actual approach velocity profiles can be determined, as outlined below:

$\frac{\kappa U}{u^*}$ given in Uehara *et al*.

$Re_* = \frac{u^* Z_0}{\nu}$ given in Uehara *et al*.

Z_0 given in Uehara *et al*.

κ given in Uehara *et al*.

ν determined from air temperature

Thus, $U = [\text{plot data}] \times Re_* \left(\frac{\nu}{Z_0 \kappa} \right)$

F. PROFILE TIME SERIES PLOTS

This appendix provides complete instantaneous flow profiles (streamwise velocity (*U*), vertical velocity (*W*) and temperature (*T*)) for the various stratification cases at both monitoring points (refer to section 5.2.1 and Figure 5.3 for monitoring point location descriptions). It is to be noted that the hybrid method was initiated after 250 simulation seconds; while statistical periods were only initiated after 600 simulation sections (refer section 6.1) and run for 500 simulation seconds. This statistical period is the standard period on which data is based on.

F.1. Neutral stratified flow

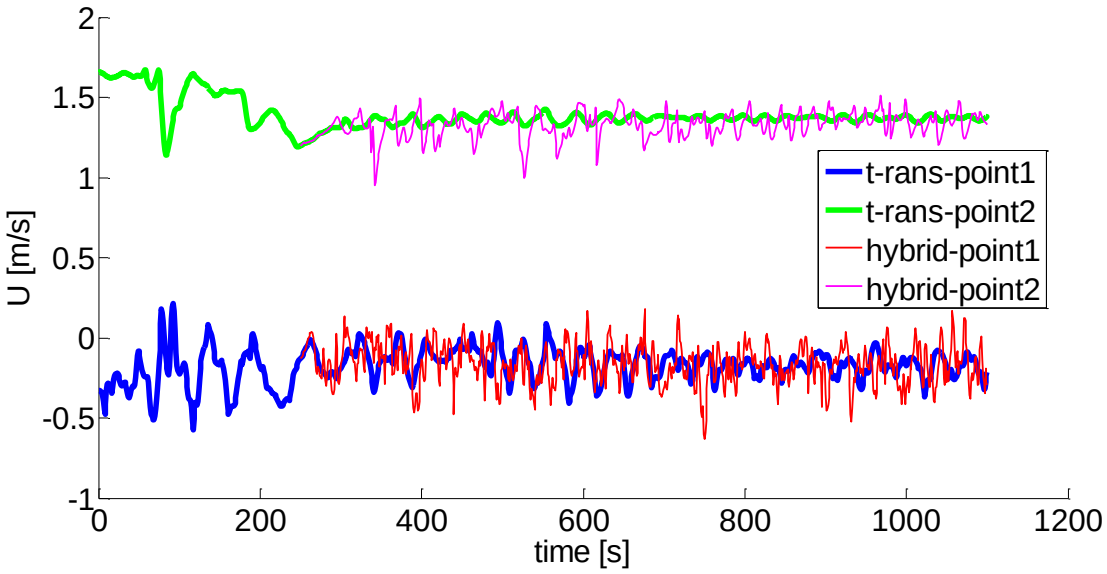

Figure 10.8: Neutral U-profile time series plot

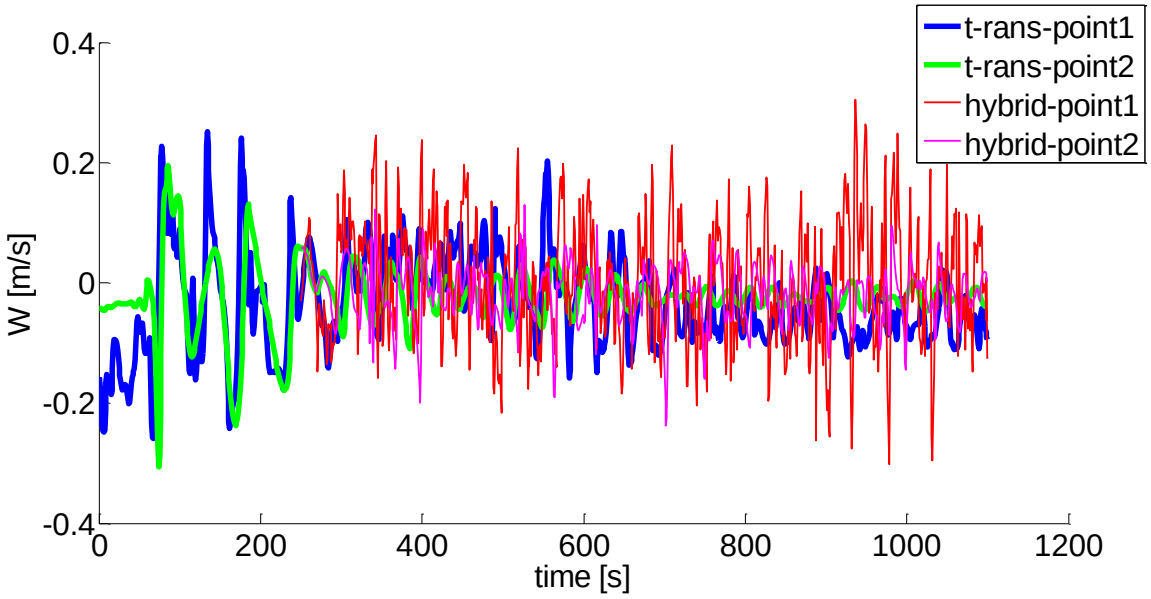

Figure 10.9: Neutral W-profile time series plot

F.2. Strong stable stratified flow

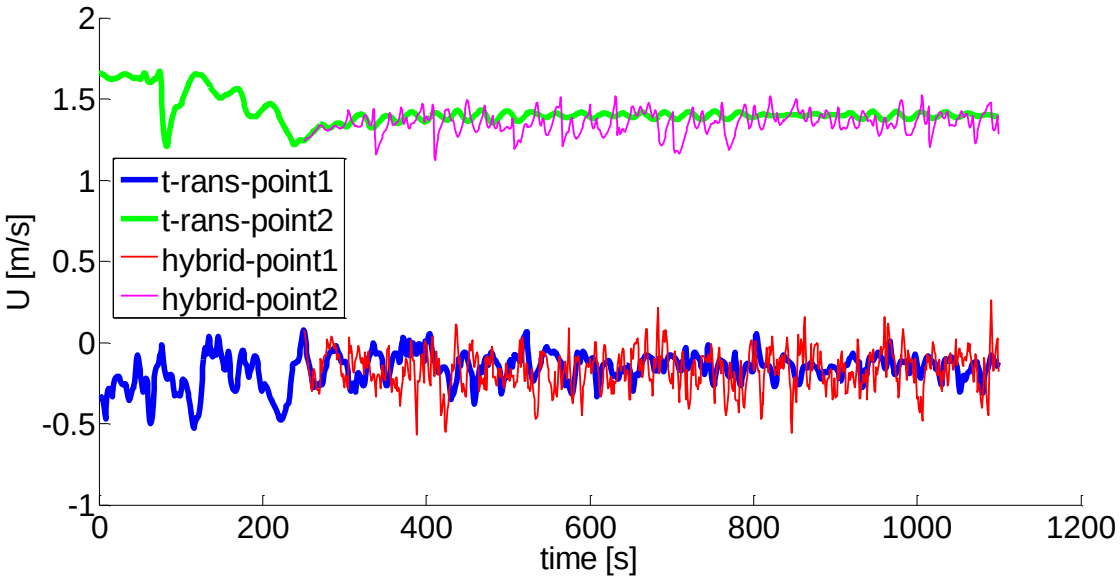

Figure 10.10: Strong stable U-profile time series plot

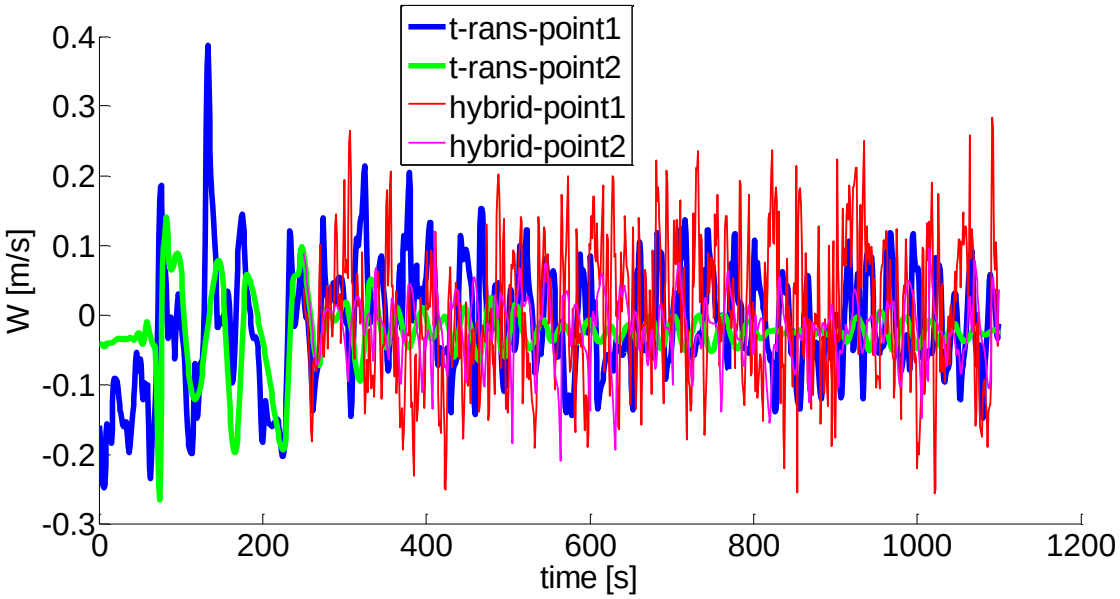

Figure 10.11: Strong stable W-profile time series plot

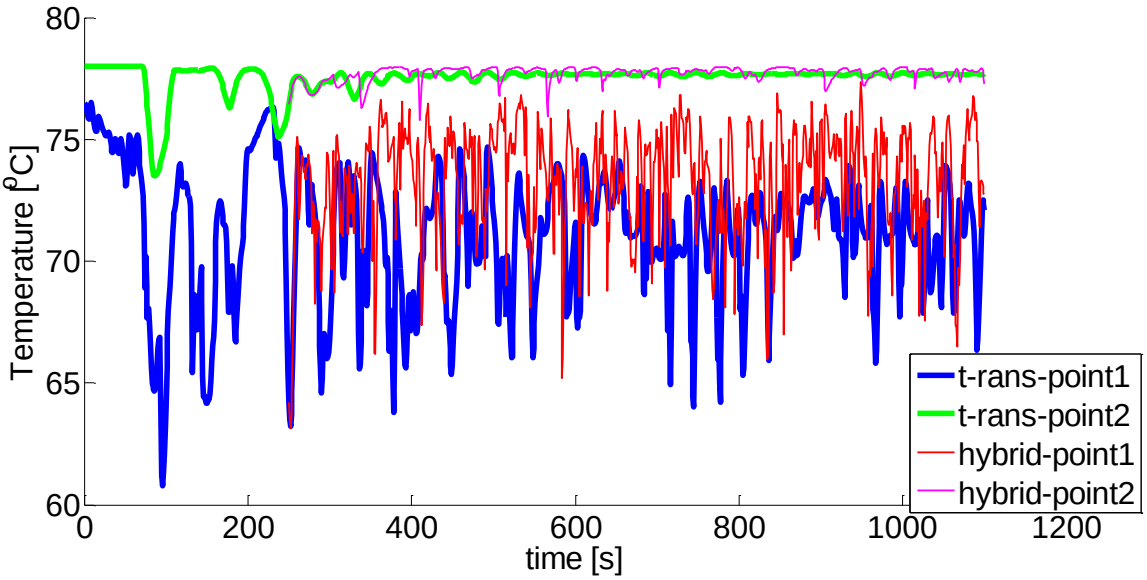

Figure 10.12: Strong stable T-profile time series plot

F.3. Weak stable stratified flow

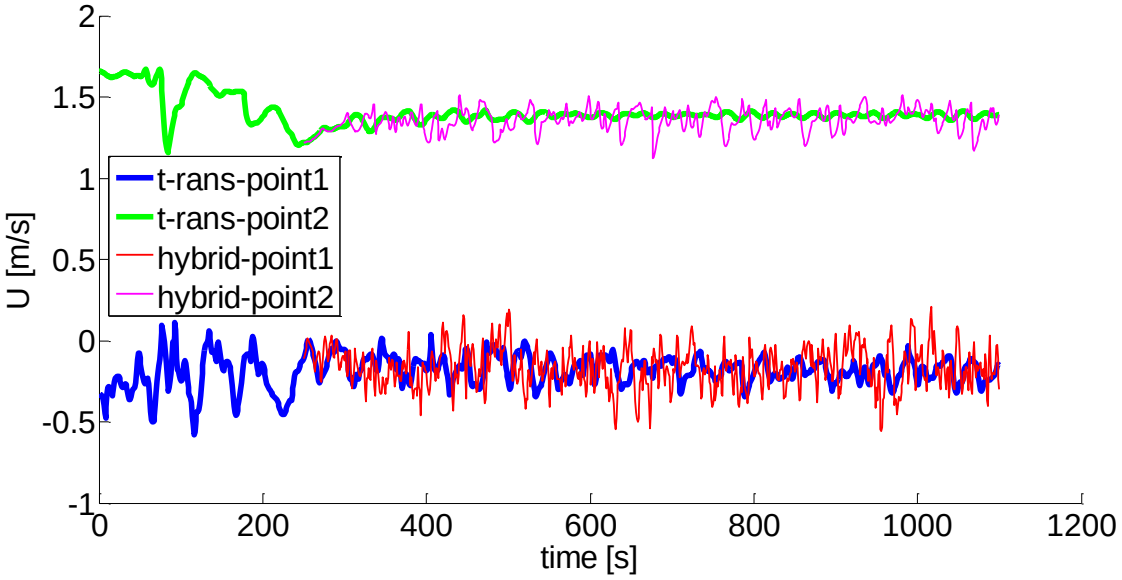

Figure 10.13: Weak stable U-profile time series plot

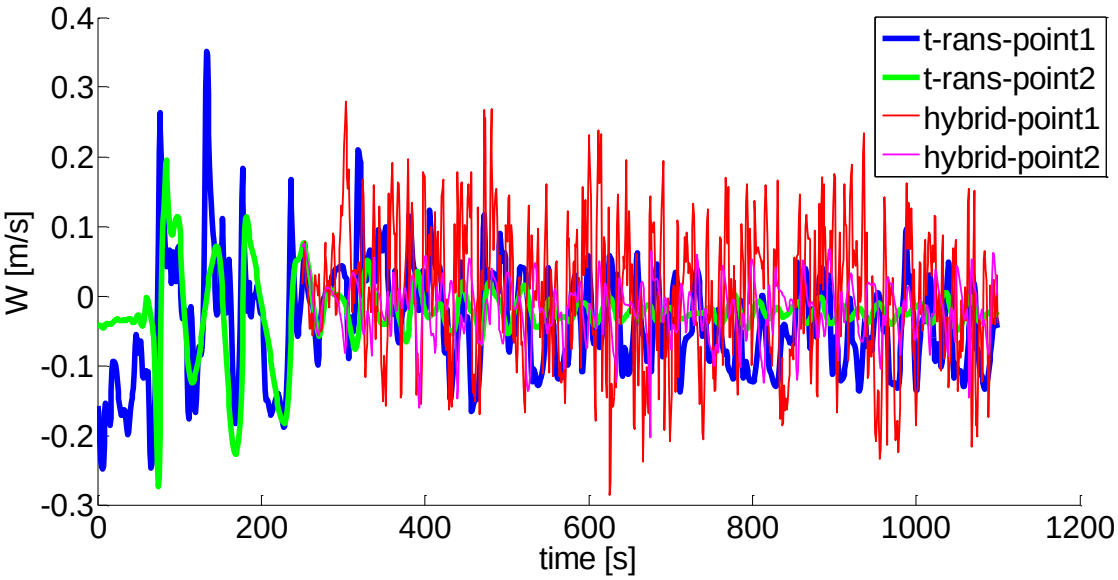

Figure 10.14: Weak stable W-profile time series plot

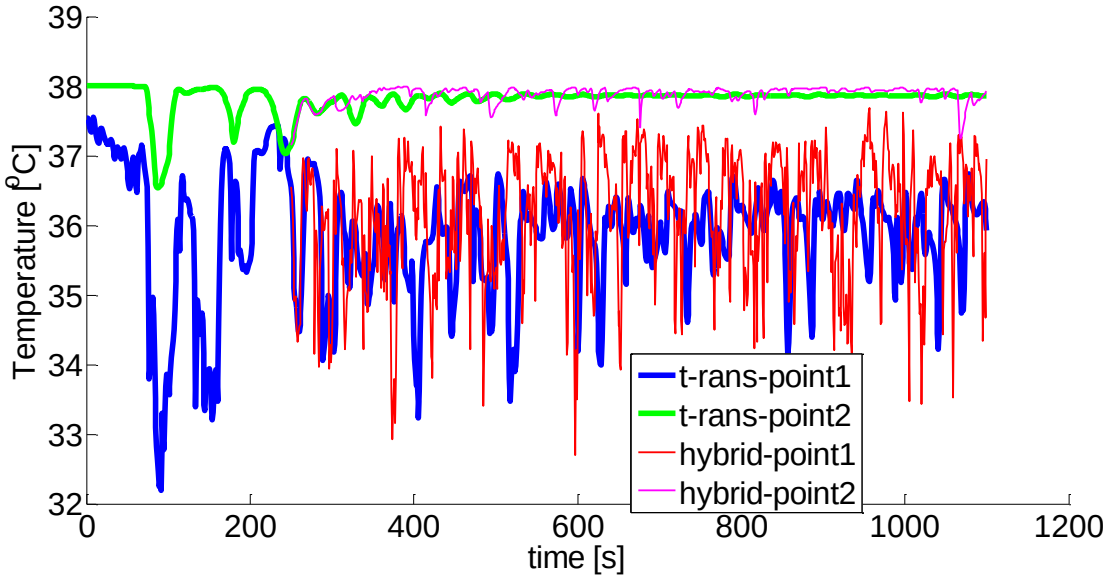

Figure 10.15: Weak stable T-profile time series plot

F.5. Weak unstable stratified flow

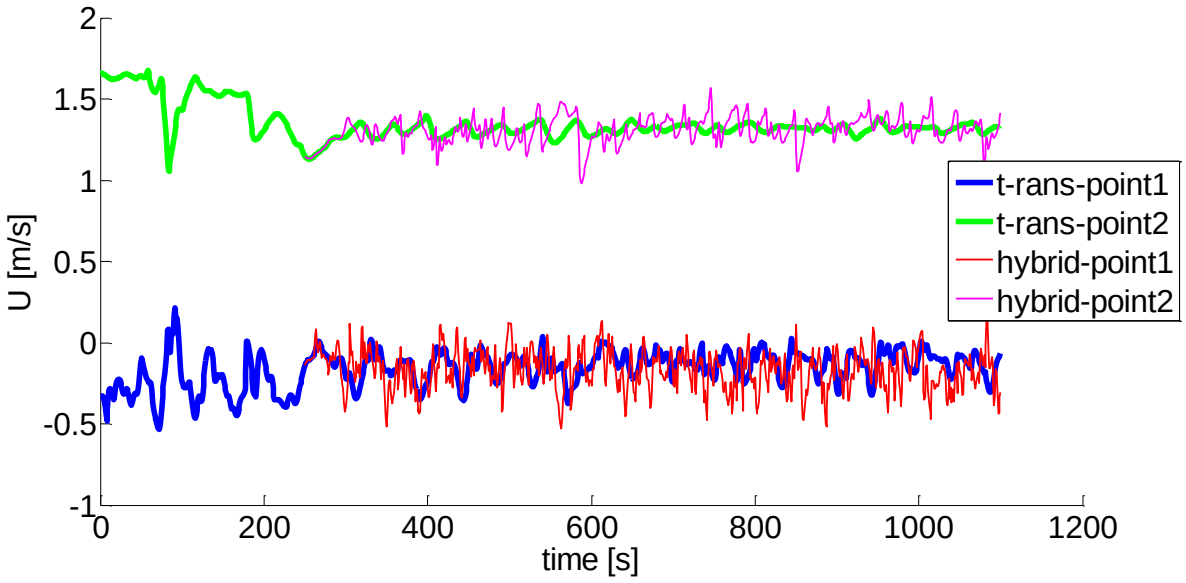

Figure 10.16: Weak unstable U-profile time series plot

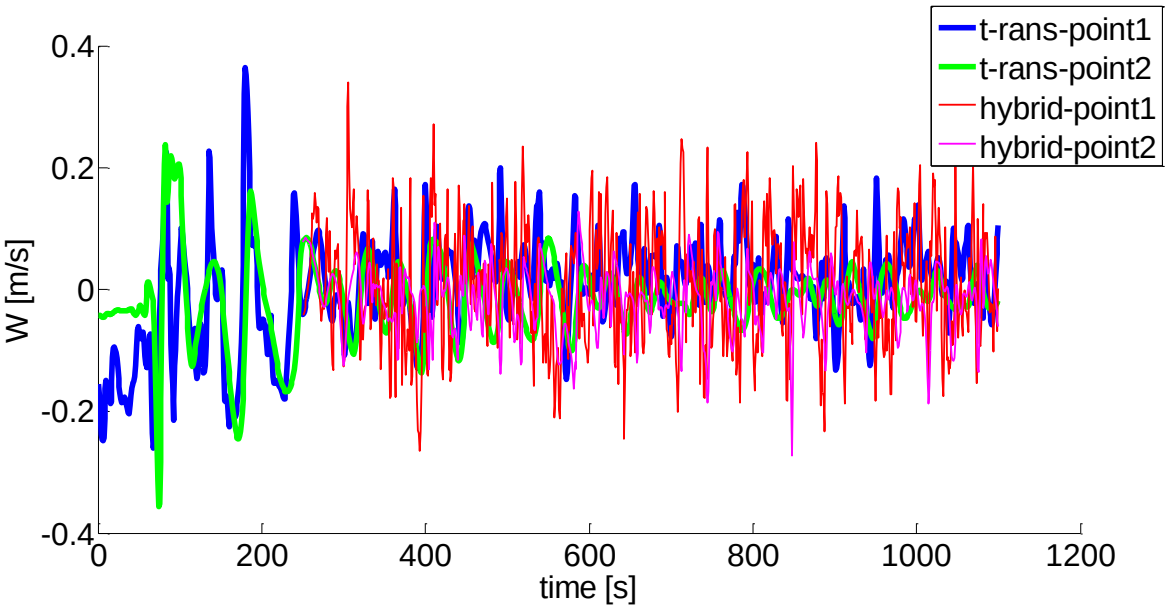

Figure 10.17: Weak unstable W-profile time series plot

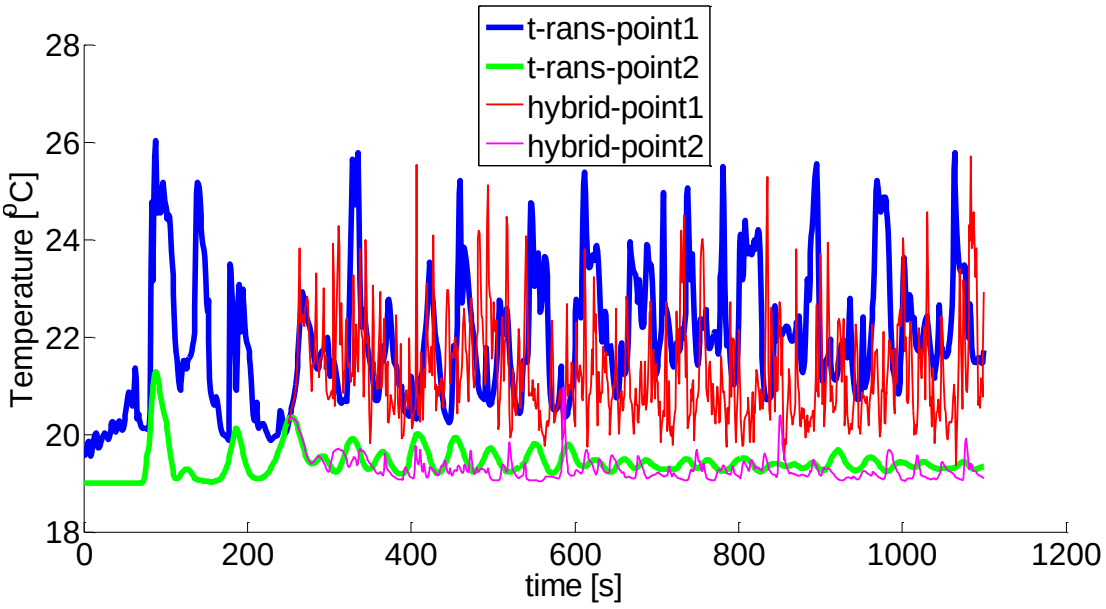

Figure 10.18: Weak unstable T-profile time series plot

F.6. Strong unstable stratified flow

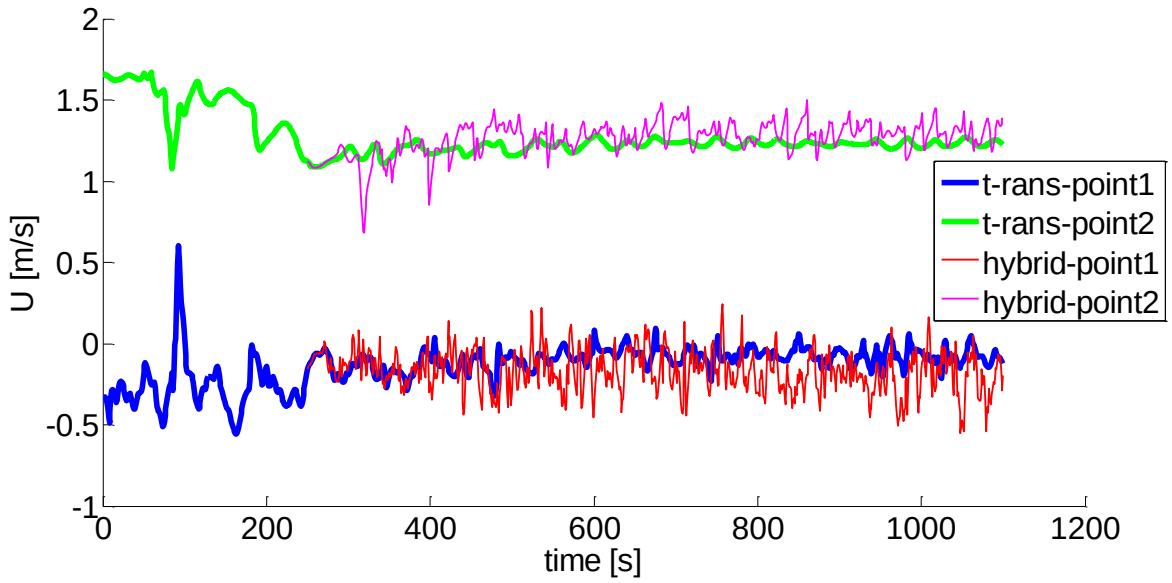

Figure 10.19: Strong unstable U-profile time series plot

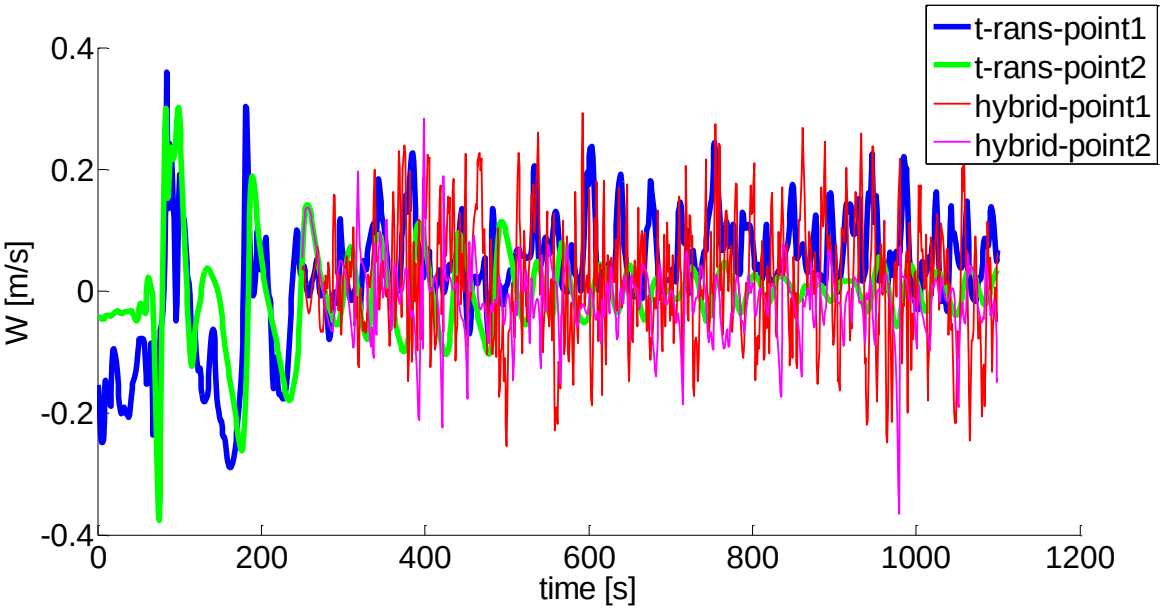

Figure 10.20: Strong unstable W-profile time series plot

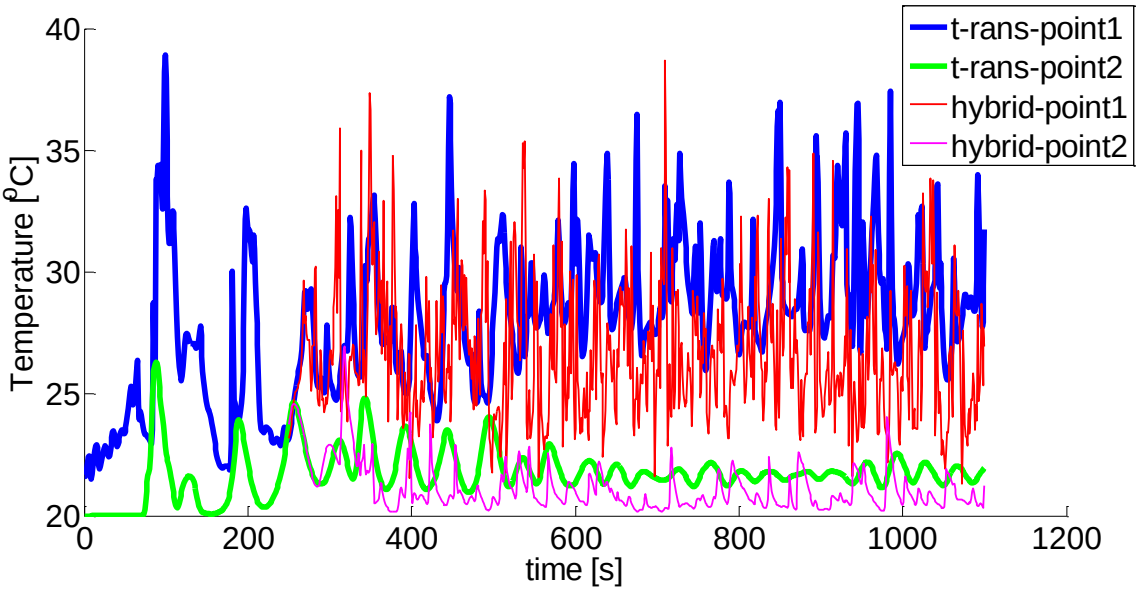

Figure 10.21: Strong unstable T-profile time series plot

G. STATISTICAL PERIOD INDEPENDENCE PLOTS

G.1. T-RANS

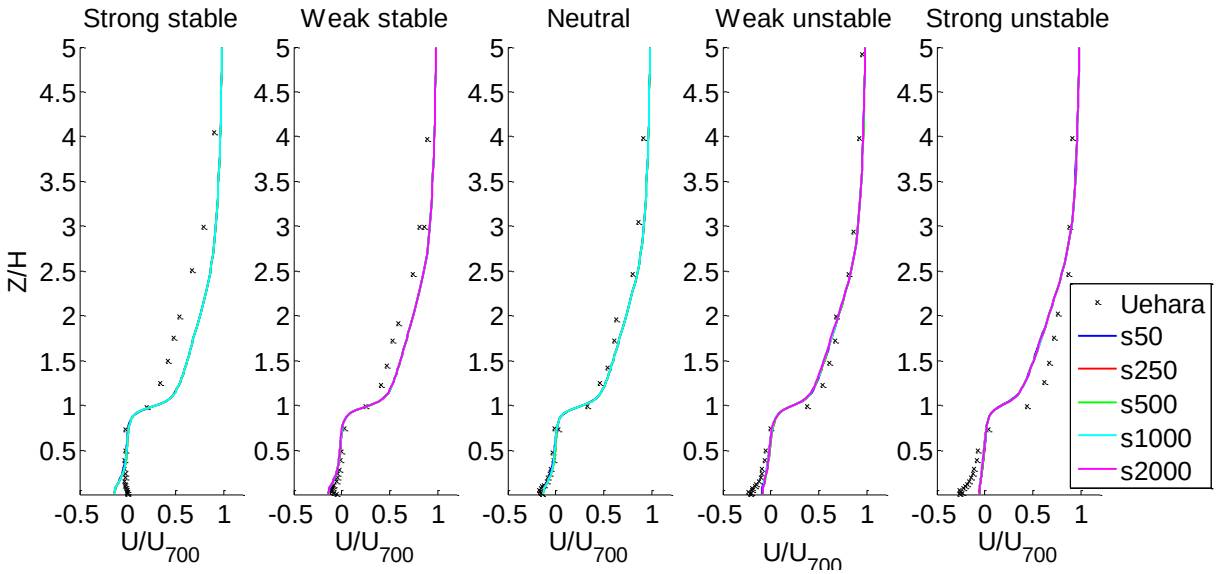

Figure 10.22: T-RANS statistical period independence U-profile

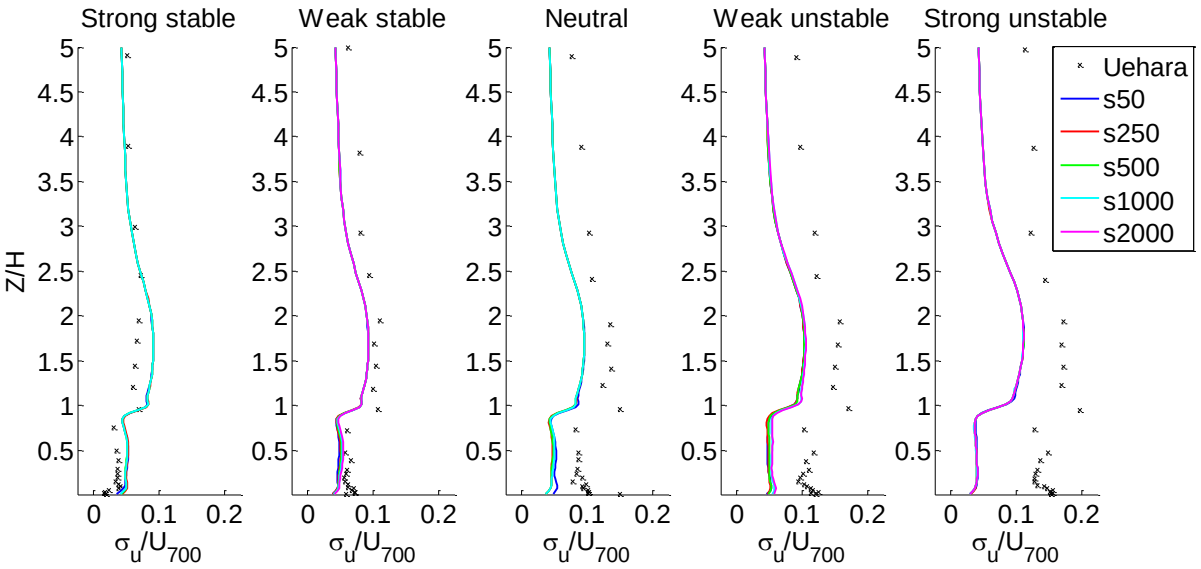

Figure 10.23: T-RANS statistical period independence σ_u-profile

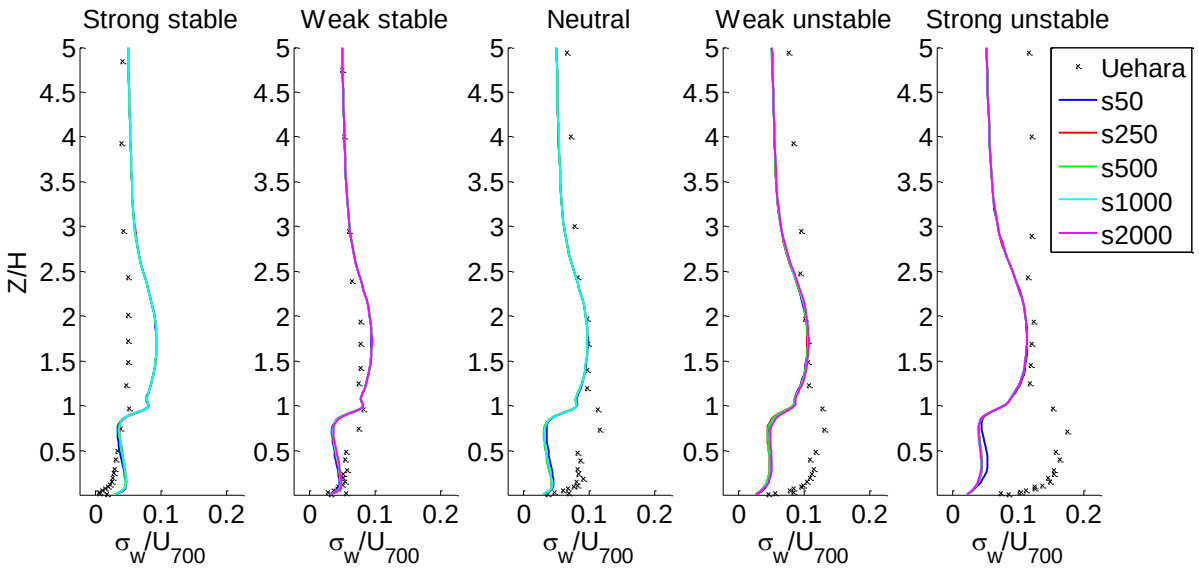

Figure 10.24: T-RANS statistical period independence σ_w-profile

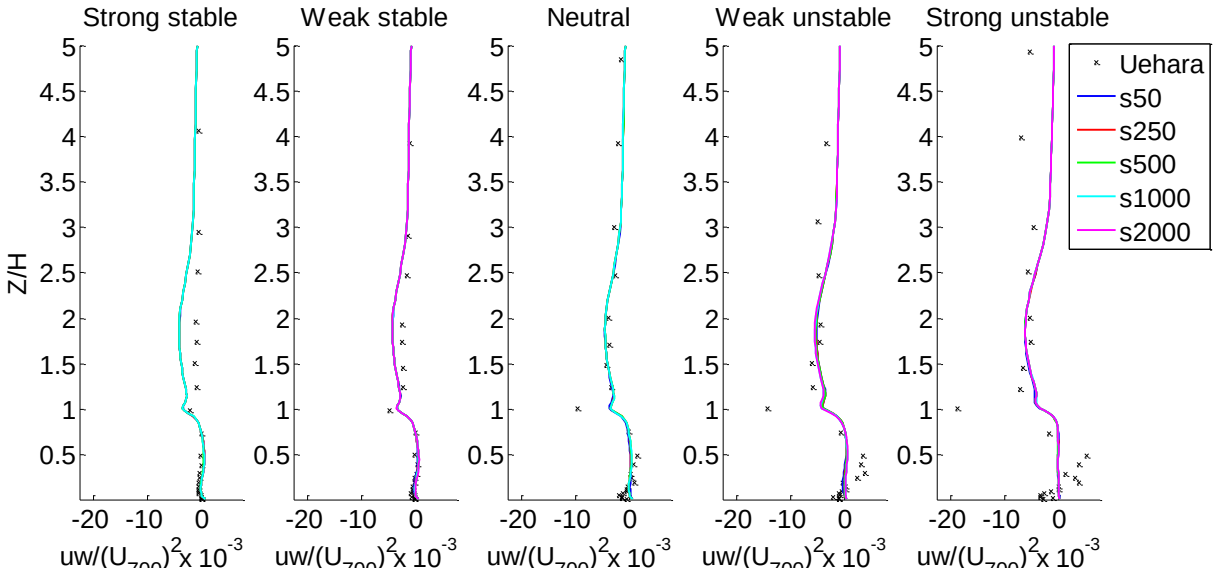

Figure 10.25: T-RANS statistical period independence UW-profile

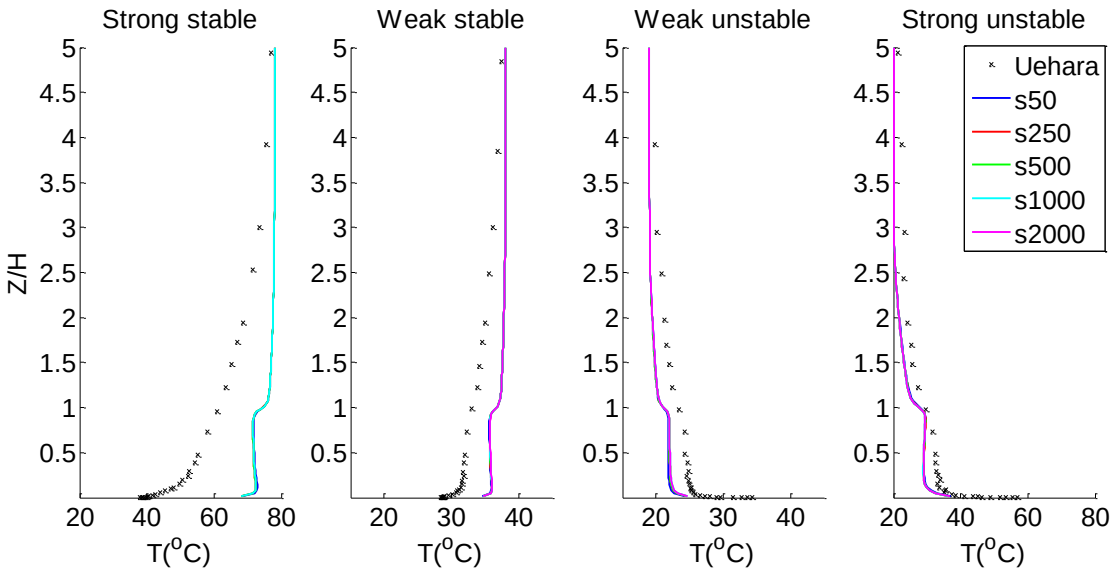

Figure 10.26: T-RANS statistical period independence T-profile

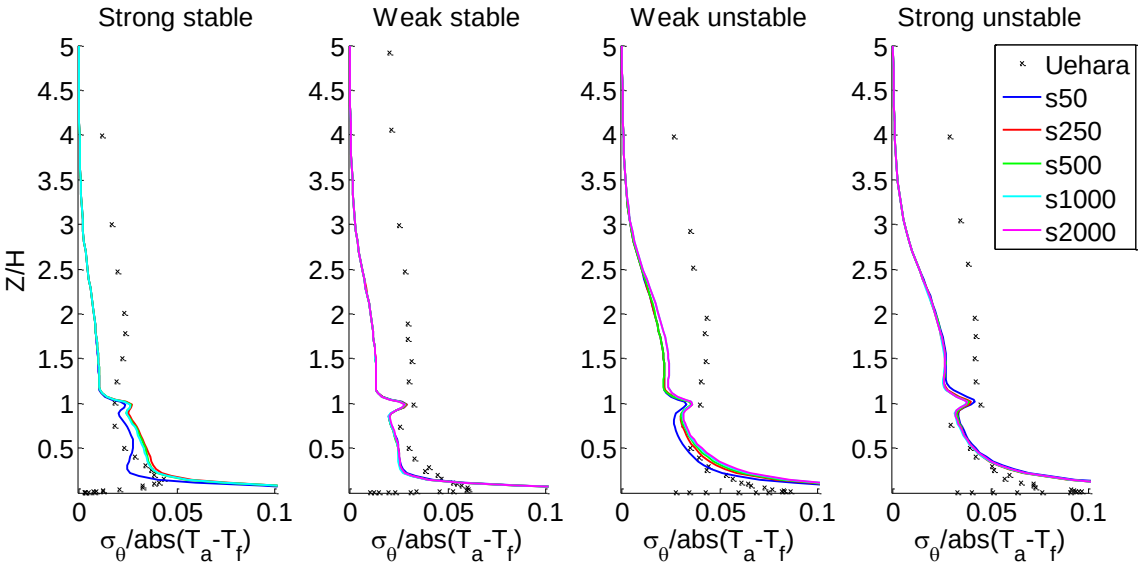

Figure 10.27: T-RANS statistical period independence σ_T-profile

G.3. HYBRID

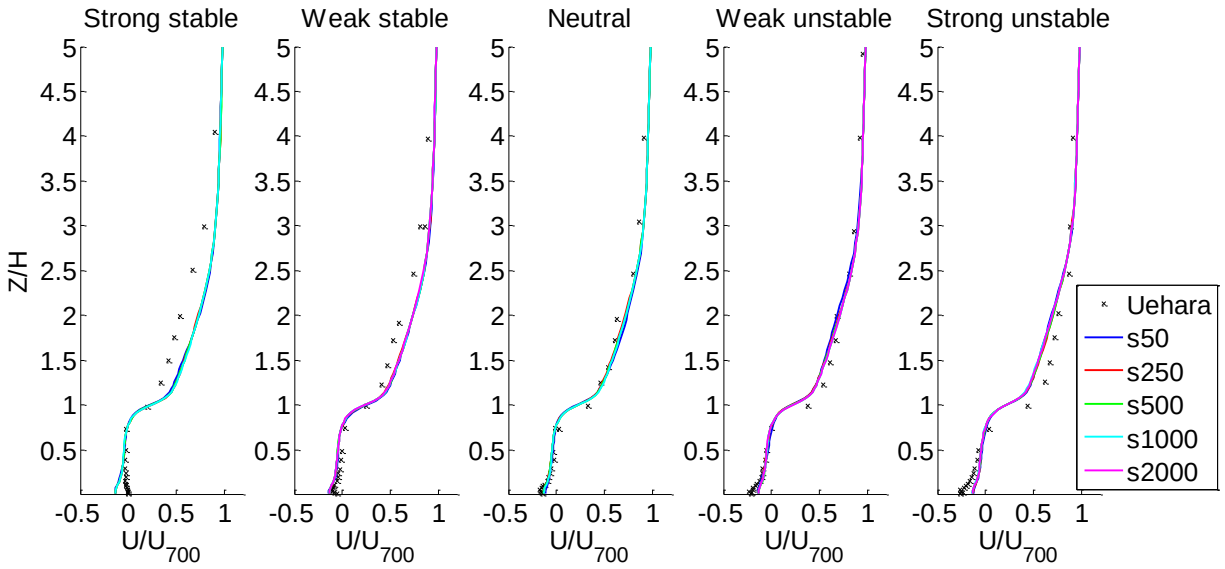

Figure 10.28: Hybrid statistical period independence U-profile

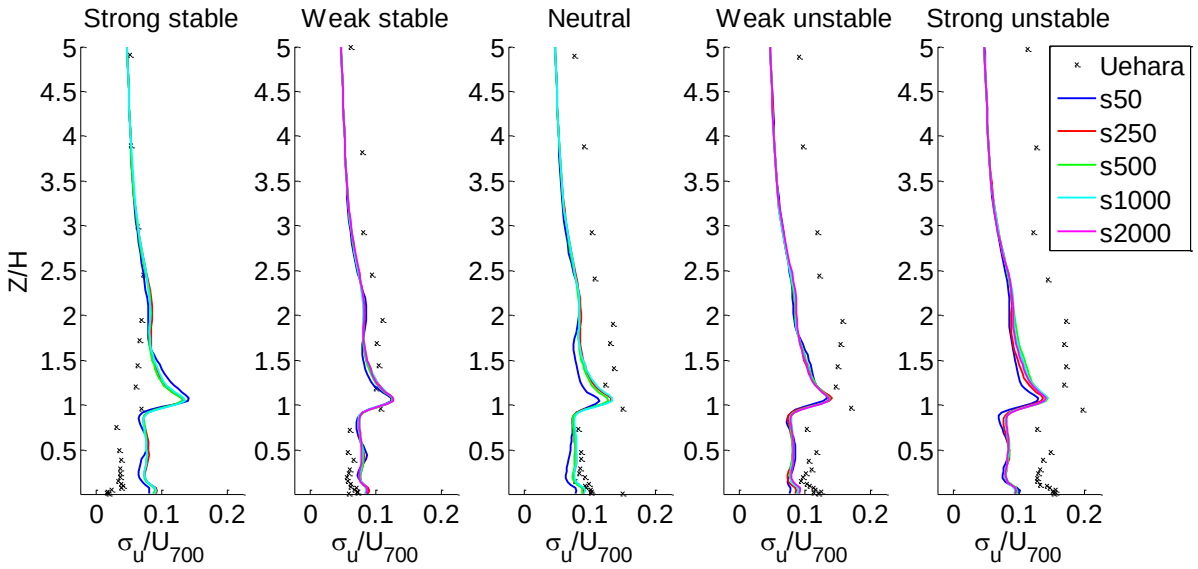

Figure 10.29: Hybrid statistical period independence σ_u-profile

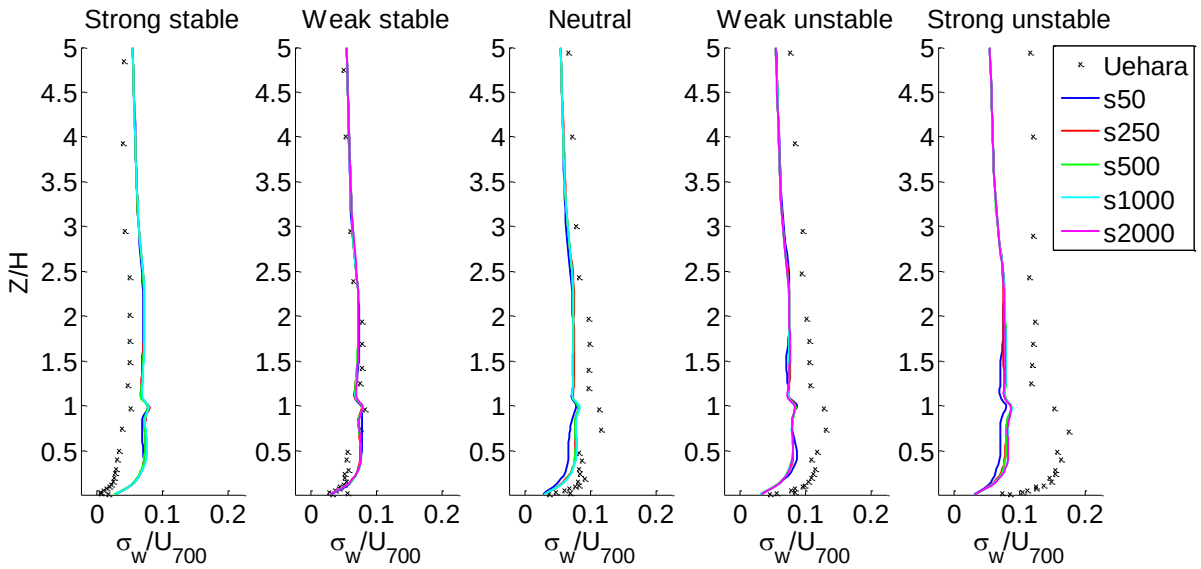

Figure 10.30: Hybrid statistical period independence σ_w-profile

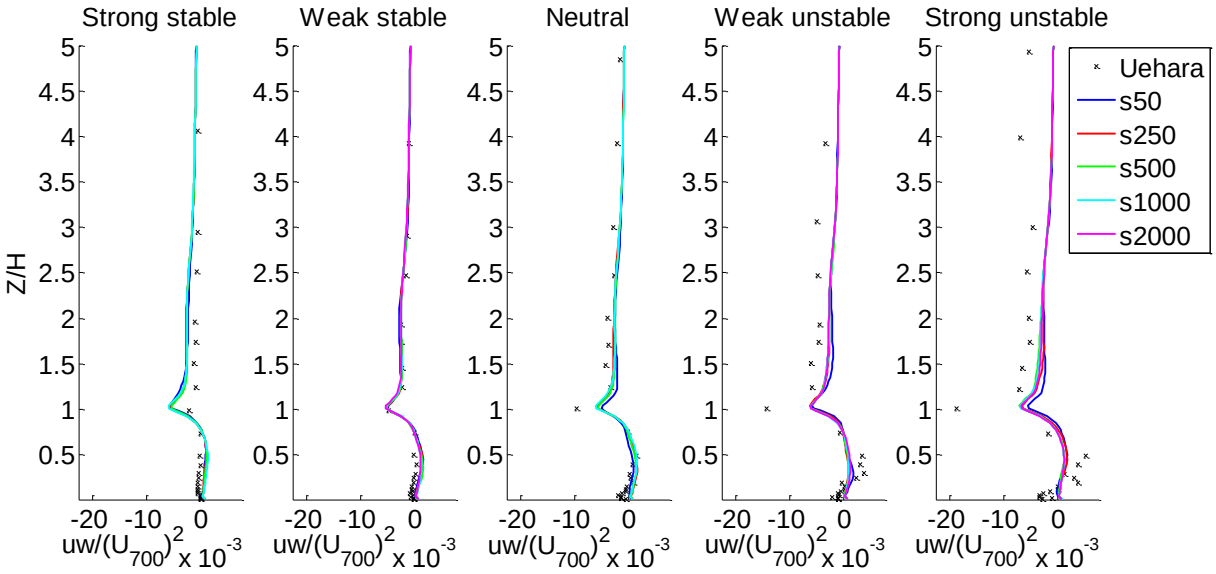

Figure 10.31: Hybrid statistical period independence UW-profile

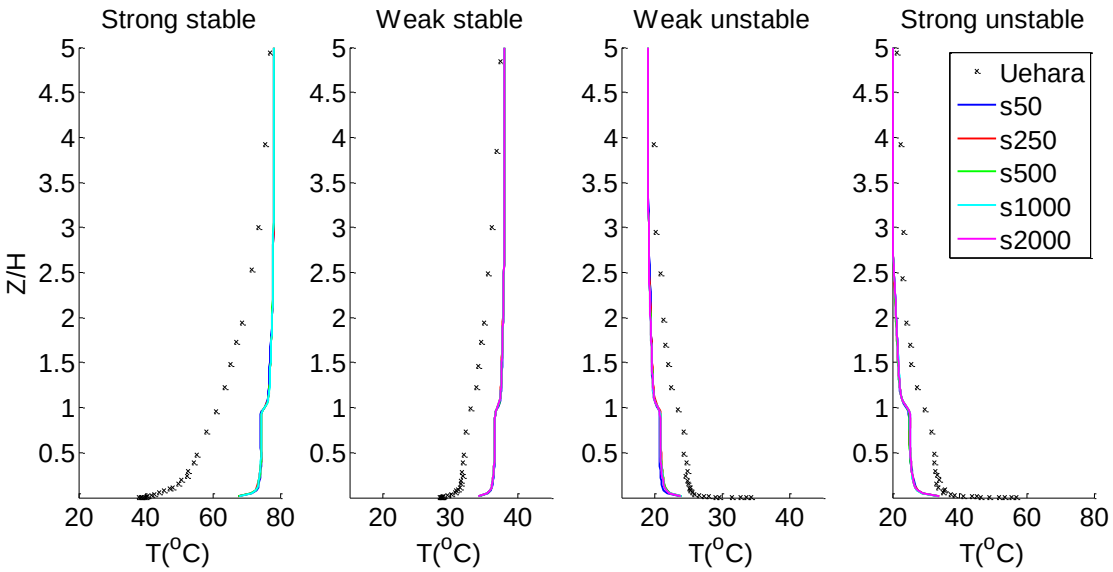

Figure 10.32: Hybrid statistical period independence T-profile

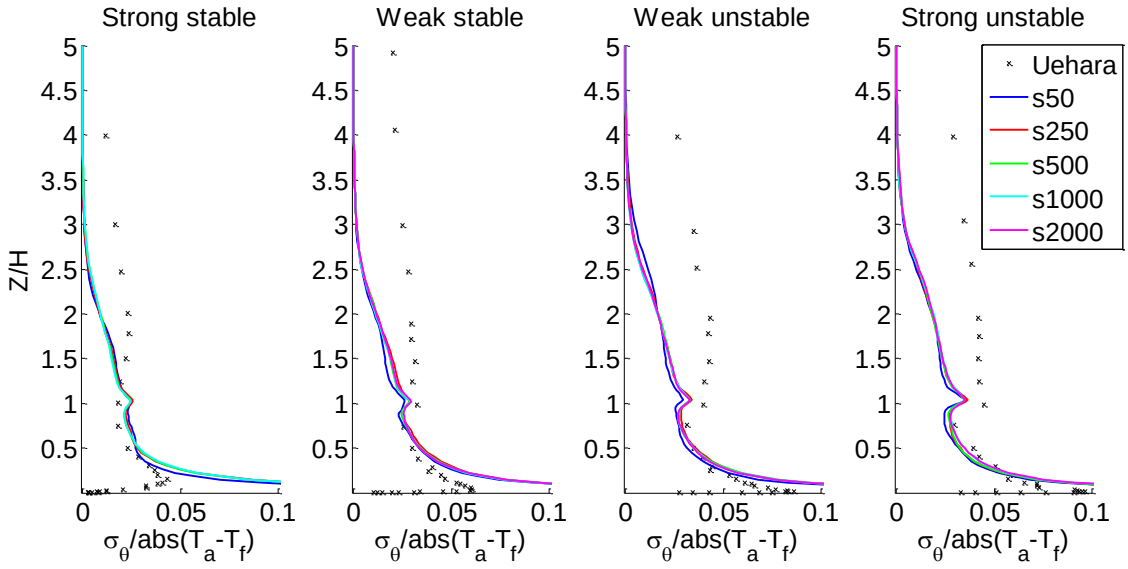

Figure 10.33: Hybrid statistical period independence σ_T-profile

H. SAMPLING CANYON LOCATION FLOW PARAMETER INFLUENCE PLOTS

H.1. T-RANS

H.1.1. Canyons 1-12

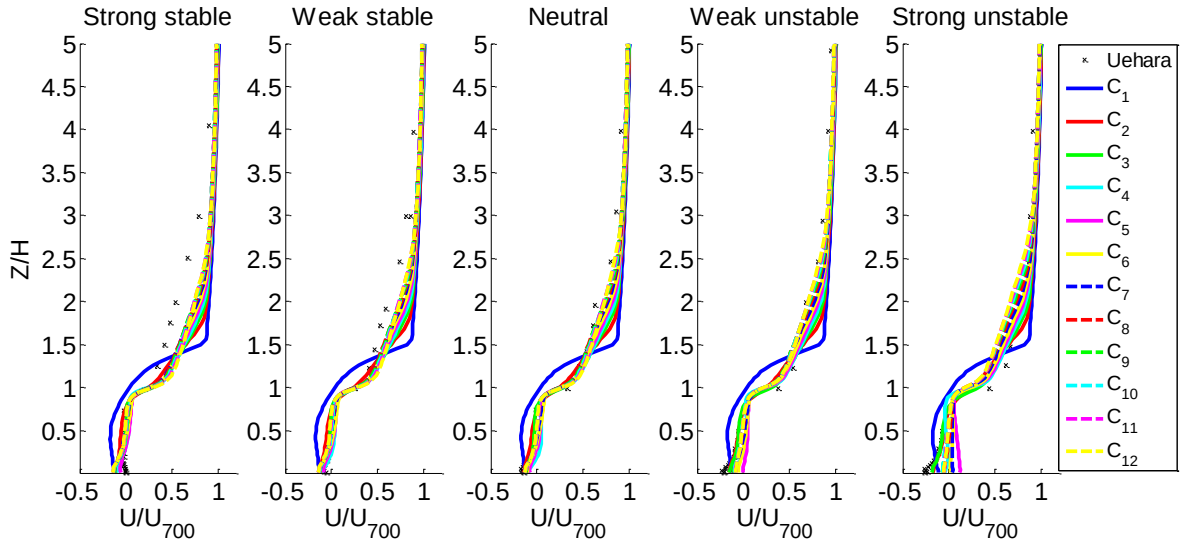

Figure 10.34: T-RANS U-profiles for canyons 1-12

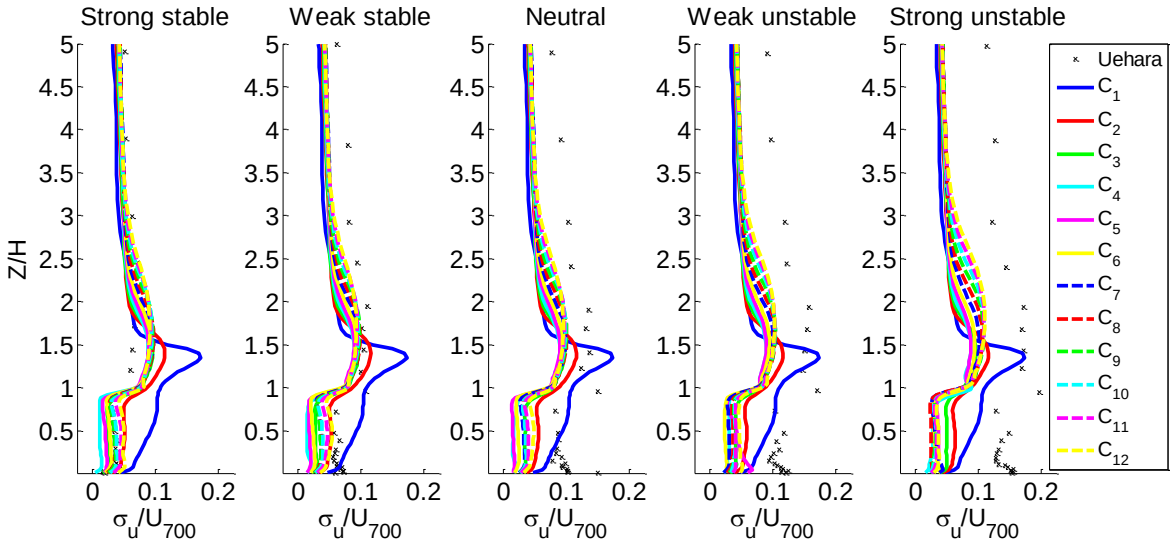

Figure 10.35: T-RANS σ_u-profiles for canyons 1-12

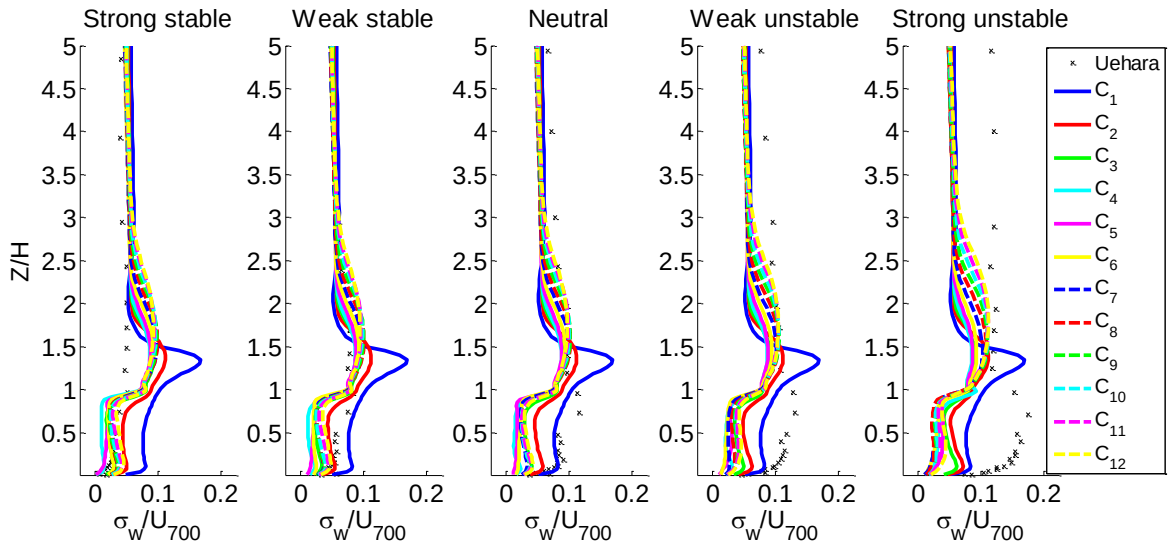

Figure 10.36: T-RANS σ_w-profiles for canyons 1-12

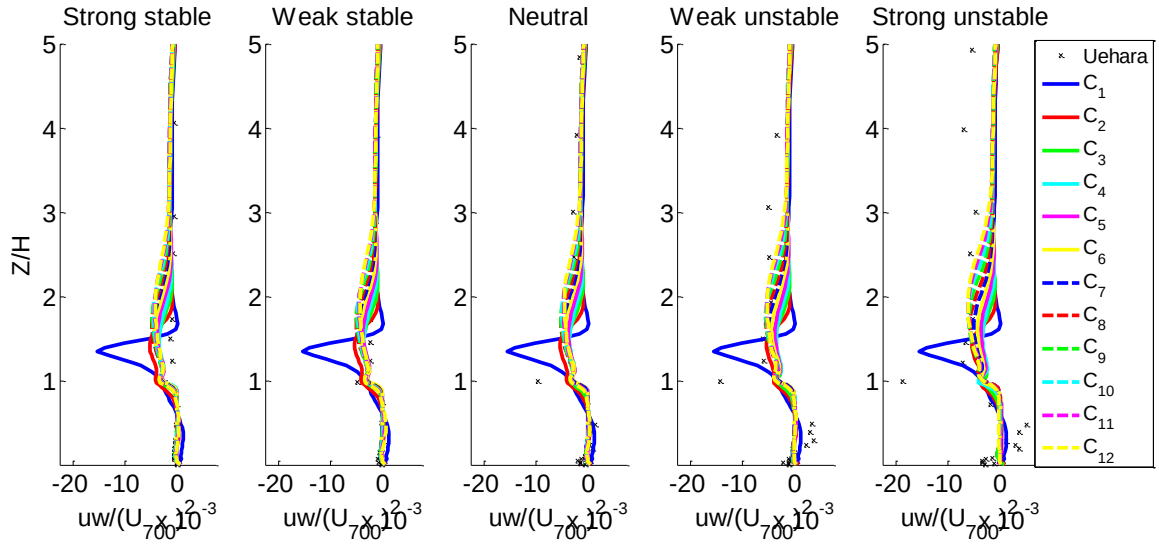

Figure 10.37: T-RANS UW-profiles for canyons 1-12

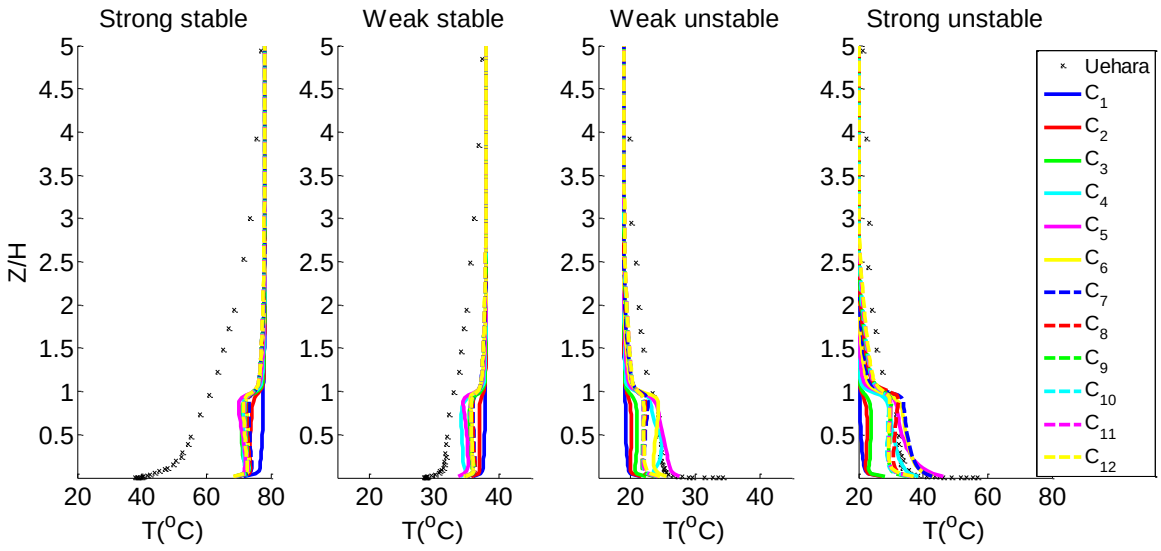

Figure 10.38: T-RANS T-profiles for canyons 1-12

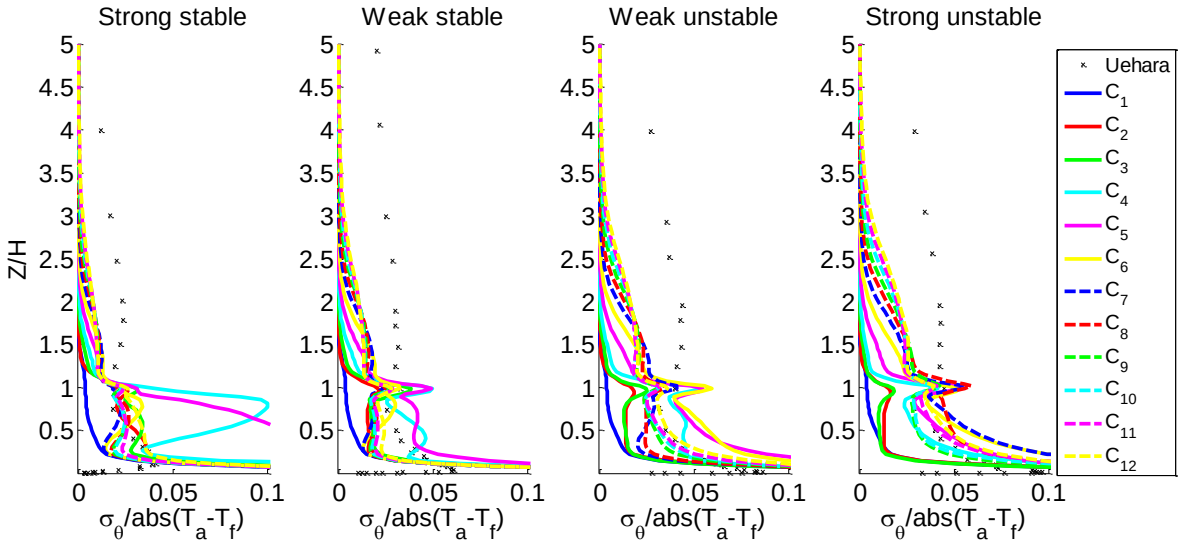

Figure 10.39: T-RANS σ_T-profiles for canyons 1-12

H.1.2. Canyons 7-15 and average canyon

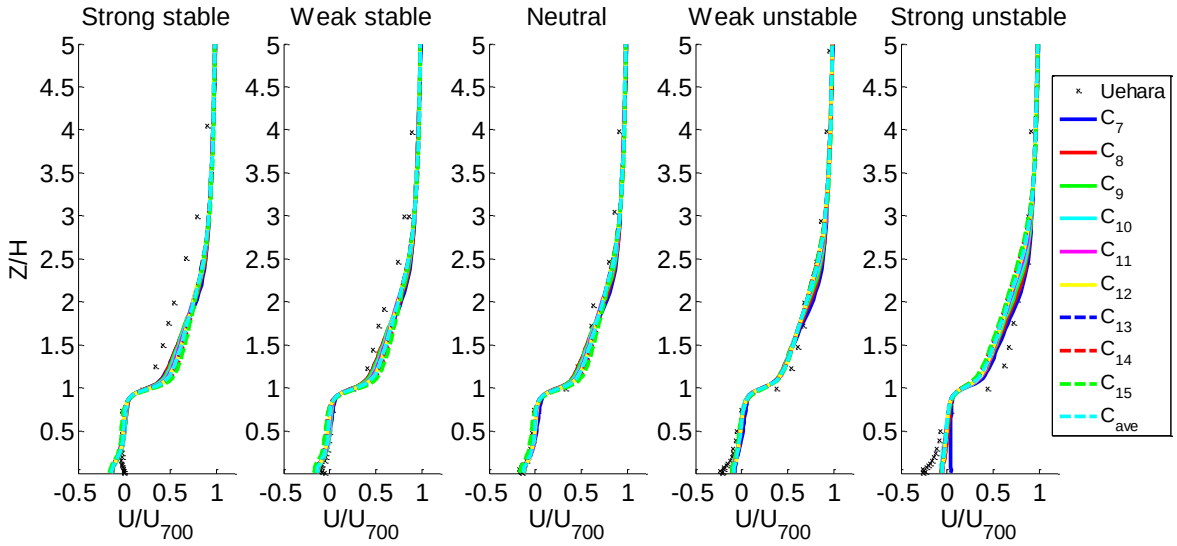

Figure 10.40: T-RANS U-profiles for canyons 1-12

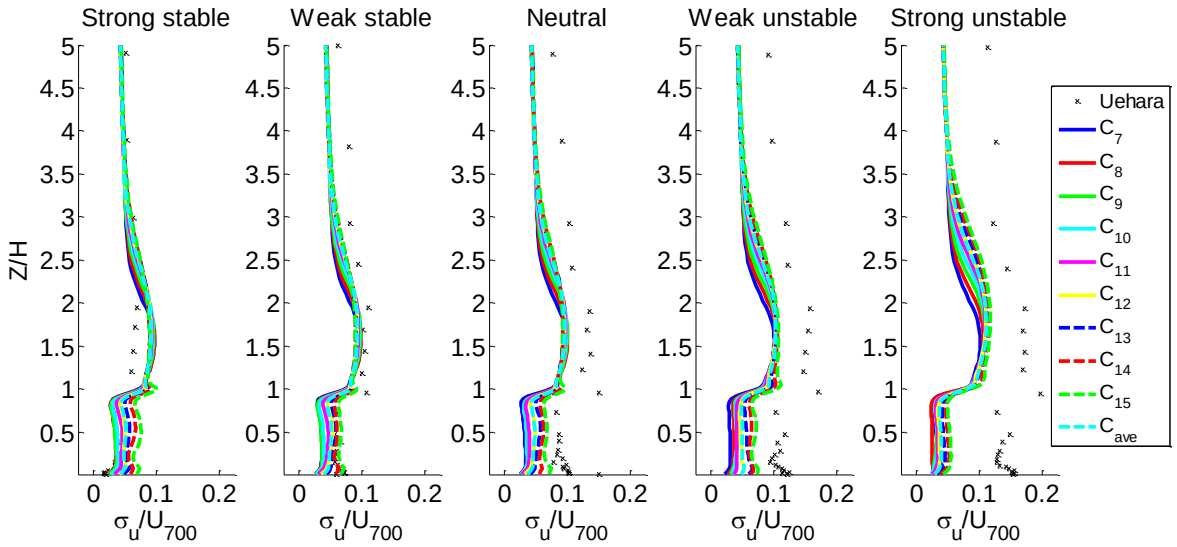

Figure 10.41: T-RANS σ_u-profiles for canyons 1-12

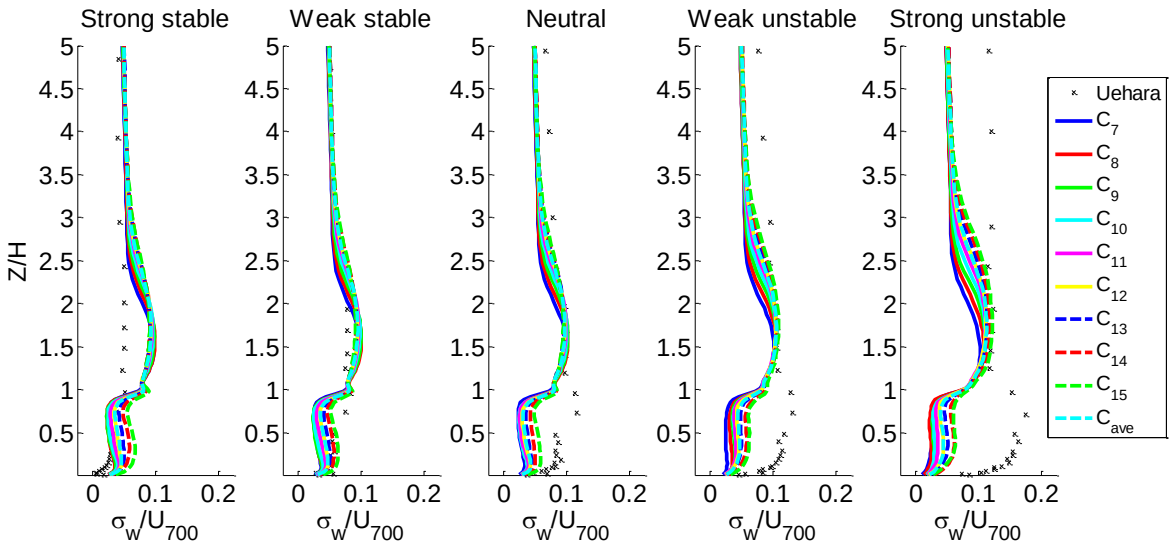

Figure 10.42: T-RANS σ_w-profiles for canyons 1-12

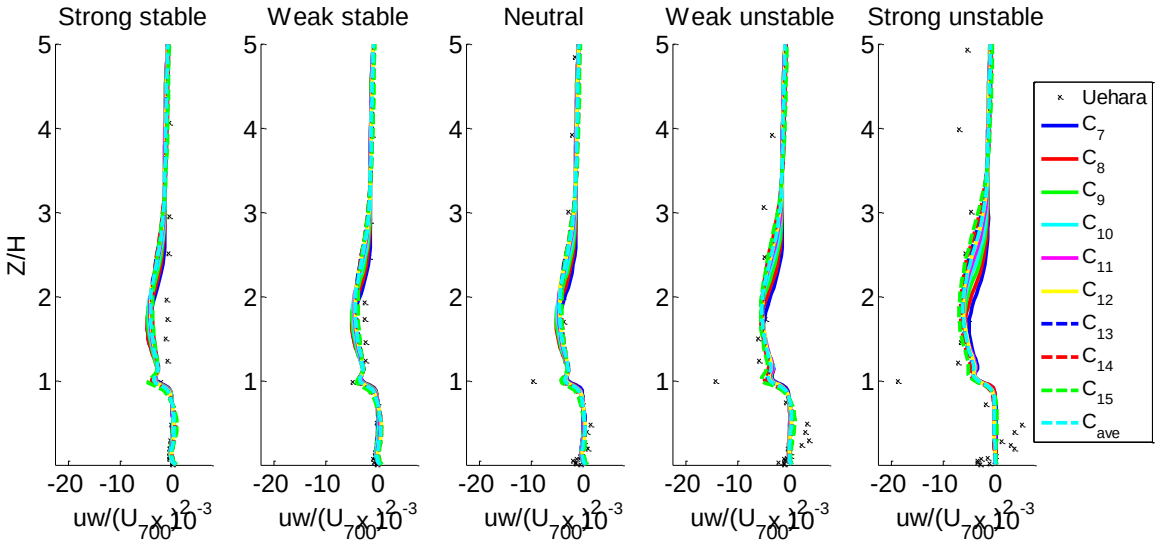

Figure 10.43: T-RANS UW-profiles for canyons 1-12

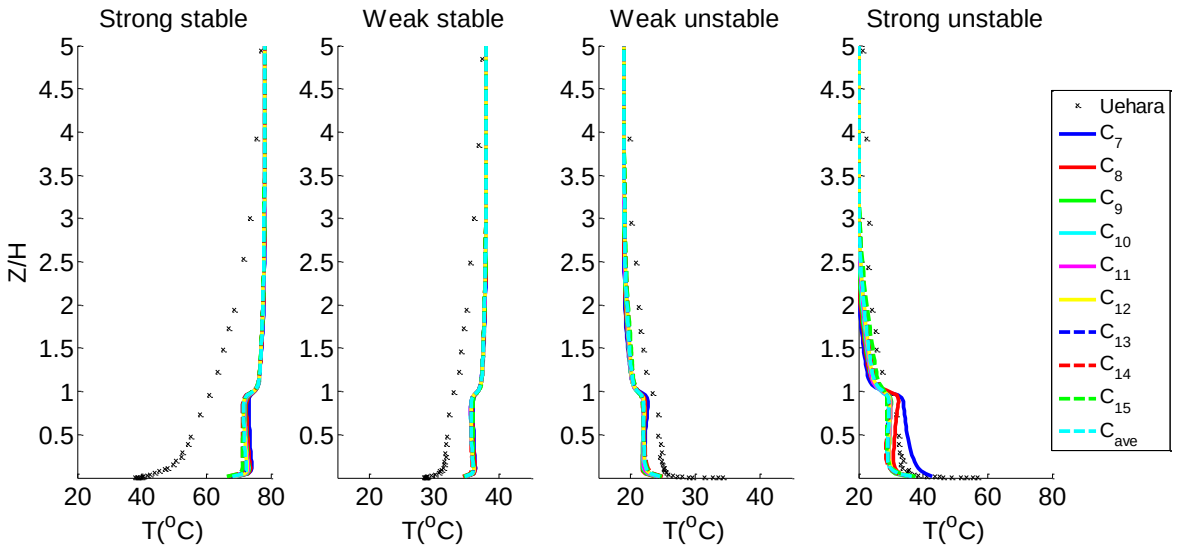

Figure 10.44: T-RANS T-profiles for canyons 1-12

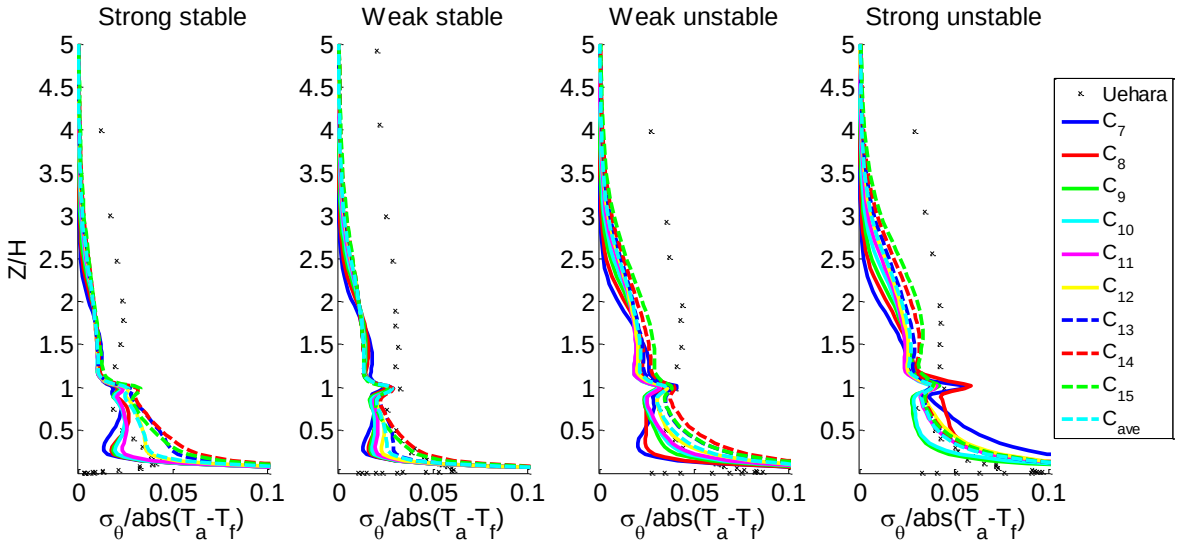

Figure 10.45: T-RANS σ_T-profiles for canyons 1-12

I. ADVECTION MODELLED AND RESOLVED CONTRIBUTION PROFILES

I.1. Standard simulations

I.1.1. Neutral stratification

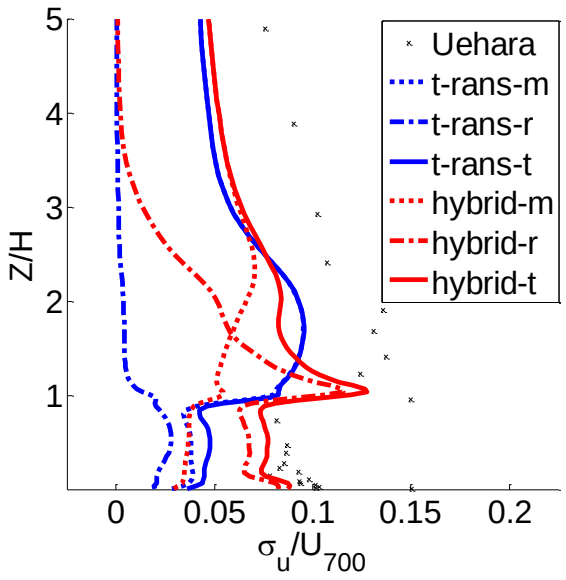

Figure 10.46: Standard case neutral σ_u modelled and resolved profiles

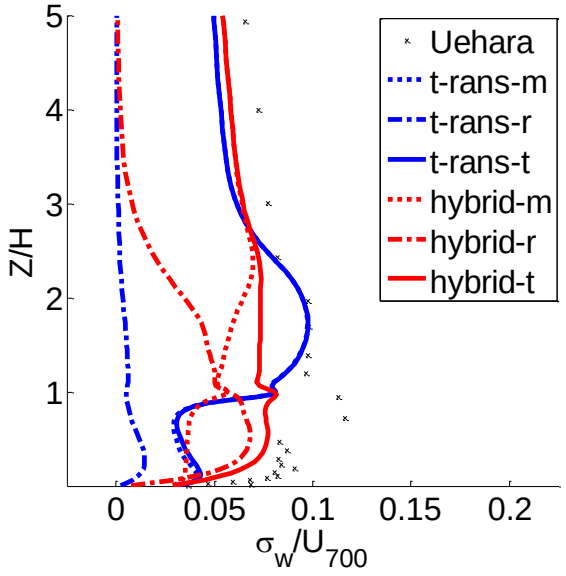

Figure 10.47: Standard case neutral σ_w modelled and resolved profiles

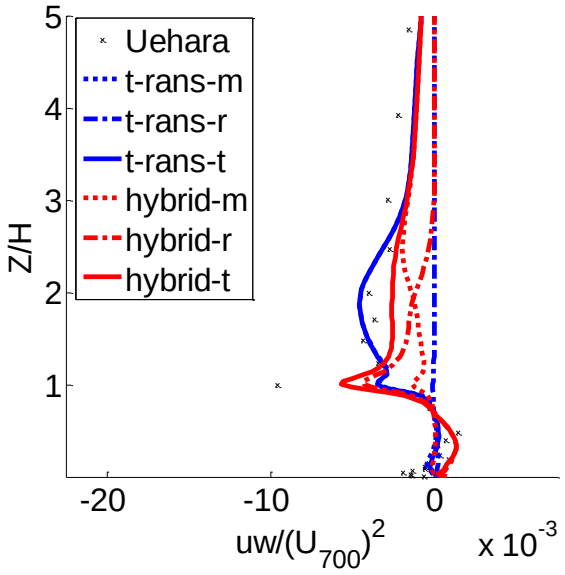

Figure 10.48: Standard case neutral uw modelled and resolved profiles

I.1.2. Stable stratification

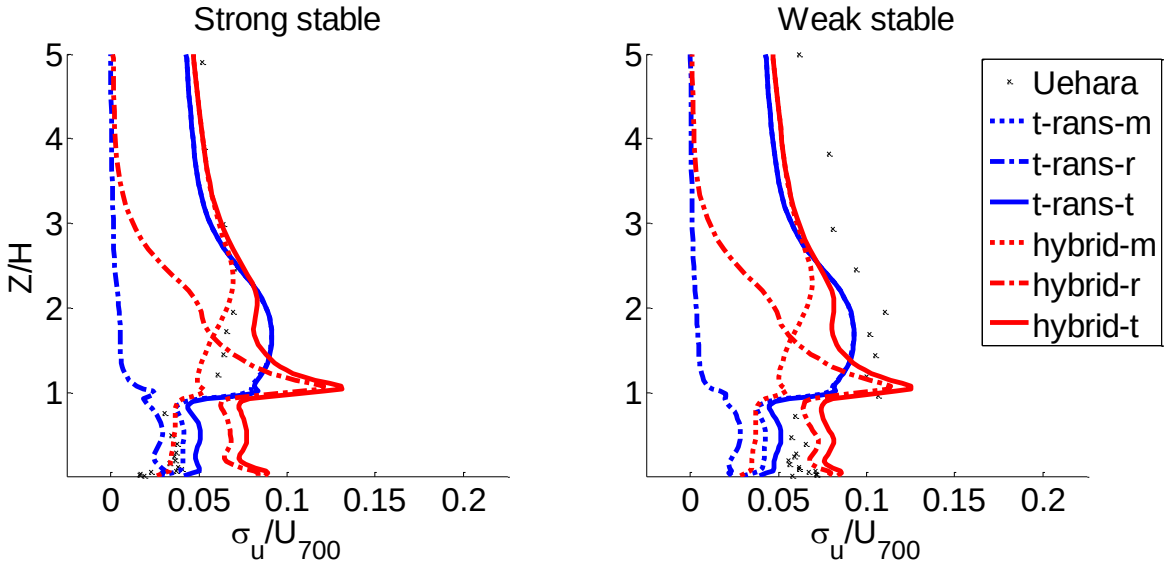

Figure 10.49: Standard case stable stratification σ_u modelled and resolved profiles

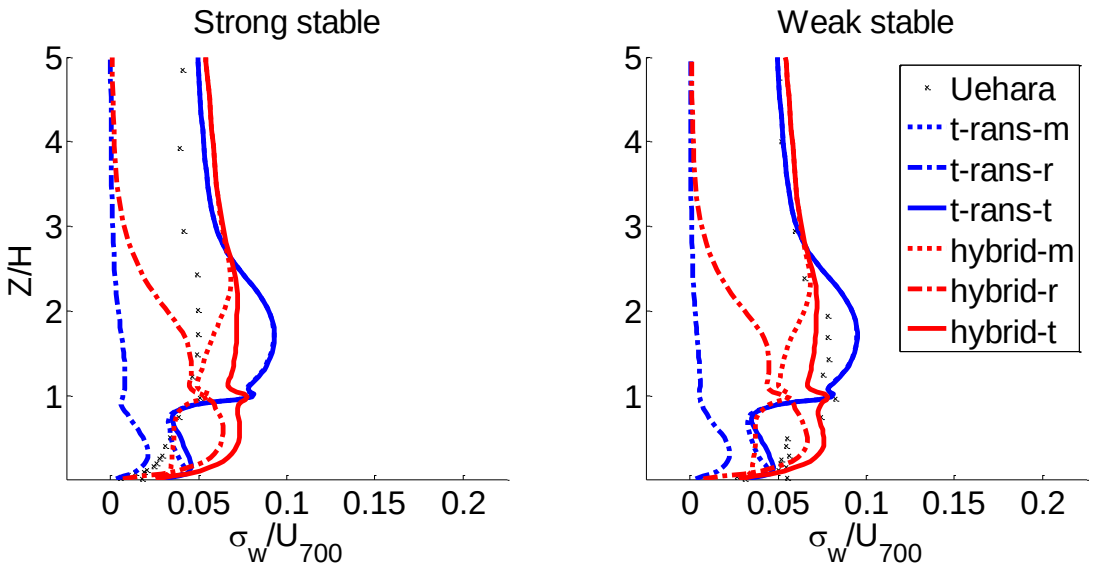

Figure 10.50: Standard case stable stratification σ_w modelled and resolved profiles

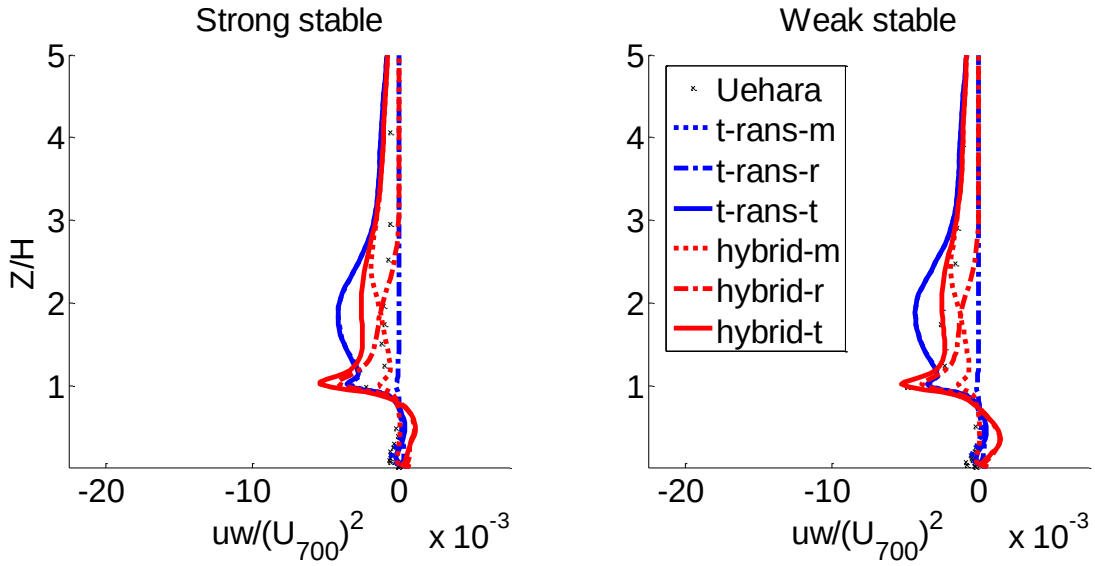

Figure 10.51: Standard case stable stratification uw modelled and resolved profiles

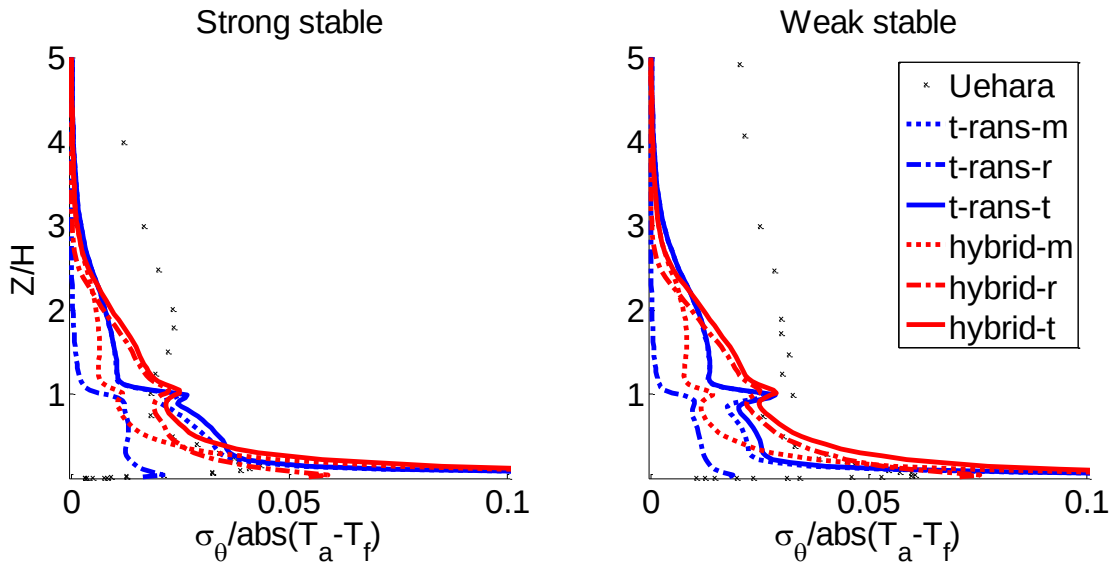

Figure 10.52: Standard case stable stratification σ_T modelled and resolved profiles

I.1.3. Unstable stratification

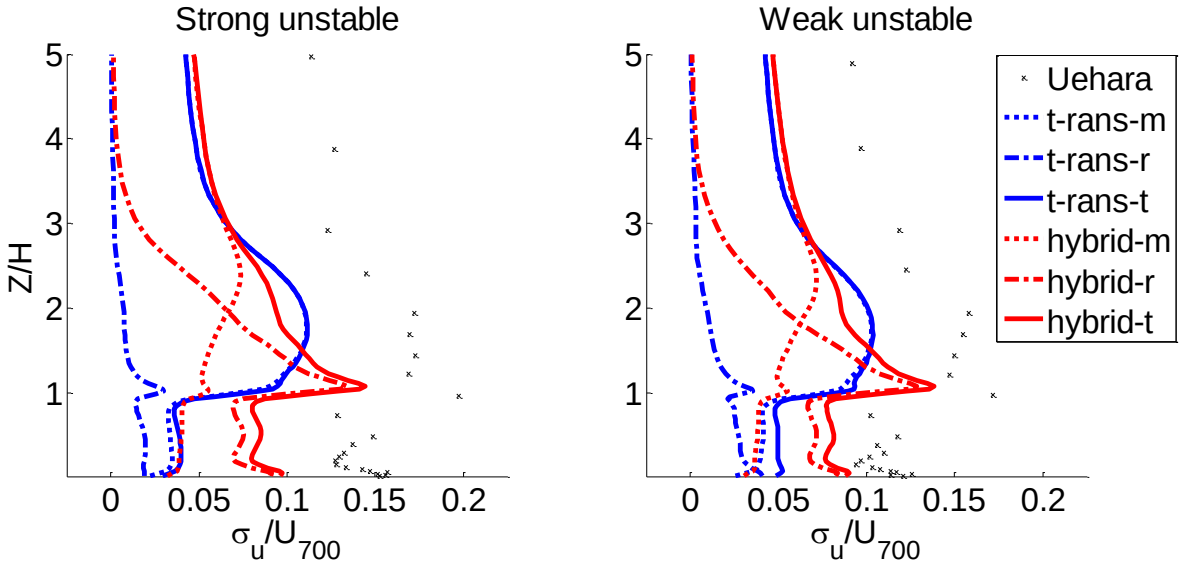

Figure 10.53: Standard case unstable stratification σ_u modelled and resolved profiles

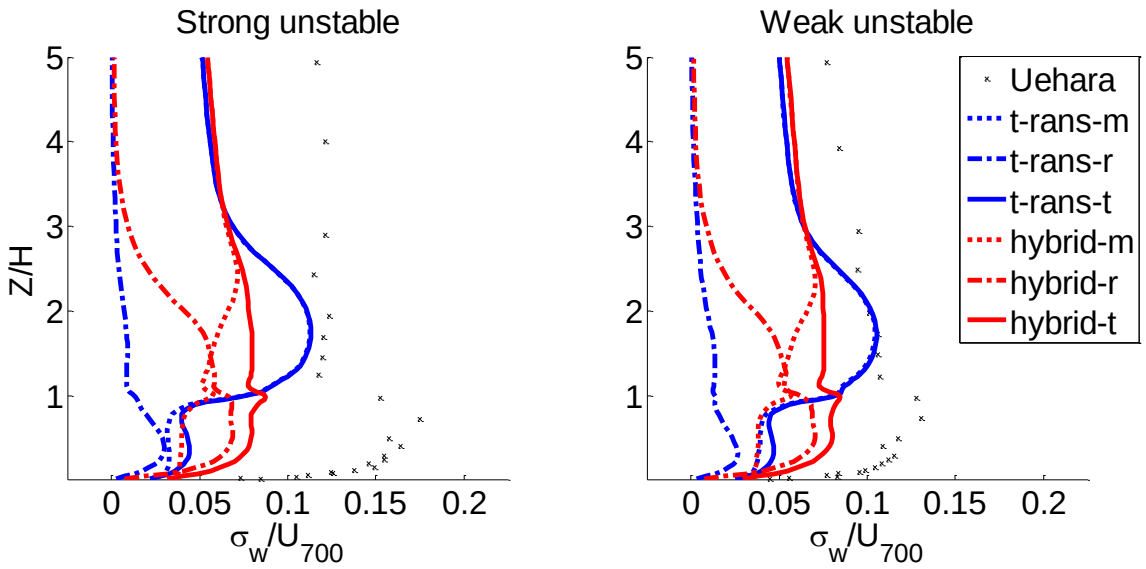

Figure 10.54: Standard case unstable stratification σ_w modelled and resolved profiles

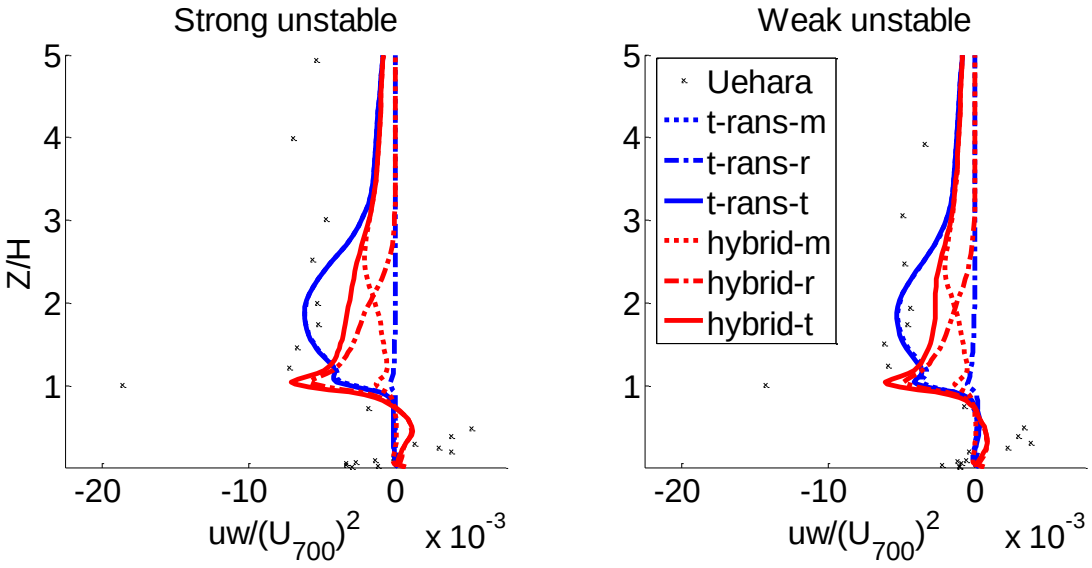

Figure 10.55: Standard case unstable stratification uw modelled and resolved profiles

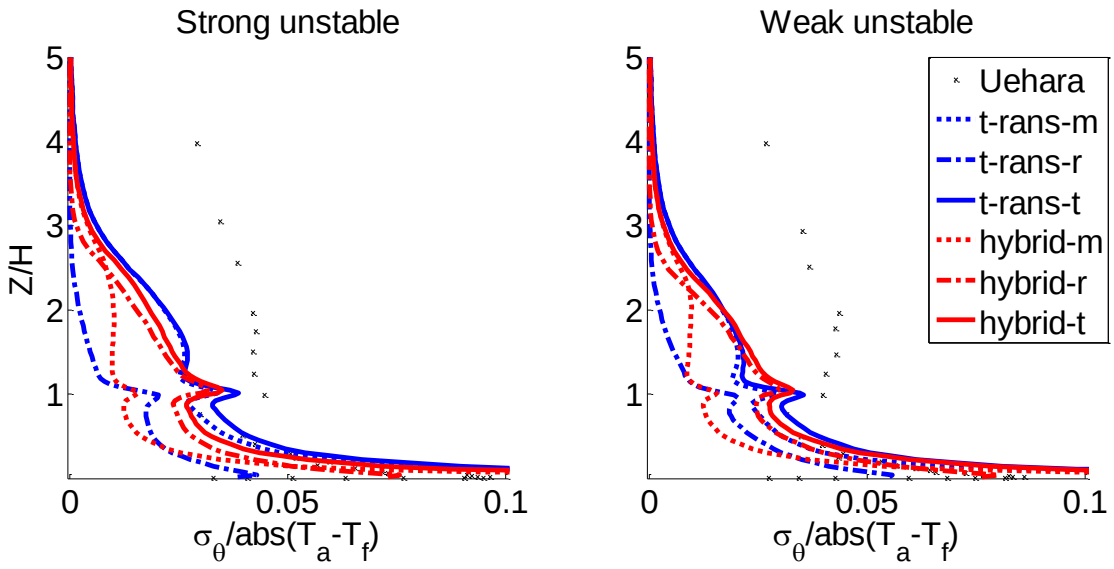

Figure 10.56: Standard case unstable stratification σ_T modelled and resolved profiles

I.2. GGDH simulations

I.2.1. Stable stratification

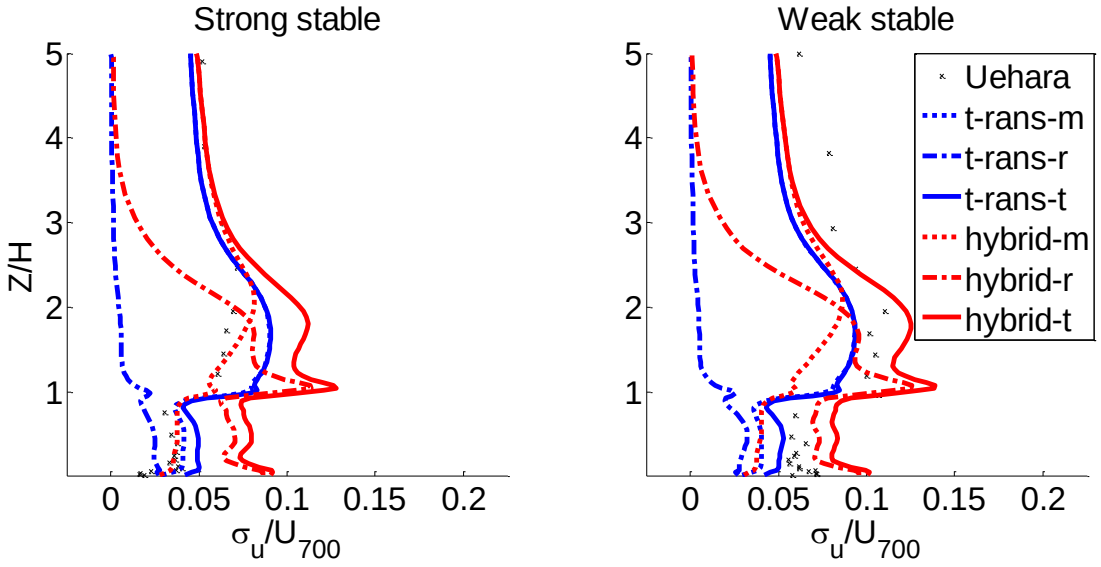

Figure 10.57: GGDH simulation stable stratification σ_u modelled and resolved profiles

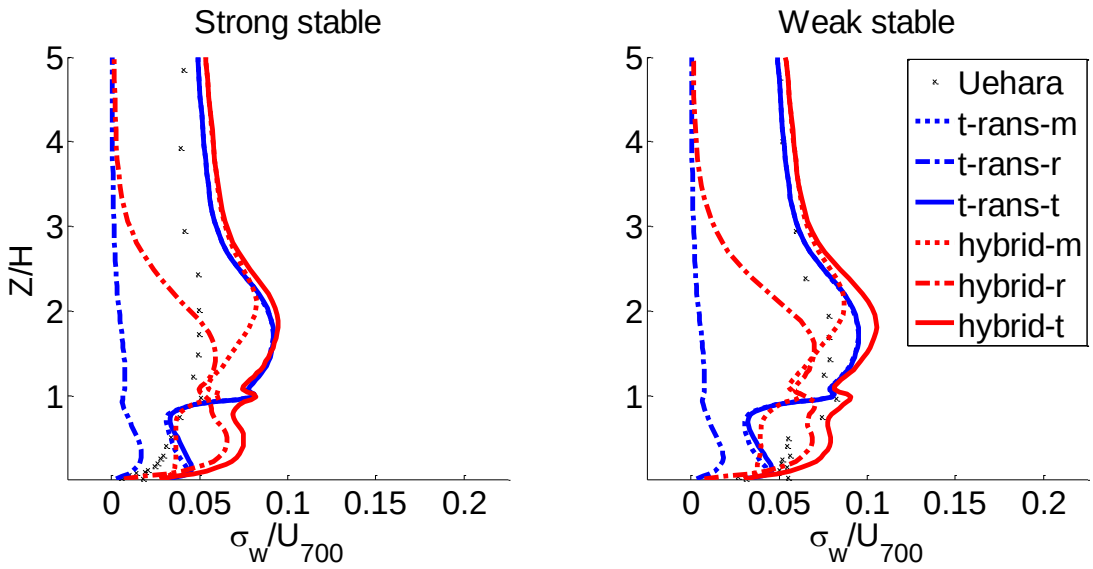

Figure 10.58: GGDH simulation stable stratification σ_w modelled and resolved profiles

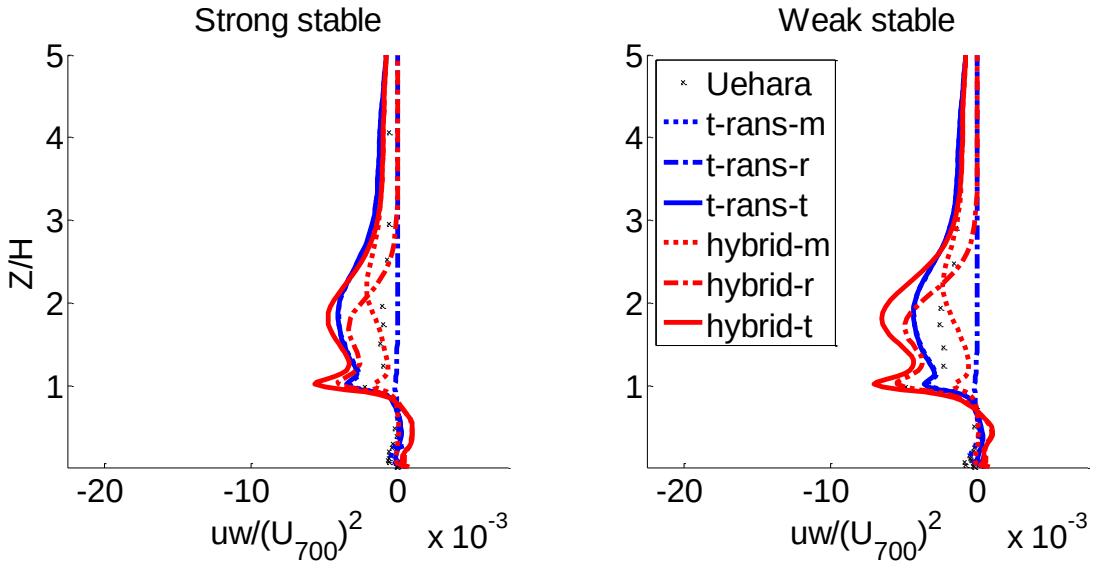

Figure 10.59: GGDH simulation stable stratification uw modelled and resolved profiles

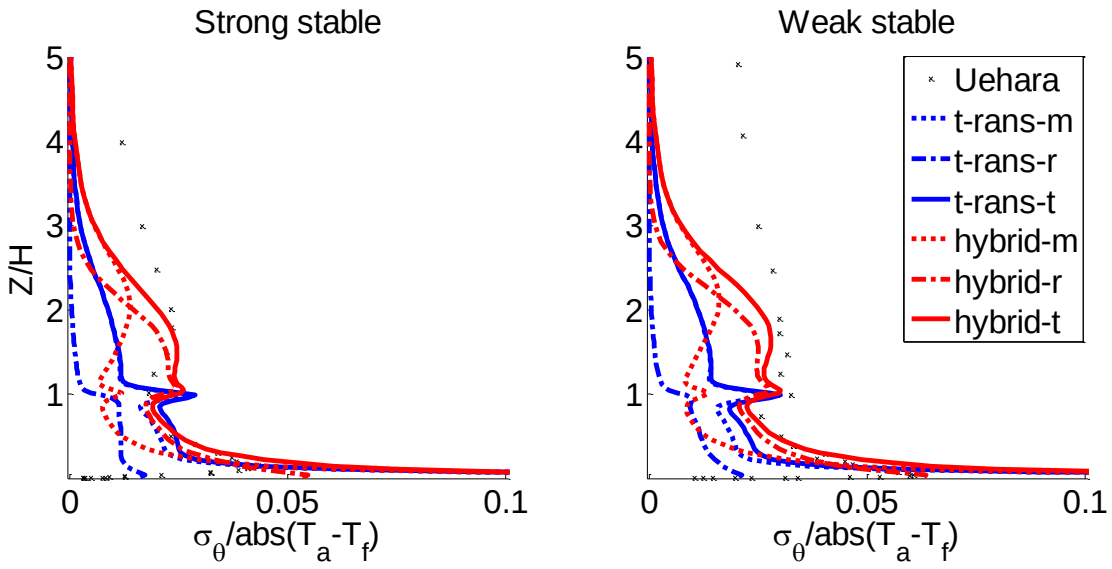

Figure 10.60: GGDH simulation stable stratification σ_T modelled and resolved profiles

I.2.2. Unstable stratification

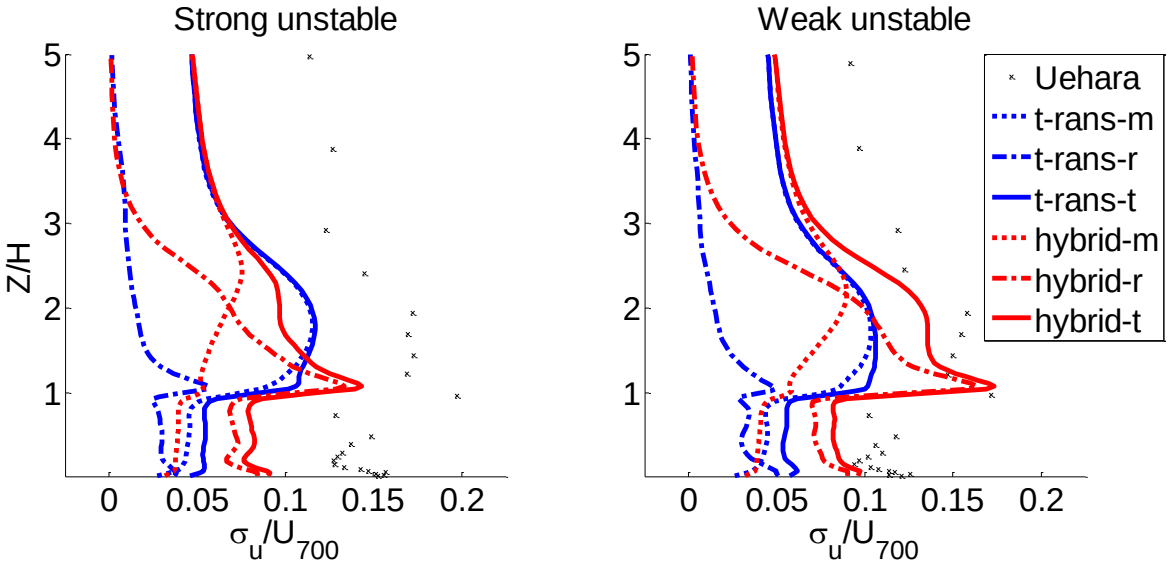

Figure 10.61: GGDH simulation unstable stratification σ_u modelled and resolved profiles

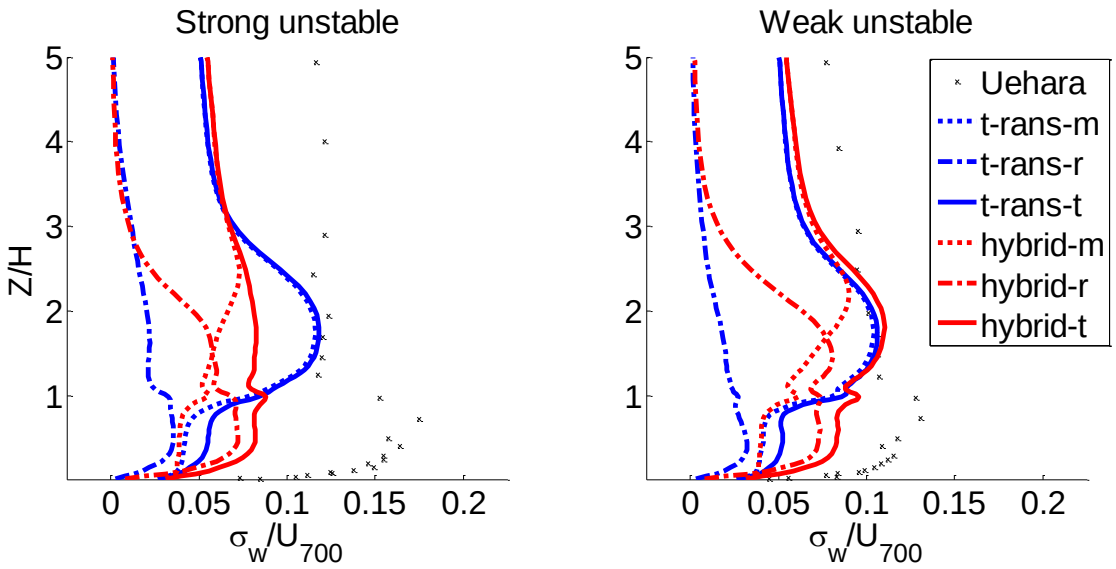

Figure 10.62: GGDH simulation unstable stratification σ_w modelled and resolved profiles

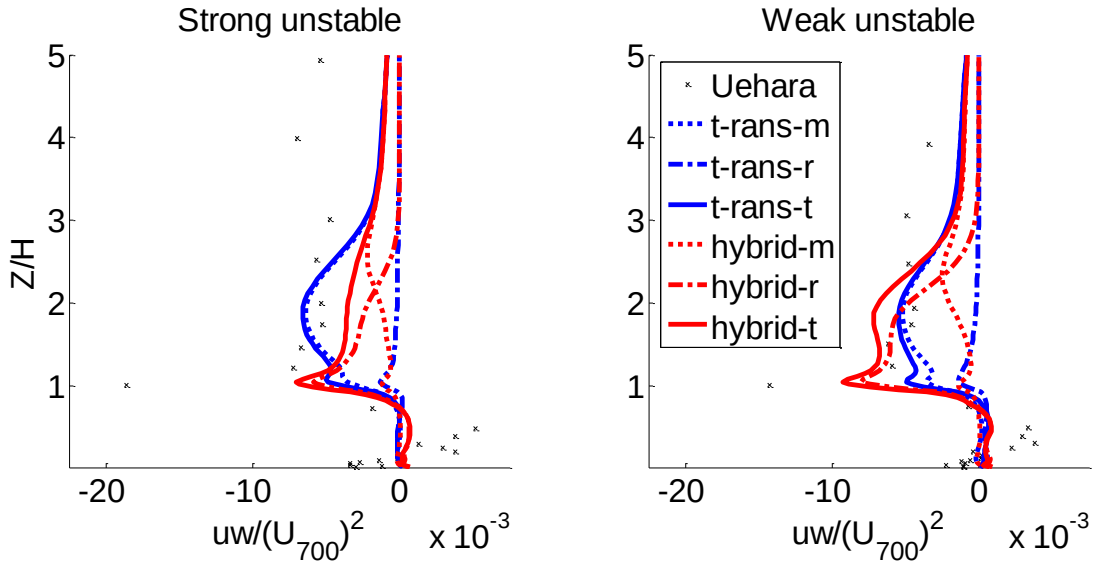

Figure 10.63: GGDH simulation unstable stratification uw modelled and resolved profiles

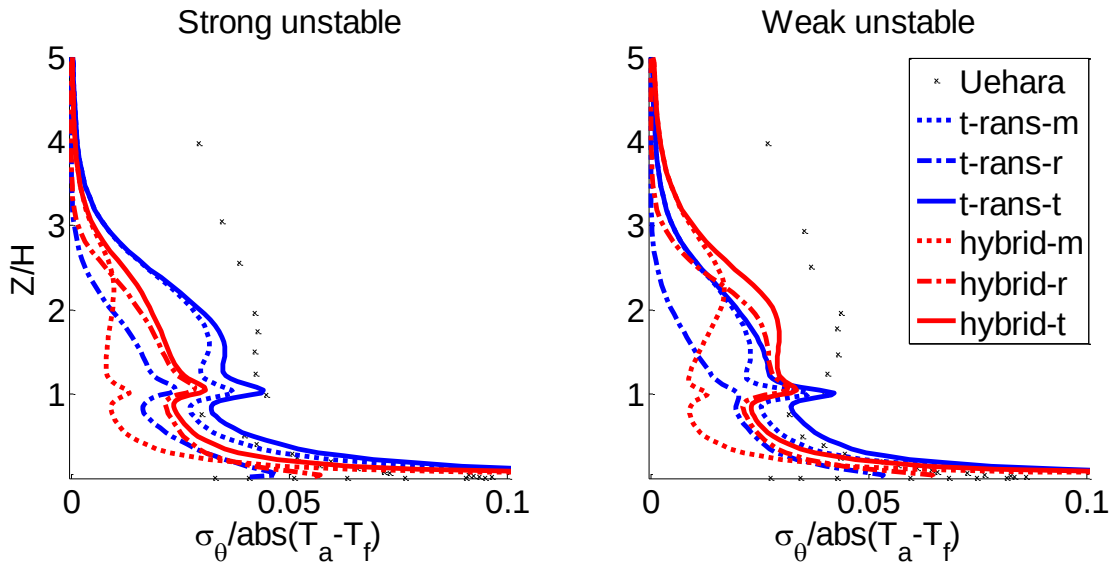

Figure 10.64: GGDH simulation unstable stratification σ_T modelled and resolved profiles

J. TIMESTEP INDEPENDENCE PLOTS

J.1. T-RANS

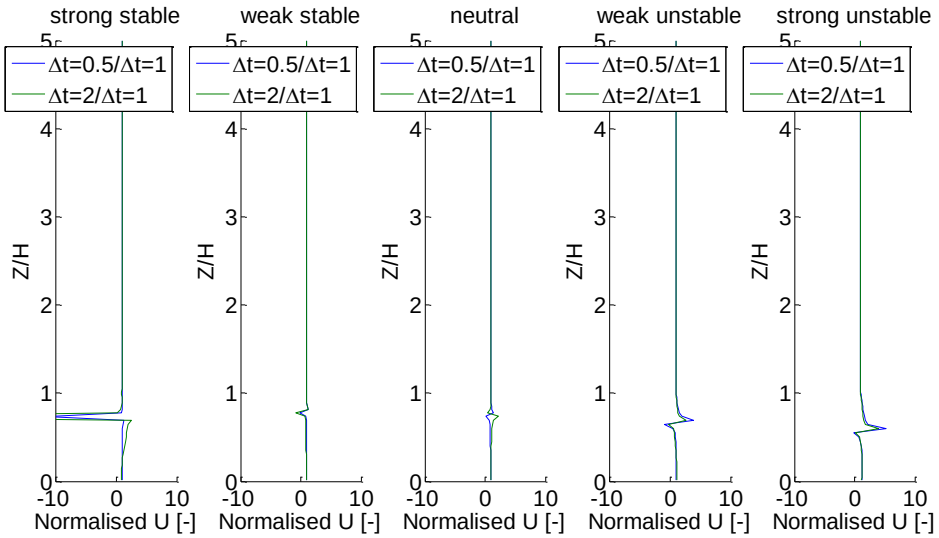

Figure 10.65: T-RANS timestep independence normalised U

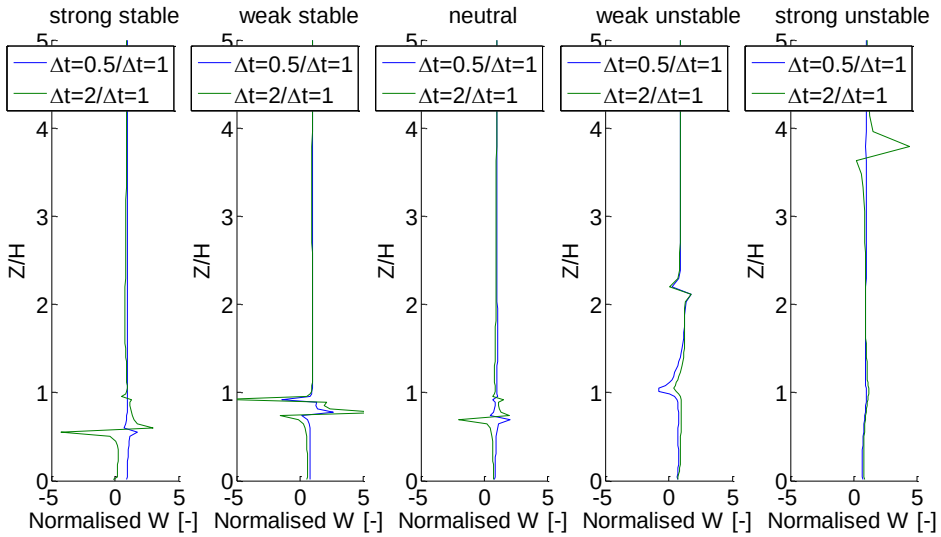

Figure 10.66: T-RANS timestep independence normalised W

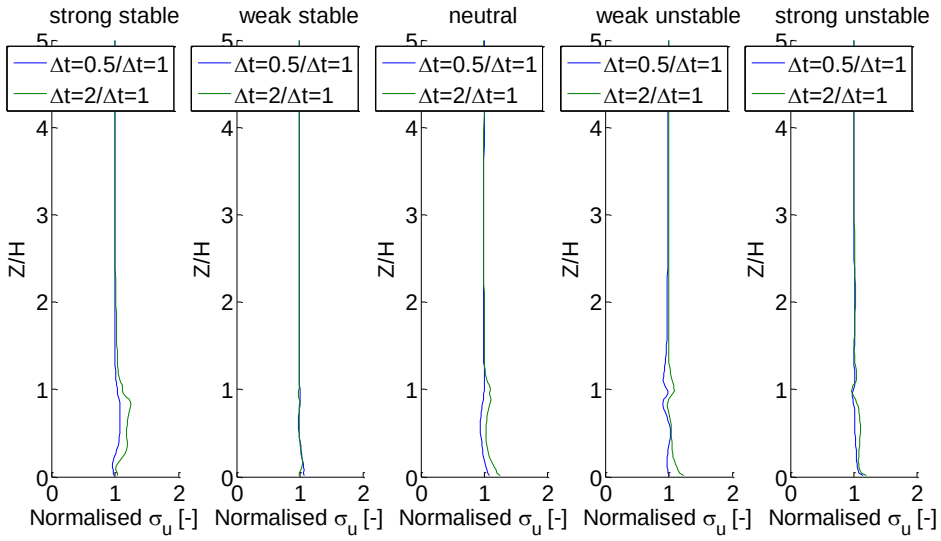

Figure 10.67: T-RANS timestep independence normalised σ_u

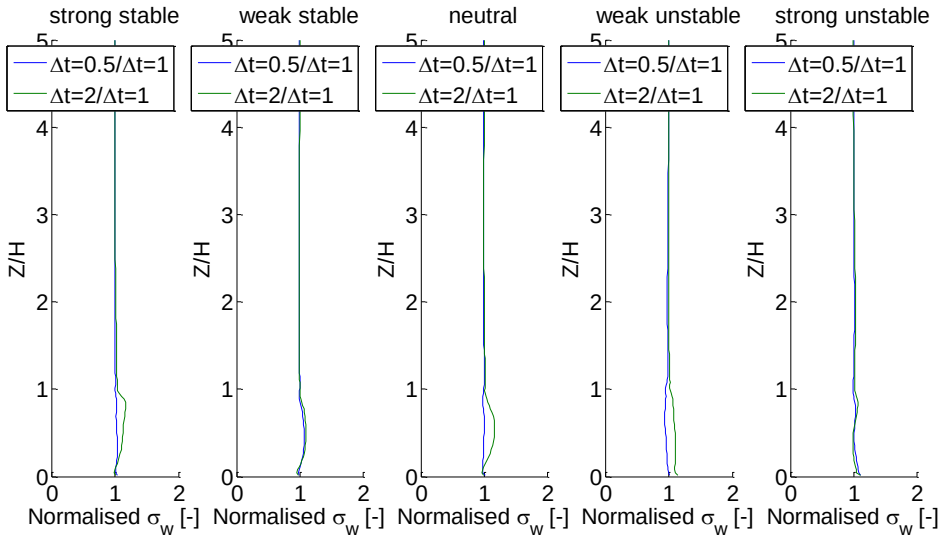

Figure 10.68: T-RANS timestep independence normalised σ_w

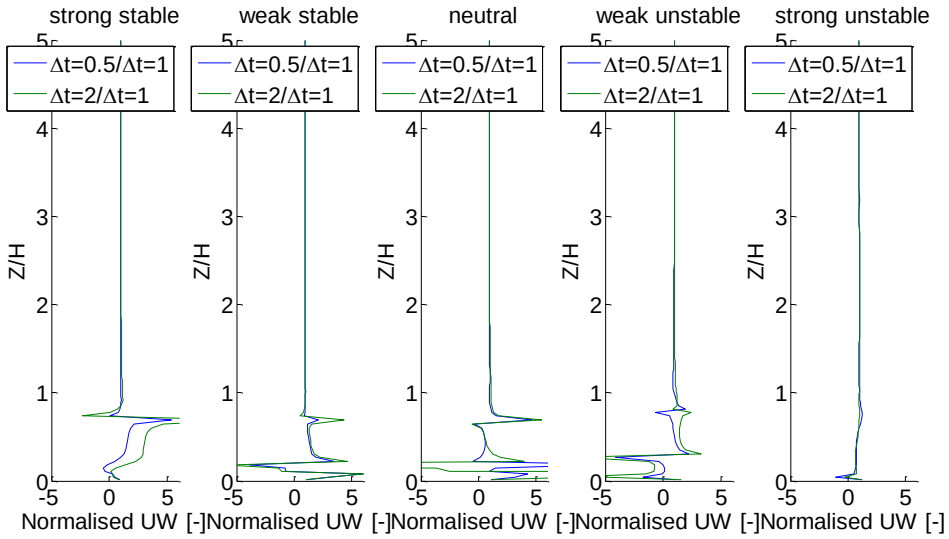

Figure 10.69: T-RANS timestep independence normalised uw

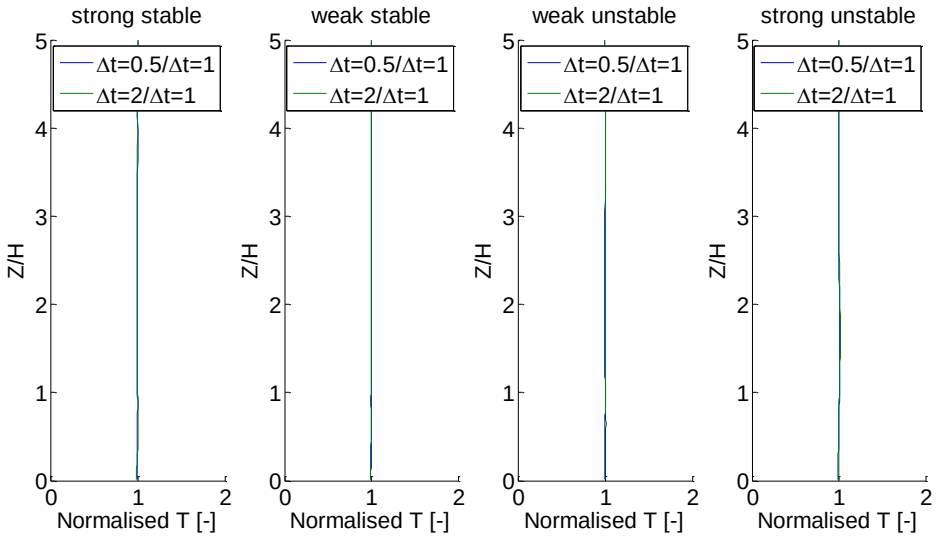

Figure 10.70: T-RANS timestep independence normalised T

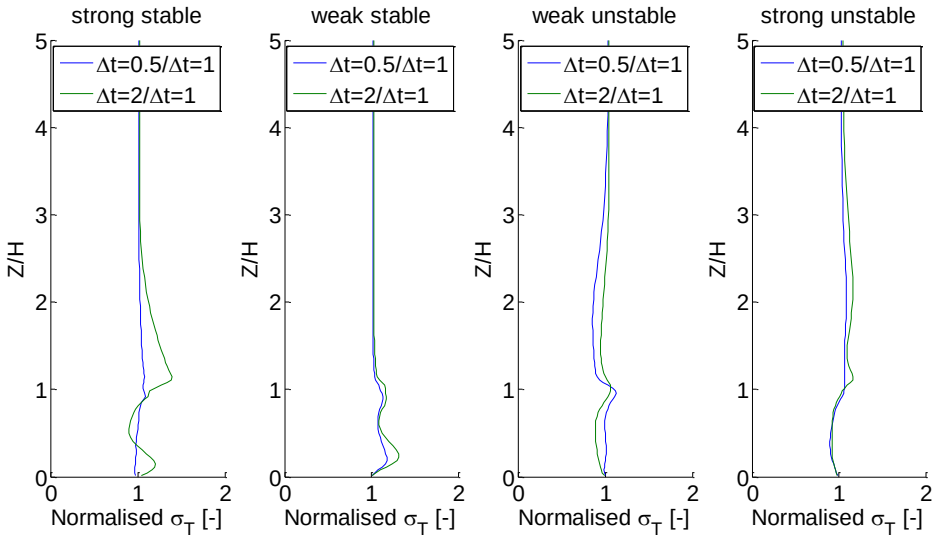

Figure 10.71: T-RANS timestep independence normalised σ_T

J.2. HYBRID LES/T-RANS

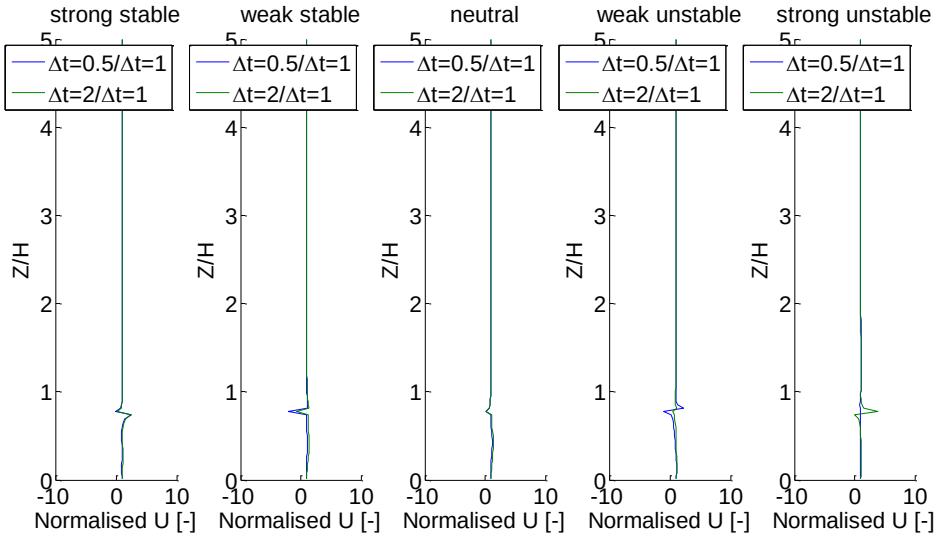

Figure 10.72: Hybrid timestep independence normalised U

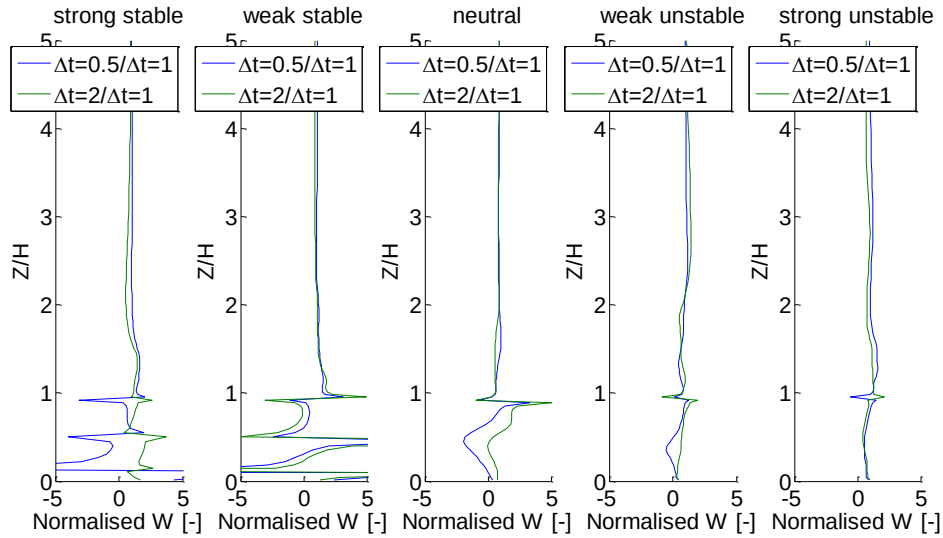

Figure 10.73: Hybrid timestep independence normalised W

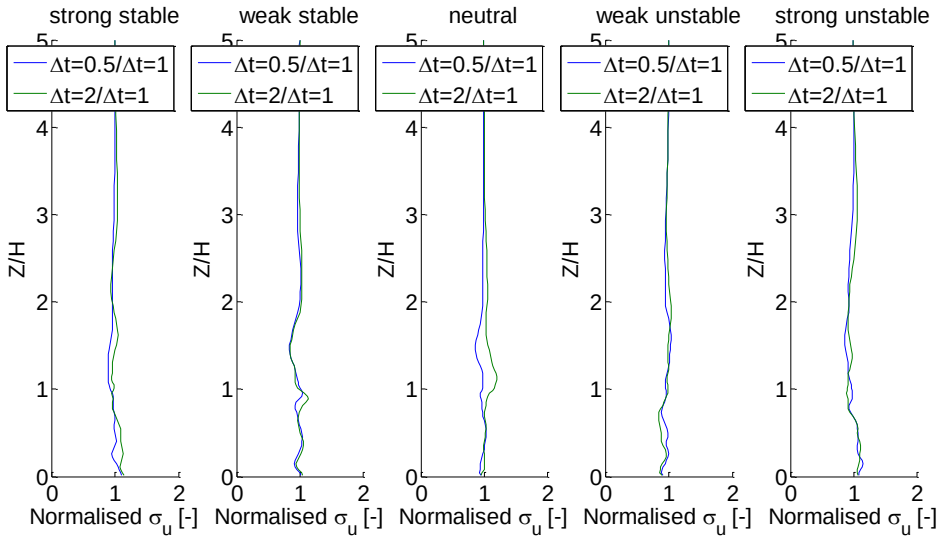

Figure 10.74: Hybrid timestep independence normalised σ_u

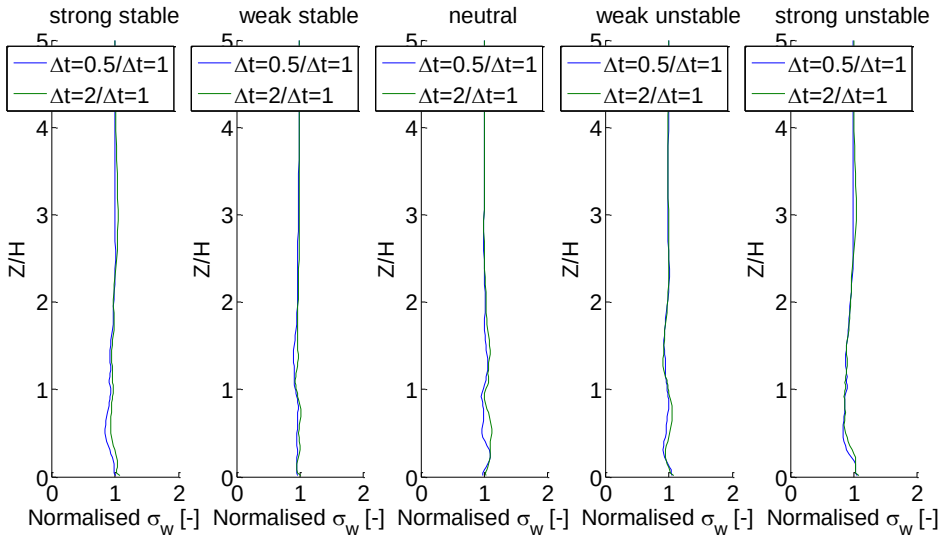

Figure 10.75: Hybrid timestep independence normalised σ_w

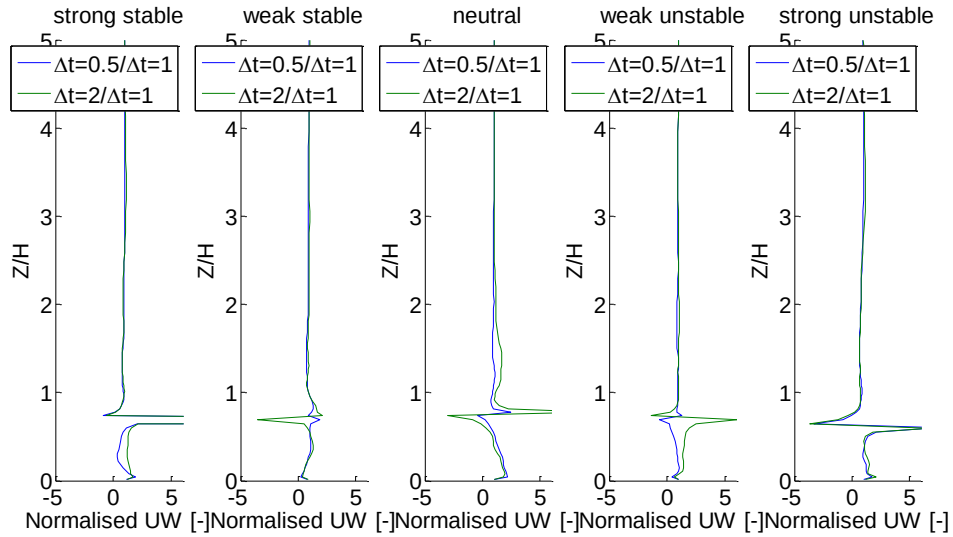

Figure 10.76: Hybrid timestep independence normalised uw

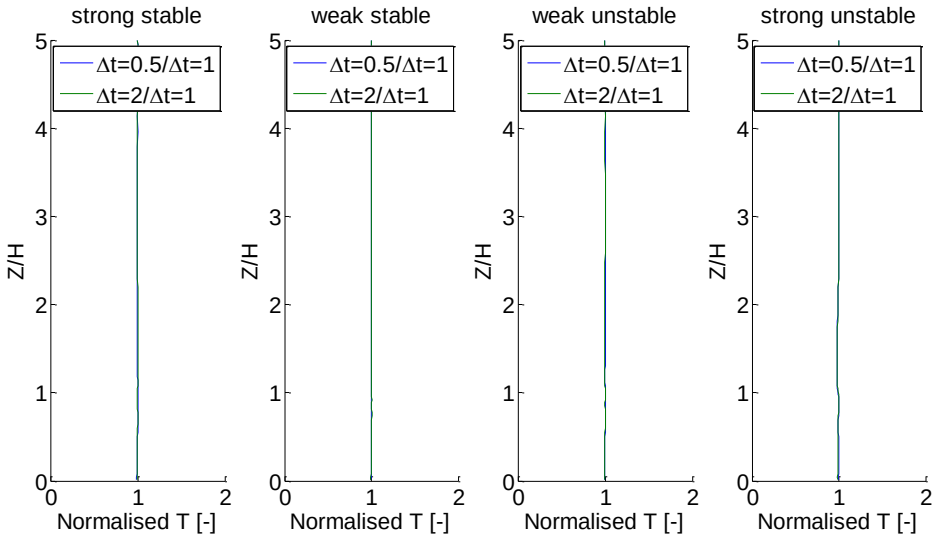

Figure 10.77: Hybrid timestep independence normalised T

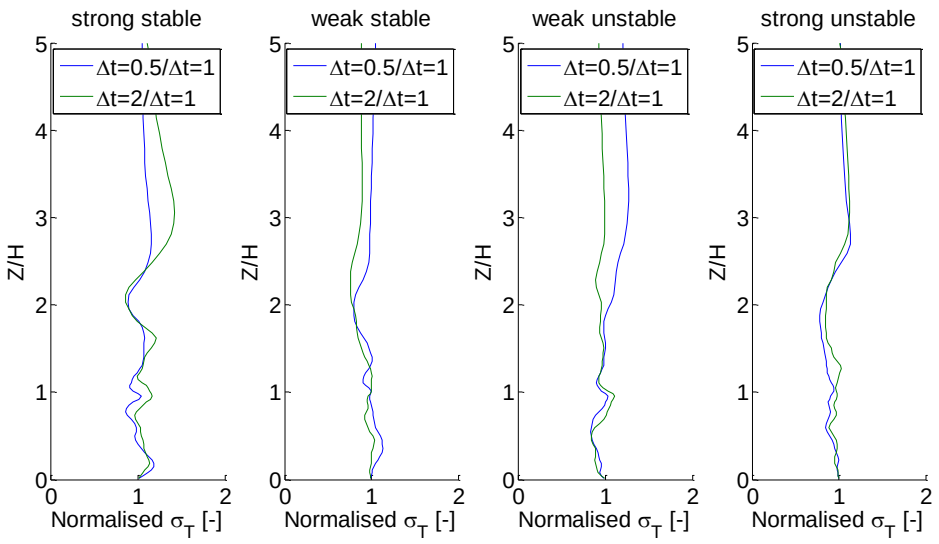

Figure 10.78: Hybrid timestep independence normalised σ_T

K. MODIFIED INLET VELOCITY INVESTIGATIONS

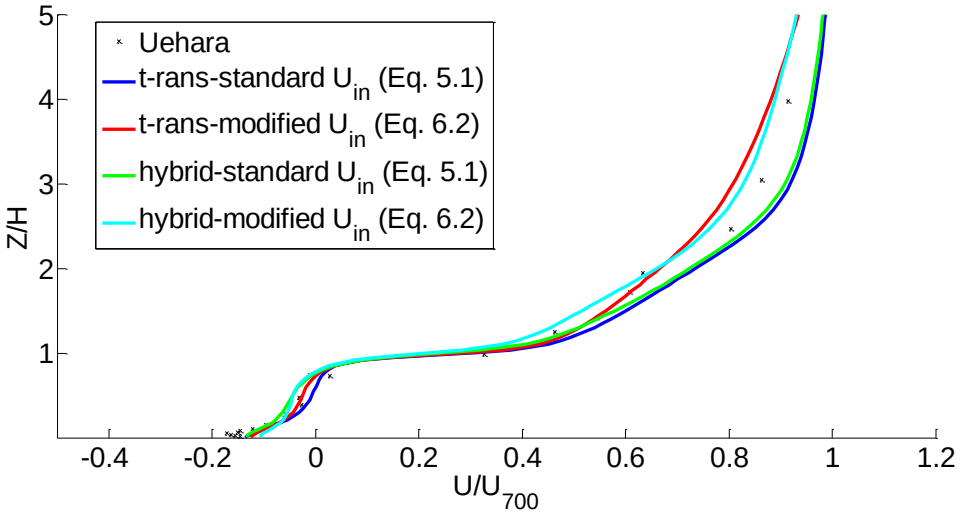

Figure 10.79: U-profile for standard and modified U_{in}

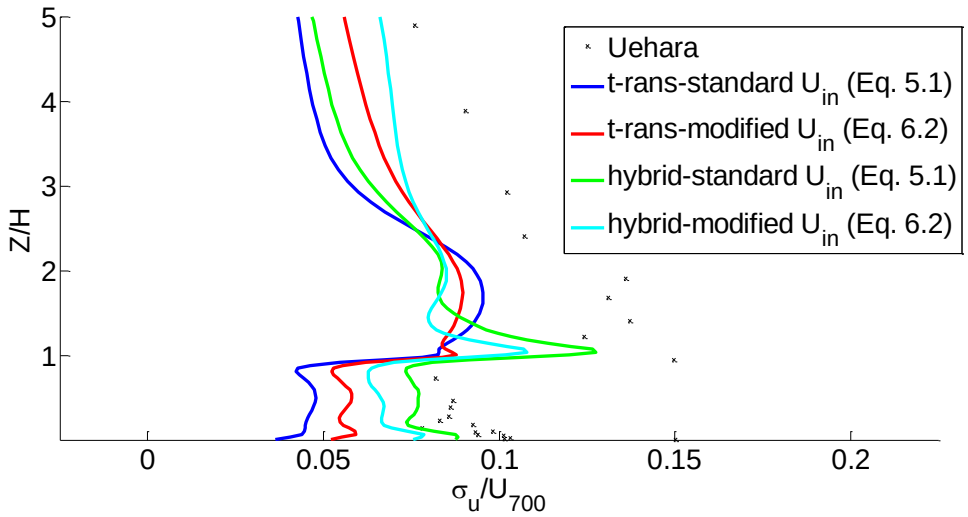

Figure 10.80: σ_u-profile for standard and modified U_{in}

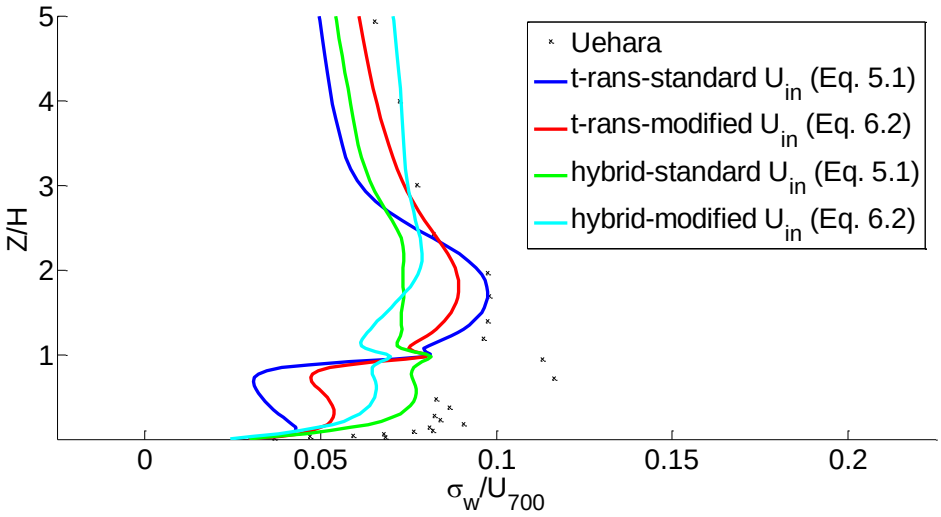

Figure 10.81: σ_w-profile for standard and modified U_{in}

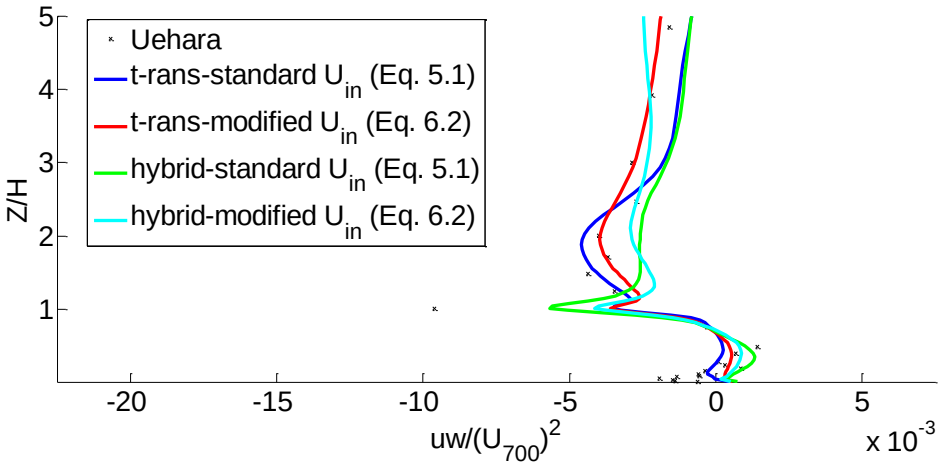

Figure 10.82: uw-profile for standard and modified U_{in}

L. INLET TURBULENT KINETIC ENERGY DISSIPATION INVESTIGATIONS

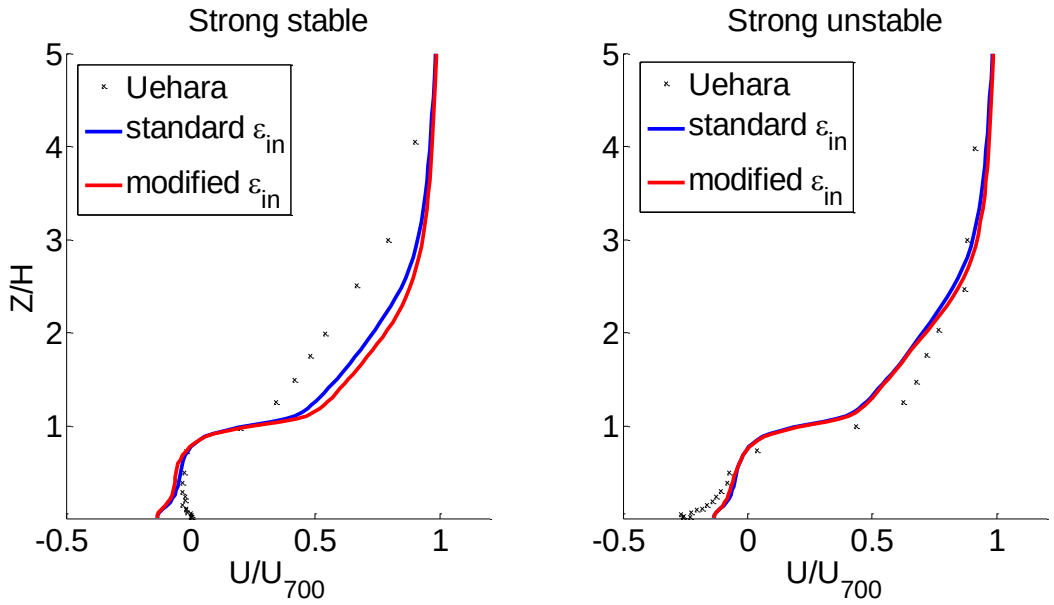

Figure 10.83: U-profile for hybrid LES/T-RANS standard and modified ε_{in}

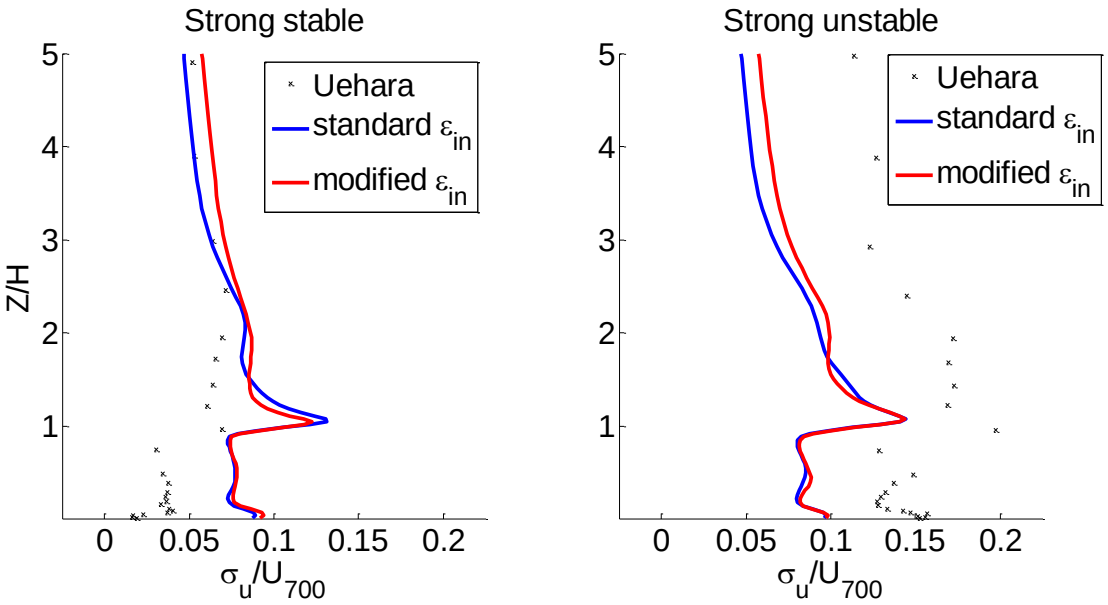

Figure 10.84: σ_u-profile for hybrid LES/T-RANS standard and modified ε_{in}

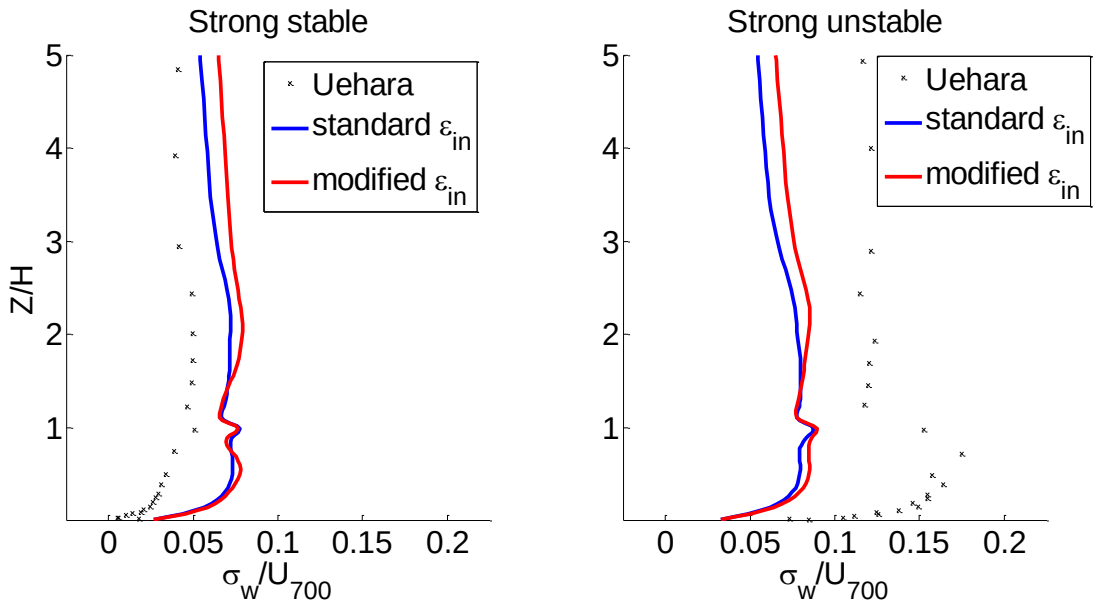

Figure 10.85: σ_w-profile for hybrid LES/T-RANS standard and modified ε_{in}

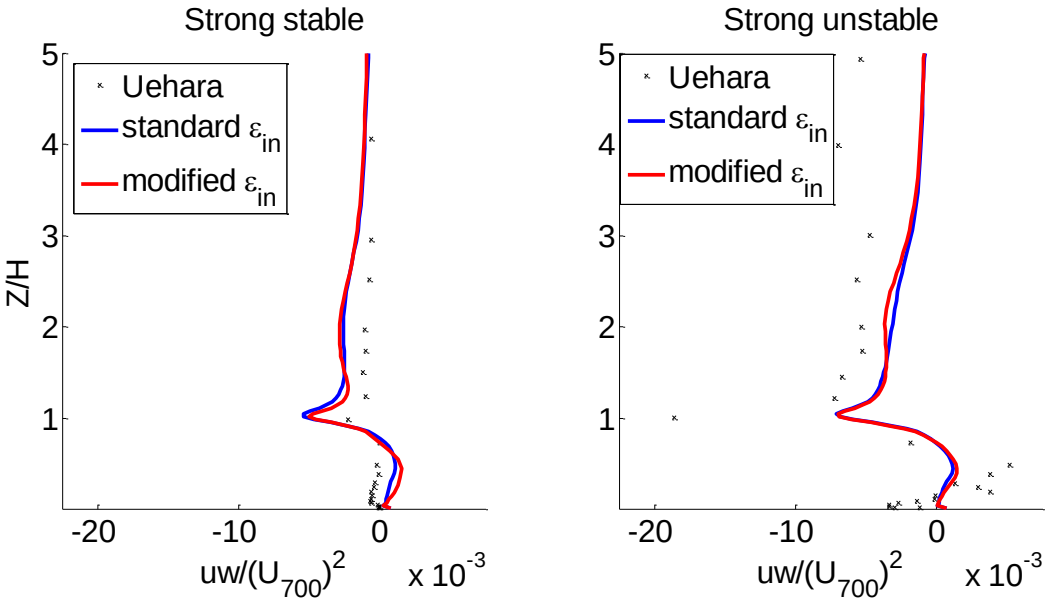

Figure 10.86: uw-profile for hybrid LES/T-RANS standard and modified ε_{in}

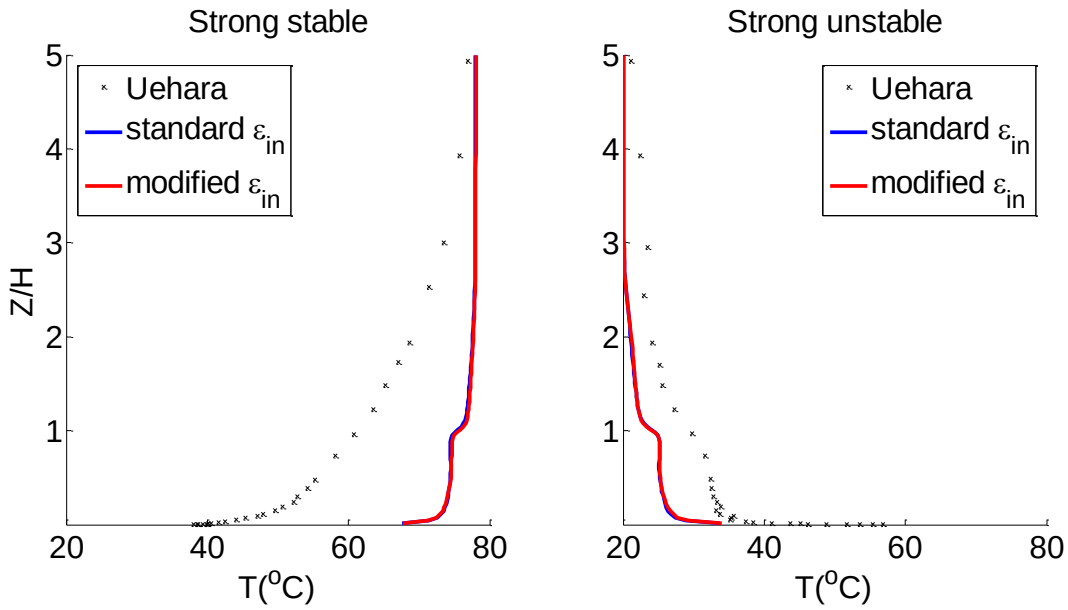

Figure 10.87: T-profile for hybrid LES/T-RANS standard and modified ε_{in}

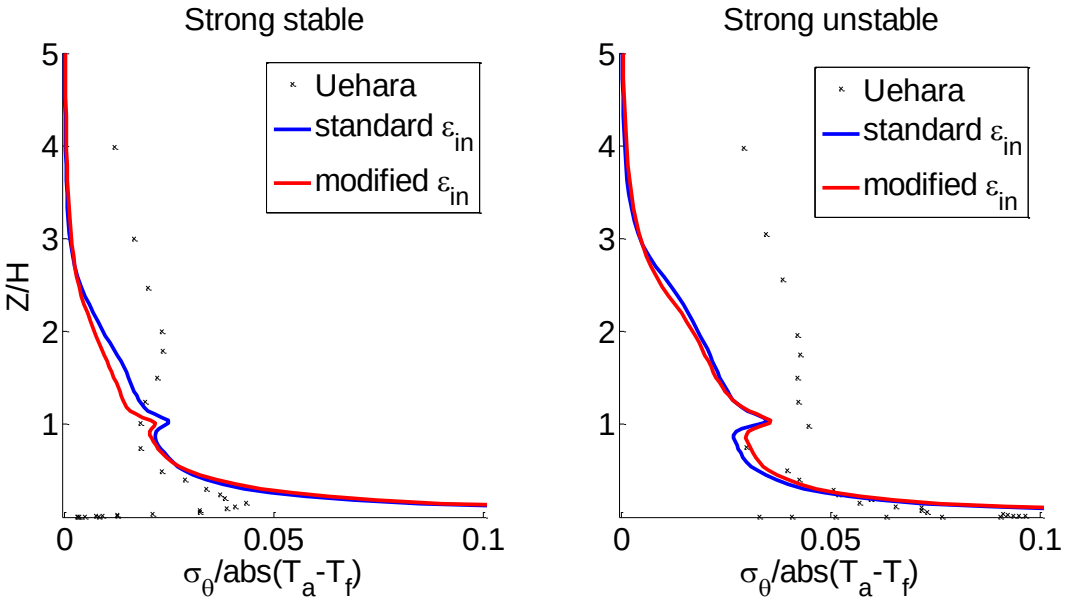

Figure 10.88: σ_T-profile for hybrid LES/T-RANS standard and modified ε_{in}

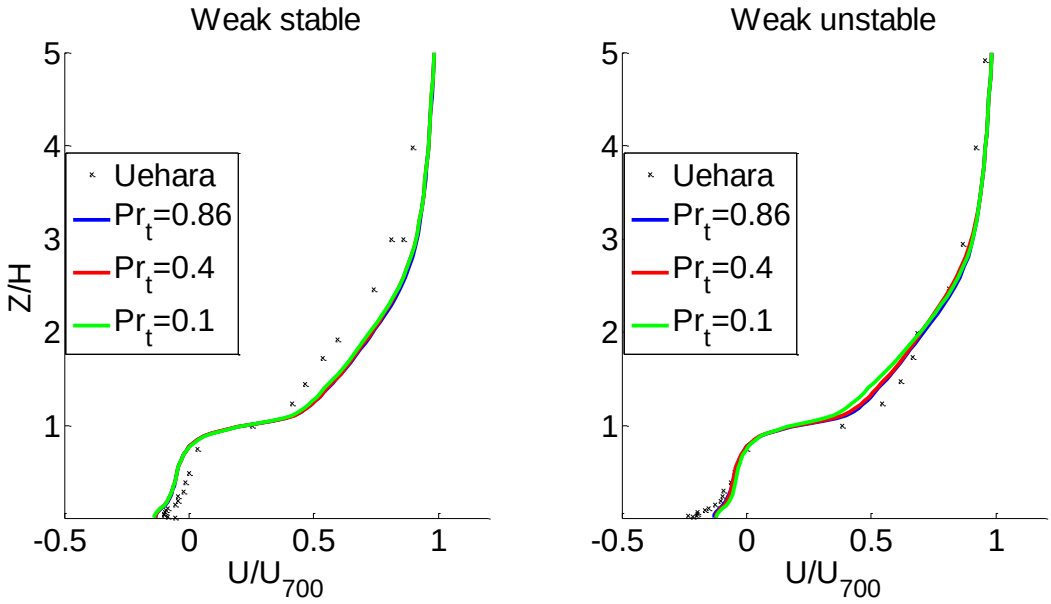

Figure 10.89: Hybrid U-profiles for investigated turbulent Prandtl numbers

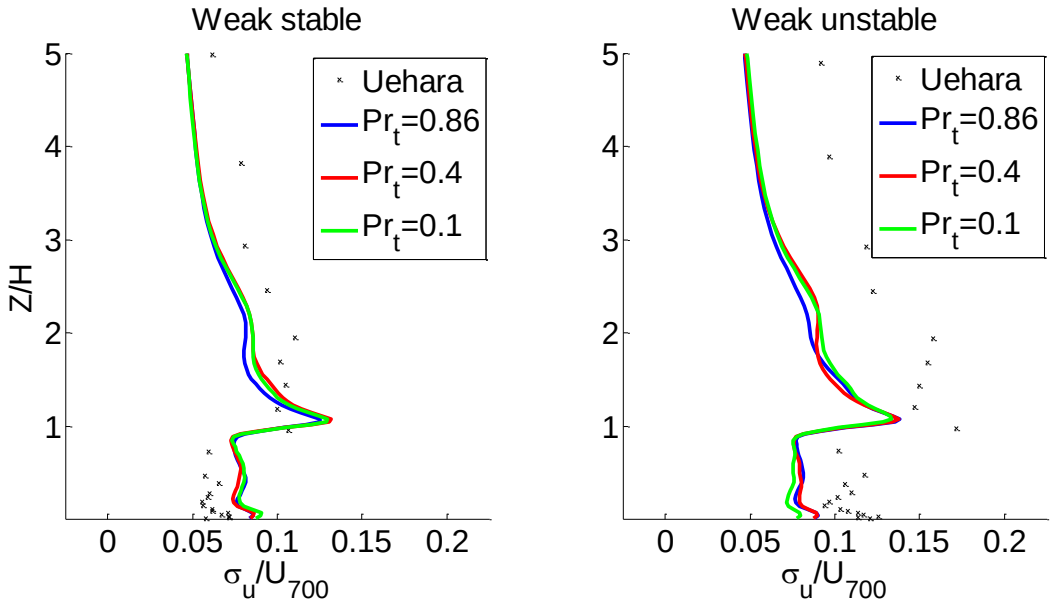

Figure 10.90: Hybrid σ_u-profiles for investigated turbulent Prandtl numbers

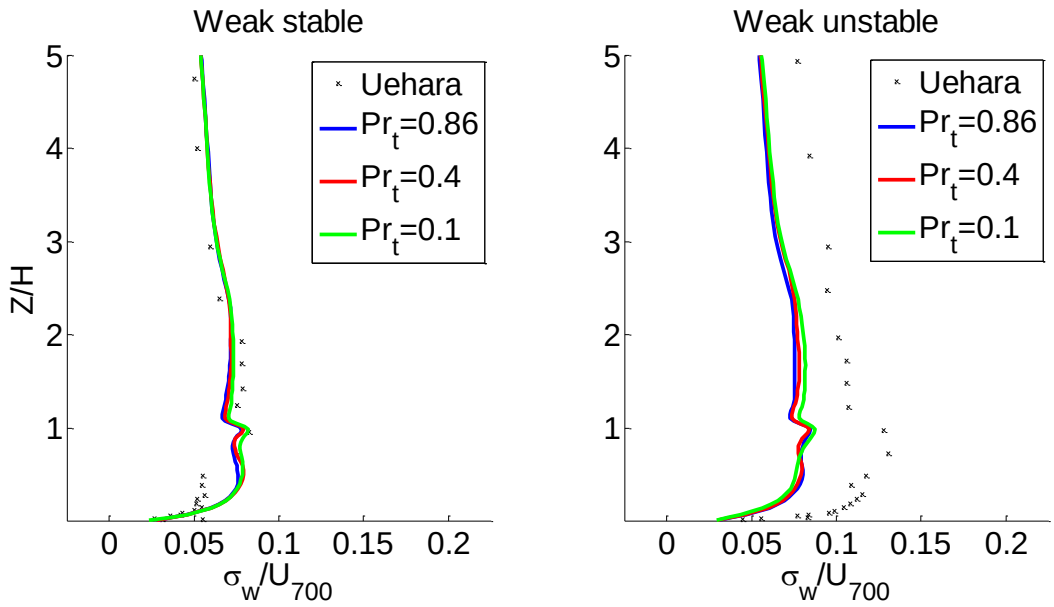

Figure 10.91: Hybrid σ_w-profiles for investigated turbulent Prandtl numbers

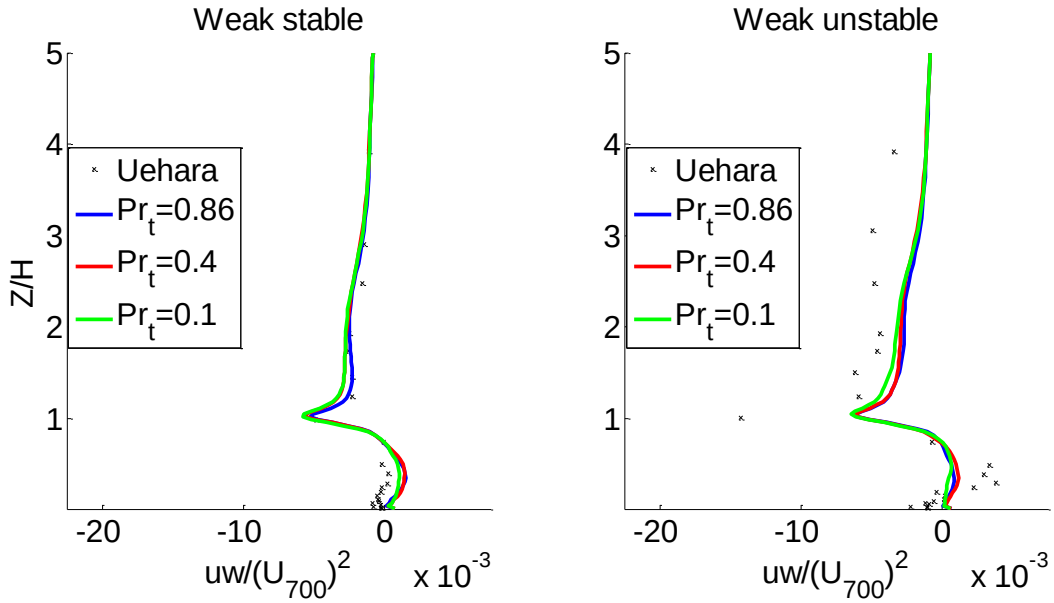

Figure 10.92: Hybrid UW-profiles for investigated turbulent Prandtl numbers

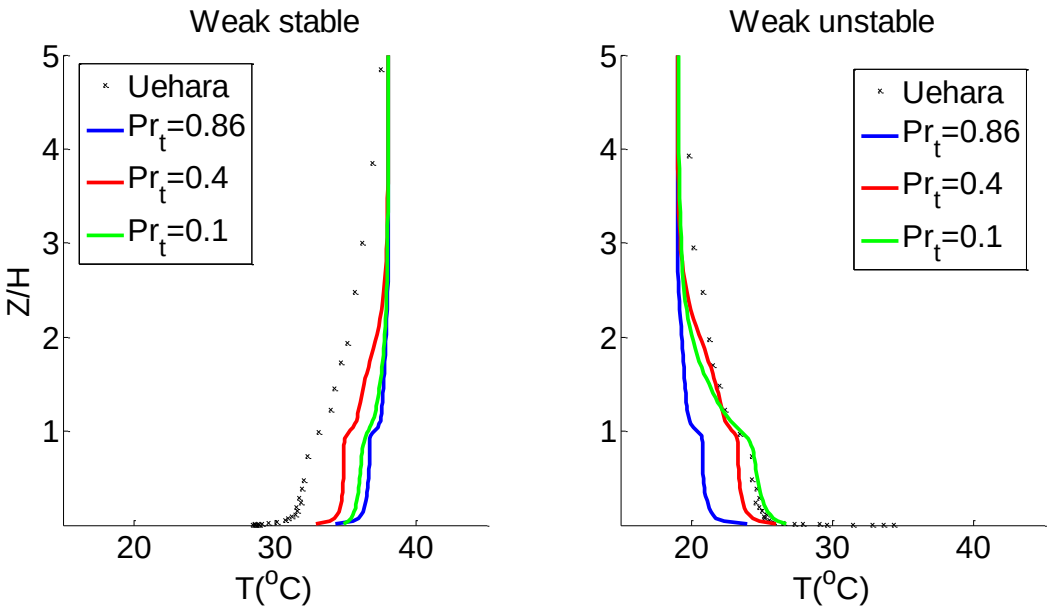

Figure 10.93: Hybrid T-profiles for investigated turbulent Prandtl numbers

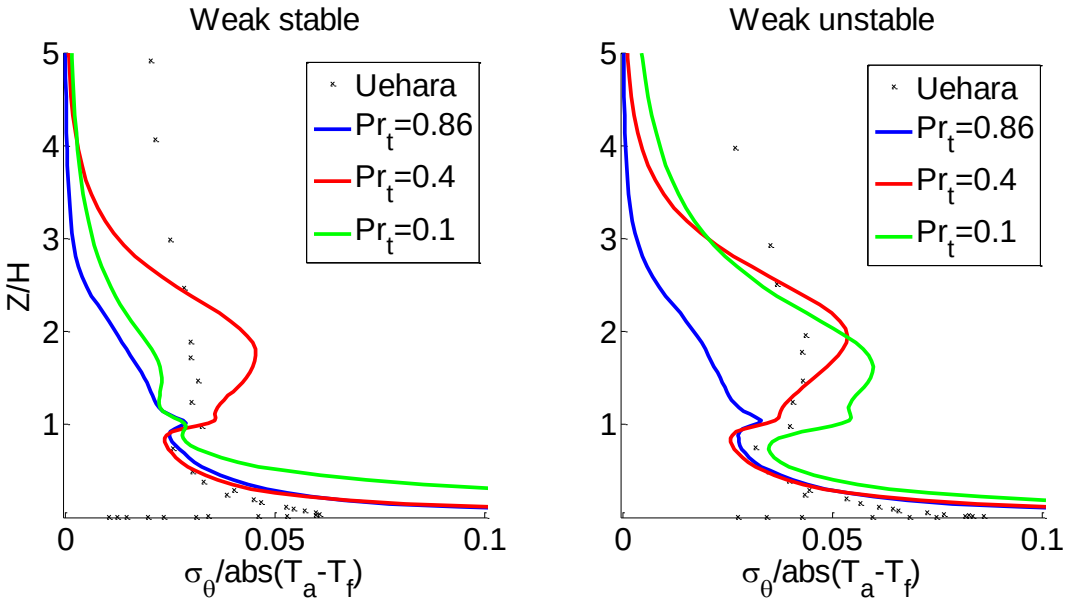

Figure 10.94: Hybrid σ_T-profiles for investigated turbulent Prandtl numbers

N. TURBULENT HEAT FLUX MODEL INVESTIGATIONS

N.1. Stable stratification

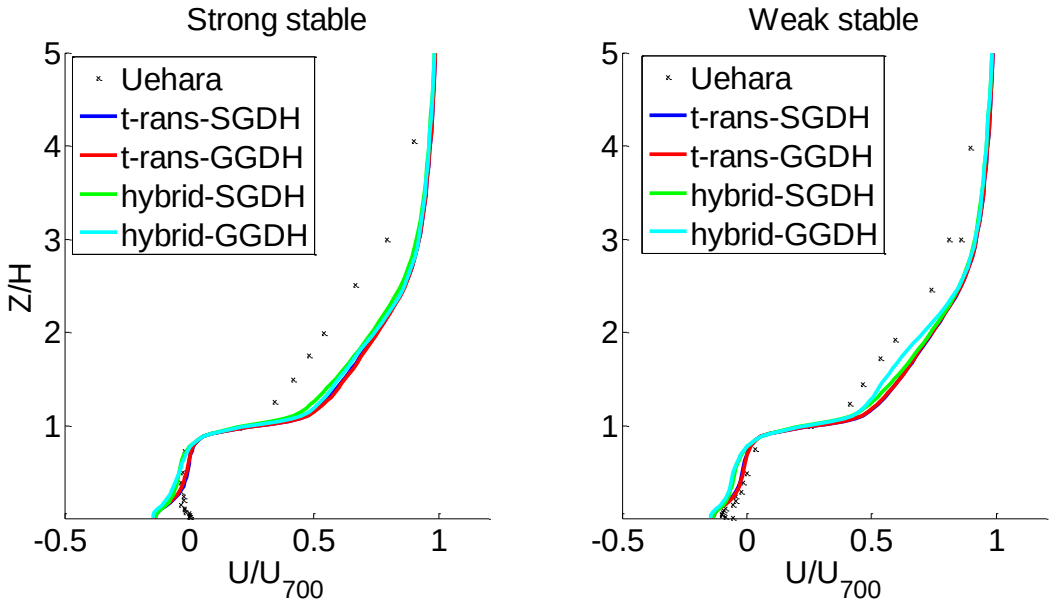

Figure 10.95: Stable stratification heat flux comparison U-profile plots

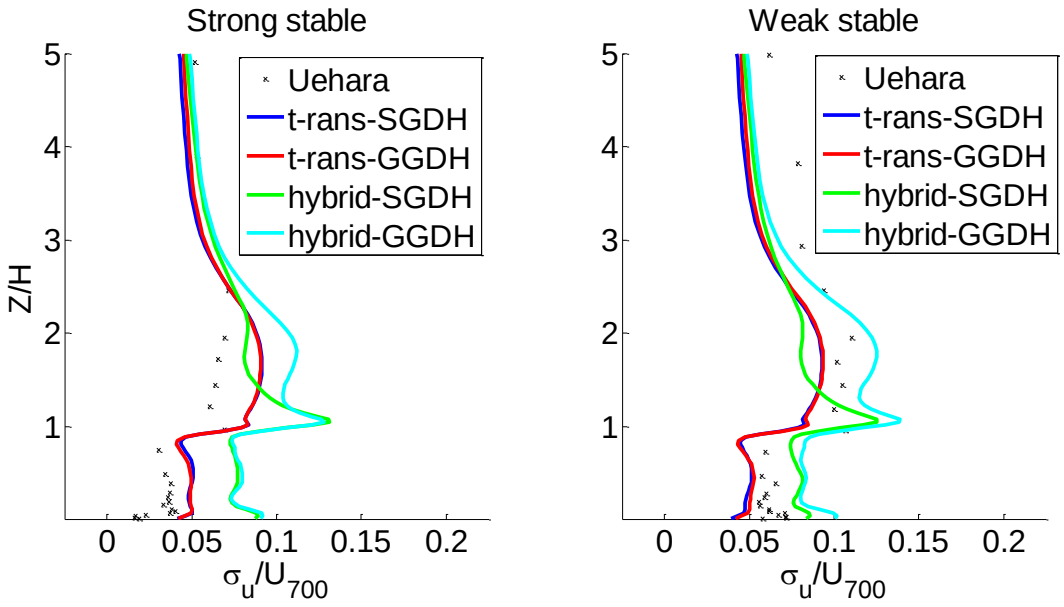

Figure 10.96: Stable stratification heat flux comparison σ_u-profile plots

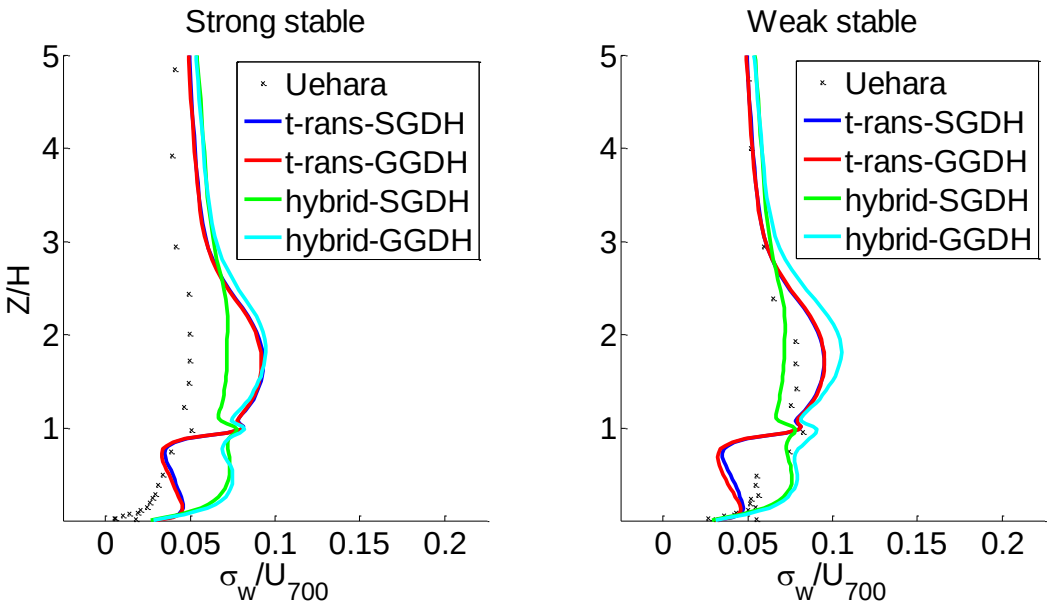

Figure 10.97: Stable stratification heat flux comparison σ_w-profile plots

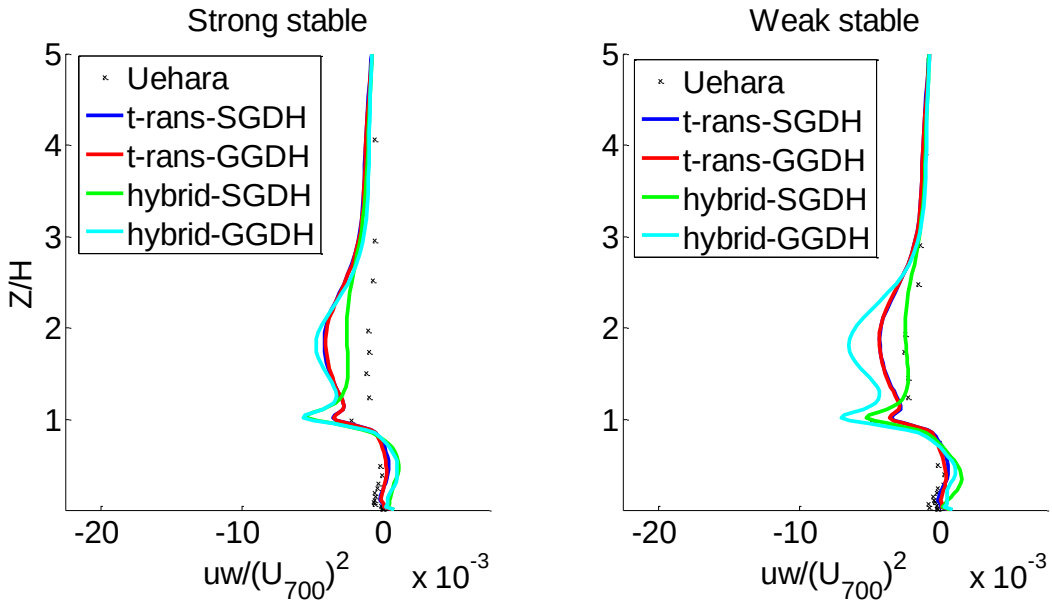

Figure 10.98: Stable stratification heat flux comparison uw-profile plots

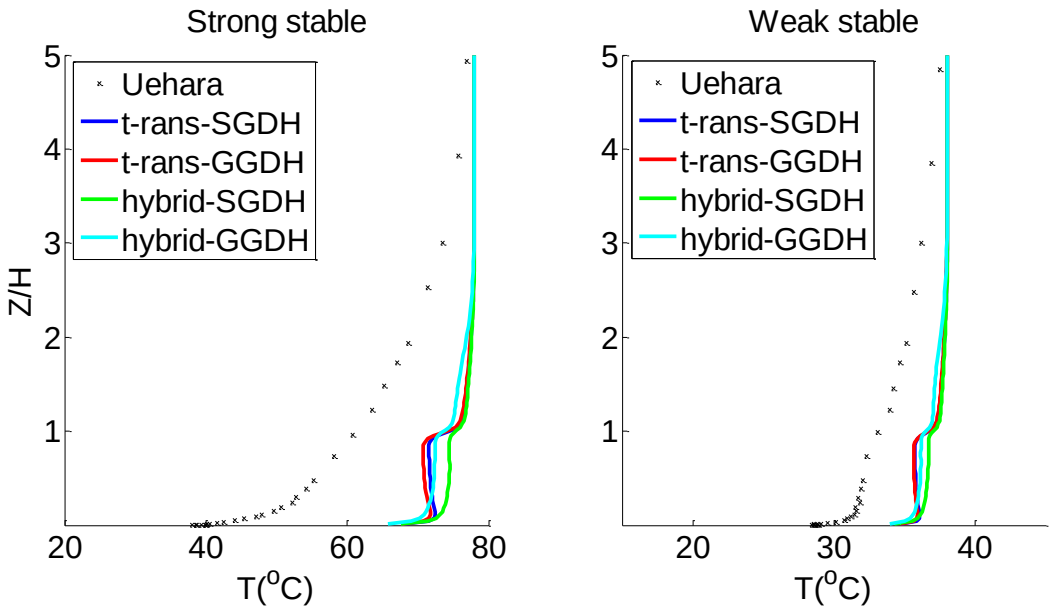

Figure 10.99: Stable stratification heat flux comparison T-profile plots

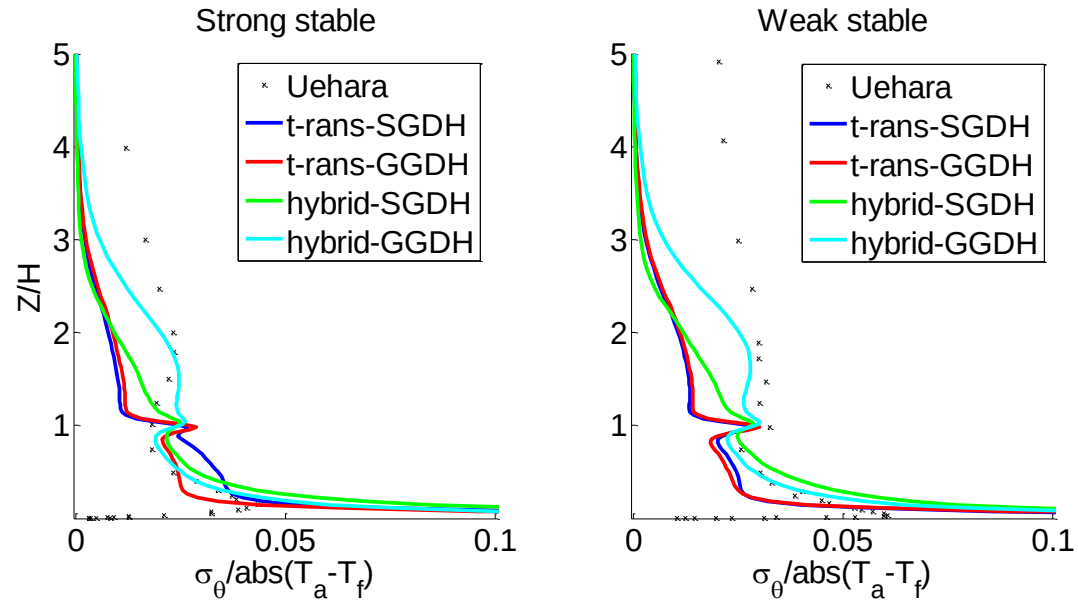

Figure 10.100: Stable stratification heat flux comparison σ_T-profile plots

N.2. Unstable stratification

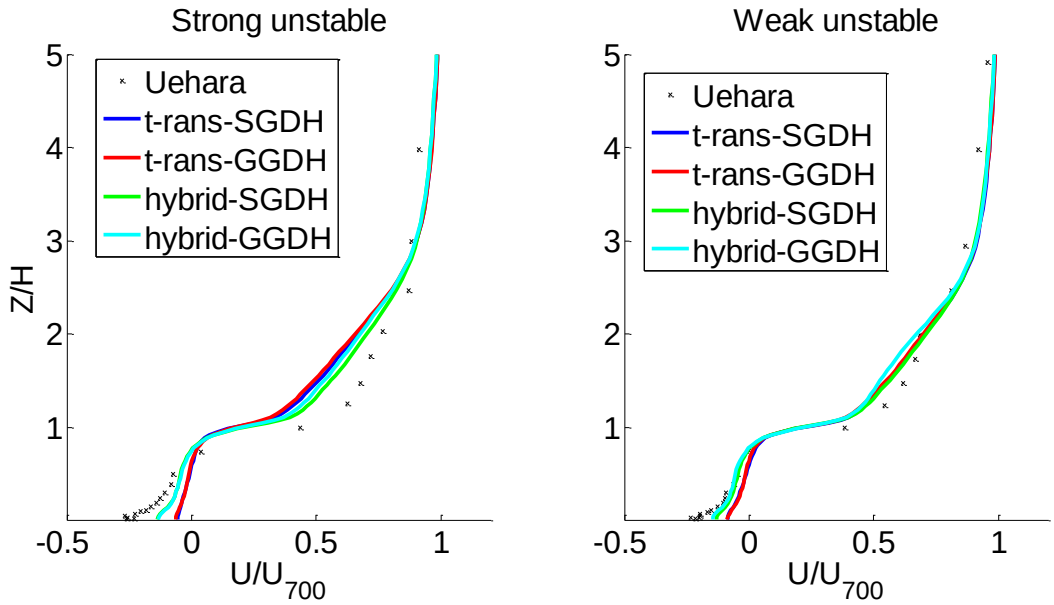

Figure 10.101: Unstable stratification heat flux comparison U-profile plots

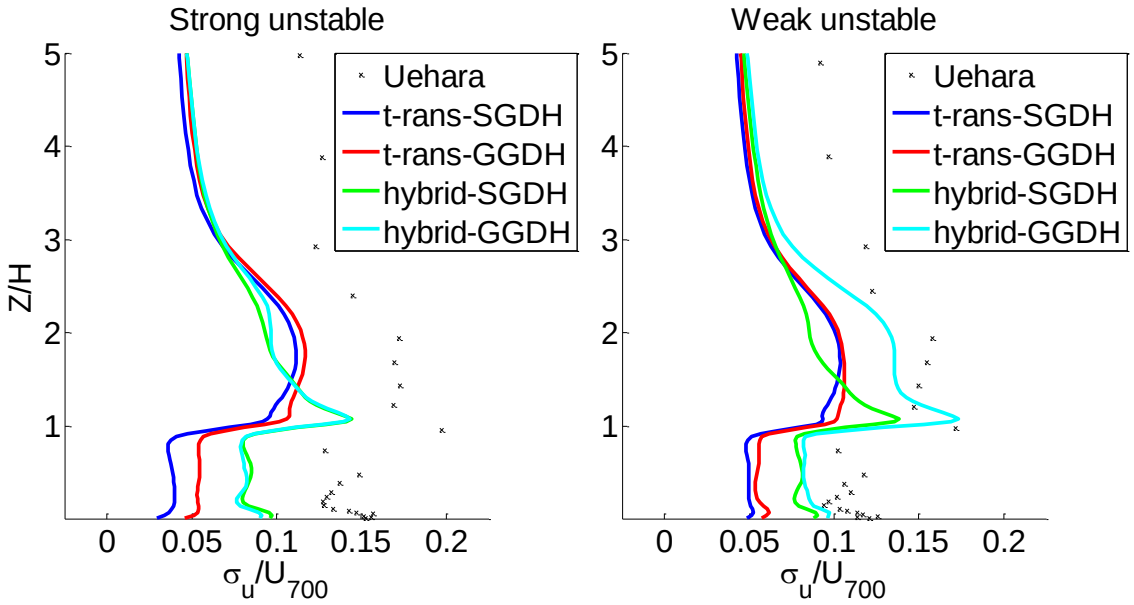

Figure 10.102: Unstable stratification heat flux comparison σ_u-profile plots

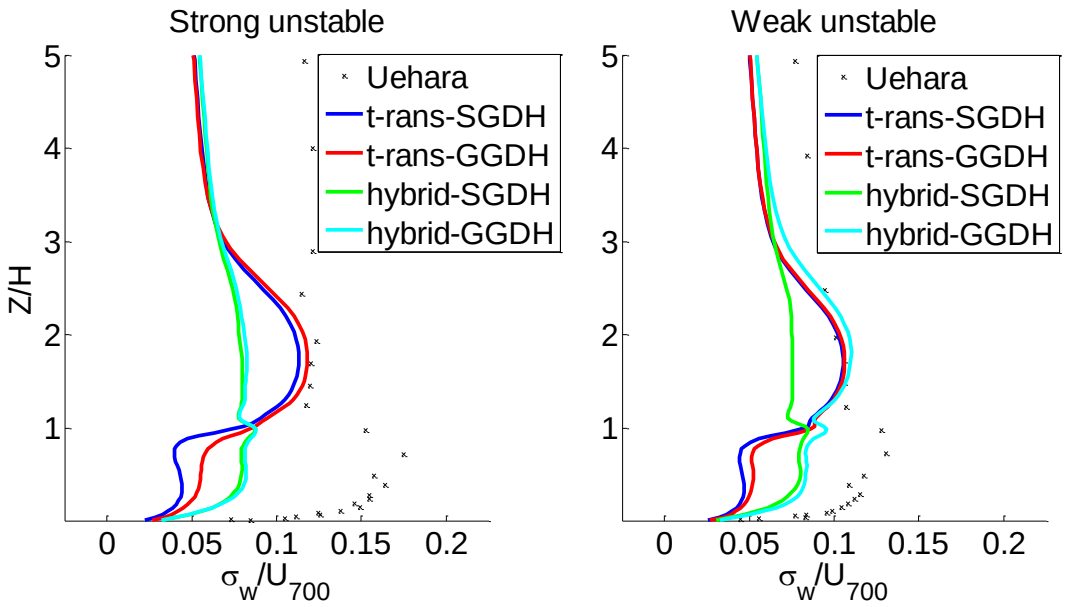

Figure 10.103: Unstable stratification heat flux comparison σ_w-profile plots

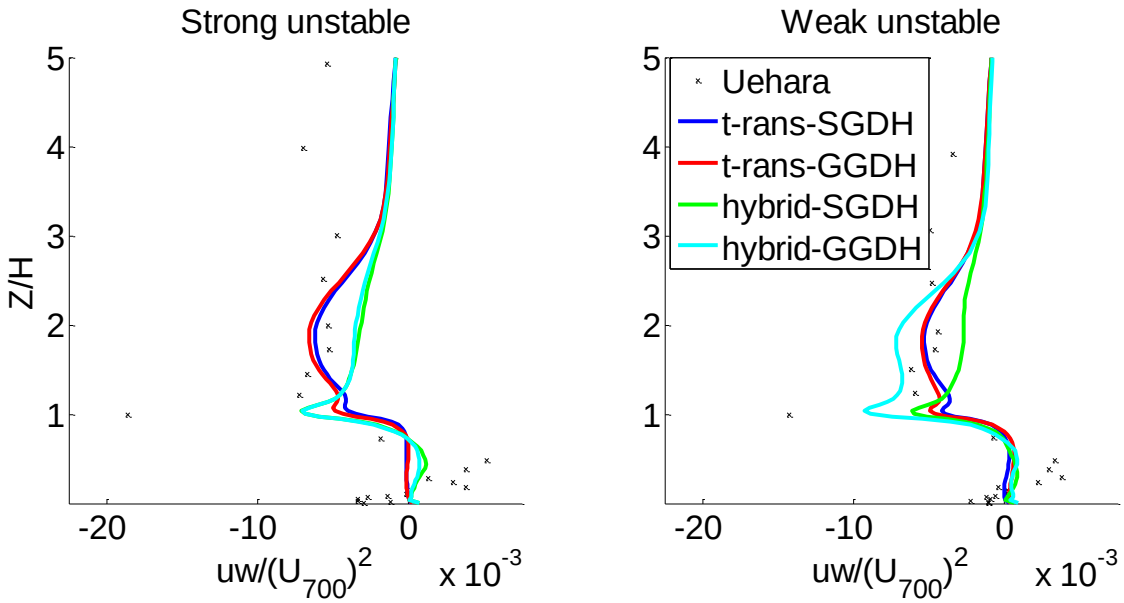

Figure 10.104: Unstable stratification heat flux comparison uw-profile plots

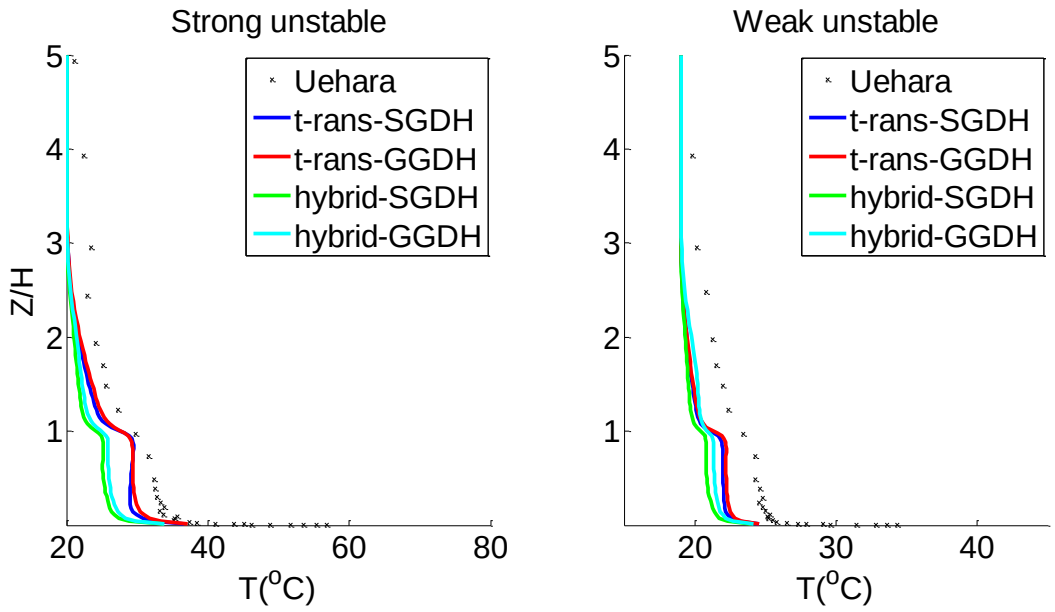

Figure 10.105: Unstable stratification heat flux comparison T-profile plots

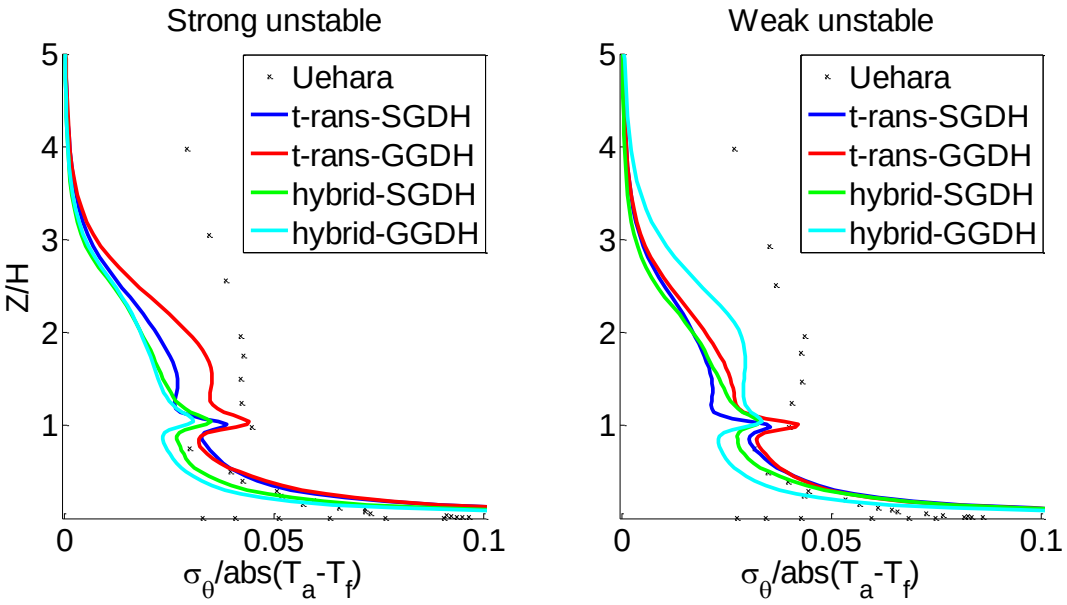

Figure 10.106: Unstable stratification heat flux comparison σ_T-profile plots

O. LES MODEL COMPARISONS WITH STANDARD MODELS

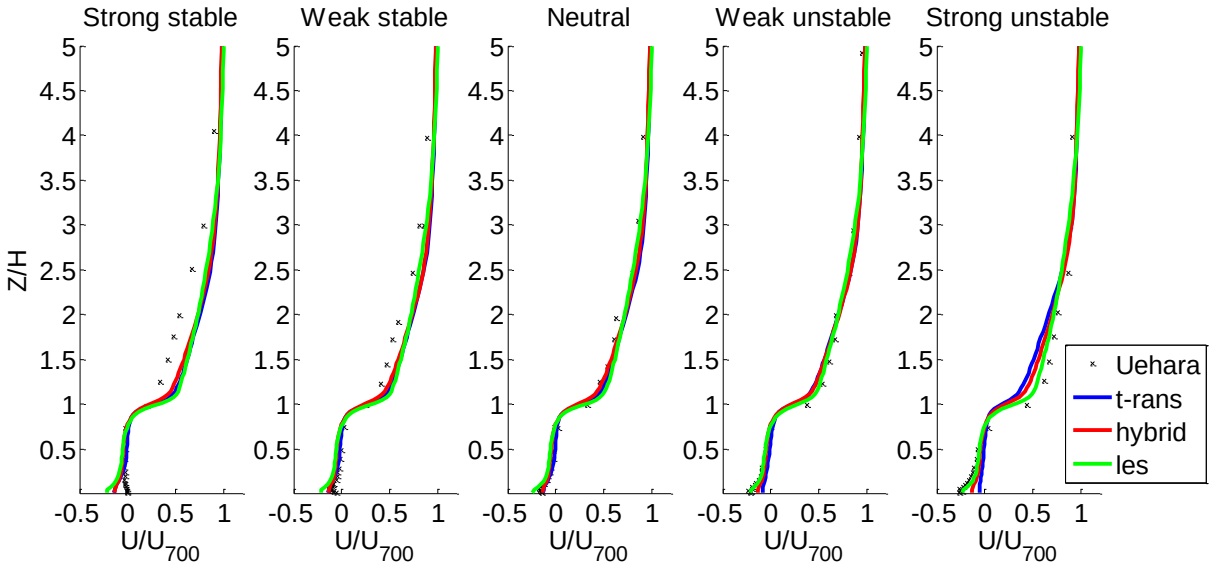

Figure 10.107: Plot of LES comparision of U-profile

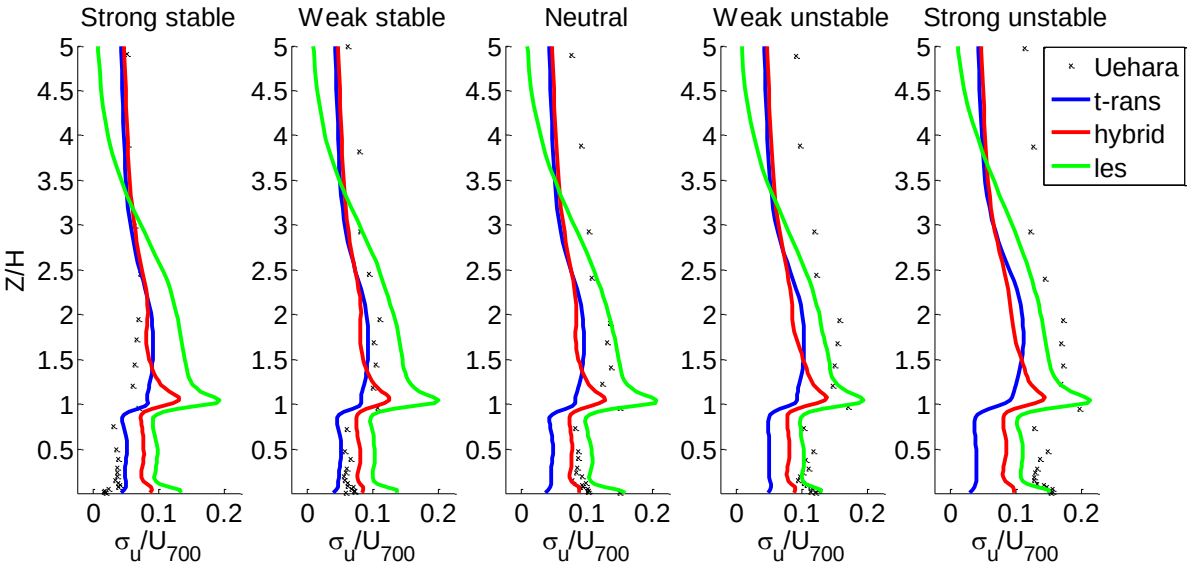

Figure 10.108: Plot of LES comparision of σ_u-profile

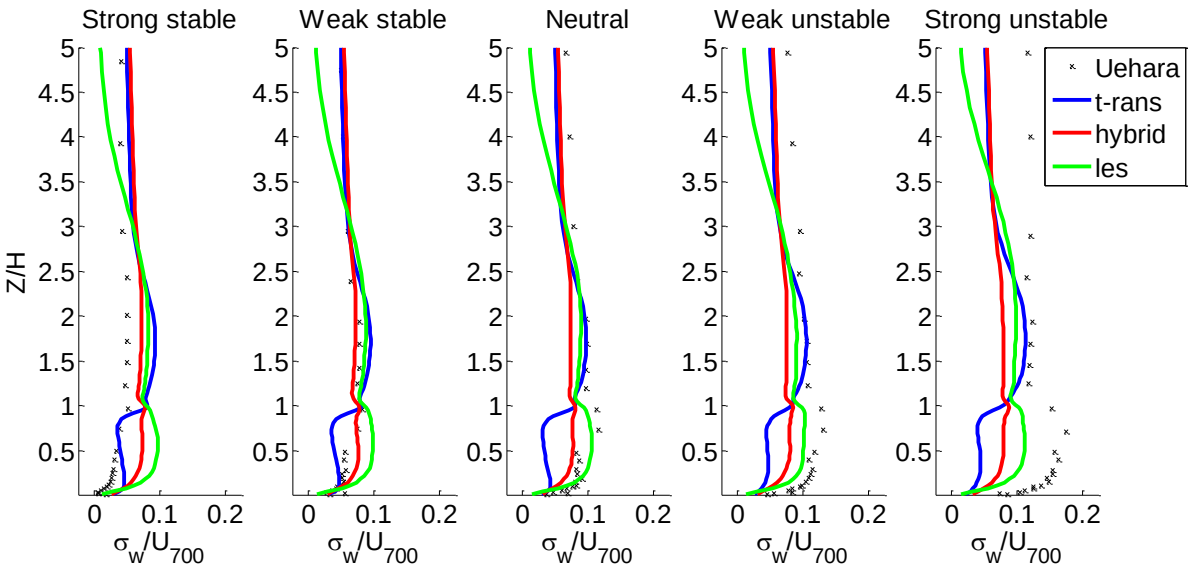

Figure 10.109: Plot of LES comparision of σ_w-profile

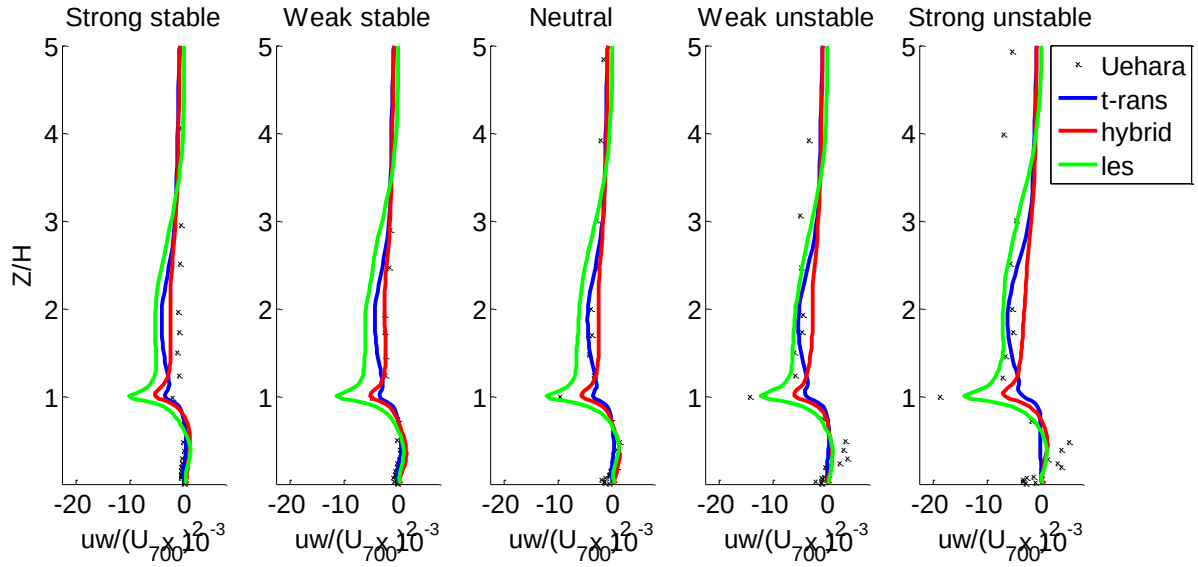

Figure 10.110: Plot of LES comparision of uw-profile

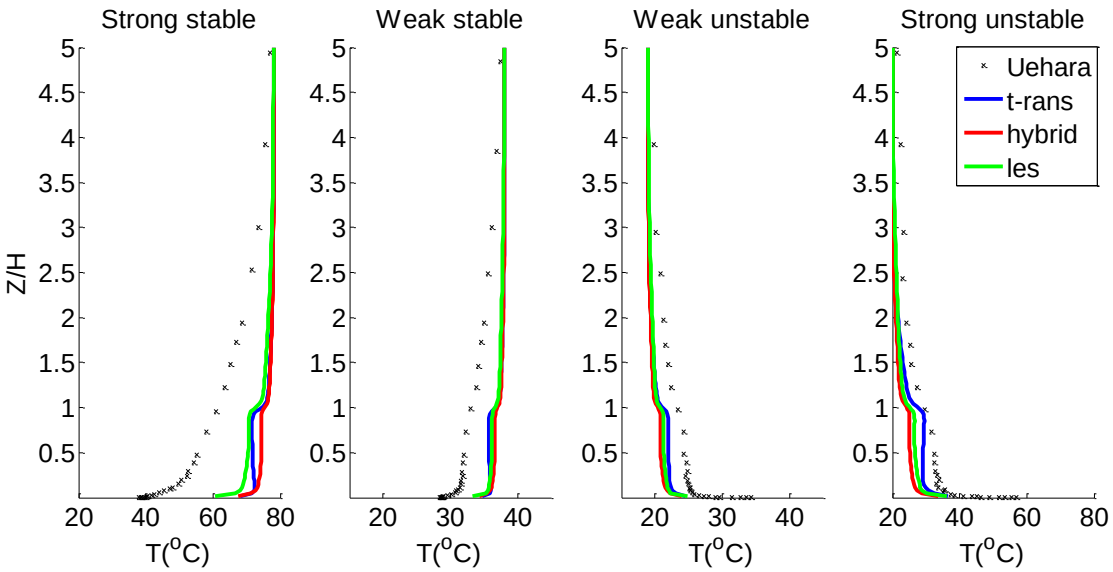

Figure 10.111: Plot of LES comparision of T-profile

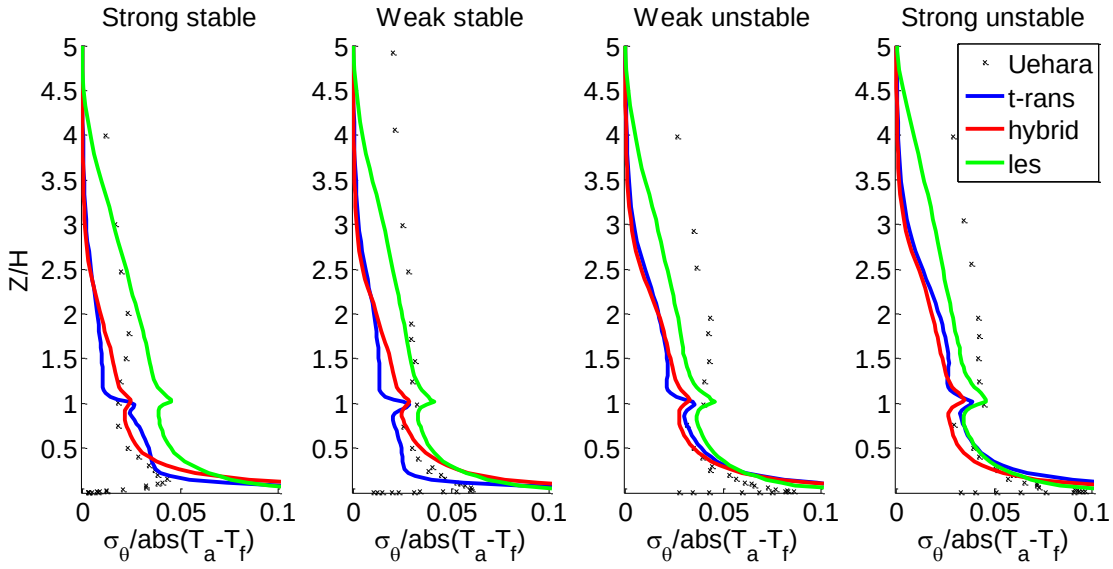

Figure 10.112: Plot of LES comparision of σ_T-profile

P. TURBULENT KINETIC ENERGY CONTOUR PLOTS

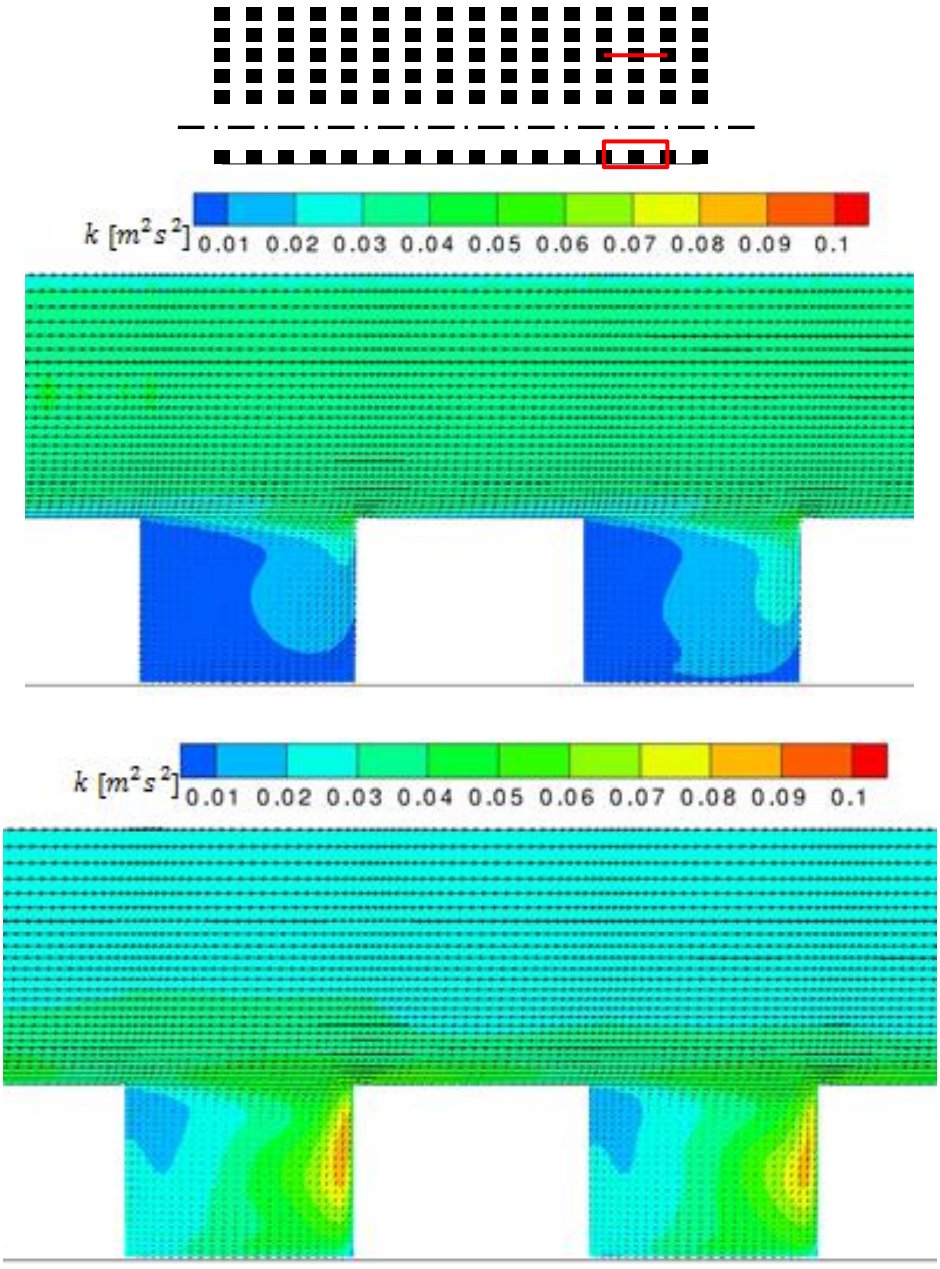

Figure 10.113: Neutral stratification k-profiles and velocity vectors

(top: T-RANS, bottom: hybrid)

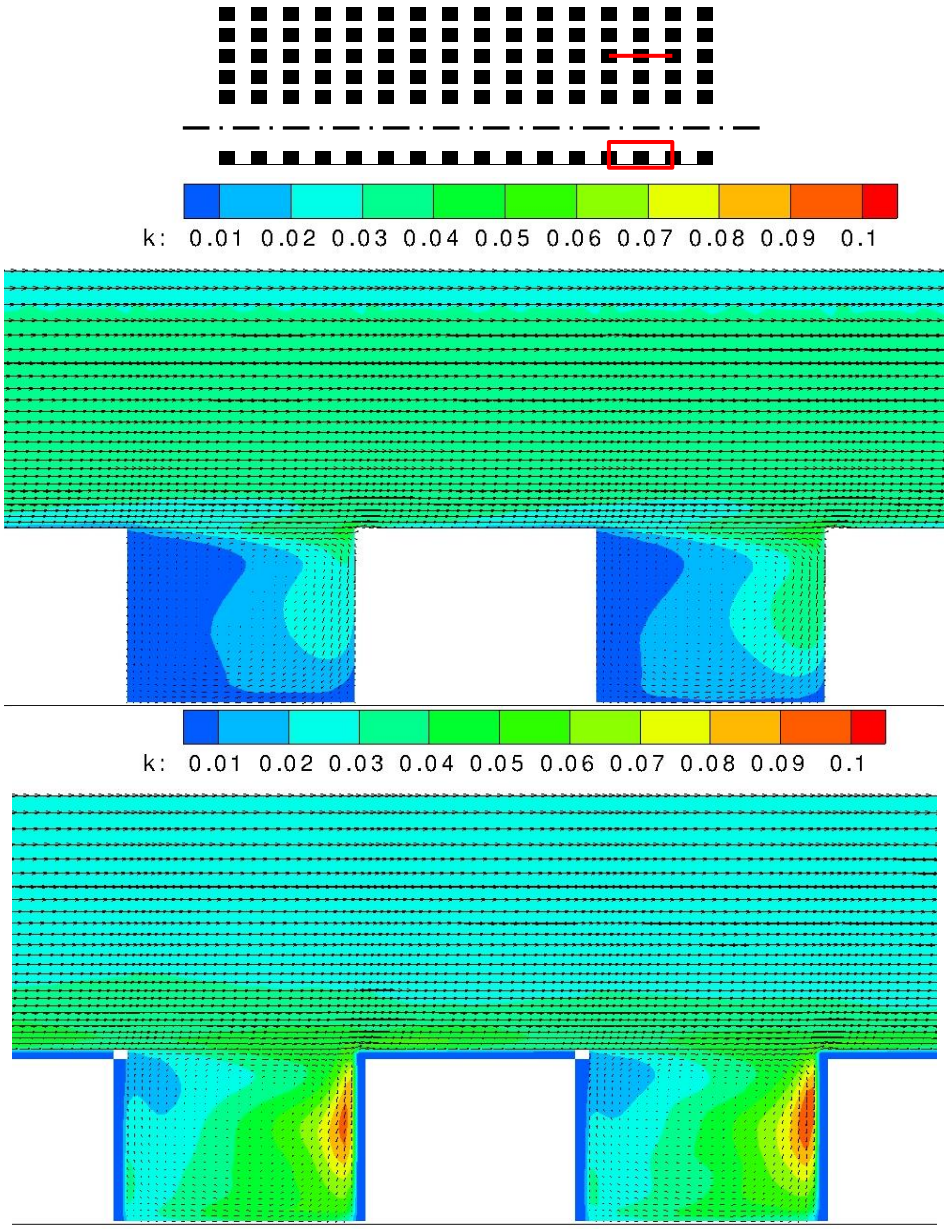

Figure 10.114: Strong stable stratification k-profiles and velocity vectors

(top: T-RANS, bottom: hybrid)

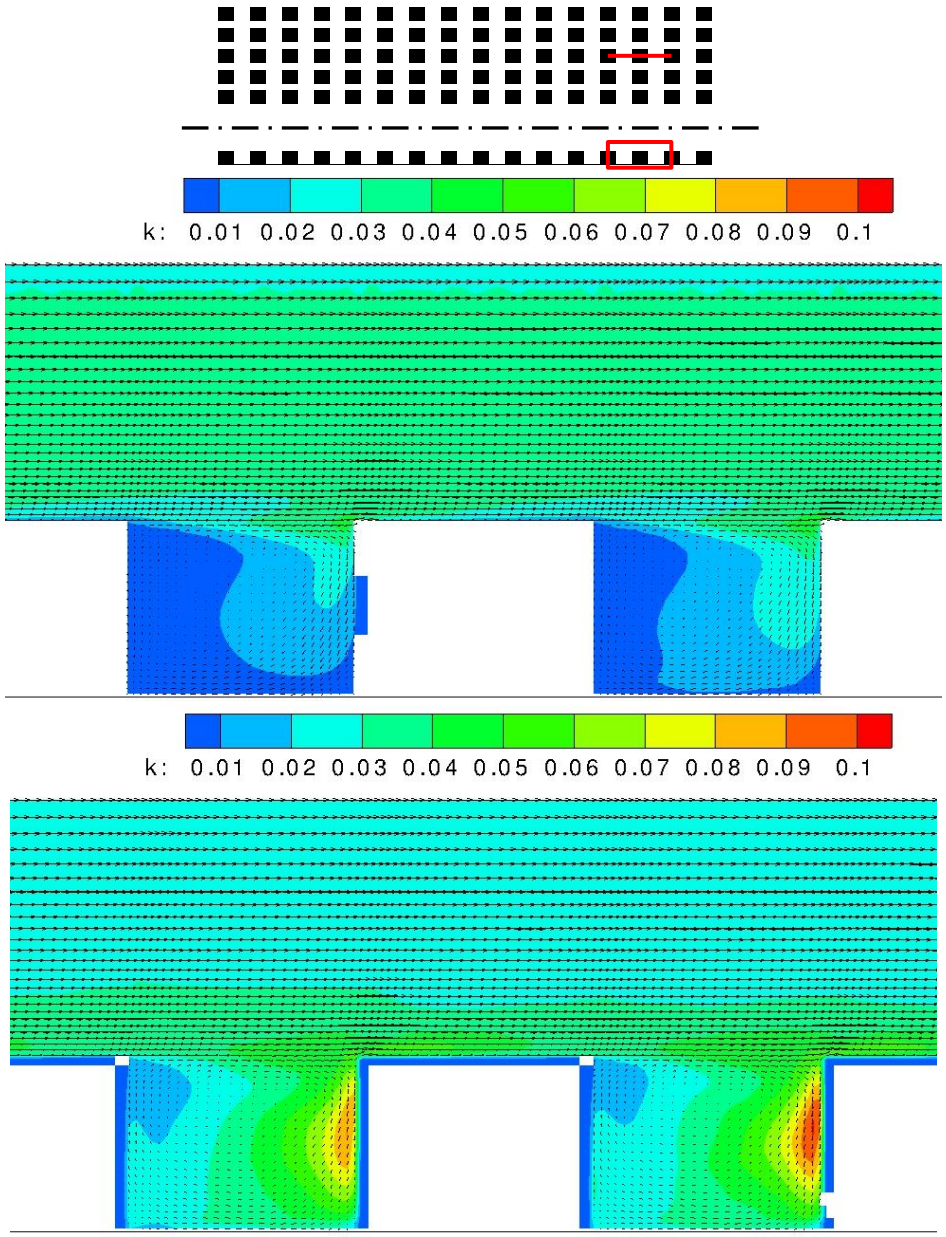

Figure 10.115: Weak stable stratification k-profiles and velocity vectors

(top: T-RANS, bottom: hybrid)

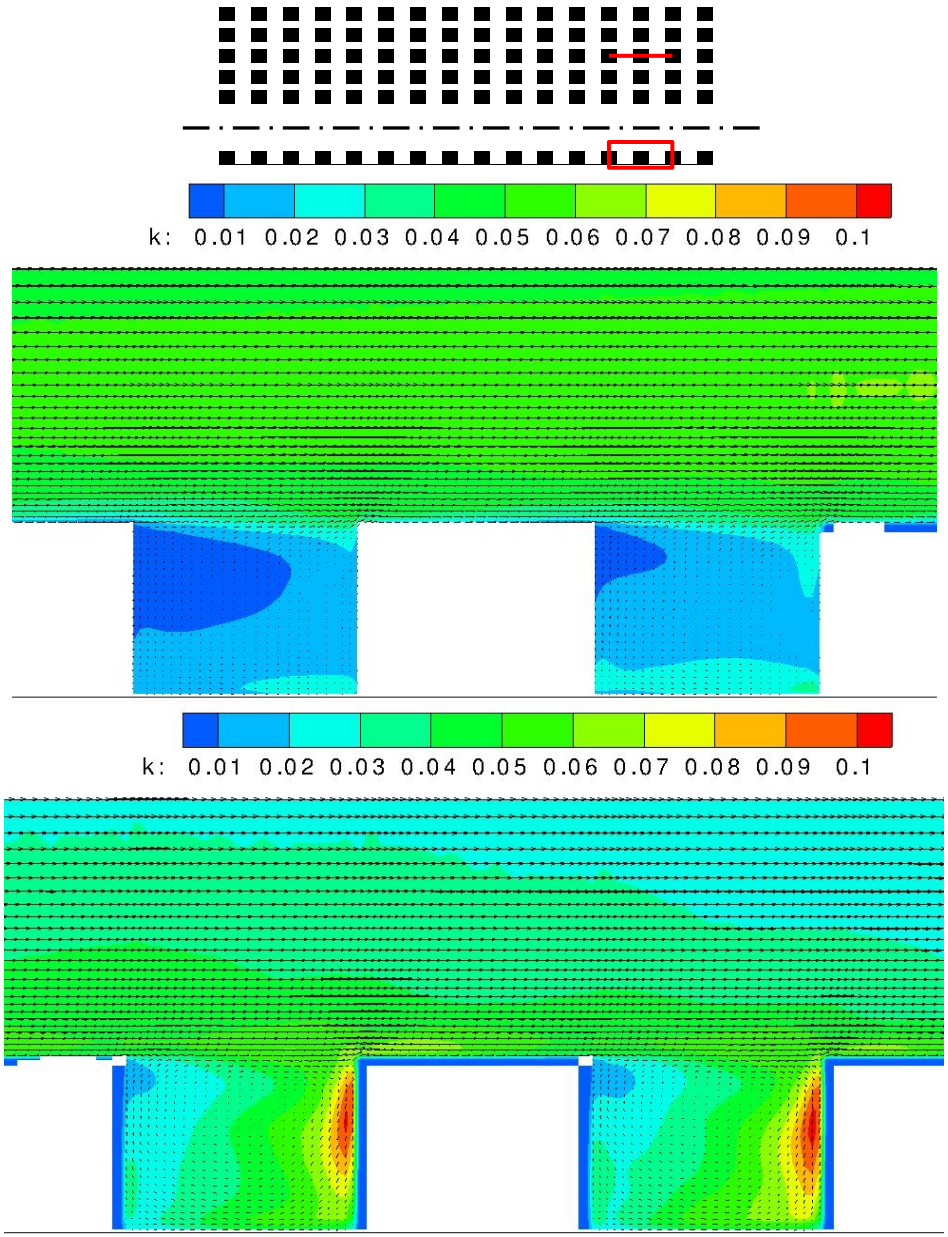

Figure 10.116: Strong unstable stratification k-profiles and velocity vectors

(top: T-RANS, bottom: hybrid)

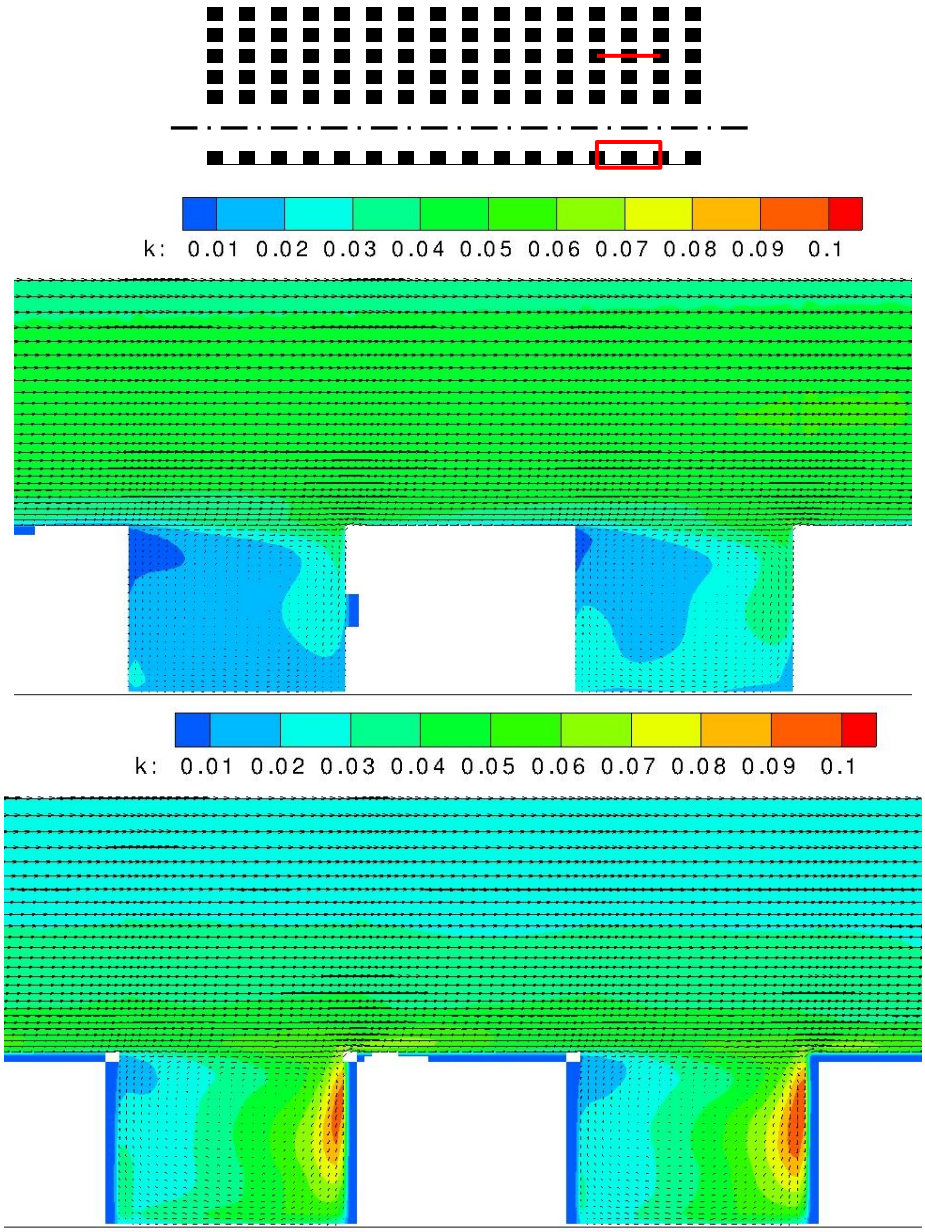

Figure 10.117: Weak unstable stratification k-profiles and velocity vectors

(top: T-RANS, bottom: hybrid)

Q. INVESTIGATION CASE SUMMARY

This appendix summarises this study's investigation cases, in the following table.

Case	Condition	Δt	model	Nu. Method	Change summary	
					summary	actual change
1	Strong unstable	0.5	T-RANS	SGDH	Time step	simulation_definition: (1) line 22 - TIMESTEP 1->0.5
2	Strong unstable	0.5	Hybrid	SGDH	Time step	simulation_definition: (1) line 22 - TIMESTEP 1->0.5
3	Strong unstable	1	T-RANS	SGDH	Base case	-
4	Strong unstable	1	Hybrid	SGDH	Base case	-
5	Strong unstable	2	T-RANS	SGDH	Time step	simulation_definition: (1) line 22 - TIMESTEP 1->2
6	Strong unstable	2	Hybrid	SGDH	Time step	simulation_definition: (1) line 22 - TIMESTEP 1->2
7	Weak unstable	0.5	T-RANS	SGDH	Time step	simulation_definition: (1) line 22 - TIMESTEP 1->0.5
8	Weak unstable	0.5	Hybrid	SGDH	Time step	simulation_definition: (1) line 22 - TIMESTEP 1->0.5
9	Weak unstable	1	T-RANS	SGDH	Base case	-
10	Weak unstable	1	Hybrid	SGDH	Base case	-
11	Weak unstable	2	T-RANS	SGDH	Time step	simulation_definition: (1) line 22 - TIMESTEP 1->2
12	Weak unstable	2	Hybrid	SGDH	Time step	simulation_definition: (1) line 22 - TIMESTEP 1->2
13	Neutral	0.5	T-RANS	SGDH	Time step	simulation_definition: (1) line 22 - TIMESTEP 1->0.5
14	Neutral	0.5	Hybrid	SGDH	Time step	simulation_definition: (1) line 22 - TIMESTEP 1->0.5
15	Neutral	1	T-RANS	SGDH	Base case	-
16	Neutral	1	Hybrid	SGDH	Base case	-
17	Neutral	2	T-RANS	SGDH	Time step	simulation_definition: (1) line 22 - TIMESTEP 1->2
18	Neutral	2	Hybrid	SGDH	Time step	simulation_definition: (1) line 22 - TIMESTEP 1->2

Case	Condition	Δt	model	Nu. Method	Change summary	
					summary	actual change
19	Weak stable	0.5	T-RANS	SGDH	Time step	simulation_definition: (1) line 22 - TIMESTEP 1->0.5
20	Weak stable	0.5	Hybrid	SGDH	Time step	simulation_definition: (1) line 22 - TIMESTEP 1->0.5
21	Weak stable	1	T-RANS	SGDH	Base case	-
22	Weak stable	1	Hybrid	SGDH	Base case	-
23	Weak stable	2	T-RANS	SGDH	Time step	simulation_definition: (1) line 22 - TIMESTEP 1->2
24	Weak stable	2	Hybrid	SGDH	Time step	simulation_definition: (1) line 22 - TIMESTEP 1->2
25	Strong stable	0.5	T-RANS	SGDH	Time step	simulation_definition: (1) line 22 - TIMESTEP 1->0.5
26	Strong stable	0.5	Hybrid	SGDH	Time step	simulation_definition: (1) line 22 - TIMESTEP 1->0.5
27	Strong stable	1	T-RANS	SGDH	Base case	-
28	Strong stable	1	Hybrid	SGDH	Base case	-
29	Strong stable	2	T-RANS	SGDH	Time step	simulation_definition: (1) line 22 - TIMESTEP 1->2
30	Strong stable	2	Hybrid	SGDH	Time step	simulation_definition: (1) line 22 - TIMESTEP 1->2
31	Strong unstable	1	T-RANS	SGDH	Modified ε_inlet	create_inlet.f90 (1) line 74 - ed=0.9*tke**2/(500.*1.8e-5) --> ed=0.9*tke**2/(2000.*1.8e-5)
32	Strong unstable	1	Hybrid	SGDH	Modified ε_inlet	create_inlet.f90 (1) line 74 - ed=0.9*tke**2/(500.*1.8e-5) --> ed=0.9*tke**2/(2000.*1.8e-5)
33	Strong stable	1	T-RANS	SGDH	Modified ε_inlet	create_inlet.f90 (1) line 74 - ed=0.9*tke**2/(500.*1.8e-5) --> ed=0.9*tke**2/(2000.*1.8e-5)
34	Strong stable	1	Hybrid	SGDH	Modified ε_inlet	create_inlet.f90 (1) line 74 - ed=0.9*tke**2/(500.*1.8e-5) --> ed=0.9*tke**2/(2000.*1.8e-5)
35	Weak unstable	1	Hybrid	SGDH	Modified Pr_t	streetcanyon.f90 (1) line 7239 from 0.86 -> 0.4

Case	Condition	Δt	model	Nu. Method	Change summary	
					summary	actual change
36	Weak unstable	1	Hybrid	SGDH	Modified Pr_t	streetcanyon.f90 (1) line 7239 from 0.86 -> 0.1
37	Weak stable	1	Hybrid	SGDH	Modified Pr_t	streetcanyon.f90 (1) line 7239 from 0.86 -> 0.4
38	Weak stable	1	Hybrid	SGDH	Modified Pr_t	streetcanyon.f90 (1) line 7239 from 0.86 -> 0.1
39	Weak unstable	1	Hybrid	SGDH	Adapted modified Pr_t	streetcanyon.f90 (1) line 2471: SU(INP)=SU(INP)-DTERM1DX-DTERM2DY-DTERM3DZ commented
40	Weak unstable	1	Hybrid	SGDH	Adapted modified Pr_t	streetcanyon.f90 (1) line 7239 from 0.86 -> 0.4 (2) line 2471: SU(INP)=SU(INP)-DTERM1DX-DTERM2DY-DTERM3DZ commented
41	Weak unstable	1	Hybrid	SGDH	Adapted modified Pr_t	streetcanyon.f90 (1) line 7239 from 0.86 -> 0.1 (2) line 2471: SU(INP)=SU(INP)-DTERM1DX-DTERM2DY-DTERM3DZ commented
42	Weak stable	1	Hybrid	SGDH	Adapted modified Pr_t	streetcanyon.f90 (1) line 2471: SU(INP)=SU(INP)-DTERM1DX-DTERM2DY-DTERM3DZ commented
43	Weak stable	1	Hybrid	SGDH	Adapted modified Pr_t	streetcanyon.f90 (1) line 7239 from 0.86 -> 0.4 (2) line 2471: SU(INP)=SU(INP)-DTERM1DX-DTERM2DY-DTERM3DZ commented
44	Weak stable	1	Hybrid	SGDH	Adapted modified Pr_t	streetcanyon.f90 (1) line 7239 from 0.86 -> 0.1 (2) line 2471: SU(INP)=SU(INP)-DTERM1DX-DTERM2DY-DTERM3DZ commented
45	Strong unstable	1	T-RANS	GGDH	Switch to GGDH	simulation_definition: (1) SGDH->GGDH; (2) FACFLX 1->0.1; (3) URF(I) (U V W T VIS VART) 0.4 0.4 0.4 0.1 0.4 0.4 0.4 0.4 0.4 0.8 0.7 0.6 0.6 -> 0.1 0.1 0.1 0.1 0.2 0.1 0.1 0.1 0.1 0.8 0.7 0.6 0.6 (4) GDS(I) (T) 1->0.1

Case	Condition	Δt	model	Nu. Method	Change summary	
					summary	**actual change**
						streetcanyon.f90 (5) comment line 2471: ! SU(INP)=SU(INP)-DTERM1DX-DTERM2DY-DTERM3DZ
46	Strong unstable	1	Hybrid	GGDH	Switch to GGDH	simulation_definition: (1) SGDH->GGDH; (2) GDS(I) (T) 1->0.1 streetcanyon.f90 (3) comment line 2471: ! SU(INP)=SU(INP)-DTERM1DX-DTERM2DY-DTERM3DZ
47	Weak unstable	1	T-RANS	GGDH	Switch to GGDH	simulation_definition: (1) SGDH->GGDH; (2) FACFLX 1->0.1; (3) URF(I) (U V W T VIS VART) 0.4 0.4 0.4 0.1 0.4 0.4 0.4 0.4 0.4 0.8 0.7 0.6 0.6 -> 0.1 0.1 0.1 0.1 0.2 0.1 0.1 0.1 0.1 0.8 0.7 0.6 0.6 (4) GDS(I) (T) 1->0.1 streetcanyon.f90 (5) comment line 2471: ! SU(INP)=SU(INP)-DTERM1DX-DTERM2DY-DTERM3DZ
48	Weak unstable	1	Hybrid	GGDH	Switch to GGDH	simulation_definition: (1) SGDH->GGDH; (2) FACFLX 1->0.1; (3) URF(I) (U V W T VIS VART) 0.4 0.4 0.4 0.1 0.4 0.4 0.4 0.4 0.4 0.8 0.7 0.6 0.6 -> 0.2 0.2 0.2 0.1 0.4 0.4 0.2 0.2 0.2 0.8 0.7 0.6 0.6; (4) GDS(I) (T) 1->0.1 streetcanyon.f90 (5) comment line 2471: ! SU(INP)=SU(INP)-DTERM1DX-DTERM2DY-DTERM3DZ
49	Weak stable	1	T-RANS	GGDH	Switch to GGDH	simulation_definition: (1) SGDH->GGDH; (2) FACFLX 1->0.1; (3) URF(I) (U V W T VIS VART) 0.4 0.4 0.4 0.1 0.4 0.4 0.4 0.4 0.4 0.8 0.7 0.6 0.6 -> 0.2 0.2 0.2 0.1 0.4 0.4 0.2 0.2 0.2 0.8 0.7 0.6 0.6

Case	Condition	Δt	model	Nu. Method	Change summary	
					summary	**actual change**
						(4) GDS(I) (T) 1->0.1 streetcanyon.f90 (5) comment line 2471: ! SU(INP)=SU(INP)-DTERM1DX-DTERM2DY-DTERM3DZ
50	Weak stable	1	Hybrid	GGDH	Switch to GGDH	simulation_definition: (1) SGDH->GGDH; (2) FACFLX 1->0.1; (3) URF(I) (U V W T VIS VART) 0.4 0.4 0.4 0.1 0.4 0.4 0.4 0.4 0.4 0.8 0.7 0.6 0.6 -> 0.2 0.2 0.2 0.1 0.4 0.4 0.2 0.2 0.2 0.8 0.7 0.6 0.6 (4) GDS(I) (T) 1->0.1 streetcanyon.f90 (5) comment line 2471: ! SU(INP)=SU(INP)-DTERM1DX-DTERM2DY-DTERM3DZ
51	Strong stable	1	T-RANS	GGDH	Switch to GGDH	simulation_definition: (1) SGDH->GGDH; (2) FACFLX 1->0.1; (3) URF(I) (U V W T VIS VART) 0.4 0.4 0.4 0.1 0.4 0.4 0.4 0.4 0.4 0.8 0.7 0.6 0.6 -> 0.2 0.2 0.2 0.1 0.4 0.4 0.2 0.2 0.2 0.8 0.7 0.6 0.6; (4) GDS(I) (T) 1->0.1 streetcanyon.f90 (5) comment line 2471: ! SU(INP)=SU(INP)-DTERM1DX-DTERM2DY-DTERM3DZ
52	Strong stable	1	Hybrid	GGDH	Switch to GGDH	simulation_definition: (1) SGDH->GGDH; (2) FACFLX 1->0.1; (3) URF(I) (U V W T VIS VART) 0.4 0.4 0.4 0.1 0.4 0.4 0.4 0.4 0.4 0.8 0.7 0.6 0.6 -> 0.2 0.2 0.2 0.1 0.4 0.4 0.2 0.2 0.2 0.8 0.7 0.6 0.6; (4) GDS(I) (T) 1->0.1 streetcanyon.f90 (5) comment line 2471: ! SU(INP)=SU(INP)-DTERM1DX-DTERM2DY-DTERM3DZ

Case	Condition	Δt	model	Nu. Method	Change summary	
					summary	**actual change**
53	Strong unstable	1	Hybrid	GGDH	Switch to modified GGDH	simulation_definition: (1) SGDH->GGDH; (3) URF(I) (U V W T VIS VART) 0.4 0.4 0.4 0.1 0.4 0.4 0.4 0.4 0.4 0.8 0.7 0.6 0.6 -> 0.2 0.2 0.2 0.1 0.2 0.2 0.4 0.4 0.4 0.8 0.7 0.6 0.6; (4) GDS(I) (T) 1->0.1 streetcanyon.f90 (5) comment line 2471: ! SU(INP)=SU(INP)-DTERM1DX-DTERM2DY-DTERM3DZ
54	Neutral	1	T-RANS	SGDH	Inlet velocity profile	create_inlet.f90 (1) line 60 - u=1.6*(z_points(k)/0.5)**(1/6) -> u=1.5384*(z_points(k)/0.7)**(1.0/4.0084)
55	Neutral	1	Hybrid	SGDH	Inlet velocity profile	create_inlet.f90 (1) line 60 - u=1.6*(z_points(k)/0.5)**(1/6) -> u=1.5384*(z_points(k)/0.7)**(1.0/4.0084)